Dissertation

On Glueballs, Pomeron, and Odderon in Holographic Quantum Chromodynamics:

From Hadron Spectroscopy to Collider Phenomenology

ausgeführt zum Zwecke der Erlangung
des akademischen Grades eines
Doktors der Naturwissenschaften

unter der Anleitung von

Univ.-Prof. Dr.techn. **Anton Rebhan**
Institut für Theoretische Physik (E136)
TU Wien

eingereicht an der
Technischen Universität Wien,
Fakultät für Physik

von

Dipl.-Ing. **Florian Hechenberger**, BSc.
Matrikelnummer: 1327739
Wienerbergstraße 12/24/12,
A-1120 Wien

Wien, am 18. Juli 2024

Florian Hechenberger
On Glueballs, Pomeron, and Odderon
in Holographic Quantum Chromodynamics:
From Hadron Spectroscopy to Collider Phenomenology

Gutachter:
Univ.-Prof. Dr.rer.nat. Reinhard Alkofer, University of Graz
Dr. Yoshitaka Hatta, Brookhaven National Laboratory

Betreuer:
Univ.-Prof. Dr.techn. Anton Rebhan, TU Wien

TU Wien
Institut für Theoretische Physik
Wiedner Hauptstrasse 8-10/E136
A-1040, Wien

To my parents,
Petra and Roland Hechenberger

Abstract

Quantum Chromodynamics (QCD) is the widely accepted theory governing the dynamics of quarks and gluons, the force carriers of the strong interaction. While many properties of hadrons, composite states of quarks bound by gluons, may be understood in terms of their quark content, gluons play a prominent role in mass generation, high-energy scattering processes, and the very nature of confinement itself. One of the most striking predictions of QCD is the existence of bound states comprised solely of valence gluons, known as glueballs. While their existence is supported by computer simulations, experimental evidence remains elusive, with theoretical computations often yielding conflicting results.

The development of high-energy colliders, culminating in the Large Hadron Collider (LHC) at CERN, has revealed a rich landscape of gluon-dominated phenomena. The Pomeron, initially postulated to explain rising total scattering cross sections in high-energy data, is now recognized as a fundamental prediction of QCD, reflecting collective gluon dynamics at high energies. Furthermore, the recent claim of the Odderon discovery at the LHC and Tevatron, the Pomeron's C-odd partner, has the potential to significantly deepen our understanding of the strong interaction by studying fundamental processes associated with it, though this claim is not without controversy.

Over the last three decades, a novel approach to understanding the fundamental nature of strongly coupled systems has emerged, known as the AdS/CFT correspondence. This duality, initially formulated between highly symmetric superstring and field theories, has found successful applications in less symmetric systems, which eventually led to the construction of holographic QCD. In this thesis, we explore the extent to which QCD in the confining phase may be described by a weakly coupled, higher-dimensional gravitational theory. We investigate glueball properties using holographic hadron spectroscopy within a type IIA superstring theory brane construction. This approach allows for the determination of glueball masses, decay channels, and mixing. We further apply holographic Regge physics through bottom-up models to analyze high-energy collider data, with a particular focus on the physics of the Pomeron and Odderon. By deepening our theoretical understanding and providing testable predictions for collider experiments, this research aims to contribute to our understanding of the strong interaction and rich gluon dynamics in the high-energy regime.

Kurzfassung

Quantenchromodynamik (QCD) ist die weithin akzeptierte Theorie, die die Dynamik von Quarks und Gluonen, den Austauschteilchen der starken Wechselwirkung, beschreibt. Während viele Eigenschaften von Hadronen, Bindungszuständen aus Quarks und Gluonen, durch die konstituierenden Quarks erklärt werden können, spielen Gluonen eine prominente Rolle bei der Erzeugung von Masse, hochenergetischen Streuprozessen und dem zugrundeliegenden Confinement. Eine der bemerkenswertesten Vorhersagen der QCD ist die Existenz von Glueballs, Bindungszuständen, die nur aus Valenzgluonen bestehen. Während ihre Existenz von Computersimulationen bestätigt wird, sind eindeutige experimentelle Nachweise ausstehend und theoretische Vorhersagen oft nicht untereinander kompatibel.

Die Entwicklung von Hochenergiebeschleunigern, die in dem Bau des Large Hadron Colliders (LHC) am CERN gipfelte, hat eine breite Landschaft an gluonendominierten Phänomenen offenbart. Das Pomeron, welches ursprünglich postuliert wurde, um den Anstieg totaler Wirkungsquerschnitte in Hochenergiedaten zu erklären, wird heute als eine fundamentale Vorhersage der QCD in Form von kollektiven Wechselwirkungen von Gluonen verstanden. Obwohl nicht unumstritten, hat die jüngste Entdeckung des Odderons am LHC und Tevatron, der Partner des Pomerons mit ungerader Ladungsparität, das Potenzial, unser Verständnis der starken Wechselwirkung durch die Untersuchung grundlegender Prozesse, die mit ihm verbunden sind, erheblich zu vertiefen.

In den letzten drei Jahrzehnten hat sich ein neuer Ansatz zum Verständnis der grundlegenden Natur stark gekoppelter Systeme entwickelt, der als AdS/CFT-Korrespondenz bekannt ist. Diese Dualität, die ursprünglich zwischen hochsymmetrischen Superstring- und Feldtheorien formuliert wurde, hat erfolgreiche Anwendungen in weniger symmetrischen Systemen gefunden, was zur Konstruktion der holographischen QCD führte. In dieser Arbeit untersuchen wir, inwieweit die stark gekoppelte Phase der QCD durch eine schwach gekoppelte, höherdimensionale Gravitationstheorie beschrieben werden kann. Wir untersuchen die Eigenschaften von Glueballs durch holographische Hadronenspektroskopie mittels einer Branenkonstruktion in Typ IIA Superstringtheorie. Dieser Ansatz ermöglicht die Bestimmung von Massen, Zerfallskanälen und Mischungen von Glueballs. Darüber hinaus konstruieren wir holographische Bottom-up-Modelle, um Daten von Hochenergiebeschleunigern im Regge-Regime zu analysieren, wobei besonderes Augenmerk auf die Physik des Pomerons und Odderons gelegt wird. Durch die Vertiefung unseres theoretischen Verständnisses und die Bereitstellung überprüfbarer Vorhersagen für Beschleuingerexperimente soll diese Forschung zu unserem Verständnis der starken Wechselwirkung und der Dynamik der Gluonen im Hochenergiebereich beitragen.

Acknowledgements

First and foremost, I would like to express my deepest gratitude to my supervisor, **Anton Rebhan**, for offering guidance, continuous encouragement, and support of all my ideas throughout this PhD journey. His expertise and mentorship have been instrumental in shaping this research and in my development as a scientist.

I am also deeply indebted to **Ismail Zahed**, who agreed to host me for a research stay at the University of Stony Brook and whose knowledge and thought-provoking discussions have significantly enriched my understanding of the subject matter.

My sincere thanks go to my colleagues, **Josef Leutgeb** and **Jonas Mager**, for support, insightful discussions, and memorable nights out on or after various work events – a welcome change to the rigors of academia.

I would also like to extend my thanks to my collaborators **Sophia Domokos**, **Nelia Mann**, and **Kiminad Mamo** for their valuable insights and contributions to concluded as well as ongoing research. Their expertise and support helped to advance this thesis.

I am further indebted to the **Austrian Science Fund (FWF)** (Project no. P33655 and PAT7221623) and the **Doktoratskolleg Particles and Interactions (DKPI)** (Project no. W1252) for the various benefits I received. Be it organizing events, lecture series, or financial support for summer schools, conferences, and foremost, my visit to Ismail Zahed.

I am deeply grateful to my best friend, **Lukas Gosch**, for the many enlightening discussions, constant encouragement, as well as support and counsel in times of hardship.

I want to express my gratitude to my late high school teacher, **Wolfgang Wenk**, who instilled in me a passion for learning and the courage to question everything.

Further, I want to extend my gratitude to **Barbara Janesch** and **Hannes Kanauf**, whose door was always open to me when I needed to spend time in the great outdoors to ponder on the nature of things or blow off some steam ski touring in Carinthia.

With all my heart, I want to thank my partner, **Theresa Janesch**, for her endless support and sympathy when research did not play out as I had hoped it would. For encouraging me to take breaks, rest, and approach problems with a calmer mind.

Finally, I dedicate this thesis to my parents, **Petra** and **Roland Hechenberger**, whose unconditional love, unwavering support, and endless sacrifices have made this journey possible. Thank you!

Contents

Introduction **1**

1 The Unexpected Journey of Hadron Physics: Quarks, Strings and the Holographic Principle **3**

2 The Status of Glueballs **5**

3 Chiral Effective Theory **7**

4 The Holographic Principle **11**
  4.1 Formal Developments 13

I The Road to Holographic QCD **17**

5 Introduction **19**

6 No Strings Attached: Witten's Model of Large-N Yang-Mills Theory **21**

7 Strings Attached: The Witten-Sakai-Sugimoto Model **23**
  7.1 Massive Pseudoscalar Mesons 28
  7.2 Vector Meson Dominance 30
  7.3 Hadronic and Radiative Meson Decays 31

II Holographic Glueball Physics **41**

8 Introduction **43**

9 The Holographic Glueball Spectrum **45**
  9.1 Spin-0 48
  9.2 Spin-1 51
  9.3 Spin-2 53
  9.4 Glueball-Meson Mixing and Mass corrections 54

10 Glueball Decays **59**

10.1 Extrapolations to Realistic Glueball Masses 61
10.2 Hadronic Glueball Decays 61
10.3 Radiative Glueball Decays 89

III Reggeons, Pomeron, and Odderon 105

11 Introduction 107

12 Pomeron and Odderon in Gauge/Gravity Duality 111
12.1 Top-Down vs. Bottom-Up 113

13 Holographic Odderon at TOTEM? 115
13.1 The Repulsive-Wall Model 115
13.2 Reggeization of the Even and Odd Spin-j Exchanges 117
13.3 Bulk Dirac Fields 127
13.4 Diffractive pp and $p\bar{p}$ Scattering 130
13.5 Eikonal Elastic Scattering 136

14 Threshold Photoproduction of Heavy Pseudoscalar Mesons 147
14.1 Bulk Action and Fields 148
14.2 Holographic Photoproduction of η_c and η_b 155
14.3 Differential Cross Section 162

Conclusions and Final Remarks 169

Appendices 173

A M-Theory Lift and Dimensional Reduction 175

B Type IIA Supergravity Equations of Motion 177

C Towards the Unquenched Glueball Spectrum from Holographic QCD 179
C.1 Spin-1 Mesons 182
C.2 Dilaton Scalar Glueball 184
C.3 Pseudovector Glueball 185
C.4 Vector Glueball 186
C.5 Tensor Glueball 190

D Kinematics 193
D.1 Two-Body Decay 193

D.2 Three-Body Decay 194
D.3 Photoproduction at Threshold 197

E Deep Inelastic Scattering in the Witten-Sakai-Sugimoto Model **199**
E.1 Kinematics 200
E.2 Differential cross section 201
E.3 Low-Energy Couplings and Pomeron propagator 204
E.4 Structure Functions from Holographic QCD 209
E.5 Results 209

F Bulk-to-Bulk Propagator in the Soft-Wall Model **215**
F.1 Conformal Limit 217
F.2 Mode Sum Representation 218

Bibliography **221**

List of Abbreviations **243**

Index **245**

List of Figures

4.1 A sketch of the AdS/CFT correspondence. Taken from Ref. [60]. 12

4.2 Exemplary Witten diagram contributing to the scalar 4-point correlator. The dashed lines connecting to the boundary (outer circle) denote bulk-to-boundary propagators, while the dashed line connecting the vertices in the interior corresponds to a bulk-to-bulk propagator. 16

7.1 (a) The near-horizon geometry in (7.1) forces the D8-branes to join smoothly at U_{KK}. (b) Brane configuration of the D4/D8 system, including $N_c - N_f$ open strings. The coordinate $x_4 \equiv \tau$ is understood as periodic. Courtesy of Andreas Schmitt. 25

10.1 Feynman diagrams contributing to the hadronic three-body decay of the exotic, diltaon, and tensor glueball into $\rho\pi\pi$ 66

10.2 Dalitz plots for the three-body decay $G_D \to \rho\pi\pi$ including a charged (a) and neutral (b) a_1 resonance. 72

10.3 Feynman diagrams contributing to the hadronic three-body decay of the pseudovector and vector glueball into $\rho\rho\pi$. 81

10.4 Dalitz plots for the three-body decay $G_{PV} \to \rho\rho\pi$ including a charged (a) and neutral (b) a_1 resonance. 81

10.5 Dalitz plots for the three-body decay $G_V \to \rho\rho\pi$ including a charged (a) and neutral (b) a_1 resonance. 85

10.6 Feynman diagrams contributing to the radiative three-body decay of the (pseudo)vector glueball into $\pi\rho\gamma$. 99

11.1 High-energy total cross sections from various experiments. Displayed is the combined data set of the PDG [9] . 108

13.1 Differential cross sections at different center of mass energies for pp scattering from the TOTEM collaboration (a) and for $p\bar{p}$ scattering from the DØ collaboration (b) [189, 217] 116

13.2 Feynman diagrams for diffractive pp scattering through (a) Pomeron and (b) Odderon exchange 116

13.3 Complex j-plane structure for the odd spin-j bulk-to-bulk propagator. The poles give rise to the vector glueball spectrum, and the cut gives rise to the Odderon. 122
13.4 Witten diagrams for diffractive pp elastic scattering through (a) Pomeron and (b) Odderon exchange 132
13.5 Total cross sections for pp and $p\bar{p}$ scattering, with the parameters given in Table 13.1 for $g^{(2)}_{\mathbb{O}\bar{\Psi}\Psi} = 15$. 141
13.6 Results for the rho (a) and slope (b) parameters versus $\sqrt{s}$ with the parameters given in Table 13.1 for $g^{(2)}_{\mathbb{O}\bar{\Psi}\Psi} = 15$. 141
13.7 (a) The real part of the pp T-matrix approaches a step function at large rapidities and large λ. (b) The differential pp cross section in (13.149) crosses the saturation (dashed) line at large rapidities and fixed $b_\perp$ for pp. 143
13.8 (a) Results for the differential pp cross section (13.146), together with a weighted linear extrapolation of the results to $\sqrt{s} = 1.96$ TeV and a comparison to the corresponding TOTEM data and extrapolation [236–240]. (b) Results for the differential $p\bar{p}$ cross section (13.146) compared to the data from DØ [217]. 144
13.9 Extrapolated differential $p\bar{p}$ cross section 145

14.1 Threshold photoproduction of $\eta_{c,b}$ through (a) s-wave pseudovector glueball exchange and (b) p-wave photon exchange. 148
14.2 Witten diagrams for threshold production of $\eta_{c,b}$ through (a) Odderon and (b) photon exchange. 148
14.3 C-even and C-odd nucleon form factors in the approximation $\kappa_N = \kappa_\gamma$ with the normalization fixed by the charge, magnetic moment and (14.59). 160
14.4 (a) Holographic differential cross section for threshold photoproduction of η_c at $W = 4.3$ GeV. The solid and dotted green lines correspond to the Dirac and Pauli contributions of p-wave photon exchange, respectively. The solid red line corresponds to the non-Reggeized Odderon exchange with $g_{B\psi} = \{1, 0.5\}$ and the solid black line to the sum of all contributions. (b) Holographic differential cross section as in (a) but with the photon contribution summed. The data points are from the Primakoff photon exchange estimate (open blue circles) in Ref. [160]. 164
14.5 (a) Holographic differential cross section for threshold photoproduction of η_c at $W = 10$ GeV with the same color coding as in Fig. 14.4a. (b) Holographic differential cross section as in (a) but with the photon contribution summed. The data points correspond to the Primakoff photon exchange (green diamonds) and Odderon exchange (red triangles), as well as their sum (black diamonds) of Ref. [159]. 165

14.6 (a) Holographic differential cross section for threshold photoproduction of η_c at $W = 50$ GeV with the same color coding as in Fig. 14.4a. (b) Holographic differential cross section as in (a) but with the photon contribution summed. 165

14.7 (a) Holographic differential cross section for threshold photoproduction of η_c at $W = 300$ GeV with the same color coding as in Fig. 14.4a. (b) Holographic differential cross section as in (a) but with the photon contribution summed. The data points correspond to the Primakoff photon exchange (blue open circles) from Ref. [160] and the Odderon models of Ref. [243] (orange diamonds) and of Ref. [244] (green-triangles). 165

14.8 (a) Holographic differential cross section for threshold photoproduction of η_b at $W = 11$ GeV with the same color coding as in Fig. 14.4a. (b) Holographic differential cross section as in (a) but with the photon contribution summed. 166

14.9 Holographic differential and total cross sections for threshold photoproduction of J/Ψ (shaded blue) [215], and the present results for η_c (shaded black with $g_{B\psi} = \{1, 0.5\}$) at $W = 4.58$ GeV (a), $W = 4.30$ GeV (b), $W = 10$ GeV (c), $W = 50$ GeV (d) and $W = 300$ GeV (e). (f) Integrated holographic cross sections for threshold photoproduction of η_c (shaded black) and J/Ψ (shaded blue) [215]. The data points are from GlueX [257] (black), SLAC [255] (magenta) and Cornell [256] (green), respectively. 167

D.1 Kinematics of the two-body decay. 193

D.2 Kinematics of the three-body decay. 195

D.3 Minimal and maximal transverse momentum transfer t_{min}, t_{max} in the physical region for η_c (a) and η_b (b) versus $W = \sqrt{s}$. The photon momentum is taken to be at the optical point $q^2 = -Q^2 = 0$, and the hadron masses are given by $M_N = 0.938$ GeV, $M_{\eta_b} = 2.984$ GeV and $M_{\eta_b} = 9.399$ GeV. 197

E.1 Deep inelastic lepton-proton scattering into a collection of final states X. 200

E.2 Double virtual forward Compton scattering. 202

E.3 Photoproduction cross section with the parameters from Table E.1 through exchange of a Reggeized tensor glueball compared to data from [278–280]. 210

E.4 Fit of the reduced cross sections within a 90% confidence interval compared to data from HERA [269, 276, 277] at a center of mass energy of $\sqrt{s} = 300$ GeV and 0.045 GeV$^2 \leq Q^2 \leq 0.40$ GeV^2. 211

E.5 Fit of the reduced cross sections within a 90% confidence interval compared to data from HERA [269, 276, 277] at a center of mass energy of $\sqrt{s} = 318$ GeV and 0.15 GeV$^2 \leq Q^2 \leq 0.40$ GeV^2. 212

E.6 Fit of the structure function $F_2(Q^2, W)$ within a 90% confidence interval compared to data from HERA [269, 276, 277] at a center of mass energy of $\sqrt{s} = 300$ GeV and 0.11 GeV$^2 \leq Q^2 \leq 0.25$ GeV^2. 213

List of Tables

4.1 Brane configuration of the $\mathrm{AdS}_5/\mathrm{CFT}_4$ correspondence. 13

7.1 Brane configuration of the D4-D8 system. 25

7.2 Parameter table of mixing angles used. The dots correspond to the variation in $\lambda = 16.63 \ldots 12.55$, while the vertical line separates the two values obtained from fitting to the equivalent photon rate (see Section 7.3.3). The vector meson sector is assumed to mix ideally. 34

7.3 Radiative decay widths of pseudoscalar and vector mesons with 't Hooft coupling $\lambda = 16.63 \ldots 12.55$. For nonmonotonic dependence on λ intermediate extremal values are also given. Ideal mixing is assumed for ω and ϕ. Except for the π^0 width [106], all experimental results are taken from the PDG [9] . 36

7.4 Radiative axial vector meson decay with $\lambda = 16.63 \ldots 12.55$ and two values of the f_1 mixing angle $\theta_f = 20.4°|26.4°$. Experimental values are from the PDG [9] except the lower values for $f_1(1285) \to \rho\gamma$, which are from VES [112]; Zanke et al. [113] propose here as experimental average 950(280) keV. 38

7.5 Equivalent photon rates of axial vector mesons for two values of the f_1 mixing angle $\theta_f = 20.4°|26.4°$ (in the latter case with M_{KK} rescaled such that m_a is raised to the experimental value which reduces ξ in (7.76) to zero); the range denoted by dots corresponds again to $\lambda = 16.63 \ldots 12.55$, where only the first value is matching the axial anomaly exactly. Experimental values from L3 [116, 117], see also [113]. 39

9.1 The holographic glueball spectrum as obtained in [74] but with eigenvalues λ_i given in units of M_{KK}. The $-$ subscript denotes states with odd τ-parity that will be discarded in the following. 48

10.1 Hadronic decays of the exotic scalar glueball G_E alternatively identified with $f_0(1500)$ and $f_0(1710)$ with masses 1506 MeV and 1712 MeV, respectively, for $\lambda = 16.63 \ldots 12.55$. In decays into two pseudoscalar mesons, the two sets of values correspond to $x = 0$ and $x = 1$ in the coupling to the quark mass term (10.7). Four-body decays have been found to be strongly suppressed [133] and are hence not listed. Partial decay widths much smaller than 1 MeV are left out. 68

10.2 Hadronic decays of the dilatonic scalar glueball G_D alternatively identified with $f_0(1500)$ and $f_0(1710)$ with masses 1506 MeV and 1712 MeV, respectively, for $\lambda = 16.63 \ldots 12.55$. In decays into two pseudoscalar mesons, the two sets of values correspond to $x = 0$ and $x = 1$ in the coupling to the quark mass term (10.28). Four-body decays have been found to be strongly suppressed [133] and are hence not listed. Partial decay widths much smaller than 1 MeV are left out. 73

10.3 Hadronic two-body decays of the exotic scalar glueball G_E with model mass of 855 MeV and extrapolated to $M = 1865$ MeV for the proposed fragmented scalar glueball in [45]. $\lambda = 16.63 \ldots 12.55$. In decays into two pseudoscalar mesons, the two sets of values correspond to $x = 0$ and $x = 1$ in the coupling to the quark mass term (10.7). Four-body decays have been found to be strongly suppressed [133] and are hence not listed. Partial decay widths much smaller than 1 MeV are left out but considered in the total hadronic decay rate. 74

10.4 Hadronic two-body decays of the dilatonic scalar glueball G_D with WSS model mass and extrapolated to $M = 1865$ MeV for the proposed fragmented scalar glueball in [45]. $\lambda = 16.63 \ldots 12.55$. In decays into two pseudoscalar mesons, the two sets of values correspond to $x = 0$ and $x = 1$ in the coupling to the quark mass term (10.28). Four-body decays have been found to be strongly suppressed [133] and are hence not listed. Partial decay widths much smaller than 1 MeV are left out but considered in the total hadronic decay rate. 74

10.5 Decays of the pseudoscalar glueball into two vector mesons $\lambda = 16.63 \ldots 12.55$. Besides the WSS model result for the pseudoscalar mass, $M_G = 1813 \pm 7$MeV, an extrapolation to 2600 MeV (motivated by lattice results) is considered. Partial decay widths much smaller than 1 MeV have been left out and can be found in [135]. 75

10.6 Hadronic decays of the pseudovector glueball with WSS model mass of $M_{PV} = 2311$ MeV. 79

10.7 Hadronic decays of the pseudovector glueball with WSS model mass $M_{PV} =$ 2311 MeV and the quenched lattice value of 2980 MeV. 80

10.8 Hadronic decays of the vector glueball with WSS model mass $M_V = 2882$ MeV (mixing between vector glueball and singlet vector mesons neglected). Because of the large width of $a_1 \to \rho\pi$, the strongly interfering direct and resonant decays into $\rho\rho\pi$ have been combined. 85
10.9 Relative branching ratios of the hadronic decays of the vector glueball with WSS model mass $M_V = 2882$ MeV and with quenched lattice QCD result [12] 3830 MeV, the latter for the sake of comparison with Ref. [161]. 86
10.10 Hadronic decays of the tensor glueball G_T with WSS model 1487 MeV mass and extrapolated to masses of 2000 and 2400 MeV, for $\lambda = 16.63 \dots 12.55$. In decays involving f_1 we additionally vary $\theta_f = 20.4° \dots 26.4°$. Partial decay widths much smaller than 1 MeV are left out. 90
10.11 Radiative decays of the exotic scalar glueball G_E extrapolated to the masses of $f_0(1500)$, $f_0(1710)$. 93
10.12 Radiative scalar glueball decay with G_D identified alternatively with $f_0(1500)$ and $f_0(1710)$ with masses 1506 MeV and 1712 MeV, respectively, for $\lambda = 16.63 \dots 12.55$. 95
10.13 Radiative decays of the exotic scalar glueball G_E with WSS model mass 855 MeV and extrapolated to the scalar glueball at 1865 MeV proposed in Ref. [45]. 95
10.14 Radiative decays of the dilaton scalar glueball G_D with WSS model mass of 1487 MeV and extrapolated to the scalar glueball at 1865 MeV proposed in Ref. [45]. 96
10.15 Radiative pseudoscalar glueball decays for $\lambda = 16.63 \dots 12.55$. Besides the WSS model result for the pseudoscalar mass, $M_G = 1813 \pm 7$MeV, extrapolations to X(2370) with mass 2395 MeV and 2600 MeV motivated by the analysis in [144] and lattice results, respectively, are considered. 97
10.16 Radiative decays of the pseudovector glueball with WSS model mass of $M_{PV} = 2311$ MeV. 99
10.17 Radiative decays of the vector glueball with WSS model mass $M_V = 2882$ MeV. 103
10.18 Radiative tensor glueball decays for $\lambda = 16.63 \dots 12.55$. Besides the pristine results for the WSS model mass of 1487 MeV, their extrapolations to glueball masses of 2000 and 2400 MeV are given. 104

13.1 Best-fit parameters for forward quantitites in pp and $p\bar{p}$ scattering for different input values of $g^{(2)}_{\mathbb{O}\bar{\Psi}\Psi}$. 140
13.2 Best fit parameters for the differential cross section data from TOTEM [236–240] and DØ [217] with a fixed Odderon coupling of $g^{(2)}_{\mathbb{O}\bar{\Psi}\Psi} = 15$. The standard error on $\mathcal{N}_{\mathrm{d}\sigma}$ is negligible. 144

C.1 Numerical results for vector meson masses. 184

C.2 Numerical results for vector meson and vector glueball masses. 189

E.1 Best fit results for a global fit of the photoproduction cross section, reduced cross section, and $F_2(Q^2,W)$ to the data of [269, 276–280] above $\sqrt{s} = 300$ GeV and for $Q^2 \leq 0.5$ GeV^2. 210

List of Publications

1. F. Hechenberger, J, Leutgeb, A. Rebhan, *Radiative meson and glueball decays in the Witten-Sakai-Sugimoto model*, Phys. Rev. D **107**, 114020 (2023), [2302.13379]
2. F. Hechenberger, K. A. Mamo and I. Zahed, *Holographic Odderon at TOTEM?*, Phys. Rev. D **109**, 036029 (2024), [2311.05973]
3. F. Hechenberger, K.A. Mamo and I. Zahed, *Threshold photoproduction of η_c and η_b using holographic QCD*, Phys. Rev. D **109**, 074013 (2024), [2401.12162]
4. F. Hechenberger, J. Leutgeb and A. Rebhan, *Spin-1 Glueballs in the Witten-Sakai-Sugimoto Model*, Phys. Rev. D **109**, 074014 (2024), 074014, [2401.17986]

Introduction

1

The Unexpected Journey of Hadron Physics: Quarks, Strings and the Holographic Principle

> *Alles ist Wechselwirkung.”*
>
> — **Alexander von Humboldt**
> Scientist

Hadron physics is the study of particles composed of quarks and gluons. The latter are the force carriers of the strong interaction whose dynamics and interactions with quarks are governed by QCD. The most well-known hadrons are mesons and baryons. Mesons, such as pions and kaons, are composed of a quark-antiquark pair. Their discovery by Powell[1] et al. [1] in 1947 confirmed Yukawa's[2] prediction of a particle mediating the strong force [2]. Like the familiar proton and neutron, baryons consist of three valence quarks. The quark model, independently proposed by Gell-Mann [3] and Zweig [4] in 1964, successfully explained the observed patterns in hadron properties and their classification into these two main categories based on valence quarks. While a hadron is a complicated bound state of a myriad of quarks and gluons, many of their properties, and in particular their quantum numbers, may be understood in terms of their valence quark content. A unique characteristic of the strong interaction is its varying strength depending on the distance between quarks. At short distances, it becomes weaker, a phenomenon known as asymptotic freedom that was demonstrated by Gross, Wilczek, and Politzer in 1973[3]. Conversely, at large distances, it strengthens, leading to confinement. This intriguing behavior underpins the formation of hadrons and their complex dynamics. Beyond mesons and baryons, QCD also predicts the existence of more exotic hadrons, such as tetraquarks (composed of two quarks and two antiquarks) and pentaquarks (composed of four quarks and one antiquark), which can not be described within the framework of the standard quark model. While theoretically possible, these states are more difficult to form and detect due to their complex internal structure and potential instability. However, significant experimental advances have also been made on that front. Among the most elusive hadrons are glueballs, hypothetical particles whose valence constituents are solely gluons. Despite their solid theoretical foundation already at an early stage during the formulation of QCD [5–8], experimental confirmation of glueballs remains a challenge due to their complex nature and mixing with conventional mesons. Thus, experimental searches at high-energy colliders and dedicated glueball experiments have yielded no undisputed signals so far. While the number of experimentally identified hadrons was once manageable, the Particle Data Group (PDG) [9] currently lists a whole zoo of hadrons with 149 established mesons[4] and 125 established baryons[5], with many additional states appearing and disappearing over time. Lattice QCD calculations have provided strong evidence for the existence of glueballs, predicting their masses [10–14] and decay properties. While lattice QCD has made significant advances due to improved algorithms and increased computational power, glueball observables are still plagued by large uncertainties. Analytical approaches like Schwinger-Dyson equations are similarly advancing [15–18] (see Ref. [19] for a review), but involve uncontrollable approximations. Therefore, complementary methods for determining decay and mixing patterns remain highly sought after.

---

[1] Powell received the 1950 Nobel Prize in Physics for developing the experimental method that led to the discovery of the pion.

[2] Yukawa received the 1949 Nobel Prize in Physics for his theoretical work on mesons and the strong force.

[3] They jointly received the 2004 Nobel Prize in Physics for their work on asymptotic freedom.

Already conceived in 1959, Regge theory [20] provided a framework to describe the scattering of hadrons and their mass spectra. Regge trajectories, relating the mass and spin of hadrons in a linear fashion, were first observed experimentally in the 1960s [21, 22]. These trajectories found a natural explanation within the framework of string theory, where hadrons are viewed as vibrating strings. Although initially developed to describe hadronic interactions, it was later discovered to provide a candidate for a consistent theory of quantum gravity. In light of this connection, the holographic principle, first conjectured within string theory [23], has opened up a new avenue to study hadrons. This principle asserts that the properties of strongly interacting field theories may be understood by studying a higher-dimensional gravitational theory.

The search for glueballs and other exotic hadrons, alongside the study of conventional mesons and baryons, continues to be an active area of research. It is driven by the desire to understand the complex dynamics of quarks and gluons and to test the predictive power of QCD in its non-perturbative regime. The exploration of hadron physics promises to reveal deeper insights into the fundamental forces of nature and drives our understanding of the very ”glue” that binds us all.

---

[4] Non $q\bar{q}$ states, such as potential glueballs, tetra-, and pentaquarks, are also listed in this category.

[5] Only counting states categorized as ”Existence is certain” and ”Existence varies from very likely to certain”.

The Status of Glueballs

2

Glueballs, hypothetical particles composed solely of gluons, have been a subject of intense theoretical and experimental interest since the inception of QCD [5–8]. While QCD predicts their existence, the definitive identification of glueballs within the hadron spectrum remains an open challenge [24–28].

The discovery of glueballs would confirm the existence of a new class of particles beyond the conventional mesons and baryons. Dedicated experiments such as WA102, GAMS, Crystal Barrel and BES III have been conducted to search for glueballs, with potential scalar f_0 candidates identified in central production processes in proton-proton collisions, antiproton-proton annihilations, and radiative J/ψ decays [29–31]. Beyond the scalar states, other potential glueball candidates include the pseudoscalar $\eta(1405)$, $\eta(1475)$, and $\iota(1440)$[1], and the tensor $f_2(1950)$, all observed in various production mechanisms and exhibiting properties suggestive of a glueball nature [34].

Lattice QCD has been instrumental in providing predictions for the glueball spectrum [10–14, 35]. These calculations, mostly performed in the quenched approximation, suggest the existence of a scalar glueball as the lightest state, followed by a tensor glueball playing a crucial role as the lightest state associated with the Pomeron [36]. Additionally, a pseudoscalar glueball is predicted to participate in the manifestation of the $U(1)_A$ anomaly, which is responsible for the large mass of the η' meson [37]. Furthermore, lattice QCD anticipates towers of glueball states with arbitrary integer spin and parity.

However, differentiating glueball states from quark-antiquark bound states (mesons) with the same quantum numbers has proven difficult due to the potential for mixing between these states. The various phenomenological models available offer divergent interpretations, particularly for the lightest glueballs. The identification of the ground-state scalar glueball has been a subject of ongoing debate. Initially, the $f_0(1500)$ meson was favored as the primary glueball candidate, albeit with significant mixing with quarkonia [38–40]. However, alternative models propose the $f_0(1710)$ meson as the dominant glueball state, with a higher glue content [41–43]. This interpretation is supported by the enhanced production rate of $f_0(1710)$ in radiative J/ψ decays, which are believed to be gluon-rich environments [44]. Nevertheless, recent analyses suggest that the glue content may be distributed across multiple scalar mesons, including a newly identified $f_0(1770)$ meson previously lumped together with the established $f_0(1710)$ [27, 45, 46].

---

[1] Historically $\iota(1440)$ and $E(1420)$, which stands for Europe, were both considered to be pseudoscalar glueball states. This view was challenged with the discovery of the η' meson. Later on it turned out that $E(1420)$ is an axial vector meson state consisting primarily of $s\bar{s}$ and was renamed $f_1(1420)$ [32, 33].

For reviews, see Refs. [25, 26, 47].

Chiral Effective Theory

3

The accurate holographic description of the rich hadron spectrum, together with its effective low-energy interactions, necessitates the inclusion of quarks of various flavors. In this chapter, we will review some key features that are seen to follow from this in the chiral limit. The global $U(N_f)_L \times U(N_f)_R = SU(N_f)_L \times SU(N_f)_R \times U(1)_V \times U(1)_A$ flavor symmetry of massless QCD permits the formulation of chiral effective theories (see [48] for a review). In nature, the $SU(N_f)_L \times SU(N_f)_R$ symmetry is only partly realized since the formation of a chiral condensate

$$\langle \psi_L^a \psi_R^b \rangle = v^3 \delta^{ab}, \tag{3.1}$$

dynamically breaks this symmetry down to its diagonal subgroup $SU(N_f)_V$. This is reflected in the wildly different masses of the 0^{-+} and 1^{--} meson spectrum when compared to their parity partners. Thus, the magnitude of chiral symmetry breaking v may be used as an order parameter to formulate effective theories. The $U(1)_A$ symmetry is anomalous and, in turn, gives rise to a pseudoscalar meson that is much heavier than the rest: the η' meson. As was shown by 't Hooft, the breaking of $U(1)_A$ and the mass of the η' meson can be understood in terms of instantons [49, 50] or, in the large N limit, as the Witten-Veneziano mechanism [51, 52]. It is thus driven by gluons, which signals a possibly large gluonic component in the wavefunction of the η' meson.

In QCD with massive fermions, chiral symmetry is also explicitly broken by the quark masses, which are given by [9]

$$\begin{aligned} m_u &= 2.16^{+0.49}_{-0.26}\,\text{MeV}, \quad & m_d &= 4.67^{+0.48}_{-0.17}\,\text{MeV}, \quad & m_s &= 93.4^{+8.6}_{-3.4}\,\text{MeV} \\ m_c &= 1.27^{+0.02}_{-0.02}\,\text{GeV}, \quad & m_b &= 4.18^{+0.03}_{-0.02}\,\text{GeV}, \quad & m_t &= 172.69^{+0.3}_{-0.3}\,\text{GeV}. \end{aligned} \tag{3.2}$$

Taken at face value, the explicit breaking of $SU(3)_L \times SU(3)_R$ for the three lightest flavors is fairly strong, though a comparison of results from chiral effective theory with experiment suggests that this approximation is still justified [48]. The following computations will also utilize the approximate three-flavor symmetry.

Die approbierte gedruckte Originalversion dieser Dissertation ist an der TU Wien Bibliothek verfügbar.
The approved original version of this doctoral thesis is available in print at TU Wien Bibliothek.
TU Bibliothek WIEN Your knowledge hub

In chiral perturbation theory one expands the interactions in powers of the pion decay constant over momenta through interactions of the form

$$\mathcal{L}_{\chi PT} \supset -\frac{1}{4} f_\pi^2 \, \mathrm{tr} \; \partial_\mu U(x) \partial^\mu U^\dagger(x), \tag{3.3}$$

where

$$U(x) = e^{i\Pi(x)/f_\pi}, \qquad \Pi(x) = \Pi^a(x)\lambda^a, \tag{3.4}$$

and $\lambda^a = 2T^a$ are the Gell-Mann matrices including $\lambda^0 = \sqrt{2/N_f}\mathbf{1}$. For the pseudoscalar sector, one thus has

$$\Pi(x) = \frac{1}{2}\begin{pmatrix} \pi^0 + \eta^8 \frac{1}{\sqrt{3}} + \eta^0 \sqrt{\frac{2}{3}} & \sqrt{2}\pi^+ & \sqrt{2}K^+ \\ \sqrt{2}\pi^- & -\pi^0 + \eta^8 \frac{1}{\sqrt{3}} + \eta^0 \sqrt{\frac{2}{3}} & \sqrt{2}K^0 \\ \sqrt{2}K^- & \sqrt{2}\bar{K}^0 & -2\eta^8 \frac{1}{\sqrt{3}} + \eta^0 \sqrt{\frac{2}{3}} \end{pmatrix}, \tag{3.5}$$

for $N_f = 3$. To justify a perturbative (derivative) expansion, the experimental value of

$$f_\pi = 130.2(1.2)/\sqrt{2} = 92.07(0.85)\mathrm{MeV} \tag{3.6}$$

quoted by the PDG [9] does not seem high enough compared to the actual mass of the pion $m_\pi = 134.98$ MeV. However, a systematic loop expansion of interactions resulting from (3.3) sets the effective expansion parameter to $4\pi f_\pi \approx 1$ GeV. The chiral Lagrangian in (3.3) is supplemented by the anomalous Wess-Zumino-Witten (WZW) [53, 54] term coupled to photons

$$\begin{aligned} \mathcal{L}_{WZW} \supset &-\frac{iN_c}{240\pi^2}\epsilon^{MNOPQ}\mathrm{tr}\,(U^\dagger\partial_M U)(U^\dagger\partial_N U)(U^\dagger\partial_O U)(U^\dagger\partial_P U)(U^\dagger\partial_Q U) \\ &-\frac{ie^2N_c}{48\pi^2}\epsilon^{MNOP}A_M F_{NO}\mathrm{tr}\Big(Q^2(\partial_P U)U^\dagger + Q^2U^\dagger(\partial_P U) \\ &\qquad + QUQU^\dagger(\partial_P U)U^\dagger\Big) \end{aligned} \tag{3.7}$$

where e is the electromagnetic coupling constant and Q is the electric charge matrix, given as

$$Q \;= \tfrac{1}{3}\begin{pmatrix} 2 & & \\ & -1 & \\ & & -1 \end{pmatrix} \tag{3.8}$$

for the $N_f = 3$ case. The WZW term successfully captures the physics responsible for the decays of pseudoscalars, most prominently π^0, into two photons[1]. The WZW Lagrangian gives a topological interpretation of the chiral anomaly in terms of a 5-dimensional theory, making holographic models particularly suited to describe the physics of this action.

---

[1] This process is used to fix the prefactor of N_c in (3.7).

One can further include mass terms for the pseudoscalars via

$$\mathcal{L}_m = v^3 \mathrm{tr}\,\left(\mathcal{M}U(x) + h.c.\right), \quad \mathcal{M} = \mathrm{diag}(m_u, m_d, m_s) \tag{3.9}$$

which results in the Gell-Mann-Oakes-Renner relation [55]

$$f_\pi^2 m_\pi^2 = 2(m_u + m_d)v^3. \tag{3.10}$$

Note that the quark masses, as well as v, are renormalization scheme dependent. However, their product on the right-hand side of (3.10) is not. Further, (3.10) displays the intimate relation between f_π and the order parameter of chiral symmetry breaking v in (3.1).

Since chiral effective theory has stood the test of time, holographic models of QCD necessarily need to capture at least some of its features. In the next chapter, we shall turn to the formulation of the holographic principle.

The Holographic Principle

4

The AdS/CFT correspondence, also known as the holographic principle or, in a somewhat more general form, as gauge/gravity duality, is a conjecture that proposes a connection between two seemingly disparate theories: quantum gravity in Anti de-Sitter (AdS) space and a Conformal Field Theory (CFT) on its boundary. The correspondence states that these two theories are equivalent, meaning one can completely describe a quantum gravitational system in the bulk AdS space by studying a CFT living on its boundary and vice versa.

It arose from studying low-energy string theory, specifically from the study of D-branes in the 1990s. D-branes are extended objects in string theory on which open strings can end. Originally proposed as a means to impose boundary conditions for the open string sector [56, 57], their dynamical importance was only later realized by Polchinski [58], which triggered the second superstring revolution and marked the advent of M-theory [59]. In 1997, Maldacena made the remarkable observation that the low-energy dynamics of the open string states of a stack of D3 branes in type IIB superstring theory, which are described by a four-dimensional (maximal) supersymmetric Yang-Mills theory[1], are in one-to-one correspondence with the closed string excitations of the $\mathrm{AdS}_5 \times S_5$ geometry generated by the same branes. At low energies, these excitations are described by type IIB supergravity, a theory of quantum gravity. Maldacena thus conjectured that these two descriptions are equivalent, as depicted in Fig. 4.1, marking the birth of the AdS/CFT correspondence. Shortly after this proposal, Gubser, Klebanov, and Polyakov [61] as well as Witten [62], put the AdS/CFT correspondence on a strong theoretical foundation by demonstrating how correlation and partition functions may be computed.

Since the literature on this topic is vast, with numerous important contributions over the last few decades, we refrain from giving a complete historical account of this topic but restrict ourselves to recapitulating key ingredients and insights necessary for the computations presented in this thesis. For a comprehensive review of the AdS/CFT correspondence, we refer the reader to Refs. [63, 64] for formal developments and to Refs. [60, 65] for phenomenological applications, respectively

---

[1] Due to this highly symmetric setup, the theory is conformal

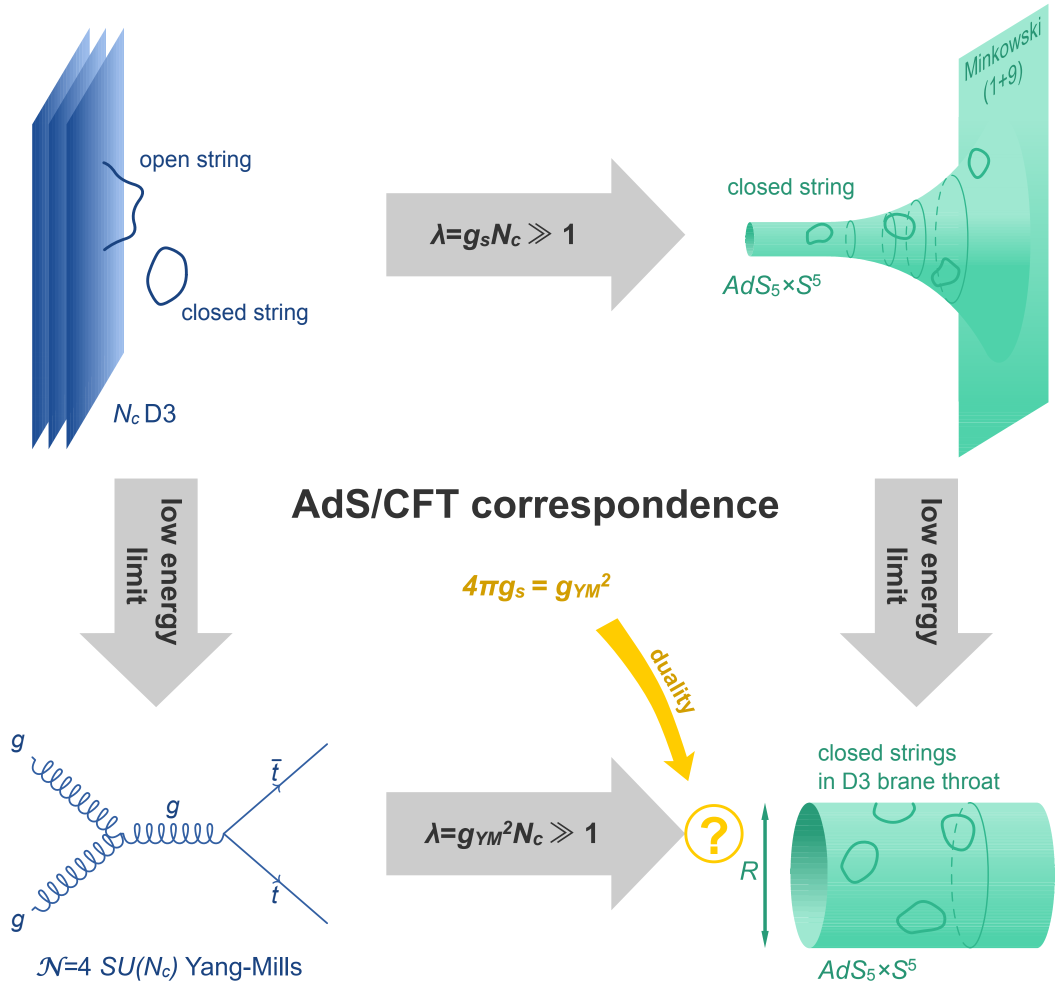
open string
closed string
N_c D3
$\lambda = g_s N_c \gg 1$
closed string
Minkowski (1+9)
$AdS_5 \times S^5$
AdS/CFT correspondence
low energy limit
low energy limit
$4\pi g_s = g_{YM}^2$
duality
g
g
g
$\bar{t}$
t
$\lambda = g_{YM}^2 N_c \gg 1$
?
R
closed strings in D3 brane throat
$\mathcal{N}$=4 $SU(N_c)$ Yang-Mills
$AdS_5 \times S^5$

Fig. 4.1.: A sketch of the AdS/CFT correspondence. Taken from Ref. [60].

x^M		0	1	2	3	4	5	6	7	8	9
N	D3	•	•	•	•						

Table 4.1.: Brane configuration of the $\mathrm{AdS}_5/\mathrm{CFT}_4$ correspondence.

4.1 Formal Developments

Some identifications are necessary to relate the two sides of the gauge/gravity duality. As first proposed by Maldacena [23], the correspondence relates $\mathcal{N} = 4$ super Yang-Mills theory with gauge group $SU(N)$ and coupling g_{YM} in flat spacetime to type IIB superstring theory on $\mathrm{AdS}_5 \times S_5$ with curvature radius R_{D3}, string length l_s and non-trivial 5-form flux F_5. This is seen to arise from studying the low-energy limit of a stack of N D3 branes, as depicted in Table 4.1. There are two ways to view the physics described by the brane background. On the one hand, we have the open string perspective, which is valid at small coupling $g_s N$. Neglecting massive excitations, the theory is described by a supersymmetric gauge theory with gauge field A_μ corresponding to string excitations longitudinal to the brane, and scalar fields encoding the transverse excitations, as well as the closed string action in the supergravity limit. In the Maldacena limit of $\alpha' \to 0$ but with field theory quantities fixed, the low-energy effective actions are seen to reduce to that of flat $\mathcal{N} = 4$ super Yang-Mills theory and type IIB supergravity on $\mathbb{R}^{(9,1)}$[2].

On the other hand, we have the closed string perspective that treats D-branes as solitonic solutions to type IIB supergravity for large R_{D3} or, equivalently, $g_s N \gg 1$. For low energies and at strong coupling, the metric sourced by the D3 branes is seen to asymptote to flat 10-dimensional Minkowski spacetime for distances far away from the horizon and to $\mathrm{AdS}_5 \times S_5$ in the so-called near-horizon limit. As shown below, this limit corresponds to the large N limit on the field theory side.

To summarize, at weak coupling one obtains the conformal $\mathcal{N} = 4$ $SU(N)$ super Yang-Mills theory as well as type IIB supergravity on $\mathbb{R}^{(9,1)}$. At strong coupling, one finds the same flat supergravity theory and additionally type IIB supergravity on $\mathrm{AdS}_5 \times S_5$. Since the flat supergravity theories match and describe the same physics, irrespective of the limit, one might conjecture that the same holds true for AdS_5 and CFT_4. It is straightforward to check that the symmetries on both sides agree.

Considering the low-energy effective actions of this theory allows us to identify the Yang-Mills coupling

$$g_{\mathrm{YM}}^2 = 2\pi g_s \tag{4.1}$$

---

[2] Note that in the naive limit of $\alpha' \to 0$, the Yang-Mills and supergravity fields do not interact.

in terms of the string coupling g_s. The 5-form flux

$$F_5 = \mathrm{d}C_4, \quad C_4 = \left(H(r)^{-1} - 1\right) \mathrm{d}x^0 \wedge \cdots \wedge \mathrm{d}x^3, \quad H(r) = 1 + \left(\frac{R_{\mathrm{D3}}}{r}\right)^4, \tag{4.2}$$

where $r^2 = x_4^2 + \cdots + x_9^2$, stabilizes the AdS$_5$ geometry and is quantized as

$$\frac{N}{(2\pi)^3 g_s l_s^4} = \frac{1}{(2\pi)^7 g_s^2 l_s^8} \int_{S_5} \star F_5. \tag{4.3}$$

This enables us to determine the AdS radius R_{D3} in terms of field theory quantities

$$2g_{\mathrm{YM}}^2 N = 2\lambda = R_{\mathrm{D3}}^4 e/\alpha'^2, \tag{4.4}$$

where we defined the 't Hooft coupling $\lambda \equiv g_{\mathrm{YM}}^2 N$ and the Regge slope $\alpha' = l_s^2$. Note that this identification involves taking the limits described above. In particular, we took $N \to \infty$ and λ large or, equivalently, $g_s \to 0$ and $\alpha'/R_{\mathrm{D3}}^2 \to 0$. In other words, we are considering weakly coupled string theory in a classical gravitational background that does not resolve the string scale. This is known as the weak form of the AdS/CFT correspondence, but it is believed that the strong form, for any N and λ, is also valid. The latter form would involve the daunting task of carrying out quantized string theory computations in a curved background, a problem that is, to date, unsolved.

To establish a formal relation between the two theories, one needs what is commonly referred to as holographic dictionary. This one-to-one map is provided by matching the symmetries on both sides of the correspondence and allows us to relate field theory operators to certain string states. Following Ref. [64], consider for example the operator

$$\mathcal{O}_\Delta(x) \equiv \mathrm{STr}\left(\phi_{i_1}(x) \cdots \phi_{i_\Delta}(x)\right), \tag{4.5}$$

where, for the sake of simplicity, we only consider the scalar fields $\phi_i(x)$ of $\mathcal{N} = 4$ super Yang-Mills theory and STr denotes the symmetrized trace over color indices. Equivalently, on the gravity side, we consider supergravity fields in the same representation as $\mathcal{O}_\Delta(x)$ and perform a Kaluza-Klein decomposition according to the symmetries of the underlying AdS$_5 \times S_5$ geometry

$$\varphi(x, z, \Omega_5) = \sum_{I=0}^{\infty} \varphi^I(x, z) Y^I(\Omega_5), \tag{4.6}$$

where (x^μ, z) are the coordinates on AdS$_5$ and $Y^I(\Omega_5)$ denotes the spherical harmonics on S_5 which satisfy

$$\Box_{S_5} Y^I(\Omega_5) = -\frac{1}{R_{\mathrm{D3}}^2} l(l+4) Y^I(\Omega_5). \tag{4.7}$$

Die approbierte gedruckte Originalversion dieser Dissertation ist an der TU Wien Bibliothek verfügbar.
The approved original version of this doctoral thesis is available in print at TU Wien Bibliothek.
TU Bibliothek WIEN Your knowledge hub

For the sake of explicitness, consider the trace of the graviton and the Ramond-Ramond 4-form

$$h_2(x,z,\Omega_5) = \sum_{I=0}^{\infty} h_2^I(x,z) Y^I(\Omega_5), \qquad C_{\alpha\beta\gamma\delta} = \sum_{I=0}^{\infty} b^I(x,z)\epsilon_{\alpha\beta\gamma\delta\epsilon}\nabla^\epsilon Y^I(\Omega_5). \quad (4.8)$$

The relevant equation of motion in type IIB supergravity

$$R_{MN} = \frac{1}{3!} F_{MOPQR} F_N{}^{OPQR} \quad (4.9)$$

reduces to a Klein-Gordon equation

$$\Box_{\mathrm{AdS}_5} s^I(x,z) = \frac{1}{R_{\mathrm{D3}}^2} l(l-4) s^I(x,z) \quad (4.10)$$

for the field

$$s^I = \frac{1}{20(l+2)}\left(h_2^I - 10(l+4)b^I\right). \quad (4.11)$$

The mass of the scalar field s^I is related to the AdS radius R_{D3} and the mode number of $Y^I(\Omega_5)$ as $m^2 R_{\mathrm{D3}}^2 = l(l-4)$. Upon the identification $\Delta = l$, (4.5) and (4.11) are in the same representation, and thus we have established a field-operator map. Of particular importance for the present work is the energy-momentum tensor T_{MN}, which naturally couples to metric fluctuations

$$g^{MN} \leftrightarrow T_{MN}. \quad (4.12)$$

Analogously, one can establish the map by considering the boundary asymptotics of a bulk field. For a field in AdS_d they are given by

$$\phi(x,z)|_{z\to 0} \sim \phi_0(x) z^{d-\Delta} + \phi_+(x) z^{\Delta}, \quad (4.13)$$

where $\phi_0(x)$ is referred to as non-normalizable mode and ϕ_+ as normalizable mode, respectively. On dimensional grounds, the latter mode may be identified with the vacuum expectation value of a field theory operator $\mathcal{O}_\Delta$. On the other hand, the non-normalizable mode is identified with the source of this operator. This can be shown explicitly by evaluating the on-shell gravity action at the boundary and leads to the Gubser-Klebanov-Polyakov-Witten (GKPW) formula[3] [61, 62]

$$Z[\Phi_0] = e^{-W[\Phi_0]} = \left\langle \exp\left(\int \mathrm{d}^d x \Phi_0 \mathcal{O}(x)\right)\right\rangle_{\mathrm{CFT}}, \quad (4.14)$$

where Φ_0 denotes the boundary value of an arbitrary 5-dimensional supergravity field in AdS_5, $W[\Phi_0] = S_{\mathrm{SUGRA}}|_{\Phi_0(x)}$ is the generating functional of connected Green's functions

---

[3] Here we give the formula in Euclidean signature, as in its original form.

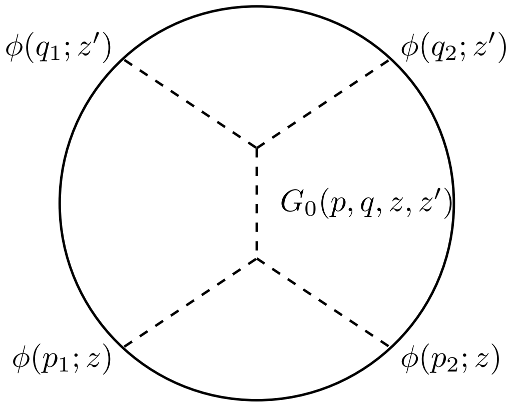

Fig. 4.2.: Exemplary Witten diagram contributing to the scalar 4-point correlator. The dashed lines connecting to the boundary (outer circle) denote bulk-to-boundary propagators, while the dashed line connecting the vertices in the interior corresponds to a bulk-to-bulk propagator.

pertinent to the dimensionally reduced type IIB supergravity action on $\mathrm{AdS}_5 \times S_5$, and $\mathcal{O}$ is a composite operator matching the representation of Φ_0. Specifically, (4.14) equates the generating functional of the CFT correlators to the action of the dual gravitational theory, evaluated on a particular classical solution that satisfies boundary conditions determined by the sources in the CFT. The connected Green's function for some composite operators $\mathcal{O}_i$ are now following from

$$\langle \mathcal{O}_1(x_1) \ldots \mathcal{O}_n(x_n) \rangle = - \frac{\delta^n W \left(\Phi_0^1(x_1), \ldots, \Phi_0^n(x_n) \right)}{\delta \Phi_0^1(x_1) \cdots \delta \Phi_0^n(x_n)} . \tag{4.15}$$

Further, (4.14) allows for a diagrammatical way to compute the field theory correlators on the gravity side in a similar fashion to Feynman diagrams. These diagrams are known as Witten diagrams, with vertices representing interactions in the bulk AdS space and lines representing the propagation of bulk fields. The boundary is represented by a circle, while the interior corresponds to AdS spacetime. An exemplary Witten diagram is given in Fig. 4.2. In the following chapters, some of these identifications will be made explicit for particular backgrounds that are suitable to describe QCD in the confining phase.

Part I

The Road to Holographic QCD

Introduction

5

> *It's a dangerous business, Frodo, going out your door. You step onto the road, and if you don't keep your feet, there's no knowing where you might be swept off to."*
>
> — **J. R. R. Tolkien**
> *The Fellowship of the Ring*

Shortly after its conception in 1997 [23], the holographic principle was applied to study numerous aspects of strongly coupled field theories [62, 63, 66, 67]. While in its original form, it has yielded valuable insights that lead to a better understanding of strongly coupled systems, such as deconfined quark-gluon plasma, the absence of confinement and chiral symmetry breaking in superconformal gauge theories necessitates a more refined holographic model to connect to real-world QCD. Already soon after Maldacena's seminal paper, Witten formulated a brane construction that is dual to pure-glue QCD in the large N limit [68] which successfully incorporates a mass gap. We will recapitulate this model in Chapter 6. A few years later, Sakai and Sugimoto [69] included chiral quarks by open strings stretching between color and flavor branes. As we will revisit in Chapter 7, it successfully reproduces chiral symmetry breaking in a geometrical fashion and leads to an effective chiral hadronic model (see Chapter 3) that semiquantitatively captures numerous features of hadron spectroscopy together with decay patterns.

In Chapter 6 we briefly recapitulate the Witten model. Next, we will turn to the construction of the Witten-Sakai-Sugimoto (WSS) model and present important results for the following glueball computations of II.

6

No Strings Attached: Witten's Model of Large-N Yang-Mills Theory

The to date most successful top-down construction dual to large N Yang-Mills theory is due to Witten [68]. It is based on an M-theory construction in $\mathrm{AdS}_7 \times S_4$, which is dual to a 6-dimensional superconformal theory on M5-branes. The superfluous dimensions are compactified in a way that breaks supersymmetry and, at low energies, is dual to a 4-dimensional large N Yang-Mills theory. In the following, we shall briefly review its construction.

The near horizon limit of a stack of N M5-branes compactified on a supersymmetry breaking ”thermal” circle of radius M_{KK}^{-1} in the fourth spatial coordinate $x_4 \equiv \tau$,

$$\tau \simeq \tau + \delta\tau = \tau + \frac{2\pi}{M_{\mathrm{KK}}}, \quad M_{\mathrm{KK}} = 3 r_{\mathrm{KK}}/L^2, \tag{6.1}$$

is given by the geometry of a doubly Wick-rotated black hole [70]

$$\mathrm{d}s^2 = \frac{r^2}{L^2}\left[f(r)\mathrm{d}x_4^2 + \eta_{\mu\nu}\mathrm{d}x^\mu \mathrm{d}x^\nu + \mathrm{d}x_{11}^2\right] + \frac{L^2}{r^2}\frac{\mathrm{d}r^2}{f\left(r\right)} + \frac{L^2}{4}\mathrm{d}\Omega_4^2, \tag{6.2}$$

where L is the AdS radius. The metric in (6.2) is stabilized by the 4-form flux

$$F_{\alpha\beta\gamma\delta} = \frac{6}{L}\sqrt{g_{S^4}}\epsilon_{\alpha\beta\gamma\delta}, \tag{6.3}$$

which is sourced by the N M5-branes. Asymptotically, this space reduces to $\mathrm{AdS}_7 \times S_4$ with a radius half that of the AdS space. Freund and Rubin previously encountered this configuration in [71] when they were searching for Kaluza-Klein reductions of unified theories to 4D. The background in (6.2) is a solution to the equations of motion following from the unique 11D IIA supergravity action whose bosonic part reads

$$S_{11} = \frac{1}{2\kappa_{11}^2}\int \mathrm{d}x\sqrt{-G}\left(R - \frac{1}{2}|F_4|^2\right) - \frac{1}{3!}\int A_3 \wedge F_4 \wedge F_4. \tag{6.4}$$

with $2\kappa_{11}^2 = (2\pi)^8 l_s^9$ the 11-dimensional Newton constant. The Witten model was shown to reproduce numerous features of low-energy Yang-Mills theory like a mass gap [68], a gluon condensate [72] and a spectrum of glueballs [73, 74] in qualitative agreement with lattice QCD [11, 12]. In holographic models, glueballs arise as fluctuations of the fields in the closed string sector of the theory. However, QCD is not only a theory of glue, but a theory of quarks bound by gluons. To understand, and therefore be able to search for glueballs, one must study their interactions with mesons, bound states of quarks of various flavors. Before turning to the glueball spectrum in Chapter 9, we will thus introduce quark flavors via open strings.

Die approbierte gedruckte Originalversion dieser Dissertation ist an der TU Wien Bibliothek verfügbar.
The approved original version of this doctoral thesis is available in print at TU Wien Bibliothek.
TU Bibliothek Your knowledge hub WIEN

7

Strings Attached: The Witten-Sakai-Sugimoto Model

In Refs. [69,75] Sakai and Sugimoto have extended Witten's D4-brane model to include N_f chiral quarks by a D-brane construction in the so-called probe limit $N_c \gg N_f$, where the flavor branes do not backreact on the original geometry. The daunting issue of going beyond the probe limit has been tackled in [76,77]. The WSS model, sometimes also referred to as the D4-D8-brane system, not only reproduces qualitatively numerous aspects of low-energy QCD and chiral effective theory but frequently achieves semi-quantitative agreement, all with a minimal number of free parameters. In this chapter, we briefly recapitulate the WSS model, carry out computations of masses and decay rates, and compare them to experiment. For a review, see Ref. [78].

After reduction of the 11-dimensional background of (6.2) to 10D by compactifying $x_{11} = 2\pi g_s l_s$ and employing the coordinate transformation $U = r^2/2L,\ R_{\mathrm{D4}} = L/2$ we arrive at the metric

$$\begin{aligned} \mathrm{d}s^2 &= \left(\frac{U}{R_{\mathrm{D4}}}\right)^{3/2}\left[\eta_{\mu\nu}\mathrm{d}x^\mu \mathrm{d}x^\nu + f(U)\mathrm{d}\tau^2\right] + \left(\frac{R_{\mathrm{D4}}}{U}\right)^{3/2}\left[\frac{\mathrm{d}U^2}{f(U)} + U^2 \mathrm{d}\Omega_4^2\right], \\ e^\phi &= g_s \left(\frac{U}{R_{\mathrm{D4}}}\right)^{3/4}, \qquad F_4 = \mathrm{d}C_3 = \frac{(2\pi l_s)^3 N_c}{V_4}\epsilon_4, \qquad f(U) = 1 - \frac{U_{\mathrm{KK}}^3}{U^3}, \end{aligned} \tag{7.1}$$

with dilaton ϕ and Ramond-Ramond three-form field[1] C_3. Later on, the dimensionless variable $u = U/U_{\mathrm{KK}}$ will also be frequently used. Here x^μ, $\mu = 0, 1, 2, 3$, are the coordinates in the flat four-dimensional directions, U is the radial holographic direction, where regularity at $U = U_{\mathrm{KK}}$ fixes

$$M_{\mathrm{KK}} = \frac{3}{2}\frac{U_{\mathrm{KK}}^{1/2}}{R_{\mathrm{D4}}^{3/2}}. \tag{7.2}$$

---

[1] Using standard string-theory conventions [79] for the normalization of Ramond-Ramond fields rather than the rescaled version of Ref. [69].

The AdS radius R_{D4} is related to the string coupling g_s and the string length l_s via the quantized charge of the 4-form flux

$$\frac{1}{(2\pi)^2 l_s^3}\int_{S_4} F_4 = 2\pi N_c, \tag{7.3}$$

which gives $R_{\text{D4}}^3 = \pi g_s N_c l_s^3$.

Through the Kaluza-Klein reductions of $S_\tau \times S_{x_{11}}$, the D4-brane system of (7.1) can be viewed as M5-branes wrapped on T^2. The dimensionally reduced action of (6.4) now reads [79]

$$\begin{aligned}
S_{IIA} &= S_{NS} + S_R + S_{\text{CS}}, \\
S_{NS} &= \frac{1}{2\kappa_{10}^2}\int \mathrm{d}^{10}x\sqrt{-g}e^{-2\phi}\left(R + 4\nabla_M\phi\nabla^M\phi - \frac{1}{2}|H_3|^2\right), \\
S_R &= \frac{1}{2\kappa_{10}^2}\int \mathrm{d}^{10}x\sqrt{-g}\left(-\frac{1}{2}|F_2|^2 - \frac{1}{2}|\tilde{F}_4|^2\right), \\
S_{\text{CS}} &= -\frac{1}{2\kappa_{10}^2}\int \mathrm{d}^{10}x\frac{1}{2}B_2\wedge F_4\wedge F_4,
\end{aligned} \tag{7.4}$$

where

$$\begin{aligned}
&F_2 = dC_1, \quad F_4 = dC_3, \\
&\tilde{F}_4 = F_4 - C_1\wedge H_3, \quad H_3 = dB_2,
\end{aligned} \tag{7.5}$$

and $2\kappa_{10}^2 = (2\pi)^7 l_s^8$. The actions S_{NS} and S_R refer to the Neveu-Schwarz (NS) and Ramond (R) sectors of the theory, respectively. They arise from the Gliozzi-Scherk-Olive (GSO) projection in the Ramond–Neveu–Schwarz (RNS) formulation of superstring theory; a consistency condition imposed that removes the tachyon from the spectrum and simultaneously ensures spacetime supersymmetry. The GSO projection acts on the fermionic states in the closed string sector, where fermions with anti-periodic boundary conditions live in the NS sector and those with periodic boundary conditions in the R sector. The NS-NS strings give rise to the graviton, dilaton, and Kalb-Ramond fields, while the R-R strings bring about various p-form fields. For details on the RNS formalism and the GSO projection, see Ref. [70]. Some calculations of the dimensional reduction that are relevant for this thesis have been relegated to Appendix A.

The probe ($N_f \ll N_c$) D8 and $\overline{\text{D8}}$-branes extend along x^μ, U, S^4, as indicated in Table 7.1, and are located in an antipodal configuration on the τ-circle. Since the geometry is cut off at a finite value of U, the branes join smoothly at U_{KK}[2] as depicted in Fig. 7.1a and thereby implement spontaneous chiral symmetry breaking $\text{U}(N_f)_L \times \text{U}(N_f)_R \to U(N_f)_V$ in a

---

[2] If one were to choose a non-antipodal embedding, the branes would join at $U_0 > U_{\text{KK}}$ (see e.g. Ref. [80]) and thus introduce an additional mass scale.

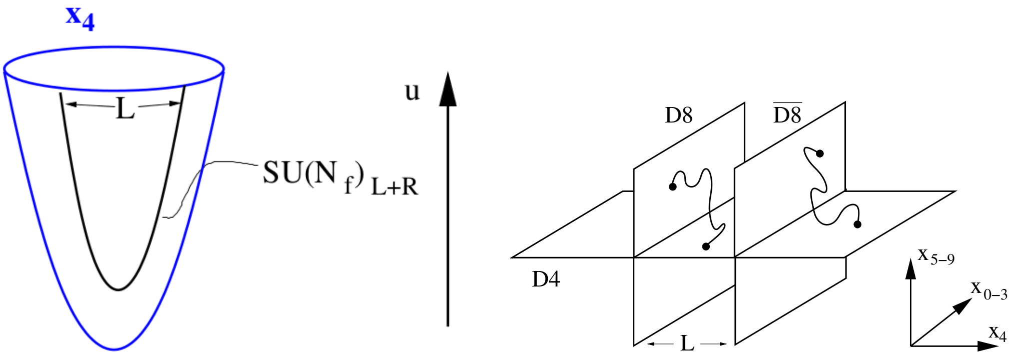

(a) (b)

Fig. 7.1.: (a) The near-horizon geometry in (7.1) forces the D8-branes to join smoothly at U_{KK}. (b) Brane configuration of the D4/D8 system, including $N_c - N_f$ open strings. The coordinate $x_4 \equiv \tau$ is understood as periodic. Courtesy of Andreas Schmitt.

geometrical way. As low energy modes, the $N_c - N_f$ strings involve chiral quarks, as depicted in Fig. 7.1b. At strong coupling and low energies, they are described by their bound states in terms of fields living on a stack of N_f coincident Dp-branes, where $p = 8$ for the WSS model. Their interactions are characterized by the sum of the Dirac-Born-Infeld (DBI) and Chern-Simons (CS) action [79]

x^M		0	1	2	3	4	5	6	7	8	9
N_c	D4	●	●	●	●	●					
N_f	$\mathrm{D8}-\overline{\mathrm{D8}}$	●	●	●	●		●	●	●	●	●

Table 7.1.: Brane configuration of the D4-D8 system.

$$
\begin{aligned}
S_{\mathrm{DBI}}^{\mathrm{Dp}} &= -T_p \int \mathrm{d}^{p+1}x e^{-\phi} \mathrm{Tr}\, \sqrt{-\det\left(g_{MN} + 2\pi\alpha' F_{MN} + B_{MN}\right)}, \\
S_{\mathrm{CS}}^{\mathrm{Dp}} &= T_p \sum_q \int_{\mathrm{Dp}} \sqrt{\hat{A}(\mathcal{R})} \mathrm{Tr}\ \exp\left(2\pi\alpha' F + B\right) \wedge C_q,
\end{aligned}
\tag{7.6}
$$

where $T_p = (2\pi)^{-p} l_s^{-(p+1)}$ is the brane tension, $F = \mathrm{d}A - iA \wedge A$ the non-abelian field strength of the brane gauge fields and $\hat{A}(\mathcal{R})$ the A-roof genus arising through anomaly inflow [81]. The latter is given by a sum over Pontryagin classes

$$
\hat{A}(\mathcal{R}) = 1 - \frac{1}{24} p_1(\mathcal{R}) + \frac{1}{5760}\left(7 p_1(\mathcal{R})^2 - 4 p_2(\mathcal{R})\right) + \ldots, \tag{7.7}
$$

where

$$
\begin{aligned}
p_1(\mathcal{R}) &= -\frac{1}{8\pi^2} \mathrm{Tr}\ \mathcal{R} \wedge \mathcal{R} \\
p_2(\mathcal{R}) &= \frac{1}{128\pi^4}\left((\mathrm{Tr}\ \mathcal{R} \wedge \mathcal{R})^2 - 2\mathrm{Tr}\ \mathcal{R} \wedge \mathcal{R} \wedge \mathcal{R} \wedge \mathcal{R}\right),
\end{aligned}
\tag{7.8}
$$

and Riemann curvature 2-form $\mathcal{R}$ is related to the Riemann tensor via

$$\mathcal{R}_{AB} = \frac{1}{2} R_{ABCD} \mathrm{d}x^C \wedge \mathrm{d}x^D. \tag{7.9}$$

The (symmetrized) trace in (7.6) runs over the $U(N)$ as well as Minkowski indices, and the sum over Ramond-Ramond q-form gauge fields in the Chern-Simons term is understood in a formal sense where the integral picks out the (p+1)-form contributions. Note that the appearance of the Kalb-Ramond field together with F is attributed to the underlying (broken) supersymmetry of the theory [70].

By dimensionally reducing the action of a probe D4-brane on S_τ

$$\begin{aligned} S_{\mathrm{D4}} \supset & - T_4 \frac{2\pi}{M_{\mathrm{KK}}} \mathrm{Tr} \int \mathrm{d}^4 x e^{-\phi} \sqrt{-g} \frac{(2\pi\alpha')^2}{2} \left|F_{\mathrm{YM}}\right|^2 \\ & + T_4 (2\pi\alpha')^2 \int C_1 \wedge F_{\mathrm{YM}} \wedge F_{\mathrm{YM}}, \end{aligned} \tag{7.10}$$

the boundary theory at $U \to \infty$ is identified with a 3+1-dimensional Yang-Mills theory, including a θ-term

$$\mathcal{L}_{\mathrm{D4}} = -\frac{1}{2g_{\mathrm{YM}}^2} \mathrm{Tr} \left|F_{\mathrm{YM}}\right|^2 + \frac{1}{2} \frac{\theta}{(2\pi)^2} \mathrm{Tr}\ F_{\mathrm{YM}} \wedge F_{\mathrm{YM}}. \tag{7.11}$$

The 't Hooft coupling λ and Yang-Mills coupling g_{YM} are hence given by

$$\lambda = g_{\mathrm{YM}}^2 N_c = 2\pi g_s l_s M_{\mathrm{KK}} N_c. \tag{7.12}$$

The Ramond-Ramond field C_1 is vanishing for the Witten background, leading to $\theta = 0$. However, when the action of 8-branes is considered, an additional term arises through Hodge duality of $F_8 = \mathrm{d}C_7 = \star F_2$ that modifies the equation of motion for C_1, eventually giving rise to the Witten-Veneziano mechanism [51, 52].

As QCD lacks a quantum number associated with $SO(5)$, we restrict the spectrum to trivial fluctuations on the S_4. The terms quadratic in the field strength of the DBI action for $p = 8$ in (7.6) can be reduced to a 5-dimensional Yang-Mills theory with action [69, 75][3]

$$S_{\mathrm{D8}}^{\mathrm{DBI}} \supset -\kappa \int \mathrm{d}^4 x\, \mathrm{d}z\, \mathrm{tr} \left(\frac{1}{2} K^{-1/3} F_{\mu\nu}^2 + M_{\mathrm{KK}}^2 K F_{\mu z}^2 \right), \tag{7.13}$$

where

$$\kappa \equiv \frac{\lambda N_c}{216\pi^3}, \qquad K(z) \equiv 1 + z^2 = U^3 / U_{\mathrm{KK}}^3, \tag{7.14}$$

---

[3] In (7.13) the Minkowski metric $\eta_{\mu\nu}$ in the mostly plus convention is used to contract the four-dimensional spacetime indices. Unless stated otherwise, this convention will be used throughout.

Die approbierte gedruckte Originalversion dieser Dissertation ist an der TU Wien Bibliothek verfügbar.
The approved original version of this doctoral thesis is available in print at TU Wien Bibliothek.
TU Bibliothek WIEN Your knowledge hub

and the remaining trace over the $U(N_f)$ indices. To arrive at (7.13), we performed a Kaluza-Klein decomposition of the flavor gauge fields

$$A_\mu(x^\mu, z) = \sum_{n=1}^{\infty} B_\mu^{(n)}(x^\mu)\psi_n(z), \quad A_z(x^\mu, z) = \sum_{n=0}^{\infty} \varphi^{(n)}(x^\mu)\phi_n(z), \tag{7.15}$$

using the complete sets $\{\psi_n(z)\}_{n\geq 1}$ and $\{\phi_n(z)\}_{n\geq 0}$. The holographic wavefunctions are normalized as

$$\kappa \int \mathrm{d}z K^{-1/3}\psi_m\psi_n = \delta_{mn}, \qquad \kappa \int \mathrm{d}z K\phi_m\phi_n = \delta_{mn}. \tag{7.16}$$

and satisfy the completeness relations

$$\kappa \sum_n K^{-1/3}\psi_n(z)\psi_n(z') = \delta(z-z'), \quad \kappa \sum_n K\phi_n(z)\phi_n(z') = \delta(z-z'). \tag{7.17}$$

The eigenvalue equation following from (7.13)

$$-K^{-1/3}\partial_z\left(K\partial_z\psi_n\right) = \lambda_n\psi_n, \qquad \lambda_n = m_n^2/M_{\mathrm{KK}}^2 \tag{7.18}$$

can be used to relate the two complete sets via $\phi_n(z) \propto \partial_z\psi_n(z)$ for $(n \geq 1)$ and the remaining massless mode is given by

$$\phi_0(z) = \frac{1}{\sqrt{\pi\kappa}M_{\mathrm{KK}}K(z)}. \tag{7.19}$$

Inserting the separation ansatz (7.15) into the DBI action (7.13) and integrating over z, we obtain

$$S_{\mathrm{D8}}^{\mathrm{DBI}} \supset -\mathrm{tr}\int \mathrm{d}^4x \left[\left(\partial_\mu\varphi^{(0)}\right)^2 + \sum_{n=1}^{\infty}\left(\frac{1}{2}\left(f_{\mu\nu}^{(n)}\right)^2 + m_n^2\left(B_\mu^{(n)} - \frac{\partial_\mu\varphi^{(n)}}{m_n}\right)^2\right)\right], \tag{7.20}$$

with the abelian field strength $f_{\mu\nu}^{(n)} = \partial_\mu B_\nu^{(n)} - \partial_\nu B_\mu^{(n)}$. Absorbing the remaining pseudoscalar fields $\varphi^{(n)}$ with $(n \geq 1)$ by the fields $B_\mu^{(n)}$, we obtain a quadratic Lagrangian of massless pseudoscalar fields and (axial) vector meson fields with masses $m_n = \sqrt{\lambda_n}M_{\mathrm{KK}}$ determined by the eigenvalue equation (7.18). Since (7.13) is invariant under $(x_1, x_2, x_3, z) \to (-x_1, -x_2, -x_3, -z)$, we can utilize the z-parity of solutions to (7.18) to determine their transformation property in the 4-dimensional theory, to wit

$$v_\mu^{(n)} \equiv B_\mu^{(2n-1)}, \qquad a_\mu^{(n)} \equiv B_\mu^{(2n)}, \tag{7.21}$$

where $v_\mu^{(n)}$ and $a_\mu^{(n)}$ refer to vector and axial vector mesons, respectively. The lightest vector meson is identified with the rho meson of mass $m_\rho = m_1 = \sqrt{0.669314}M_{\mathrm{KK}}$, with the traditional value [69, 75] of $M_{\mathrm{KK}} = 949$ MeV corresponding to $m_\rho = 776.4$ MeV. The remaining field $\varphi^{(0)}$ is identified as the multiplet of massless pion fields produced by chiral symmetry breaking. The $\mathrm{U}(N_f)_A$-valued Goldstone boson field is given by the holonomy

$$U(x) = e^{i\Pi^a(x)\lambda^a/f_\pi} = \mathrm{P}\ \exp i\int_{-\infty}^{\infty} \mathrm{d}z\, A_z(z,x), \tag{7.22}$$

with $\Pi(x)$ already given in (3.5) and $A_z = \Pi(x^\mu)K^{-1}/\sqrt{\kappa\pi M_{\mathrm{KK}}^2}$.

The pion decay constant is determined by matching to an expansion of the kinetic part of the chiral action[4]

$$S_{\text{chiral}}^{kin} = \int \frac{f_\pi^2}{4}\mathrm{tr}\,\left(U^{-1}\partial_\mu U\right)^2, \tag{7.23}$$

and given by

$$f_\pi^2 = \frac{\lambda N_c}{54\pi^4} M_{\mathrm{KK}}^2. \tag{7.24}$$

Conventionally fixing $f_\pi \approx 92.4$ MeV one obtains $\lambda \approx 16.63$. Matching instead the string tension

$$\sigma_s = \frac{1}{2\pi l_s^2}\sqrt{-g_{tt}g_{xx}}\bigg|_{U=U_{\mathrm{KK}}} = \frac{2}{27\pi}\lambda M_{\mathrm{KK}}^2 \tag{7.25}$$

to the large-N_c lattice result of $\sqrt{\sigma_s} \approx 440$ MeV [83], gives a smaller 't Hooft coupling $\lambda \approx 12.55$ and thus also pion decay constant $f_\pi \approx 80.3$ MeV. Studies of the spectrum of higher-spin mesons in the WSS model [84] also seem to favor a smaller value. In the following, the variation of $\lambda \approx 16.63 \ldots 12.55$ shall serve as an error estimate of the predictions of the model.

7.1 Massive Pseudoscalar Mesons

In holographic models, the anomalous breaking of $U(1)_A$ is tied to the lowest Ramond-Ramond p-form C_p [85–87] in the Chern-Simons action in (7.6). [5]. In QCD, the $U(1)_A$ transformation of the quark fields may be compensated by a shift of the θ parameter. As was shown in (7.11), the θ parameter is identified with Ramond-Ramond 1-form C_1. This gives rise to a Witten-Veneziano [51, 52] mass term for the singlet pseudoscalar η_0. In particular, anomaly cancellation [81] requires a gauge invariant redefinition of the Ramond-Ramond field strength F_2

$$\tilde{F}_2 = 3\, l_s \frac{U_{\mathrm{KK}}^3}{U^4}\frac{M_{\mathrm{KK}}}{2\pi}\left(\theta + \frac{\sqrt{2N_f}}{f_\pi}\eta_0\right) \mathrm{d}U \wedge dx^4. \tag{7.26}$$

---

[4] In Ref. [69] it was shown that (7.13) also reproduce the full Skyrme action [82].

[5] This action is of order $1/N_c$ and thus $U(1)_A$ is restored in the strict large-N_c limit.

Die approbierte gedruckte Originalversion dieser Dissertation ist an der TU Wien Bibliothek verfügbar.
The approved original version of this doctoral thesis is available in print at TU Wien Bibliothek.
TU Bibliothek, WIEN Your knowledge hub

Correspondingly, the correct kinetic term in the bulk action is now given by

$$S_{C_1} = -\frac{1}{2\kappa_{10}^2}\int \mathrm{d}^{10}x\sqrt{-g}|\tilde{F}_2|^2, \tag{7.27}$$

from which one obtains the Witten-Venziano mass[6] [69]

$$m_0^2 = \frac{2N_f}{f_\pi^2}\chi_g = \frac{\lambda^2}{27\pi^2}\frac{N_f}{N_c}M_{\mathrm{KK}}^2, \tag{7.28}$$

where χ_g is the topological susceptibility. Using $N_f = N_c = 3$, and $\lambda = 16.63\dots 12.55$ we obtain

$$m_0 = 967\dots 730 \text{ MeV}. \tag{7.29}$$

A deformation resulting in mass terms for the other pseudoscalar mesons may be generated through either worldsheet instantons [88, 89] or non-normalizable modes of bifundamental fields corresponding to open-string tachyons [80, 90–92]. The resulting Lagrangian can be shown to be of the form in (3.9) and hence reproduces the Gell-Mann-Oakes-Renner relation. Without a precise understanding of how this deformation is achieved, we tentatively propose an isospin symmetric Lagrangian of the form

$$\begin{aligned} \mathcal{L}_m^{\mathcal{M}} &= \mu \mathrm{Tr}\left(\mathcal{M}\,U(x) + h.c.\right), \\ \mathcal{M} &= \mathrm{diag}(m_u, m_d, m_s), \end{aligned} \tag{7.30}$$

where $m_u = m_d = \hat{m}$ and an unfixed overall scale μ. The resulting masses in the pseudoscalar meson sector are given by [93]

$$\begin{aligned} m_\pi^2 &= 2\hat{m}\mu, \qquad & m_K^2 &= (\hat{m} + m_s)\mu, \\ m_1^2 &= \frac{2}{3}m_K^2 + \frac{1}{3}m_\pi^2, \qquad & m_8^2 &= \frac{4}{3}m_K^2 - \frac{1}{3}m_\pi^2, \end{aligned} \tag{7.31}$$

and

$$m_{\eta,\eta'}^2 = \frac{1}{2}m_0^2 + m_K^2 \mp \sqrt{\frac{m_0^4}{4} - \frac{1}{3}m_0^2(m_K^2 - m_\pi^2) + (m_K^2 - m_\pi^2)^2}, \tag{7.32}$$

for the mass eigenstates

$$\begin{aligned} \eta &= \eta_8 \cos\theta_P - \eta_0 \sin\theta_P, \\ \eta' &= \eta_8 \sin\theta_P + \eta_0 \cos\theta_P, \end{aligned} \tag{7.33}$$

---

[6] We see that the limit $N_c \to \infty$ indeed restores the broken $U(1)_A$ symmetry by yielding a massless Nambu-Goldstone boson.

with mixing angle

$$\theta_P = \frac{1}{2}\arctan\frac{2\sqrt{2}}{1-\frac{3}{2}m_0^2/(m_K^2-m_\pi^2)}. \tag{7.34}$$

Using the isospin symmetric parameters

$$m_\pi^2 = m_{\pi_0}^2 \approx (135\text{ MeV})^2, \tag{7.35}$$

and

$$m_K^2 = \frac{1}{2}(m_{K_\pm}^2 + m_{K_0}^2) - \frac{1}{2}(m_{\pi_\pm}^2 - m_{\pi_0}^2) \approx (495\text{ MeV})^2, \tag{7.36}$$

as well as the pseudoscalar singlet mass in (7.29), we obtain $\theta_P \approx -14.31^\circ \cdots -24.15^\circ$ and $m_\eta \approx 520\ldots470$, $m_{\eta'} \approx 1080\ldots890$ MeV. In the following, we shall vary θ_P in (7.34) together with λ, but fix m_η and $m_{\eta'}$ to their experimental values in the evaluation of phase space integrals. Further, the explicit quark masses will not modify the results for the chiral couplings, but only appear in phase space factors.

7.2 Vector Meson Dominance

The holographic principle relates non-normalizable modes to external sources. By utilizing the local $U(1)_V$ bulk symmetry, electromagnetic interactions are obtained by asymptotic values of the corresponding gauge field on the D8-brane [75]

$$\lim_{z\to\pm\infty} A_\mu(x,z) = A_{L,R\mu}(x) = eQA_\mu^{\text{em}}(x). \tag{7.37}$$

The ansatz in (7.15) is thus now given by

$$A_\mu(x^\mu,z) = A_{L\mu}(x^\mu)\psi_+(z) + A_{R\mu}(x^\mu)\psi_-(z) + \sum_{n=1}^{\infty} v_\mu^{(n)}(x^\mu)\psi_n(z), \tag{7.38}$$

with the non-normalizable zero modes $\psi_\pm(z)$, $\partial_z\psi_\pm(z) \propto \phi_0(z)$ defined as

$$\psi_\pm(z) \equiv \frac{1}{2}\left(1 \pm \psi_0(z)\right), \qquad \psi_0(z) \equiv \frac{2}{\pi}\arctan z. \tag{7.39}$$

To distinguish between the different fields we introduce the notation

$$\mathcal{V}_\mu \equiv \frac{1}{2}\left(A_{L\mu} + A_{R\mu}\right), \qquad \mathcal{A}_\mu \equiv \frac{1}{2}\left(A_{L\mu} - A_{R\mu}\right), \tag{7.40}$$

for photons and would-be axial photons, such that

$$A_\mu(x^\mu, z) = \mathcal{V}_\mu(x^\mu) + \mathcal{A}_\mu(x^\mu)\psi_0(z) + \sum_{n=1}^{\infty} v_\mu^{(n)}(x^\mu)\psi_{2n-1}(z) + \sum_{n=1}^{\infty} a_\mu^{(n)}(x^\mu)\psi_{2n}(z). \tag{7.41}$$

The first term in (7.13) can thus be expanded as

$$\begin{aligned}
\frac{\kappa}{2}\int \mathrm{d}z K^{-1/3} F_{\mu\nu}^2 \supset & \frac{a_{\mathcal{V}\mathcal{V}}}{2}\mathrm{tr}\,\left(\partial_\mu \mathcal{V}_\nu - \partial_\nu \mathcal{V}_\mu\right)^2 + \frac{a_{\mathcal{A}\mathcal{A}}}{2}\mathrm{tr}\,\left(\partial_\mu \mathcal{A}_\nu - \partial_\nu \mathcal{A}_\mu\right)^2 \\
& + \frac{1}{2}\mathrm{tr}\,\left(\partial_\mu v_\nu^{(n)} - \partial_\nu v_\mu^{(n)}\right)^2 + \frac{1}{2}\mathrm{tr}\,\left(\partial_\mu a_\nu^{(n)} - \partial_\nu a_\mu^{(n)}\right)^2 \\
& + a_{\mathcal{V}v^n}\mathrm{tr}\left(\left(\partial_\mu \mathcal{V}_\nu - \partial_\nu \mathcal{V}_\mu\right)\left(\partial_\mu v_\nu^{(n)} - \partial_\nu v_\mu^{(n)}\right)\right) \\
& + a_{\mathcal{A}a^n}\mathrm{tr}\left(\left(\partial_\mu \mathcal{A}_\nu - \partial_\nu \mathcal{A}_\mu\right)\left(\partial_\mu a_\nu^{(n)} - \partial_\nu a_\mu^{(n)}\right)\right),
\end{aligned} \tag{7.42}$$

with coupling constants

$$\begin{aligned}
a_{\mathcal{V}v^n} &= \kappa\int dz K^{-1/3}\psi_{2n-1}, \quad a_{\mathcal{V}\mathcal{V}} = \kappa\int dz K^{-1/3}, \\
a_{\mathcal{A}a^n} &= \kappa\int dz K^{-1/3}\psi_{2n}\psi_0, \quad a_{\mathcal{A}\mathcal{A}} = \kappa\int dz K^{-1/3}\psi_0^2.
\end{aligned} \tag{7.43}$$

Due to the non-diagonal terms in (7.42), the photon field is mixed with the diagonal states of the vector meson nonet, ρ^0, ω and ϕ. Higher order terms omitted in (7.42) correspond to interactions. They do, however, not include the photon, which only couples through the mixing terms in (7.42), thereby realizing Vector Meson Dominance (VMD) [94–97].

7.3 Hadronic and Radiative Meson Decays

In this section, some exemplary decay rates previously studied in Ref. [98], to which the interested reader is referred for details, are presented. On the one hand, they serve as a prelude for the following glueball computations and, on the other hand, to gauge to what extent the results of the WSS model are credible. Some shortcomings will be addressed, together with modifications that may be used to account for them. If not stated otherwise, masses of particles are taken from the averages listed in the PDG [9] as well as the J^{PC} naming convention[7] of pseudoscalar 0^{+-} and vector 1^{--} for $q\bar{q}$ states with vanishing angular momentum ($l = 0$) and scalar 0^{++}, axial vector 1^{++} and pseudovector 1^{+-} for their orbital excitations ($l = 1$). The same naming convention will be used for the glueball states later on.

---

[7] See Chapter 15 of [9] for details.

Die approbierte gedruckte Originalversion dieser Dissertation ist an der TU Wien Bibliothek verfügbar.
The approved original version of this doctoral thesis is available in print at TU Wien Bibliothek.
TU Bibliothek Your knowledge hub WIEN

7.3.1 Hadronic Vector and Axial Vector Meson Decays

We obtain vertices between vector, axial vector, and pseudoscalar mesons through the commutator terms in the DBI action (7.13). Restricting to two flavors, the ρ meson couples to two pions via

$$\begin{aligned}\mathcal{L}_{\rho\pi\pi} &= -g_{\rho\pi\pi}\varepsilon_{abc}(\partial_\mu \pi^a)\rho^{b\mu}\pi^c,\\ g_{\rho\pi\pi} &= \int \mathrm{d}z \frac{1}{\pi K}\psi_1 = 33.98\,\lambda^{-\frac{1}{2}}N_c^{-\frac{1}{2}}.\end{aligned}$$

Using the kinematic relations and formulas given in Appendix D, we readily obtain the spin averaged, squared amplitude

$$\begin{aligned}|\mathcal{M}_{\rho\to\pi\pi}|^2 &= \sum_{\lambda_\rho}\frac{1}{3}\epsilon^{(\rho)}_\mu\epsilon^{(\rho)*}_\nu\mathcal{M}^\mu_{\rho\pi\pi}\mathcal{M}^{\nu*}_{\rho\pi\pi}\\ &= \frac{g^2_{\rho\pi\pi}}{3}m_\rho^2\left(1-\frac{4m_\pi^2}{m_\rho^2}\right)\end{aligned} \tag{7.44}$$

and the partial decay rate

$$\Gamma_{\rho\to\pi\pi} = \frac{1}{8\pi}\frac{|\mathbf{p}_\pi|}{m_\rho^2}\,|\mathcal{M}_{\rho\to\pi\pi}|^2\,, \tag{7.45}$$

yielding $\Gamma_{\rho\to\pi\pi} = 98.0\ldots130$ MeV for $\lambda = 16.63\ldots12.55$. This somewhat underestimates the experimental result of about 150 MeV.

Analogously, we obtain interactions involving an axial vector meson

$$\begin{aligned}\mathcal{L}_{a_1\rho\pi} &= g_{a_1\rho\pi}\varepsilon_{abc}a^a_\mu\rho^{b\mu}\pi^c,\\ g_{a_1\rho\pi} &= 2M_{\mathrm{KK}}\sqrt{\frac{\kappa}{\pi}}\int \mathrm{d}z\,\psi_2'\psi_1 = -34.43\,\lambda^{-\frac{1}{2}}N_c^{-\frac{1}{2}}M_{\mathrm{KK}}.\end{aligned} \tag{7.46}$$

Note that these interactions can also be obtained via the substitution $\partial_\mu A_z \to -a^n_\mu\partial_z\psi_{2n}$ in (7.44). The decay rate of isotriplet axial vector mesons into $\rho\pi$ is obtained from

$$\Gamma_{a_1\to\rho\pi} = 2\times\frac{1}{8\pi}\frac{|\mathbf{p}_\pi|}{m_{a_1}^2}\,|\mathcal{M}_{\rho\to\pi\pi}|^2\,, \tag{7.47}$$

with a factor of 2 to account for the two differently charged combinations $\rho^\pm\pi^\mp$ and

$$|\mathcal{M}_{a_1\to\rho\pi}|^2 = \frac{1}{3}\left(\frac{g_{a_1\rho\pi}}{2m_{a_1}m_\rho}\right)^2\left(m_{a_1}^4 - 2m_{a_1}^2\left(m_\pi^2-5m_\rho^2\right)+\left(m_\pi^2-m_\rho^2\right)^2\right) \tag{7.48}$$

The WSS model predicts the mass of the a_1 meson relatively close to its experimental value of 1186.5 MeV. However, the partial decay rate of $425\ldots563$ MeV resulting from (7.46)

Die approbierte gedruckte Originalversion dieser Dissertation ist an der TU Wien Bibliothek verfügbar.
The approved original version of this doctoral thesis is available in print at TU Wien Bibliothek.
TU Bibliothek WIEN Your knowledge hub

already saturates the experimental total width of 420(35) MeV[8] [9] . Whereas, according to [99], only roughly 60% of its width is due to S-wave $\rho\pi$ decays with subsequent decays into three pions[9]. Due to its large width, we shall treat the a_1 meson as a resonant contribution to the three-body decays computed in Chapter 10.

From the discussion above, we can conclude that the WSS model reproduces hadronic decays quite well when restricted to the light quark flavors with $N_f = 2$. With the strange quark included, several shortcomings arise. While the ρ and ω meson are nearly degenerate in mass, the ϕ meson is significantly heavier. Nevertheless, we shall consider the case $N_f = 3$, giving rise to the K, η, and η' pseudoscalar, K^*, ω, and ϕ vector, and f_1, f_1', $K_1(1270)$, and $K_1(1400)$ axial vector mesons with their masses raised accordingly when evaluating phase space integrals, but assuming the same coupling $g_{K^*K\pi} = g_{\phi KK} = g_{\rho\pi\pi}$, and so on. For example, this gives $\Gamma(K^* \to K\pi) = 28\ldots37$ MeV and $\Gamma(\phi \to K\bar{K}) = 2.12\ldots2.82$ MeV, which are about 40% and 20% smaller than the results quoted by the PDG [9] , respectively. Besides extrapolating to their experimental masses, we consider mixing in the pseudoscalar (see Section 7.1) and axial vector meson sector. In particular the f_1 and f_1' mesons mix according to

$$\begin{aligned} |f_1(1285)\rangle &= \cos\theta_f|\bar{n}n\rangle - \sin\theta_f|\bar{s}s\rangle \\ |f_1(1420)\rangle &= \sin\theta_f|\bar{n}n\rangle + \cos\theta_f|\bar{s}s\rangle, \end{aligned} \tag{7.49}$$

so that ideal mixing corresponds to $\theta_f = 0$. Later on, in Section 7.3.3, we will fix the mixing angle from its equivalent photon rate to $\theta_f = 20.4|26.4°$.

The physical strange axial vector mesons $K_1(1270)$ and $K_1(1400)$ are mixtures of K_{1A} (1^{++}) and the excited axial vector meson K_{1B} (1^{+-}) [100]. Because in the WSS model, there is no 1^{+-} nonet of ordinary mesons, only K_{1A} is present, which couples to the physical K_1 mesons according to their mixing defined by

$$|K_{1A}\rangle = \cos\theta_K|K_1(1400)\rangle + \sin\theta_K|K_1(1270)\rangle. \tag{7.50}$$

Due to this shortcoming, we will not attempt to compute the hadronic and radiative decays of $K_1(1270)$ and $K_1(1400)$. However, they will be considered as physical states appearing via (7.50) when computing decays of glueballs in Chapter 10. In Refs. [100, 101] the favored mixing angle is quoted as $|\theta_K| \approx 33°$, which we will adopt in the following.

The ω and ϕ meson are almost ideally mixed, which will be assumed in all decay rates collected in tables. We shall, however, sometimes comment in the continuous text on the effects of a small mixing. For easier reference, we have collected the mixing angles in

---

[8] Albeit with experimental results varying from 250 to 600 MeV.

[9] The ρ meson almost exclusively decays into a charged pion pair [9] .

θ_f	θ_P	θ_V	θ_K
$20.4 \,\vert\, 26.4°$	$-14.31...-24.15°$	$35.26°$	$33°$

Table 7.2.: Parameter table of mixing angles used. The dots correspond to the variation in $\lambda = 16.63\ldots 12.55$, while the vertical line separates the two values obtained from fitting to the equivalent photon rate (see Section 7.3.3). The vector meson sector is assumed to mix ideally.

Table 7.2. Unless stated otherwise, we shall exclusively use those values. The pseudoscalar mesons of the $N_f = 3$ nonet are too light to decay into pairs of vector mesons. However, through VMD, these interactions will give rise to the anomalous $\pi \to 2\gamma$ decays. The corresponding Lagrangian including vector mesons is obtained from the CS-term

$$\begin{aligned} S_{\mathrm{CS}} &\supset T_8 \int \mathrm{tr}\,\left(\exp\left(2\pi\alpha' F_2 + B_2\right) \wedge C_3\right) \\ &\supset \frac{N_c}{96\pi^2}\epsilon^{\mu\nu\rho\sigma z} \int \mathrm{tr}\,\left(3A_z F_{\mu\nu}F_{\rho\sigma} - 4A_\mu \partial_z A_\nu F_{\rho\sigma}\right), \end{aligned} \tag{7.51}$$

and given by

$$\mathcal{L}_{\Pi v^m v^n} = \frac{N_c}{4\pi^2 f_\pi} c_{v^n v^m} \epsilon^{\mu\nu\rho\sigma} \mathrm{tr}\,\left(\Pi \partial_\mu v_\nu^{(n)} \partial_\rho v_\sigma^{(m)}\right), \tag{7.52}$$

with coupling constants

$$c_{v^n v^m} = \frac{1}{\pi}\int \mathrm{d}z K^{-1}\psi_{2n-1}\psi_{2m-1} = \left\{\frac{1350.83}{\lambda N_c}, \ldots\right\}, \tag{7.53}$$

as originally studied in [75]. Only the decay $\phi \to \pi\rho$ would be above the mass threshold but is forbidden due to the assumed ideal mixing. We shall return to this particular decay channel later on when also discussing the decay $\phi \to \pi\gamma$, which is inherited from this reaction.

As was the case for the pseudoscalars, the axial vector mesons for $N_f = 3$ are below the mass threshold for decays into two vector mesons. However, the CS-term in (7.51) contains interactions between two vector mesons and one axial vector meson

$$\mathcal{L}_{v^m v^n a^p} = -\frac{N_c}{4\pi^2} d_{v^m v^n a^p} \epsilon^{\mu\nu\rho\sigma} \mathrm{tr}\,\left(v_\mu^{(m)} a_\nu^{(p)} \partial_\rho v_\sigma^{(n)}\right), \tag{7.54}$$

with

$$d_{v^m v^n a^p} = \int \mathrm{d}z \psi_{2m-1}\psi'_{2n-1}\psi_{2p},\,, \tag{7.55}$$

that will, through VMD, give rise to radiative decays.

TU Bibliothek Your knowledge hub WIEN
Die approbierte gedruckte Originalversion dieser Dissertation ist an der TU Wien Bibliothek verfügbar.
The approved original version of this doctoral thesis is available in print at TU Wien Bibliothek.

7.3.2 Radiative Pseudoscalar Meson Decays

The heaviest pseudoscalar meson described by the WSS model with $N_f = 3$ is the η' meson. With a mass of about 1 GeV, it lies below the mass threshold for the production of two vector mesons. However, through VMD, one can obtain from (7.52) decays into two photons realized through the interaction

$$\mathcal{L}_{\Pi\mathcal{V}\mathcal{V}} = -\frac{N_c}{4\pi^2 f_\pi} c_{\mathcal{V}\mathcal{V}} \epsilon^{\mu\nu\rho\sigma} \mathrm{tr}\left(\Pi \partial_\mu \mathcal{V}_\nu \partial_\rho \mathcal{V}_\sigma\right), \tag{7.56}$$

where the sum over the entire tower of vector mesons yields

$$c_{\mathcal{V}\mathcal{V}} = \sum_m c_{\mathcal{V}v^m} a_{\mathcal{V}v^m} = \frac{1}{\pi}\int \mathrm{d}z K^{-1} = 1. \tag{7.57}$$

The decay rate is obtained as

$$\Gamma_{\Pi\to\gamma\gamma} = \frac{1}{2}\frac{1}{8\pi}\frac{|\mathbf{p}_\gamma|}{m_\Pi^2}\frac{1}{2}|\mathcal{M}_{\Pi\to\mathcal{V}\mathcal{V}}|^2 \tag{7.58}$$

with

$$|\mathcal{M}_{\Pi\to\mathcal{V}\mathcal{V}}|^2 = \frac{e^4 N_c^2}{2\pi^4 f_\pi^2}\left(\mathrm{tr}\left(T_\Pi Q^2\right)\right)^2 m_\Pi^4, \tag{7.59}$$

where the additional factor of $1/2$ is due to identical outgoing states. In Table 7.3 we collect various radiative decays rates of pseudoscalar mesons for $\lambda = 16.63\ldots12.55$ and compare them to the experimental values quoted by the PDG [9] . Since the choice $\lambda = 16.63$ corresponds to the correct pion decay constant, only the first value matches the experimental decay rate for $\pi^0 \to 2\gamma$. Due to the mixing angle θ_P given in (7.34), the variation in $\lambda = 16.63\ldots12.55$ is non-monotonic for decays involving η or η'. The extremal value is also given for intermediate values of λ exceeding the bound.

7.3.3 Radiative Vector and Axial Vector Meson Decays

Using VMD, the interaction between a photon, a vector meson, and a pseudoscalar meson is obtained from (7.52) as

$$\mathcal{L}_{\Pi\mathcal{V}v^n} = \frac{N_c}{4\pi^2 f_\pi} c_{\mathcal{V}v^n} \epsilon^{\mu\nu\rho\sigma} \mathrm{tr}\left(\Pi \partial_\mu v_\nu^{(n)} \partial_\rho \mathcal{V}_\sigma + \Pi \partial_\mu \mathcal{V}_\nu \partial_\rho v_\sigma^{(n)}\right), \tag{7.60}$$

with coupling constant

$$c_{\mathcal{V}v^n} = \frac{1}{\pi}\int \mathrm{d}z K^{-1}\psi_{2n-1} = \{33.9839,\ldots\}(N_c\lambda)^{-1/2}. \tag{7.61}$$

	$\Gamma^{\text{exp.}}$[keV]	Γ^{WSS}[keV]
$\pi^0 \to 2\gamma$	0.00780(12)	0.00773...0.0102
$\eta \to 2\gamma$	0.515(18)	0.480...0.978
$\eta' \to 2\gamma$	4.34(14)	5.72...5.87...5.75
$\rho^0 \to \pi^0\gamma$	70(12)	56.2...98.6
$\rho^\pm \to \pi^\pm\gamma$	68(7)	56.2...98.6
$\rho^0 \to \eta\gamma$	45(3)	40.3...90.5
$\omega \to \pi^0\gamma$	725(34)	521...915
$\omega \to \eta\gamma$	3.9(4)	4.87...10.9
$\eta' \to \rho^0\gamma$	$55.4(1.9)^{\text{fit}}$,$68(7)^{\text{av.}}$	54.1...59.2...58.5
$\eta' \to \omega\gamma$	$4.74(20)^{\text{fit}}$,$5.8(7)^{\text{av.}}$	5.37...5.89...5.81
$\phi \to \pi^0\gamma$	5.6(2)	0
$\phi \to \eta\gamma$	55.3(1.2)	84.7...92.8...91.6
$\phi \to \eta'\gamma$	0.264(10)	0.525...1.18
$K^{*0} \to K^0\gamma$	116(10)	124...218
$K^{*\pm} \to K^\pm\gamma$	50(5)	31.0...54.5

Table 7.3.: Radiative decay widths of pseudoscalar and vector mesons with 't Hooft coupling $\lambda = 16.63 \ldots 12.55$. For nonmonotonic dependence on λ intermediate extremal values are also given. Ideal mixing is assumed for ω and ϕ. Except for the π^0 width [106], all experimental results are taken from the PDG [9] .

Note that one may use again the completeness relation (7.17) to eliminate the summed-over modes. The partial width following from (7.60) is obtained as

$$\Gamma_{v^n \to \Pi\gamma} = \frac{1}{8\pi} \left|\mathcal{M}_{v^n \to \Pi\mathcal{V}}\right|^2 \frac{|\mathbf{p}_\mathcal{V}|}{m_v^2}, \tag{7.62}$$

with the spin-averaged squared amplitude

$$\left|\mathcal{M}_{v^n \to \Pi\mathcal{V}}\right|^2 = \frac{c^2_{\mathcal{V}v^n} e^2 N_c^2}{96\pi^4 f_\pi^2} \left(\text{tr}\ (T_\Pi T_{v^n} Q) + \text{tr}\ (T_\Pi Q T_{v^n})\right)^2 \left(m_\Pi^2 - m_{v^n}^2\right)^2 . \tag{7.63}$$

In Table 7.3 we list the radiative decays involving a pseudoscalar meson, a vector meson, and one photon. As stated above, the mixing angle θ_V is assumed to be ideal $\theta_V = \arctan 1/\sqrt{2}$. Fitting it, for example, through the ratio of their decay widths into $\pi^0\gamma$ [9] , 5.6/725, one obtains an (almost ideal) mixing angle of $\theta_V = \theta_V^{\text{ideal}} + 3.32°$, as in [102]. This would give $\Gamma^{\text{WSS}}(\phi \to \pi\gamma) = 4 \ldots 7$ keV and $\Gamma^{\text{WSS}}(\omega \to \eta\gamma) = 3.94 \ldots 9.46$, consistent with experiment, but at the cost of overestimating $\Gamma^{\text{WSS}}(\eta' \to \omega\gamma) = 6.92 \ldots 8.29$. For the hadronic decay $\phi \to \rho\pi$, which is the dominant decay channel in $\phi \to 3\pi$ [103–105], we obtain $\Gamma_{\phi\to\rho\pi} = 189 \ldots 440$ keV. Currently, the PDG lists no average for either process. A common feature shared by many holographic models [75, 107–109], and also the hidden local symmetry approach [110], is the vanishing of the coupling of an axial vector meson to a pseudoscalar meson and one photon. In the WSS model, this interaction arises from (7.46) with coupling

$$g_{a_1\pi\mathcal{V}} = 2M_{\text{KK}}\sqrt{\frac{\kappa}{\pi}}\int \mathrm{d}z\psi_2' = 0, \tag{7.64}$$

which integrates to zero due to the negative z-parity of the integrand. This is in agreement with the rather small $a_1^\pm \to \pi^\pm\gamma$ width observed in experiment that cannot be explained by naive VMD models [111].

Employing VMD on (7.54), the interaction Lagrangian between one axial vector meson, one vector meson, and one photon is readily obtained

$$\mathcal{L}_{\mathcal{V}v^n a^p} = -\frac{N_c}{4\pi^2} d_{\mathcal{V}v^n a^p}\epsilon^{\mu\nu\rho\sigma}\text{tr}\,\left(v_\mu^{(n)} a_\nu^{(p)}\partial_\rho\mathcal{V}_\sigma\right), \tag{7.65}$$

with

$$d_{\mathcal{V}v^n a^p} = \int \mathrm{d}z\psi_{2n-1}'\psi_{2p} = \{-2497.14,\dots\}N_c^{-1}\lambda^{-1}. \tag{7.66}$$

Carrying out the spin-averaging and the polarization sums gives

$$|\mathcal{M}_{a^p\to v^n\mathcal{V}}|^2 = \frac{d^2_{\mathcal{V}v^n a^p}\left(m^2_{a^p} - m^2_{v^n}\right)^2\left(m^2_{a^p} + m^2_{v^n}\right)N_c^2}{96\pi^4 m^2_{a^p} m^2_{v^n}}\left(\text{tr}\,\left(eQT_{a^p}T_{v^n}\right)\right)^2. \tag{7.67}$$

The numerical results for the decay width

$$\Gamma_{a^p\to v^n\gamma} = \frac{1}{8\pi}\frac{|\mathbf{p}_\mathcal{V}|}{m^2_{a^p}}|\mathcal{M}_{a^p\to v^n\mathcal{V}}|^2 \tag{7.68}$$

are listed in Table 7.4. Again, ideal mixing between ω and ϕ is assumed. Non-ideal mixing with $\theta_V \approx 38.6^\circ$ would marginally increase $\phi\gamma$ over $\omega\gamma$ for $f_1(1285)$, at the cost of decreasing it for $f_1(1420)$. In accordance with the Landau-Yang theorem [114, 115], the would-be two-photon interactions resulting from (7.54) vanish, since the radial derivative would act on the constant bulk-to-boundary propagator of one of the on-shell photons. If either of the photons is off-shell, we may use the equation of motion of the bulk-to-boundary propagator

$$\left(1+z^2\right)^{1/3}\partial_z\left[\left(1+z^2\right)\partial_z\mathcal{J}(Q,z)\right] = \frac{Q^2}{M^2_{\text{KK}}}\mathcal{J}(Q,z), \tag{7.69}$$

and expand (7.69) for small momenta Q

$$\mathcal{J}(Q,z) = 1 + \frac{Q^2}{M^2_{\text{KK}}}\beta(z) + \mathcal{O}(Q^4). \tag{7.70}$$

Die approbierte gedruckte Originalversion dieser Dissertation ist an der TU Wien Bibliothek verfügbar.
The approved original version of this doctoral thesis is available in print at TU Wien Bibliothek.
TU Bibliothek WIEN Your knowledge hub

	Γ^{exp}[keV]	Γ^{WSS}[keV]
$a_1(1260) \to \rho\gamma$		28.9...50.8
$a_1(1260) \to \omega\gamma$		247...434
$f_1(1285) \to \rho\gamma$	1380(300)...640(240)	295...518|270...473
$f_1(1285) \to \omega\gamma$		31.3...54.9|28.6...50.2
$f_1(1285) \to \phi\gamma$	17(7)	2.44...4.29|3.97...6.98
$f_1(1420) \to \rho\gamma$		73.0...128|119...209
$f_1(1420) \to \omega\gamma$		7.80...13.7|12.7...22.3
$f_1(1420) \to \phi\gamma$	164(55)	52.9...92.9|48.3...84.8

Table 7.4.: Radiative axial vector meson decay with $\lambda = 16.63 \ldots 12.55$ and two values of the f_1 mixing angle $\theta_f = 20.4°|26.4°$. Experimental values are from the PDG [9] except the lower values for $f_1(1285) \to \rho\gamma$, which are from VES [112]; Zanke et al. [113] propose here as experimental average 950(280) keV.

The function $\beta(z)$ is now seen to follow from

$$\partial_z \beta = \frac{z}{(1+z^2)}\, {}_2F_1\left(\frac{1}{3}, \frac{1}{2}, \frac{3}{2}, -z^2\right), \tag{7.71}$$

and we obtain a non-vanishing coupling

$$\begin{aligned} d_{\mathcal{V}v^* a^p} =& \frac{Q^2}{M_{\text{KK}}^2} \int \mathrm{d}z \partial_z \beta(z) \psi_{a^p} + \mathcal{O}(Q^4) \\ =& \frac{Q^2}{M_{\text{KK}}^2} c_{\mathcal{V}v^* a^p}, \qquad c_{\mathcal{V}v^* a^p} = 101.309 N_c^{-1/2} \lambda^{-1/2}. \end{aligned} \tag{7.72}$$

The corresponding partial decay widths for a longitudinal γ_L^* or transversal γ_T^* virtual photon are given by

$$\begin{aligned} \Gamma_{f_1(1285)\to\gamma_L^*\gamma_T} =& \frac{2}{3}\left(\frac{c_{\mathcal{V}v^* a} m_a^2 N_c}{8\pi^2 M_{\text{KK}}^2}\right)^2 \frac{1}{8\pi} \frac{|\mathbf{p}|}{m_a^2} \left(\frac{5e^2}{18}\cos\theta_f - \frac{e^2}{9\sqrt{2}}\sin\theta_f\right)^2 Q^2, \\ \Gamma_{f_1(1285)\to\gamma_T^*\gamma_T} =& \mathcal{O}\left(Q^6\right), \end{aligned} \tag{7.73}$$

and

$$\Gamma_{f_1(1420)\to\gamma_L^*\gamma_T} = \frac{2}{3}\left(\frac{c_{\mathcal{V}v^* a} m_a^2 N_c}{8\pi^2 M_{\text{KK}}^2}\right)^2 \frac{1}{8\pi} \frac{|\mathbf{p}|}{m_a^2} \left(\frac{5e^2}{18}\sin\theta_f + \frac{e^2}{9\sqrt{2}}\cos\theta_f\right)^2 Q^2, \tag{7.74}$$

up to $\mathcal{O}(Q^4)$. The so-called equivalent photon rate is given by

$$\tilde{\Gamma}_{\gamma\gamma} = \lim_{Q^2\to 0} \frac{m_a^2}{Q^2} \frac{1}{2} \Gamma\left(a \to \gamma_L^* \gamma_T\right), \tag{7.75}$$

	$\tilde{\Gamma}_{\gamma\gamma}^{\mathrm{exp}}$[keV]	$\tilde{\Gamma}_{\gamma\gamma}^{\mathrm{WSS}}$[keV]
$a_1\,(1260)$	-	1.60...2.12|1.39...1.85
$f_1\,(1285)$	3.5(8)	3.84...5.09|2.39...3.17
$f_1\,(1420)$	3.2(9)	3.50...4.64|2.19...2.90

Table 7.5.: Equivalent photon rates of axial vector mesons for two values of the f_1 mixing angle $\theta_f = 20.4°|26.4°$ (in the latter case with M_{KK} rescaled such that m_a is raised to the experimental value which reduces ξ in (7.76) to zero); the range denoted by dots corresponds again to $\lambda = 16.63 \ldots 12.55$, where only the first value is matching the axial anomaly exactly. Experimental values from L3 [116, 117], see also [113].

and listed in Table 7.5. Using (7.73) and (7.74) we can determine the mixing angle via

$$\tan^2\left(\theta_f - \arctan\frac{\sqrt{2}}{5}\right) = \left(\frac{m_{f_1}}{m_{f_1'}}\right)^{1+\xi} \frac{\tilde{\Gamma}_{\gamma\gamma}^{f_1'\,\mathrm{exp}}}{\tilde{\Gamma}_{\gamma\gamma}^{f_1\,\mathrm{exp}}}, \tag{7.76}$$

where we introduced an additional parameter ξ to account for the additional powers of M_{KK}^{-2} in the coupling $d_{\mathcal{V}v^*a^p}$. The traditional form of (7.76) with $\xi = 0$ leads to $\theta_f = 26.4°$ [113], while $\xi = 4$, as in the WSS model, leads to $\theta_f = 20.4°$. Both in Table 7.4 and Table 7.5 θ_f is thus varied as $\theta_f = 20.4°|26.4°$ to account for the extrapolation of masses of $f_1(1285)$ and $f_1(1420)$ to their realistic values, in conjunction with a rescaling of M_{KK} by $m_a^{\mathrm{exp}}/m_a^{\mathrm{WSS}}$, therefore setting $\xi = 0$ in (7.76). For both choices of $\lambda = 16.63 \ldots 12.55$, the WSS model shows quite good agreement with experiment, somewhat favoring a higher value of λ for $f_1(1285)$ and a lower value for $f_1(1285)$. No experimental data is available for the equivalent photon rate of the isotriplet axial vector mesons.

Part II

Holographic Glueball Physics

Introduction

8

> "People assume that time is a strict progression of cause to effect, but actually, from a non-linear, non-subjective viewpoint, it's more like a big ball of wibbly-wobbly, timey-wimey stuff."
>
> — **The Doctor**
> *Doctor Who*

In this part we continue the analytical explorations made using gauge/gravity duality, which has been employed for studying glueball spectra in strongly coupled nonabelian theories shortly after the discovery of the AdS/CFT correspondence [73, 74, 118–122]. After setting up the holographic model due to Witten, Sakai, and Sugimoto and testing its validity in Part I, we will now turn to holographic glueball physics. In Chapter 9 we compute the holographic glueball spectrum as originally obtained in [74]. For the glueball sector with even C parity, we will utilize the 11-dimensional formulation of the theory presented in Chapter 6. For the C-odd sector, the computations are carried out in the 10-dimensional formulation of Chapter 7. After determining the mass spectrum, we will study mixing with mesons and mass corrections arising from the DBI action. Next, we will turn to interactions arising from the DBI and CS action of the D8-branes, compute various hadronic and radiative decay rates, and compare them to the available experimental data.

This part is based on the results in Refs. [123, 124] and structured as follows. In Chapter 9 we compute the holographic glueball spectrum and in Chapter 10 we consider hadronic and radiative glueball decays.

9

The Holographic Glueball Spectrum

Triggered by the seminal works of Refs. [118, 119], the computation of the glueball spectrum based on the AdS/CFT correspondence has been an active area of research [73, 74, 120–122]. While this initial top-down approach lead to valuable insights, they miss the connection to QCD at high energies. This inspired bottom-up model building for glueball physics [125–131], with either AdS_5 geometries using a cut-off (”hard wall”) or by introducing a non-constant background dilaton field (”soft wall”) to model confinement. Soft wall models introduce a crucial ingredient of QCD: a running coupling. While for now, we shall restrict ourselves to top-down holographic QCD, in Part III we will explore soft wall models in more detail and show that the resulting mass spectra reproduce the Regge behavior observed in the hadron spectrum. The results presented in this chapter are based on the computations from Ref. [74] and, in the case of the form fields, rederived in the string frame. The states are grouped in sections according to their spin and arranged in order of increasing mass for easier reference. This organizing scheme will be used throughout this part of the thesis.

From the string theory perspective, the color singlet states of the pure Yang-Mills theory are comprised of states pertaining to the closed string sector. As such, and in the supergravity limit, they arise as fluctuations of the metric G_{AB} and 3-form potential A_{ABC} in the 11-dimensional M-theory lift. In the 10-dimensional string frame, they are identified with fluctuations of the metric g_{MN}, dilaton ϕ, Kalb-Ramond B_{MN}, and Ramond-Ramond C_M, C_{MNO} fields. Especially for the metric fluctuations, the computation in 11 dimensions is more tractable since the numerous scalar fluctuations are easier to disentangle. The equation of motion following from the variation of the action (6.4) with respect to the metric is given by

$$R_{AB} - \frac{1}{2} R G_{AB} = \frac{1}{2 \cdot 4!} \left(F_A{}^{A_1 A_2 A_3} F_{B A_1 A_2 A_3} - \frac{1}{2} F^{A_1 A_2 A_3 A_4} F_{A_1 A_2 A_3 A_4} G_{AB} \right) \tag{9.1}$$

It is readily checked that the background (6.2) together with the 4-form flux F_4 induced by the M5-branes solves the equations of motion. The latter serves as a cosmological constant that stabilizes the AdS space, realizing the venerable idea of Freund-Rubin compactifications

[71]. To proceed with the computation of the spectrum, (9.1) is linearized in fluctuations of $G_{AB} \to G_{AB} + \delta G_{AB}$, where δG_{AB} corresponds to the graviton. In particular, one obtains

$$\begin{aligned} -\frac{1}{2}\nabla^2 \delta G_{AB} - \frac{1}{2}\nabla_A \nabla_B \delta G + \frac{1}{2}\nabla^C (\nabla_A \delta G_{BC} + \nabla_B \delta G_{AC}) \\ - \left(R - \frac{1}{4} F^{A_1 A_2 A_3 A_4} F_{A_1 A_2 A_3 A_4} \right) \delta G_{AB} = 0 \end{aligned} \tag{9.2}$$

where $\delta G = G^{AB} \delta G_{AB}$ is the trace. Note that (6.2) represents an Einstein space, being the product space of $\mathrm{AdS}_7 \times S_4$. Using $R_{AB}^{\mathrm{AdS}_D} = -(D-1)/L^2 G_{AB}$ and $R_{AB}^{S_n} = (n-1)/(L/2)^2 G_{AB}$ one readily obtains $R = 6/L^2$. Further $F^{A_1 A_2 A_3 A_4} F_{A_1 A_2 A_3 A_4} = 36/L^2$ and hence, for the particular background (6.2), the linearized equations of motion governing the dynamics of the metric fluctuations are given by

$$-\frac{1}{2}\nabla^2 \delta G_{AB} - \frac{1}{2}\nabla_A \nabla_B \delta G + \frac{1}{2}\nabla^C (\nabla_A \delta G_{BC} + \nabla_B \delta G_{AC}) + \frac{6}{L^2} \delta G_{AB} = 0 \tag{9.3}$$

Note that in the above equation, as well as for the following equations, the transverse-traceless gauge for δG_{MN} was employed. This drastically simplifies the computations. In particular, it enforces vanishing fluctuations of the Ricci scalar, which would be given by

$$R^{(1)} = \nabla^A \nabla^B \delta G_{AB} - \nabla^2 \delta G - \delta G^{AB} R_{AB}. \tag{9.4}$$

For the form fields, working in the 10D string frame is more convenient. The equations of motion follow by variation of (7.4) with respect to the various form fields and are given by

$$\begin{aligned} \nabla_M \tilde{F}^{MN} - \frac{1}{3!} \tilde{F}^{N O_1 O_2 O_3} H_{O_1 O_2 O_3} &= 0, \\ \nabla_O \left(e^{-2\phi} H^{OMN} + C_P \tilde{F}^{OPMN} \right) - \frac{1}{2! \cdot (4!)^2 \sqrt{-g}} \epsilon^{MNO_1 \dots O_8} F_{O_1 \dots O_4} F_{O_5 \dots O_8} &= 0 \\ \nabla_P \tilde{F}^{PMNO} - \frac{1}{3! \cdot 4! \sqrt{-g}} \epsilon^{MNOP_1 \dots P_7} H_{P_1 P_2 P_3} \hat{F}_{P_4 \dots P_7} &= 0. \end{aligned} \tag{9.5}$$

The complete set of equations of motion, including the ones for the dilaton and metric, can be found in Appendix B. Linearizing these equations with respect to the fluctuations

TU Bibliothek Your knowledge hub
WIEN
Die approbierte gedruckte Originalversion dieser Dissertation ist an der TU Wien Bibliothek verfügbar.
The approved original version of this doctoral thesis is available in print at TU Wien Bibliothek.

of $C_1,\ B_2$ and C_3, and taking into account that neither C_1 nor B_2 are sourced by the D4-branes, one obtains

$$\begin{aligned} \nabla_M F^{MN} &= 0, \\ \nabla_O\left(e^{-2\phi}H^{OMN}\right) - \frac{3R_{\text{D4}}^3\sqrt{\hat{g}_{S_4}}}{2!\cdot 4!\sqrt{-g}g_s}\epsilon^{MNO_1\dots O_4}F_{O_1\dots O_4} &= 0, \\ \nabla_P F^{PMNO} - \frac{3R_{\text{D4}}^3\sqrt{\hat{g}_{S_4}}}{3!\cdot\sqrt{-g}g_s}\epsilon^{MNOP_1\dots P_3}H_{P_1P_2P_3} &= 0. \end{aligned} \tag{9.6}$$

It will further prove useful to transform the components of the various dynamical fields of the preceding actions to an orthonormal basis. After this transformation, the covariant derivatives can be replaced by ordinary derivatives. This can be achieved by utilizing tetrads $e^{\hat{A}}_{A}$ and $E^{\hat{A}}_{A}$, which are defined through the relation

$$g_{MN} = \eta_{\hat{M}\hat{N}}e^{\hat{M}}_{M}e^{\hat{N}}_{N}, \quad G_{AB} = \eta_{\hat{A}\hat{B}}E^{\hat{A}}_{A}E^{\hat{B}}_{B}, \tag{9.7}$$

where the hatted indices pertain to the ”flat” coordinates, as opposed to the ”curved” indices without hat.

Witten’s construction, which has been briefly summarized in Chapter 6, involves a supersymmetry breaking compactification that leads to gauginos and, at the one-loop level, adjoint scalars with masses above the compactification scale M_{KK}. However, most of the glueball states lie above this scale as well. On the other hand, as originally found in Refs. [73, 74], the dimensionless ratio of masses between various glueball states is in qualitative agreement with lattice QCD [11, 12]. The compactified, supersymmetry breaking coordinate τ introduces an additional parity transformation, which has no interpretation for the closed string states and also no analog in QCD. Hence, and since there are various superfluous states which do not seem to be reproduced on the lattice, the glueball states with odd τ parity will be discarded.

Due to the supergravity limit, the spectrum truncates at states with spin-2. Their quantum numbers, and in particular their charge and parity assignments, can be deduced from their couplings to the 4D boundary gauge theory and are summarized in Table 9.1. We shall not make these computations explicit since they are already thoroughly documented in the existing literature [73, 74, 119].

G_{AB}				A_{ABC}		
G_{MN}	$G_{M,11}$	$G_{11,11}$	$\sqrt{\lambda_i} = \frac{M_i}{M_{\mathrm{KK}}}$	$A_{MN,11}$	A_{MNO}	$\sqrt{\lambda_i} = \frac{M_i}{M_{\mathrm{KK}}}$
$G_{\mu\nu}$ 2^{++}	C_μ $1^{++}_{(-)}$	ϕ 0^{++}	1.567	$B_{\mu\nu}$ 1^{+-}	$C_{\mu\nu\rho}$ $0^{+-}_{(-)}$	2.435
$G_{\mu\tau}$ $1^{-+}_{(-)}$	C_τ 0^{-+}		1.886	$B_{\mu\tau}$ $1^{--}_{(-)}$	$C_{\mu\nu\tau}$ 1^{--}	3.037
$G_{\tau\tau}$ 0^{++}			0.901	$G^{\alpha}_{\ \alpha}$ 0^{++}		3.575

Table 9.1.: The holographic glueball spectrum as obtained in [74] but with eigenvalues λ_i given in units of M_{KK}. The $-$ subscript denotes states with odd τ-parity that will be discarded in the following.

9.1 Spin-0

9.1.1 The "Exotic" Scalar Glueball

The lightest glueball state, which is dubbed ”exotic” [73] due to having one polarization along the compactified τ direction, is obtained from

$$
\begin{aligned}
\delta G_{\tau\tau} &= -\frac{r^2}{\mathcal{N}_E\, L^2} f(r) S_4(r) G_E(x^\sigma),\\
\delta G_{\mu\nu} &= \frac{r^2}{\mathcal{N}_E\, L^2} S_4(r) \left[\frac{1}{4}\eta_{\mu\nu} - \left(\frac{1}{4} + \frac{3r_{\mathrm{KK}}^6}{5r^6 - 2r_{\mathrm{KK}}^6}\right)\frac{\partial_\mu\partial_\nu}{M^2}\right] G_E(x^\sigma),\\
\delta G_{11,11} &= \frac{r^2}{\mathcal{N}_E\, 4L^2} S_4(r) G_E(x^\sigma),\\
\delta G_{rr} &= -\frac{L^2}{\mathcal{N}_E\, r^2 f(r)} \frac{3r_{\mathrm{KK}}^6}{5r^6 - 2r_{\mathrm{KK}}^6} S_4(r) G_E(x^\sigma),\\
\delta G_{r\mu} = \delta G_{\mu r} &= \frac{90 r^7 r_{\mathrm{KK}}^6}{\mathcal{N}_E\, M^2 L^2 \left(5r^6 - 2r_{\mathrm{KK}}^6\right)^2} S_4(r) \partial_\mu G_E(x^\sigma),
\end{aligned}
\tag{9.8}
$$

where $S_4(r)$ obeys the eigenvalue equation

$$
\frac{\mathrm{d}}{\mathrm{d}r}\left(r^7 - r\, r_{KK}^6\right)\frac{\mathrm{d}}{\mathrm{d}r} S_4(r) + \left(L^4 M_E^2 r^3 + \frac{432 r^5 r_{\mathrm{KK}}^{12}}{\left(5r^6 - 2r_{KK}^6\right)^2}\right) S_4(r) = 0. \tag{9.9}
$$

The boundary conditions $S_4'(r = r_{\mathrm{KK}}) = 0,\ S_4(r = \infty) = 0$ give a mass of $M_E = 855$ MeV for the lowest mode, significantly lighter than the roughly 1700 MeV obtained using

Die approbierte gedruckte Originalversion dieser Dissertation ist an der TU Wien Bibliothek verfügbar.
The approved original version of this doctoral thesis is available in print at TU Wien Bibliothek.
TU Bibliothek WIEN Your knowledge hub

Die approbierte gedruckte Originalversion dieser Dissertation ist an der TU Wien Bibliothek verfügbar.
The approved original version of this doctoral thesis is available in print at TU Wien Bibliothek.
TU Bibliothek WIEN Your knowledge hub

quenched lattice QCD [11, 12].

The normalization constant $\mathcal{N}_E$ is inferred through the kinetic term

$$\mathcal{L}_4|_{G_E^2} = \mathcal{C} \int \mathrm{d}r \frac{r^3 S_4(r)^2}{2L^3 \mathcal{N}_E^2} \frac{5}{8} G_E \left(\Box - M_E^2\right) G_E, \tag{9.10}$$

where the constant $\mathcal{C}$ arising from the dimensional reduction is given by

$$\mathcal{C} = \left(\frac{L}{2}\right)^4 \Omega_4 \frac{1}{2\kappa_{11}^2} (2\pi)^2 R_4 R_{11}. \tag{9.11}$$

Requiring a canonical normalization

$$\mathcal{L}_4|_{G_E^2} = \frac{1}{2} G_E \left(\Box - M_E^2\right) G_E \tag{9.12}$$

the normalization is obtained as

$$\mathcal{N}_E = 0.008751 \lambda^{\frac{1}{2}} N_c M_{\mathrm{KK}}, \tag{9.13}$$

where we used

$$\int \mathrm{d}r \frac{5}{8} \frac{r^3 S_4(r)^2}{L^3} = 0.0918315 \frac{r_{\mathrm{KK}}^4}{L^3}. \tag{9.14}$$

9.1.2 The Dilaton Scalar Glueball

The (predominantly) dilatonic 0^{++} glueball is obtained from

$$\begin{aligned}
\delta G_{\mu\nu} &= \frac{r^2}{\mathcal{N}_D L^2} T_4(r) \left(\eta_{\mu\nu} - \frac{\partial_\mu \partial_\nu}{\Box}\right) G_D(x^\sigma), \\
\delta G_{11,11} &= -3 \frac{r^2}{\mathcal{N}_D L^2} T_4(r) G_D(x^\sigma),
\end{aligned}$$

with an undetermined normalization parameter $\mathcal{N}_D$. The mode equation is found to be

$$\frac{\mathrm{d}}{\mathrm{d}r} \left(r^7 - r\, r_{KK}^6\right) \frac{\mathrm{d}}{\mathrm{d}r} T_4(r) + L^4 M_D^2 r^3 T_4(r) = 0, \tag{9.15}$$

with a mass of $M_D = 1487$ MeV, after imposing the boundary conditions $T_4'(r = r_{\mathrm{KK}}) = 0,\ T_4(r = \infty) = 0$. This is to be compared to the lattices result of about 1700 MeV [11, 12][1] and in the right ballpark for the usually quoted glueball candidates $f_0(1500)$ and $f_0(1710)$. The mass of the former seems almost to match exactly, which makes an identification with $f_0(1500)$ quite tempting. However, as we shall see later in Section 10.2.1, the decay pattern instead matches that of $f_0(1710)$ rather well.

---

[1] In Ref. [13] it was found that unquenching effects are mostly negligible, especially for the 0^{++} glueball. We comment on unquenching effects in Appendix C by utilizing a geometry that includes the first-order backreaction of the flavor branes on the original background in (7.1).

The kinetic and mass term for G_D reads

$$\mathcal{L}_4|_{G_D^2} = \mathcal{C} \int \mathrm{d}r \frac{6r^3 T_4(r)^2}{L^3 \mathcal{N}_D^2} G_D \left(\Box - M_D^2\right) G_D \tag{9.16}$$

The radial integration for the lightest mode yields the constant

$$\int \mathrm{d}r \frac{6r^3 T_4(r)^2}{L^3} = 1.35282 \frac{r_{\mathrm{KK}}^4}{L^3}, \tag{9.17}$$

which fixes the normalization to

$$\mathcal{N}_D = 0.0335879 \lambda^{\frac{1}{2}} N_c M_{\mathrm{KK}}. \tag{9.18}$$

9.1.3 The Pseudoscalar Glueball

For the form fields, it is more convenient to work in the 10D string frame with the equations of motion following from the action (7.4). The pseudoscalar 0^{-+} glueball is obtained from the Ramond-Ramond sector of the theory. In particular, it is given by the τ component of $C_1 = C_\tau \mathrm{d}\tau$ or from $\delta G_{\tau 11}$ of the 11-dimensional theory, sometimes referred to as graviphoton. Note that C_1 is the only Ramond-Ramond form field that does not result from a compactification of A_3. The linearized equations of motion are solved by the ansatz

$$C_\tau = e^{-\phi} e^{\hat{\tau}}_{\tau} V_4(u) \tilde{G}(x^\mu) = \frac{\sqrt{f(u)}}{g_s} V_4(u) \tilde{G}(x^\mu), \tag{9.19}$$

provided that $V_4(u)$ obeys

$$\partial_u (u^4 - u) V_4'(u) + \frac{9}{4} u \left(\frac{M_{PS}^2}{M_{\mathrm{KK}}^2} + \frac{1}{u^2 - u^5} \right) V_4(u) = 0, \tag{9.20}$$

Note that the appearance of the dilaton in (9.19) is purely conventional and was introduced to match the mode equation of [74] after transforming $u = r^2/r_{\mathrm{KK}}^2$. This is due to the conventional form of the Ramond-Ramond action of (7.4), which does not contain explicit powers of g_s and hence the dilaton. As a leading order expansion in terms of the string coupling, one would expect a spherical string worldsheet with genus $k = 0$ and hence Euler characteristic of $\chi = 2$, leading to a prefactor of $e^{-\chi\phi}$. A simple field redefinition of $C_1 = e^{-\phi}\tilde{C}_1,\ F_2 = e^{-\phi}\tilde{F}_2 = e^{-\phi}\mathrm{d}\tilde{C}_1 - \mathrm{d}\phi \wedge \tilde{C}_1$, and analogously for C_3, leads to the same prefactor of $e^{-2\phi}$ for all actions [70]. The normalizable modes $C_\tau^{(2)}$ corresponding to glueball fluctuations obey the boundary conditions $C_\tau^{(2)}(U = \infty) = C_\tau^{(2)}(U = U_{\mathrm{KK}}) =$

$0,\ \partial_U C_\tau^{(2)}(U = U_{\rm KK}) \neq 0$, with the mass of the lowest lying state given by $M_{PS} = 1789$ MeV. This is about 800 MeV below the mass obtained using quenched lattice QCD [11, 12]. However, as discussed in Section 9.4, the pseudoscalar glueball receives a small mass correction through its mixing with the η' meson due to the Witten-Veneziano mechanism. To quadratic order, the Lagrangian is given by

$$\begin{aligned}\mathcal{L}_R^{(2)}|_{\tilde G} &= -\frac{2\pi}{M_{\rm KK}\mathcal{N}_{PS}^2 g_s^2}\frac{V_4}{2\kappa_{10}^2}\int_1^\infty \mathrm{d}u \frac{1}{2}U_{\rm KK}^2 R_{\rm D4}^3 u V_4(u)^2 \tilde G(x^\mu)\left(\Box - M_{PS}^2\right)\tilde G(x^\mu) \\ &= \frac{1}{2}\tilde G(x^\mu)\left(\Box - M_{PS}^2\right)\tilde G(x^\mu)\end{aligned} \tag{9.21}$$

where

$$\mathcal{N}_{PS}^2 = \frac{\lambda M_{\rm KK}^2 N_c^2}{486\pi^2}\int_1^\infty \mathrm{d}u V_4(u)^2, \tag{9.22}$$

and thus

$$\mathcal{N}_{PS} = 0.00642887 M_{\rm KK} N_c \sqrt{\lambda}. \tag{9.23}$$

9.2 Spin-1

9.2.1 The Pseudovector Glueball

The 1^{+-} pseudovector glueball is obtained from the fluctuations

$$a_{\mu\nu 11} = B_{\mu\nu} = g_s \frac{c(u)}{\mathcal{N}_{PV}}\tilde B_{\mu\nu}(x^\mu), \quad a_{\mu\tau r} = C_{\mu\tau r} = \frac{3}{2\mathcal{N}_{PV}\Box}\frac{2c(u)}{u}\eta_{\mu\nu}\epsilon^{\nu\rho\sigma\kappa}\partial_\rho \tilde B_{\sigma\kappa}(x^\mu), \tag{9.24}$$

where $c(u) = u^{3/2}/g_s N_4(u)$ obeys the mode equation

$$\partial_u(u^4 - u)N_4'(u) + \frac{9}{4}u\left(\frac{M_{PV}^2}{M_{\rm KK}^2} + \frac{1-3u^3}{u^2}\right)N_4(u) = 0. \tag{9.25}$$

The appearance of both $C_{\mu\tau r}$ and $B_{\mu\nu}$ is tied to the topological mass term in the CS action of (7.4). A consistent solution to the linearized equations of motion and a canonical kinetic term in the action of (7.4) is only obtained when both fluctuations are included. The quadratic Lagrangian in (7.4) reduces to

$$(\mathcal{L}_{NS}^{(2)} + \mathcal{L}_R^{(2)})|_{G_{PV}} = -\frac{1}{2\kappa_{10}^2}\frac{1}{4g_s^2}\frac{R_{\rm D4}^6}{U_{\rm KK}}\sqrt{\hat g_{S_4}}\frac{u}{u^3-1}a(u)^2\tilde B_{\mu\nu}\left(M^2 - \Box\right)\tilde B_{\mu\nu}. \tag{9.26}$$

By imposing the boundary conditions $N_4'(U_{\rm KK}) = 0$ and $N_4(\infty) = 0$, the lightest mode has mass $M_{PV} = 2311$ MeV, which is about 600 MeV below the quenched lattice result [11, 12] and about 1 GeV below the unquenched result [13]. Further, the normalization is found to be

$$\mathcal{N}_{PV}^2 = \frac{3}{16}\frac{\lambda N_c^2}{(2\pi)^2 M_{\text{KK}}^4 R_{\text{D4}}^6}\int_1^\infty \mathrm{d}u u N_4(u)^2, \quad u = \frac{U}{U_{\text{KK}}} \tag{9.27}$$

with

$$\mathcal{N}_{PV} = 0.0332045\frac{\sqrt{\lambda}N_c}{M_{\text{KK}}^2 R_{\text{D4}}^3} \tag{9.28}$$

differing from [132] by a factor of r_{KK}^3 through the dimensionless ansatz in (9.24).

9.2.2 The Vector Gluebal

The 1^{--} vector glueball is obtained from the fluctuations

$$C_{\mu\nu\tau} = \frac{a(u)}{\mathcal{N}_V}\tilde{C}_{\mu\nu}(x^\mu), \quad B_{\mu u} = \frac{3g_s}{2\mathcal{N}_V\Box}\frac{u^2}{u^3-1}a(u)\eta_{\mu\kappa}\epsilon^{\kappa\nu\rho\sigma}\partial_\nu\tilde{C}_{\rho\sigma}(x^\mu), \tag{9.29}$$

where $a(u) = e^{-\phi}\left(e^{\hat{x}}{}_x\right)^2 e^{\hat{\tau}}{}_\tau M_4(u) = \sqrt{u^3-1}/g_s M_4(u)$. As was the case for the pseudovector glueball, the appearance of both $C_{\mu\nu\tau}$ and $B_{\mu u}$ is tied to the topological mass term in the CS action of (7.4). $M_4(u)$ obeys the mode equation

$$\partial_u(u^4-u)M_4'(u) + \frac{9}{4}u\left(\frac{M_V^2}{M_{\text{KK}}^2}\frac{(2-3u^3)u}{u^3-1}\right)M_4(r) = 0, \tag{9.30}$$

which slightly differs from the one obtained in [74] after transforming to $u = r^2/r_{\text{KK}}^2$ but a matching mass spectrum, hinting at a typo. By imposing the boundary conditions $M_4'(U_{\text{KK}}) = 1$ and $M_4(\infty) = 0$, the lightest mode has mass $M_V = 2882$ MeV, which is about 1 GeV below the (quenched) lattice result [11, 12]. The quadratic Lagrangian reduces to

$$(\mathcal{L}_{NS}^{(2)} + \mathcal{L}_R^{(2)})|_{G_V} = -\frac{1}{2\kappa_{10}^2}\frac{1}{4g_s^2}\frac{R_{\text{D4}}^6}{U_{\text{KK}}}\sqrt{\hat{g}_{S_4}}\frac{u}{u^3-1}a(u)^2\tilde{C}_{\mu\nu}\left(M_V^2-\Box\right)\tilde{C}_{\mu\nu}. \tag{9.31}$$

leading to the normalization condition

$$\mathcal{N}_V^2 = \frac{3}{16}\frac{\lambda N_c^2}{(2\pi)^2 M_{\text{KK}}^4 R_{\text{D4}}^6}\int_1^\infty \mathrm{d}u u M_4(u)^2, \quad u = \frac{U}{U_{\text{KK}}}, \tag{9.32}$$

with

$$\mathcal{N}_V = 0.0142218\frac{\sqrt{\lambda}N_c}{M_{\text{KK}}^2 R_{\text{D4}}^3} \tag{9.33}$$

for the ground state vector glueball. Recall that the holographic coordinate z of the joined D8-brane system covers the radial coordinate U twice, therefore the parity under $z \to -z$

Die approbierte gedruckte Originalversion dieser Dissertation ist an der TU Wien Bibliothek verfügbar.
The approved original version of this doctoral thesis is available in print at TU Wien Bibliothek.
TU Bibliothek WIEN Your knowledge hub

reflects the τ parity. The glueball modes under consideration in this thesis all have even τ parity. However, the transformation to an orthonormal frame employed above corresponds to $a(z) = zM_4(z)$, and therefore, $M_4(z)$ has odd parity on the joint flavor branes.

9.3 Spin-2

Tensor Glueball

The 2^{++} tensor glueball fluctuation reads

$$\delta G_{\mu\nu} = q_{\mu\nu} \frac{r^2}{L^2 \mathcal{N}_T} T_4(r) G_T(x^\sigma), \tag{9.34}$$

where $q_{\mu\nu}$ is a symmetric, transverse, and traceless polarization tensor, which is normalized such that $q_{\mu\nu} q^{\mu\nu} = 1$, differing from [133] .

$T_4(r)$ satisfies the same eigenvalue equation and boundary conditions as in the case of the dilatonic scalar glueball, (9.15), but it acquires a different normalization. To second order in fluctuations, the Lagrangian reads

$$\begin{aligned} \mathcal{L}_4|_{G_T^2} &= \mathcal{C} \int \mathrm{d}r \frac{r^3 T_4(r)^2}{4L^3 \mathcal{N}_T^2} G_T \left(\Box - M^2\right) G_T \\ &= \frac{1}{2} G_T \left(\Box - M^2\right) G_T, \end{aligned} \tag{9.35}$$

with

$$\int \mathrm{d}r \frac{r^3 T_4(r)^2}{2L^3} = 0.112735 \frac{r_{\mathrm{KK}}^4}{L^3}, \tag{9.36}$$

fixing the normalization to

$$\mathcal{N}_T = 0.00969598 \lambda^{\frac{1}{2}} N_c M_{\mathrm{KK}} = \frac{\mathcal{N}_D}{2\sqrt{3}}. \tag{9.37}$$

The degeneracy in mass of some glueball states is a feature shared by many holographic models due to the high symmetry of the considered backgrounds. In the WSS model, the dilaton scalar and tensor glueball are around 1500 MeV, while quenched lattice QCD [11, 134] finds 1700 and 2400 MeV, respectively. The unquenched result of [13] points to an even higher value of 2600 MeV.

9.4 Glueball-Meson Mixing and Mass corrections

The DBI action in (7.6) leads to mass corrections for fluctuations involving the Kalb-Ramond field B_2. Additionally, this field leads to mixing with the flavor gauge fields. Within the WSS model, the pseudoscalar and vector glueball are the only states with even τ parity that mix with ordinary mesons. In the following section, we shall compute these corrections and gauge their importance for the evaluation of decay rates in Chapter 10.

9.4.1 Pseudoscalar glueball

In Ref. [135] it was shown that the Witten-Veneziano mechanism (see Section 7.1) gives rise to a kinetic mixing term

$$S_R \supset \int \mathrm{d}^4x \zeta_2 \partial_\mu \eta_0 \partial_\mu \tilde{G}, \qquad \zeta_2 = 0.0112\lambda\sqrt{\frac{N_f}{N_c}} \tag{9.38}$$

between the pseudoscalar glueball and the abelian part of the pseudoscalar meson nonet. To order N_f/N_c, the Lagrangian of this system can be diagonalized via a non-unitary field redefinition

$$\eta_0 \to \eta_0 \zeta_2 \tilde{G}, \qquad \tilde{G} \to \tilde{G}, \tag{9.39}$$

therefore raising the mass of the pseudoscalar glueball to

$$M_{PS}^2(1+\zeta_2^2) = (1819.7 \ldots 1806.5\ \mathrm{MeV})^2, \tag{9.40}$$

and passing on the interactions of η_0 to the pseudoscalar glueball. Since the dominant decay modes of the pseudoscalar glueball arise through this mixing, we shall also consider the mass correction of the pseudoscalar glueball when computing decay rates.

9.4.2 Pseudovector Glueball

The terms bilinear in the Kalb-Ramond field B_2 of the DBI action in (7.6) generate a mass correction for the pseudovector glueball of order$\mathcal{O}(N_f/N_c)$

$$\begin{aligned} S_{\mathrm{DBI}} &= -\int \mathrm{d}^4x \frac{1}{2}\delta\lambda_{PV} M_{\mathrm{KK}}^2 \eta^{\mu\nu}\tilde{V}_\mu \tilde{V}_\nu, \\ \delta\lambda_{PV} &= \frac{\lambda^3 N_f N_c}{54(2\pi)^5 M_{\mathrm{KK}}^2 R_{\mathrm{D4}}^6 M_V^2} \int \mathrm{d}z (1+z^2)^{2/3} N_4(z)^2 = 0.00351\lambda^2 \frac{N_f}{N_c}. \end{aligned} \tag{9.41}$$

This amounts to an increase in mass of about 8%, which will not be considered when evaluating decay rates. As opposed to the previous case, there is no mixing since the 1^{+-} spin-1 nonet, which would include the $b_1,\ h_1$ and K_{1B} mesons, is absent in the WSS model.

9.4.3 Vector Glueball

Mass Correction

As for the pseudovector glueball, the DBI action gives rise to a term quadratic in the Kalb-Ramond field B_2. Since we are working in the probe approximation, this term will be treated as a perturbation, with the holographic wave function $M_4(z)$ unchanged. Explicitly, it is given by

$$\begin{aligned}
S_{\mathrm{DBI}} &= -T_8 \mathrm{tr} \int \mathrm{d}^9 x e^{-\phi} \sqrt{-g_{MN} + (2\pi\alpha')F_{MN} + B_{MN}} \\
&\supset -T_8 N_f \left(\frac{8\pi^2}{3}\right) \int \mathrm{d}^4 x \mathrm{d}z \sqrt{-g_{D8}} e^{-\phi} \frac{1}{2} g^{\mu\nu} g^{zz} B_{\mu z} B_{\nu z} \\
&= -\frac{2\lambda^3 N_f N_c}{27(2\pi)^5 R_{\mathrm{D4}}^6} \int \mathrm{d}^4 x \mathrm{d}z (1+z^2) M_4(z)^2 \frac{1}{2\Box} \eta^{\mu\nu} V_\mu V_\nu \qquad (9.42) \\
&= -\int \mathrm{d}^4 x \frac{1}{2} \delta\lambda_V M_{\mathrm{KK}}^2 \eta^{\mu\nu} V_\mu V_\nu, \\
\delta\lambda_V &= \frac{2\lambda^3 N_f N_c}{27(2\pi)^5 M_{\mathrm{KK}}^2 R_{\mathrm{D4}}^6 M_V^2} \int \mathrm{d}z (1+z^2) M_4(z)^2 = 0.00233 \lambda^2 \frac{N_f}{N_c},
\end{aligned}$$

where we projected out the spin-1 part of $\tilde{C}_{\rho\sigma}(x^\mu)$ with $\tilde{C}_{\rho\sigma}(x^\mu) = \frac{1}{\sqrt{\Box}} \epsilon_{\rho\sigma}{}^{\kappa\lambda} \partial_\kappa V_\lambda(x^\mu)$. For $N_f = 3, N_c = 3, \lambda = 16.63 \ldots 12.55$ this amounts to an increase of the mass of the vector glueball of $100 \ldots 57$ MeV, i.e., only $3.4 \ldots 2\%$. However, these mass corrections would need to be considered in conjunction with the mass mixing of the next section.

Mixing With Vector Mesons

Additionally, there is a parametrically more important term of order $\sqrt{N_f/N_c}$, mixing the vector glueball and the singlet flavor gauge field $\hat{v} = v^{a=0}$. It is given by

$$\begin{aligned} S_{DBI} &= -T_8 \mathrm{tr} \int \mathrm{d}^9 x e^{-\phi} \sqrt{-g_{MN} + (2\pi\alpha')F_{MN} + B_{MN}} \\ &\supset - \int \mathrm{d}^4 x \xi_n \eta^{\mu\nu} \hat{v}^n_\mu (x^\mu) V_\nu (x^\mu), \\ \xi_n &= \frac{\kappa\lambda}{2\pi M_V} \frac{M_{\mathrm{KK}}}{R^3_{\mathrm{D4}}} \mathrm{tr}\, T^0 \int \mathrm{d}z (1+z^2) M_4(z) \psi'_{2n-1}(z) \\ &= \{-0.0180, -0.0165, 0.005, \dots\} \lambda M^2_{\mathrm{KK}} \sqrt{\frac{N_f}{N_c}}, \end{aligned} \tag{9.43}$$

for the first three vector meson modes. To fully decouple the singlet vector mesons from the vector glueball, one would need to solve the eigenvalue problem for the whole tower of vector mesons and also the higher vector glueball modes. To gauge the importance of this term, we shall restrict ourselves to the ground state wave functions. The combined Lagrangian of the singlet vector meson-vector glueball system reads to quadratic order

$$\mathcal{L}^{(2)}_{V,\hat{v}} = - \int \mathrm{d}^4 x \left(\frac{1}{4} \hat{f}^2_{\mu\nu} + \frac{1}{2} m^2 \eta^{\mu\nu} \hat{v}_\mu \hat{v}_\nu + \xi_1 \eta^{\mu\nu} \hat{v}_\mu V_\nu + \frac{1}{4} F^2_{\mu\nu} + \frac{1}{2} M^2_V \eta^{\mu\nu} V_\mu V_\nu \right), \tag{9.44}$$

with degenerate vector meson masses. The Lagrangian is readily diagonalized by a unitary field redefinition

$$\begin{aligned} V_\mu &\to \tilde{V}_\mu \cos\theta - \tilde{v}_\mu \sin\theta, \\ \hat{v}_\mu &\to \tilde{V}_\mu \sin\theta + \tilde{v}_\mu \cos\theta, \end{aligned} \tag{9.45}$$

with mixing angle

$$\theta = \frac{1}{2} \arctan \frac{2\xi_1}{M^2_V - m^2}, \tag{9.46}$$

and masses

$$\begin{aligned} \tilde{m}^2 &= m^2 \left(\cos^2\theta + \frac{M^2_V}{m^2} \sin^2\theta - \frac{2\xi_1}{m^2} \sin\theta\cos\theta \right), \\ \tilde{M}^2_V &= M^2_V \left(\cos^2\theta + \frac{m^2}{M^2_V} \sin^2\theta + \frac{2\xi_1}{M^2_V} \sin\theta\cos\theta \right). \end{aligned} \tag{9.47}$$

For example, for $N_f = 2$, where ρ and ω are approximately degenerate, we obtain

$$\theta = -(1.52 \dots 1.18)^\circ \tag{9.48}$$

with $M_V = \sqrt{\lambda_V + \delta\lambda_V} M_{\text{KK}} = (2949 \ldots 2921)$ MeV. After the diagonalization, the masses are only slightly changed and given by

$$\begin{aligned} \tilde{m} &= 773 \ldots 774 \text{ MeV} \\ \tilde{M}_V &= 2950 \ldots 2921 \text{ MeV}, \end{aligned} \tag{9.49}$$

which would make the ω meson 2-3 MeV lighter than the ρ, while in reality it is roughly 12 MeV heavier. The mass corrections (9.42) and (9.47) as well as the mixing (9.45) are rather small; we shall, therefore, stick to the leading order results when computing decay rates.

The effects may be more significant when the corresponding meson modes are similar in mass to the vector glueball, as is the case for charmonia. However, in reality, the latter owe much of their mass to their quarks, which are massless in the WSS model. Despite this limitation, it is still possible to explore the extra decay modes of vector charmonia that could result from a mixing with vector glueballs. After determining the decay channels in Chapter 10, we can assess whether certain mesons could owe some decay modes to a mixing with the vector glueball.

Glueball Decays

10

The interactions between glueballs and ordinary mesons are obtained by expanding (7.6) in perturbations of the metric h_{MN}, dilaton ϕ, and form fields $C_1,\ C_3,\ B_2$. Three- and four-point vertices containing only a single glueball field solely arise from the DBI action and the CS action for metric and form field fluctuations, respectively. Besides possible mixing terms, the latter thus only contain anomalous interactions.

The fluctuations of G and A_3 of the 11-dimensional theory can be translated according to the M-theory lift discussed in Appendix A. For the particular metric of (6.2) and linearized in perturbations, one obtains the perturbed string frame metric

$$\begin{aligned}
g_{\mu\nu} =& \frac{r^3}{L^3}\left[\left(1+\frac{L^2}{2r^2}\delta G_{11,11}\right)\eta_{\mu\nu}+\frac{L^2}{r^2}\delta G_{\mu\nu}\right]\\
g_{\tau\tau} =& \frac{r^3 f}{L^3}\left[1+\frac{L^2}{2r^2}\delta G_{11,11}+\frac{L^2}{r^2 f}\delta G_{44}\right]\\
g_{rr} =& \frac{L}{rf}\left[1+\frac{L^2}{2r^2}\delta G_{11,11}+\frac{r^2 f}{L^2}\delta G_{rr}\right]\\
g_{r\mu} =& \frac{r}{L}\delta G_{r\mu}\\
g_{\Omega\Omega} =& \frac{r}{L}\left(\frac{L}{2}\right)^2\left(1+\frac{L^2}{2r^2}\delta G_{11,11}\right)\\
e^{4\phi/3} =& \frac{r^2}{L^2}\left(1+\frac{L^2}{r^2}\delta G_{11,11}\right),
\end{aligned} \tag{10.1}$$

and the form fields

$$C_M = \delta G_{M11}, \quad B_{MN} = a_{MN11}, \quad C_3 = A_{MNO} + a_{MNO}, \tag{10.2}$$

up to conventional factors of $e^{-\phi}$.

Decays of the lightest, ”exotic” scalar glueball, as described by the WSS model, have first been considered in Ref. [136] and revisited and extended in Ref. [133]. There, it was found to have rather large partial decay widths, neither permitting an identification with the $f_0(1500)$ or $f_0(1710)$ meson, which are alternatingly quoted as the lightest glueball state. However, it might fit the proposed ”fragmented” glueball of Refs. [27, 45, 46], which corresponds to a broad scalar glueball state that is distributed over the resonances

$f_0(1710)$, the recently discovered $f_0(1770)$, $f_0(2020)$, and $f_0(2100)$. This lead Ref. [133] to the conclusion that the lowest scalar glueball, be it either $f_0(1500)$ or $f_0(1710)$, should instead be identified with the predominantly dilatonic metric fluctuation. From these holographic computations and the ones in Refs. [93, 137], it appears that $f_0(1710)$ is the favored scalar glueball candidate. The computations of Ref. [133] were revisited and extended to radiative decays in Ref. [98] , where they were found to have surprisingly large radiative decay widths in the keV range instead of the often quoted eV range.

Decays of the pseudoscalar glueball, which was historically thought to be the lightest glueball[1], were considered in the holographic computations of Ref. [139] and in Ref. [135] together with a small kinetic mixing with the η_0 meson from the Witten-Veneziano mechanism. The latter work found that it predominantly decays into pairs of vector mesons, with decays into pseudoscalars strongly suppressed. Conventionally, the pseudoscalar glueball is considered to have a mass mixing [37, 140], which is absent in the WSS model. On the lattice, one usually finds values around 2600 MeV [11, 12], which is also gaining support by other theoretical computations [141] as well as experiment [142]. Though, based on the lattice computations of Ref. [143], a recent study carried out by the BES III collaboration [144] claims a resonance around 2395 MeV to be the long-sought pseudoscalar glueball[2]. In the following, we shall thus consider extrapolations to both values.

In Ref. [132] decays of the pseudovector glueball arising from fluctuations of B_2 were considered, which found it to be a rather broad resonance. However, there are additional couplings to axial vector and vector mesons as well as a contribution that arises from the dualization of C_3 in the CS term, which has been overlooked and was considered only later in Ref. [124] together with decays of the vector glueball. These additional contributions somewhat reduce the total width of the pseudovector glueball, though it is probably still too broad to be identified in experiment. Nevertheless, the spin-1 fluctuations play a prominent role in the physics of the Odderon, which will be discussed in Part III.

Tensor glueball decays within the WSS were also first considered in [133] , together with extrapolations of the glueball mass to 2000 MeV, motivated by Pomeron physics [36] (see Part III) and 2400 MeV, as suggested from (quenched) lattice computations [11, 12][3]. Indeed, with a mass of 1936 MeV, $f_2(1950)$ is close to the value motivated by Pomeron physics and has also been argued for in Ref. [145].

---

[1] Prominent candidates include $\eta(1405)$ and $\iota(1440)$, which was later split into $\eta(1405)$ and $\eta(1475)$ [138].

[2] In their partial wave analysis they quote the significance of the resonance X(2600) initially observed in Ref. [142] as 4.2σ, but do not include it in the optimal solution.

[3] The partial results on the unquenched glueball spectrum in [13] suggest an even heavier state with mass of 2620(50) MeV. Since backreaction effects are neglected in the following computations of decay rates, we shall instead stick to the result of quenched lattice QCD when performing extrapolations. Some preliminary results on backreaction effects of the flavor branes on the mass spectrum are given in Appendix C.

Except for the scalar glueball candidates $f_0(1500)$, $f_0(1710)$ and the tensor glueball, when identified with the leading state on the pomeron trajectory with a mass of 2000 MeV [36], there are only predictions for masses from lattice QCD and functional methods [17] available. Since both methods seem to agree qualitatively, we shall, therefore, give results for decay rates not only using the pristine WSS model masses but also extrapolate to the aforementioned values or altogether restrict to dimensionless ratios instead.

This chapter is a comprehensive review and, in some cases, also an extension of the decay rates obtained in Refs. [93, 98, 124, 132, 133, 135, 137]. The three-body decays originally neglected in Ref. [98] will be discussed, as well as results from Refs. [93, 133, 137] extended to the case of massive pseudoscalars. Additionally, the minor differences in the notation of the aforementioned publications have been standardized.

10.1 Extrapolations to Realistic Glueball Masses

As was shown in the preceding chapter, the glueball spectrum is unambiguously determined by dimensionless eigenvalue equations. As such, their physical masses are given by eigenvalues in units of M_{KK}^2. The latter is fixed by the mass of the ρ meson, as is required from the pole in the time-like photon propagator in VMD theories. While the ratio of mass eigenvalues qualitatively agrees with lattice QCD results, the overall scale is mismatched when M_{KK} is fixed by the mass of the ρ meson. The eigenvalues of the wave equations are a measure of how deep the holographic wave functions penetrate into the bulk. Correspondingly, the results of overlap integrals between states with a large mass difference are probably overestimated. To account for this shortcoming, the factors of M_{KK} in the normalization factors of the holographic glueball wave functions are rescaled as $M_{\mathrm{KK}} \to M_{\mathrm{KK}} M_G / M_G^{\mathrm{WSS}}$. All other explicit factors of M_{KK}, in particular those in the DBI action, are considered to be fixed.

10.2 Hadronic Glueball Decays

We shall restrict ourselves to the leading interactions arising through expansion of the D8-brane action in (7.6). Higher order contributions have, for example, been studied in Refs. [132, 133] and found not only to be parametrically suppressed in N_c and λ but are also accompanied by numerically small values of the corresponding overlap integrals.

10.2.1 Spin-0

Exotic Scalar Glueball

By inducing the fluctuations of (9.8) in the DBI action of (7.6), one obtains the couplings of pseudoscalars to G_E given by

$$\mathcal{L}_{G_E\Pi\Pi} - \mathrm{tr}\left\{c_1\left[\partial_\mu\Pi\partial_\nu\Pi\frac{\partial_\mu\partial_\nu}{M_E^2}G_E + \frac{1}{2}\left(\partial_\mu\Pi\right)^2\left(1-\frac{\Box}{M_E^2}\right)G_E\right] + \breve{c}_1\partial_\mu\Pi\partial_\mu\Pi G_E\right\} \tag{10.3}$$

with coupling constants ($H_E \equiv S_4/\mathcal{N}_E$)

$$c_1 = \int \mathrm{d}z\frac{\overline{H}_E}{\pi K} = \frac{62.6554}{\sqrt{\lambda}M_{\mathrm{KK}}N_c}, \qquad \breve{c}_1 = \int \mathrm{d}z\frac{H_E}{4\pi K}\frac{16.3904}{\sqrt{\lambda}M_{\mathrm{KK}}N_c}. \tag{10.4}$$

Through the Witten-Veneziano mass term (7.27), one obtains an additional coupling between the scalar glueballs and η_0. For the exotic scalar glueball, it is given by

$$\mathcal{L}_{\eta_0} \supset -\frac{5}{2}m_0^2\eta_0^2\breve{c}_0 G_E, \tag{10.5}$$

with

$$\breve{c}_0 = \frac{3}{4}U_{\mathrm{KK}}^3\int_{U_{\mathrm{KK}}}^{\infty}\mathrm{d}U\,H_E(U)U^{-4} = \frac{15.829}{\sqrt{\lambda}N_c M_{\mathrm{KK}}}. \tag{10.6}$$

Assuming that this coupling of the exotic scalar glueball to the pseudoscalar singlet carries over to quark masses

$$\mathcal{L}_{G_E q\bar{q}} = 5\breve{c}_m G_E \mathcal{L}_m^{\mathcal{M}} \tag{10.7}$$

with $\breve{c}_m$ being of the same order as $\breve{c}_0$, i.e.

$$\breve{c}_m = x\breve{c}_0, \quad x = \mathcal{O}(1), \tag{10.8}$$

we get

$$\mathcal{L}_{G_E\eta\eta'} = \frac{5}{2}(1-x)\breve{c}_0\sin(2\theta_P)m_0^2 G_E\eta\eta'. \tag{10.9}$$

As discussed in Ref. [93], this correlates the flavor asymmetries in the decay pattern in two pseudoscalars with the $\eta\eta'$ partial width. Note that this term with $x \neq 0$ reflects the flavor asymmetries originally absent in the chiral WSS model.
All together we obtain the coupling of the exotic scalar glueball to $\eta\eta$ as

$$\begin{aligned}\mathcal{L}_{G_E\eta\eta} = \frac{5}{2}\breve{c}_0 m_0^2(x-1)\sin\theta_P^2 G_E\eta\eta - \frac{5}{2}\breve{c}_0 x m_\eta^2 G_E\eta\eta\\ -\frac{c_1}{2}\partial_\mu\eta\partial_\nu\eta\left(\frac{1}{2}\eta^{\mu\nu}\left(1-\frac{\Box}{M_E^2}\right)+\frac{\partial^\mu\partial^\nu}{M_E^2}\right)G_E - \frac{\breve{c}_1}{2}\partial_\mu\eta\partial^\mu\eta G_E.\end{aligned} \tag{10.10}$$

Die approbierte gedruckte Originalversion dieser Dissertation ist an der TU Wien Bibliothek verfügbar.
The approved original version of this doctoral thesis is available in print at TU Wien Bibliothek.
TU Bibliothek WIEN Your knowledge hub

For pions and kaons, we have

$$|\mathcal{M}_{G_E\to PP}| = \frac{1}{4}\left|20\breve{c}_0 m_P^2 x + 2\breve{c}_1(M_E^2 - 2m_P^2) + c_1 M_E^2\right|, \tag{10.11}$$

and for η

$$|\mathcal{M}_{G_E\to\eta\eta}| = \frac{1}{4}\left|-20\breve{c}_0 m_0^2(x-1)\sin\theta_P^2 + 20\breve{c}_0 m_P^2 x + 2\breve{c}_1(M_E^2 - 2m_P^2) + c_1 M_E^2\right|, \tag{10.12}$$

from which the η' amplitude is obtained by the replacement $\sin\theta_P \to \cos\theta_P$. In both cases, the decay width is given by

$$\Gamma_{G_E\to PP} = \frac{n_P}{2}\frac{1}{8\pi}\left|\mathcal{M}_{G_E\to PP}\right|^2\frac{|\mathbf{p}_P|}{M_E^2}, \tag{10.13}$$

where P refers to pions ($n_P = 3$), kaons ($n_P = 4$) or $\eta^{(\prime)}$ ($n_P = 1$) mesons.

The interaction Lagrangian of the exotic scalar glueball with two vector mesons is given by

$$\begin{aligned}
\mathcal{L}_{G_E vv} = -\,\mathrm{tr}\,\Bigg\{ & c_2^{mn} M_{\text{KK}}^2 \left[v_\mu^{(m)} v_\nu^{(n)} \frac{\partial_\mu\partial_\nu}{M_E^2} G_E + \frac{1}{2} v_\mu^{(m)} v^{(n)\mu}\left(1 - \frac{\Box}{M_E^2}\right) G_E \right] \\
&+ c_3^{mn}\left[F_{\mu\rho}^{(m)} F_{\nu\rho}^{(n)} \frac{\partial_\mu\partial_\nu}{M_E^2} G_E - \frac{1}{4} F_{\mu\nu}^{(m)} F_{\mu\nu}^{(n)}\left(1 + \frac{\Box}{M_E^2}\right) G_E \right] \\
&+ 3c_4^{mn}\frac{M_{\text{KK}}^2}{M_E^2} v_\mu^{(n)} F_{\mu\nu}^{(m)} \partial_\nu G_E + \breve{c}_2^{mn} M_{\text{KK}}^2 v_\mu^{(m)} v_\mu^{(n)} G_E \\
&+ \frac{1}{2}\breve{c}_3^{mn} F_{\mu\nu}^{(m)} F_{\mu\nu}^{(n)} G_E \Bigg\},
\end{aligned} \tag{10.14}$$

with coupling constants

$$\begin{aligned}
c_2^{mn} &= \kappa \int \mathrm{d}z K \psi'_{2m-1}\psi'_{2n-1}\overline{H}_E = \frac{\{7.116,\dots\}}{\sqrt{\lambda}M_{KK}N_c}, \\
c_3^{mn} &= \kappa \int \mathrm{d}z K^{-1/3} \psi_{2m-1}\psi_{2n-1}\overline{H}_E = \frac{\{69.769,\dots\}}{\sqrt{\lambda}M_{KK}N_c} \\
c_4^{mn} &= \kappa \int \mathrm{d}z \,\frac{20zK}{(5K-2)^2}\psi_{2m-1}\psi'_{2n-1}H_E = \frac{\{-10.5798,\dots\}}{\sqrt{\lambda}M_{\text{KK}}N_c}, \\
\breve{c}_2^{mn} &= \frac{\kappa}{4}\int \mathrm{d}z K \psi'_{2m-1}\psi'_{2n-1}H_E = \frac{\{2.966,\dots\}}{\sqrt{\lambda}M_{KK}N_c} \\
\breve{c}_3^{mn} &= \frac{\kappa}{4}\int \mathrm{d}z K^{-1/3}\psi_{2m-1}\psi_{2m-1}H_E = \frac{\{18.122,\dots\}}{\sqrt{\lambda}M_{KK}N_c},
\end{aligned} \tag{10.15}$$

where we have defined

$$\overline{H}_E = \left[\frac{1}{4} + \frac{3}{5K-2}\right] H_E. \tag{10.16}$$

The numerical results for the coupling constants in (10.15) are for $m = n$, a convention that will be used throughout. From (10.14) we obtain the spin-averaged squared amplitude

$$\begin{aligned}|\mathcal{M}_{G_E\to vv}|^2 =& \frac{\operatorname{tr} T_v T_v^2}{4m_v^4}\Big(2m_v^4(2M_{\mathrm{KK}}^4(4(3\breve{c}_2^2 + 2\breve{c}_2 c_2 + c_2^2) + 12c_4(\breve{c}_2 - c_2) + 27c_4^2) \\ &+ 4M_E^2 M_{\mathrm{KK}}^2(6\breve{c}_2\breve{c}_3 - 2\breve{c}_2 c_3 + c_2\breve{c}_3 + 6\breve{c}_3 c_4 - 3c_3c_4) + M_E^4(c_3 - 2\breve{c}_3)^2) \\ &- 16m_v^6(M_{\mathrm{KK}}^2(6\breve{c}_2\breve{c}_3 - 4\breve{c}_2 c_3 + 2c_2\breve{c}_3 + 3\breve{c}_3 c_4 - 6c_3c_4) \\ &+ M_E^2(2\breve{c}_3^2 - 3\breve{c}_3 c_3 + c_3^2)) - 4M_E^2 M_{\mathrm{KK}}^4(2\breve{c}_2 + c_2)m_v^2(2(\breve{c}_2 + c_2) - 3c_4) \\ &+ M_E^4 M_{\mathrm{KK}}^4(2\breve{c}_2 + c_2)^2 + 16(3\breve{c}_3^2 - 4\breve{c}_3 c_3 + 2c_3^2)m_v^8\Big),\end{aligned} \tag{10.17}$$

where we restricted to the case $v_1 = v_2$ and suppressed the superscripts mn on the couplings for better readability. T_v denotes the generators of the vector meson nonet (c.f. (3.5)). In the following, we shall also use T_a and T_s for the axial vector[4] and pseudoscalar mesons, respectively. When evaluating the decay rate

$$\Gamma_{G_E\to vv} = \frac{1}{2}\frac{1}{8\pi}\frac{|\mathbf{p}_v|}{M_E^2}|\mathcal{M}_{G_E\to vv}|^2, \tag{10.18}$$

and also for all the following decay rates, we restrict to couplings only involving the ground state (axial) vector mesons, i.e., $m = n = 1$. For decay rates involving non-chiral interactions, as in (10.13), we will give explicit formulas. Otherwise, we refer to Appendix D for the suitable formulas.

The coupling of the exotic scalar glueball to one axial vector meson and one pseudoscalar meson is given by

$$\mathcal{L}_{G_E a\Pi} = 2c_6^m M_{\mathrm{KK}} \operatorname{tr}\left(\partial_\mu \Pi a_\nu^{(m)}\right)\frac{\partial^\mu\partial^\nu}{M_E^2} G_E, \tag{10.19}$$

with

$$c_6^m = \sqrt{\frac{\kappa}{\pi}}\int \mathrm{d}z\, \psi'_{2m}\left[\frac{1}{4} + \frac{3}{5K-2}\right] H_E = \frac{\{57.659, \dots\}}{M_{\mathrm{KK}} N_c\sqrt{\lambda}}.$$

---

[4] Recall that only K_{1A} is present in the WSS model.

The spin-averaged squared amplitude following from (10.19) is given by

$$|\mathcal{M}_{G_E\to a\Pi}|^2 = (c_6 M_{\text{KK}}\text{tr}\, T_s T_a)^2 \left(1-\frac{m_a^2+m_\Pi^2}{M_E^2}\right)^2 \left(M_E^2-\frac{(M_E^2+m_a^2-m_\Pi^2)^2}{4m_a^2}\right), \tag{10.20}$$

As we will discuss shortly, the decay into $a_1\pi$ should be considered with subsequent decay into $\rho\pi\pi$, since the latter also appears as a direct decay channel.

The four-point vertices coupling the exotic scalar glueball to two pseudoscalars and one vector meson are obtained from

$$\begin{aligned}\mathcal{L}_{G_E\Pi\Pi v} = 2ic_5^m &\left[\partial_\mu\Pi[\Pi, v_\nu^{(m)}]\frac{\partial_\mu\partial_\nu}{M_E^2}G_E+\frac{1}{2}\partial_\mu\Pi[\Pi, v_\mu^{(m)}]\left(1-\frac{\Box}{M_E^2}\right)G_E\right]\\ &+2i\breve{c}_5^m\partial_\mu\Pi[\Pi, v_\mu^{(m)}]G_E\end{aligned} \tag{10.21}$$

with

$$\begin{aligned}c_5^m &= \frac{1}{\pi}\int \mathrm{d}z\, K^{-1}\psi_{2m-1}\overline{H}_E = \frac{\{2856.25,\dots\}}{\lambda M_{\text{KK}}N_c^{3/2}},\\ \breve{c}_5^m &= \frac{1}{4\pi}\int \mathrm{d}z K^{-1}\psi_{2m-1}H_E = \frac{\{718.659,\dots\}}{\lambda M_{\text{KK}}N_c^{3/2}}.\end{aligned} \tag{10.22}$$

The spin-averaged, squared amplitude is given by

$$\begin{aligned}|\mathcal{M}_{G_E\to\Pi\Pi v}|^2 = \frac{\text{tr}\, T_{s_1}[T_{s_2},T_v]^2}{4M_E^4m_v^2}&\Big(-2M_E^2(m_v^2+s_{12})+M_E^4+(m_v^2-s_{12})^2\Big)\\ &\times\Big(c_5(3M_E^2-m_v^2+s_{12})+2\breve{c}_5M_E^2\Big)^2,\end{aligned} \tag{10.23}$$

where s_{12} is the squared center of mass energy of the pseudoscalar meson subsystem, and we neglected the resonant contribution from $G_E\to a\Pi\to v\Pi\Pi$.

Discussion

Restricting ourselves to two- and three-body decays, the resulting hadronic partial decay widths are collected in Table 10.1. Even when the mass is raised above the mass threshold of two ρ mesons, the dominant decay channel is that into two pseudoscalar mesons, with the strongest decay into pairs of Kaons for $x = 1$. In the phenomenological analysis of Ref. [146], the reaction $G\to a_1\pi$ is the dominant decay channel of the scalar glueball. Explicitly, we obtain $\Gamma_{G_E\to a_1\pi} = 0.61\dots0.81$ MeV for a glueball of mass 1600 MeV, which was used there. This is much lower than their quoted result of 177 MeV. The other decay channels of the scalar glueball in [146] also do not match the decay pattern of the exotic scalar glueball in the WSS model. Albeit sharing the significantly suppressed decays into $a_1\pi$ of the exotic scalar glueball, the dilaton glueball, whose decay rates are

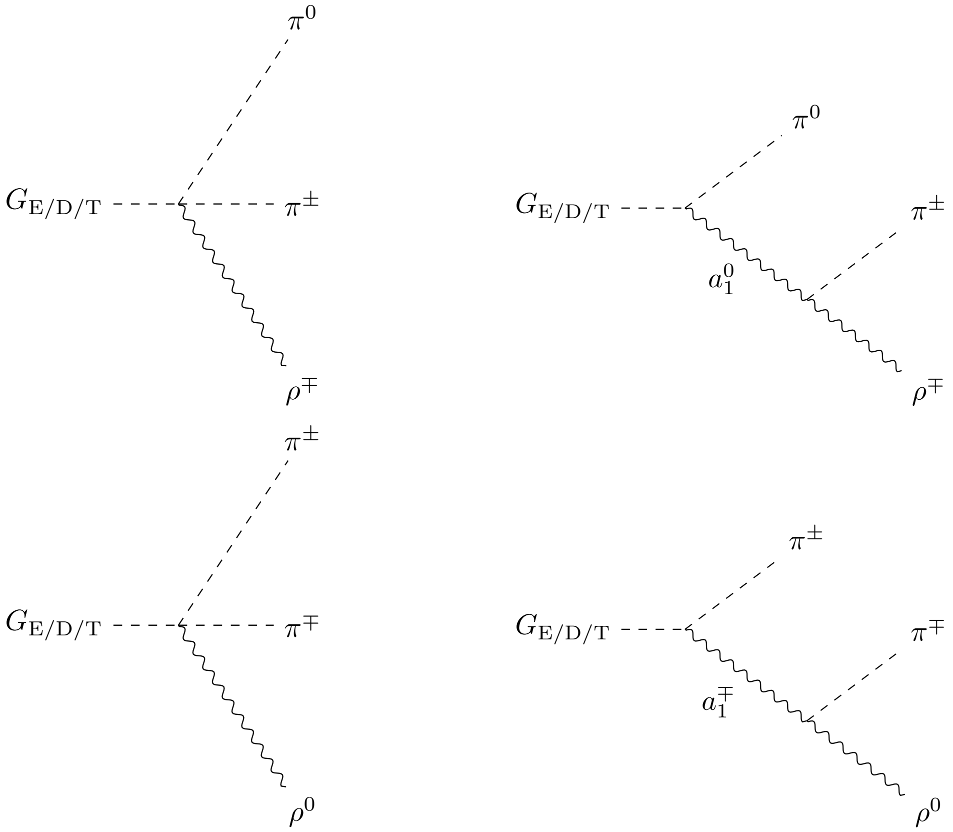
π^0
$G_{\mathrm{E/D/T}}$
$\pi^\pm$
$\rho^\mp$
π^0
$G_{\mathrm{E/D/T}}$
$\pi^\pm$
a_1^0
$\rho^\mp$
$\pi^\pm$
$G_{\mathrm{E/D/T}}$
$\pi^\mp$
ρ^0
$\pi^\pm$
$G_{\mathrm{E/D/T}}$
$\pi^\mp$
$a_1^\mp$
ρ^0

Fig. 10.1.: Feynman diagrams contributing to the hadronic three-body decay of the exotic, diltaon, and tensor glueball into $\rho\pi\pi$

computed in the following section, seems to fit the decay patterns of their analysis better. We also note that the corresponding decay rates in Ref. [98] are too small by a factor of 1/3 since the charged contributions were not summed over. This does, however, not change the conclusion. Recall that the a_1 meson is a rather broad resonance, whose width and mass are well captured by the WSS model (see Section 7.3). It is therefore summed as a resonant contribution for the decays $G_{E,D,T} \to \rho\pi\pi$ with a width given by (7.47). The corresponding Feynman diagrams are depicted in Fig. 10.1. The interference effects in these processes are rather mild, leading to an increase of the partial width of about 15%. However, in Section 10.2.2, we shall see an example where the interference effects resulting from the a_1 meson are relatively strong and might help in experimental identification. The decay of the exotic scalar glueball into 4π, including the resonant decay into $\rho\pi\pi$, worked out in Ref. [133] , have been found to be negligible even in the case of massless pseudoscalars. However, with the glueball mass adjusted to higher values, as suggested by lattice QCD and in Ref. [45], the partial decay widths into two pseudoscalar and one vector meson are again in the MeV range. This decay channel will become even more important when considering radiative decays in Section 10.3, which were omitted in Ref. [98] . Overall, the exotic scalar glueball, even though being the lightest glueball of the WSS model, has a relatively large hadronic decay width, neither fitting the decay patterns of the usually quoted glueball candidates $f_0(1500)$ and $f_0(1710)$ for either value of $x = 0$ or $x = 1$. In Refs. [133, 137] it was thus concluded to be dismissed as a glueball candidate. It might, however, play a role in the scenario of a fragmented scalar glueball, which will be discussed in Section 10.2.1. At this point, we refrain from giving a thorough comparison with recent measurements involving the resonances $f_0(1500)$ and $f_0(1710)$ since they do not match the decay patterns of the exotic scalar glueball well. We shall, however, make a more detailed comparison with experimental data for the dilaton scalar glueball in the next section.

Dilaton Scalar Glueball

By inducing the fluctuations of (9.15) in the D8-brane action (7.6), the coupling of two pseudoscalar mesons to G_D is obtained as

$$\mathcal{L}_{G_D\Pi\Pi} = d_1 \mathrm{tr}\, \partial_\mu \Pi \partial_\nu \Pi \left(\eta^{\mu\nu} - \frac{\partial^\mu \partial^\nu}{\Box} \right) G_D, \tag{10.24}$$

where

$$d_1 = \frac{17.2261}{\sqrt{\lambda} M_{\mathrm{KK}} N_c}. \tag{10.25}$$

	$\Gamma_{G_E(1506)}$ [MeV]	$\Gamma_{G_E(1712)}$ [MeV]
$G_E \to \pi\pi$	135...179|142...189	154...205|161...213
$G_E \to KK$	120...158|229...304	152...202|255...338
$G_E \to \eta\eta$	31.3...45.4|57.7...76.4	40.0...56.9|65.1...86.3
$G_E \to \eta\eta'$	0.21...0.22|0	3.12...3.26|0
$G_E \to \rho\rho$	-	0.77...1.02
$G_E \to \omega\omega$	-	0.19...0.26
$G_E \to a_1\pi, \rho\pi\pi$	28.2...48.6	86.8...149
$G_E \to K^*K\pi$	-	3.29...5.77
$G_E \to$ Hadrons	314...432|458...619	424...598 | 556...769

Table 10.1.: Hadronic decays of the exotic scalar glueball G_E alternatively identified with $f_0(1500)$ and $f_0(1710)$ with masses 1506 MeV and 1712 MeV, respectively, for $\lambda = 16.63\ldots 12.55$. In decays into two pseudoscalar mesons, the two sets of values correspond to $x = 0$ and $x = 1$ in the coupling to the quark mass term (10.7). Four-body decays have been found to be strongly suppressed [133] and are hence not listed. Partial decay widths much smaller than 1 MeV are left out.

As was the case for the exotic scalar glueball in the previous section, through the η_0 mass term of (7.27), one obtains additional couplings between the dilaton scalar glueball and η_0 [93, 137]

$$\mathcal{L}_{\eta_0} \supset \frac{3}{2} m_0^2 \eta_0^2 d_0 G_D, \tag{10.26}$$

with ($H_D \equiv T_4/\mathcal{N}_D$)

$$d_0 = 3U_{\text{KK}}^3 \int_{U_{\text{KK}}}^{\infty} \mathrm{d}U\, H_D(U) U^{-4} = \frac{17.915}{\sqrt{\lambda} N_c M_{\text{KK}}}. \tag{10.27}$$

As in Refs. [93, 137], a scalar glueball coupling to the quark mass terms of the form

$$\mathcal{L}_{G_D q\bar{q}} = -3 d_m G_D \mathcal{L}_m^{\mathcal{M}} \tag{10.28}$$

is assumed, with d_m being of the same order as d_0, i.e.

$$d_m = x d_0, \quad x = \mathcal{O}(1). \tag{10.29}$$

This leads to a $G_D\eta\eta'$ interaction given by

$$\mathcal{L}_{G_D\eta\eta'} = -\frac{3}{2}(1-x) d_0 \sin(2\theta_P) m_0^2 G_D \eta\eta'. \tag{10.30}$$

With these modifications, we get the coupling of the dilaton glueball to $\eta\eta$ as

$$\begin{aligned}\mathcal{L}_{G_D\eta\eta} =& \frac{3}{2} d_0 m_0^2 (1-x) \sin\theta_P^2 G_D \eta\eta + \frac{3}{2} d_0 x m_\eta^2 G_D \eta\eta \\ &+ \frac{d_1}{2} \partial_\mu \eta \partial_\nu \eta \left(\eta^{\mu\nu} - \frac{\partial^\mu \partial^\mu}{\Box}\right) G_D.\end{aligned} \tag{10.31}$$

The coupling to the η' meson is obtained by the substitution $\cos\theta_P^2 \to \sin\theta_P^2$. The partial decay width for G_D decaying into two identical pseudoscalar mesons is obtained as

$$\Gamma_{G_D \to PP} = \frac{n_P}{2} \frac{d_1^2 M_D^3}{256\pi} \left(1 - 4\frac{m_P^2}{M_D^2}\right)^{1/2} \left(1 + \alpha \frac{m_P^2}{M_D^2}\right)^2, \tag{10.32}$$

where

$$\alpha = 4\left(3\frac{d_0}{d_1} x - 1\right), \tag{10.33}$$

for pions and kaons, and

$$\alpha = 4\left[3\frac{d_0}{d_1}\left(x + \frac{m_0^2}{m_P^2} \sin^2\theta_P (1-x)\right) - 1\right], \tag{10.34}$$

for $\eta\eta$, and again with the replacement $\sin\theta_P \to \cos\theta_P$ for $\eta'\eta'$.
The trilinear coupling of a dilatonic scalar glueball to one axial vector and one pseudoscalar meson is given by

$$\mathcal{L}_{G_D \Pi} = -2 d_6^m M_{\text{KK}} \text{tr}\left(\partial_\mu \Pi a_\nu^{(m)}\right) \left(\eta^{\mu\nu} - \frac{\partial^\mu \partial^\nu}{\Box}\right) G_D, \tag{10.35}$$

with

$$d_6^m = \sqrt{\frac{\kappa}{\pi}} \int \mathrm{d}z\, \psi'_{2m} H_D = \frac{\{11.768, \dots\}}{M_{\text{KK}} N_c \sqrt{\lambda}}. \tag{10.36}$$

The pertinent squared amplitude is given by

$$\begin{aligned}|\mathcal{M}_{G_D \to a\Pi}|^2 =& \left(\frac{d_6 M_{\text{KK}} \text{tr}\, T_s T_a}{2 M_D^2 m_a}\right)^2 \left(M_D^2 + m_a^2 - m_\Pi^2\right)^2 \\ & \times \left(M_D^4 - 2M_D^2\left(m_a^2 + m_\Pi^2\right) + \left(m_a^2 - m_\Pi^2\right)^2\right).\end{aligned} \tag{10.37}$$

In a similar fashion, we obtain the interaction terms of the dilatonic scalar glueball with two vector mesons as

$$\mathcal{L}_{G_D vv} = \text{tr} \int \mathrm{d}^4 x \left(d_3^{mn} \eta^{\rho\sigma} F_{\mu\rho}^{(m)} F_{\nu\sigma}^{(n)} + d_2^{mn} M_{\text{KK}}^2 v_\mu^{(m)} v_\nu^{(n)}\right) \left(\eta^{\mu\nu} - \frac{\partial^\mu \partial^\nu}{\Box}\right) G_D, \tag{10.38}$$

where the coupling constants are given by

$$\begin{aligned} d_2^{mn} &= \kappa \int \mathrm{d}z\, K\psi'_{2n-1}\psi'_{2m-1}H_D = \frac{\{4.3714,\dots\}}{\lambda^{\frac{1}{2}}N_c M_{\mathrm{KK}}}, \\ d_3^{mn} &= \kappa \int \mathrm{d}z\, K^{-1/3}\psi_{2n-1}\psi_{2m-1}H_D = \frac{\{18.873,\dots\}}{\lambda^{\frac{1}{2}}N_c M_{\mathrm{KK}}}. \end{aligned} \tag{10.39}$$

For the case of identical outgoing states, the spin-averaged, squared amplitude following from (10.38) is given by

$$\begin{aligned} |\mathcal{M}_{G_D\to vv}|^2 = \left(\frac{\mathrm{tr}\, T_v T_v}{2m_v^2}\right)^2 \Big(& d_2^2 M_{\mathrm{KK}}^4 (M_D^4 + 32 m_v^4) \\ & + 8 d_2 d_3 M_{\mathrm{KK}}^2 m_v^4 (7M_D^2 - 16 m_v^2) \\ & + 6 d_3^2 m_v^4 (3M_D^4 - 16 M_D^2 m_v^2 + 24 m_v^4)\Big) \end{aligned} \tag{10.40}$$

Interactions between the dilaton scalar glueball, two pseudoscalars, and one vector meson are given by

$$\mathcal{L}_{G_D\Pi\Pi v} = 2i\,\mathrm{tr}\; d_5^m \partial_\mu \Pi[\Pi, v_\nu^{(m)}] \left(\eta_{\mu\nu} - \frac{\partial_\mu\partial_\nu}{M_D^2}\right) G_D, \tag{10.41}$$

with coupling

$$d_5^m = \frac{1}{\pi}\int \mathrm{d}z K^{-1}\psi_{2m-1}H_D = \frac{\{724.367,\dots\}}{\lambda M_{\mathrm{KK}} N_c^{3/2}}. \tag{10.42}$$

The squared amplitude for the three-body decay into a pair of pseudoscalars and a vector meson is given by

$$\begin{aligned} |\mathcal{M}_{G_D\to v\Pi\Pi}|^2 = & \left(\frac{d_5 \mathrm{tr}\, T_{s_1}[T_{s_2}, T_v]}{2M_D^2 m_v}\right)^2 \left(m_{\Pi_1}^2 + m_{\Pi_2}^2 - s_{13} - s_{23}\right)^2 \\ & \times \left(2M_D m_v + m_{\Pi_1}^2 + m_{\Pi_2}^2 - s_{13} - s_{23}\right) \\ & \times \left(2M_D m_v - m_{\Pi_1}^2 - m_{\Pi_2}^2 + s_{13} + s_{23}\right), \end{aligned} \tag{10.43}$$

where s_{ij} is the squared center of mass energy of the subsystem of vector meson and pseudoscalar, and we neglected the resonant contribution from $G_D \to a\Pi \to v\Pi\Pi$

Discussion

In Table 10.2 the hadronic two- and three-body decays are collected for ideal mixing in the vector meson sector[5]. Above the threshold of two ρ mesons, when the mass is extrapolated to that of $f_0(1710)$[6], the decay channel $G_D \to \rho\rho$ is dominant, even exceeding the decays into kaon pairs. Coming back to the comparison with [146], where the decays $G \to a_1\pi$ are quoted as the dominant decay channels of a scalar glueball, we find a remarkable agreement with their results into two vector mesons. However, for a scalar glueball with mass of 1600 MeV, as in [146], one obtains $\Gamma_{G_D \to a_1\pi} = 1.11 \ldots 1.48$ MeV, which is well below their result of 177 MeV. On the experimental side stand measurements made by Crystal Barrel [149] that quote a branching ratio $\Gamma_{f_0(1500)\to a_1\pi}/\Gamma_{f_0(1500)\to 4\pi}$ of 12(5)%, which amounts to $6.34(38)$ MeV. This is about an order of magnitude above the WSS model result of $\Gamma_{G_D\to a_1\pi} = 0.51 \ldots 0.68$ MeV. We also note that the corresponding decay rates in Ref. [98] are too small by a factor of 1/3 since the charged contributions were not summed over. This does, however, not change the conclusion therein. Our results for decays into two vector mesons are compatible with those of Ref. [150], but as we shall see later in Section 10.3.1, the radiative decay rates obtained therein differ from ours by an order of magnitude. The PDG [9] lists an average for the partial decay width $f_0(1500) \to \pi\pi$ with a central value of 37 MeV, which is underestimated by the WSS model for this particular glueball mass. On the other hand, for vanishing $\eta\eta'$ decay rates ($x \sim 1$), the decay patterns of $f_0(1710)$ (or $f_0(1770)$) seem to match the branching ratio of $\mathcal{B}(f_0(1710) \to \eta\eta')/\mathcal{B}(f_0(1710) \to \pi\pi) < 1.61 \times 10^{-3}$ obtained by BES III [151]. The latter also contradicts the results of the phenomenological analysis found in Refs. [45, 46]. Additionally, the PDG [9] lists an average for the branching ratio $\Gamma(f_0(1710) \to \pi\pi)/\Gamma(f_0(1710) \to KK) = 0.23(5)$ and [148] found $\Gamma(f_0(1710) \to \eta\eta)/\Gamma(f_0(1710) \to KK) = 0.48(15)$, both of which are only 5% below the WSS model result with $x \sim 1$. The decay rates into two vector mesons obtained in Ref. [150] (44.4 MeV for $\rho\rho$ and 34.6 MeV for $\omega\omega$) are close to our findings. The WSS model prediction for $f_0(1710) \to \omega\omega$ aligns well with the measured branching ratios of radiative J/ψ decays in $\gamma f_0(1710) \to \gamma K\bar{K}$ and $\gamma f_0(1710) \to \gamma\omega\omega$ [9]. The PDG [9] lists the measurement $\mathcal{B}(K\bar{K}) = 0.38^{+0.09}_{-0.19}$ [152] and $0.36(12)$ obtained in the phenomenological analysis of Ref. [153] for the same branching ratio. Both values are consistent with the WSS model result from Ref. [137] of approximately 0.35. With $\mathcal{B}(K\bar{K}) = 0.36(12)$ and the total decay width of $f_0(1710)$ [9] of 123(18) MeV, the partial decay width for $f_0(1710) \to \omega\omega$ is about 15(8) MeV. On the other hand, the holographic prediction for G_D is between 16.6 and 22.0 MeV. We thus identify $f_0(1710)$ with the (dilaton) scalar glueball with quark mass coupling of $x \sim 1$. As was the case for the exotic scalar glueball, decays into one vector meson and two pseudoscalars with subsequent decays into four pions are strongly suppressed [133] [7]. For the decays $G_D \to \pi\pi\rho$, the resonant contribution of a_1 with width given by (7.47) was coherently summed, as depicted in the Feynman diagrams of Fig. 10.1. The interference is more strongly pronounced as in

---

[5] See the discussion in Section 10.2.1 for non-ideal mixing

---

[6] This is assumed to be 1712 MeV based on the average of the T-matrix pole results of [147] and [148].

[7] For massive pseudoscalars the results for $G_D \to 4\pi$, which is dominated by the resonant decay $G_D \to \rho\pi\pi \to 4\pi$, would be smaller by a factor of about 2.

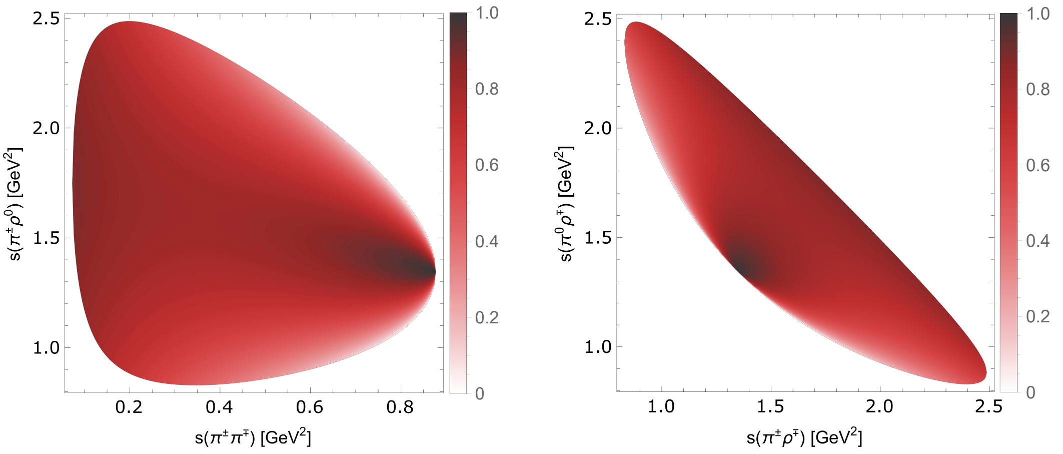

(a)

(b)

Fig. 10.2.: Dalitz plots for the three-body decay $G_D \to \rho\pi\pi$ including a charged (a) and neutral (b) a_1 resonance.

the corresponding decay of the exotic scalar glueball, reducing the partial decay width by almost 50%. However, since this decay channel is subleading, it might prove difficult to discern from the background in an experiment. Nevertheless, in Fig. 10.2 we show the Dalitz plot for the decay channel $G_D \to \rho\pi\pi$.

A Fragmented Scalar Glueball?

In Refs. [27, 45, 46] it was proposed that the scalar glueball is an even broader resonance than the WSS model suggests and is instead distributed over numerous other resonances, including $f_0(1500)$ and $f_0(1710)$. This so-called fragmented glueball is supposed to have a mass of 1865 MeV and a width of 370(50) MeV. In the following section, we shall entertain this idea by extrapolating the decay widths of the dilaton and exotic scalar glueball to the proposed fragmented scalar glueball. Especially the exotic scalar glueball is too broad to be identified with either $f_0(1500)$ or $f_0(1710)$, making its interpretation in terms of a fragmented glueball particularly suited.

In Table 10.3 and Table 10.4 the partial decay rates for the model masses as well as an extrapolation to 1865 MeV are collected for the exotic and dilaton scalar glueball, respectively. Depending on the magnitude of the coupling to quark mass terms, parametrized by x, both fluctuations seem to match this scenario, when their masses are adjusted accordingly. The exotic scalar glueball even exceeds the width of 370(50) MeV by over a factor 2, while the dilaton scalar glueball is only for $x = 1$ slightly above the lower bound. Considering

	$\Gamma_{G_D(1506)}$[MeV]	$\Gamma_{G_D(1712)}$[MeV]
$G_D \to \pi\pi$	12.6...16.7|15.4...20.4	14.6...19.3|17.0...22.5
$G_D \to KK$	4.43...5.87|50.4...66.8	7.49...9.93|49.4...65.4
$G_D \to \eta\eta$	1.93...3.82|14.1...18.7	2.77...4.96|13.9...18.4
$G_D \to \eta\eta'$	0.29...0.30|0	4.35...4.54|0
$G_D \to \rho\rho$	-	53.5...71.0
$G_D \to \omega\omega$	-	16.6...22.0
$G_D \to a_1\pi,\ \rho\pi\pi$	0.96...1.67	2.92...4.81
$G_D \to$ Hadrons	20.2...28.3| 80.8...107	102...137|153...204

Table 10.2.: Hadronic decays of the dilatonic scalar glueball G_D alternatively identified with $f_0(1500)$ and $f_0(1710)$ with masses 1506 MeV and 1712 MeV, respectively, for $\lambda = 16.63\ldots12.55$. In decays into two pseudoscalar mesons, the two sets of values correspond to $x = 0$ and $x = 1$ in the coupling to the quark mass term (10.28). Four-body decays have been found to be strongly suppressed [133] and are hence not listed. Partial decay widths much smaller than 1 MeV are left out.

the previously neglected mixing of the scalar glueball sector induced by the DBI action, might remedy this slight mismatch. This is, however, beyond the scope of this work.

Pseudoscalar Glueball

The pseudoscalar glueball arises as fluctuation of the Ramond-Ramond 1-form field C_1 and obtains a kinetic mixing with the singlet η_0 (see Section 9.4.1)

$$\eta_0 \to \eta_0 + \zeta_2\, G_{PS} = \eta_0 + 0.01118\sqrt{N_f/N_c}\,\lambda\, G_{PS}. \tag{10.44}$$

In Ref. [135], it was shown that the pseudoscalar glueball's primary decay mode, the decay into two vector mesons, is inherited from the singlet pseudoscalar meson through mixing. The relevant interaction Lagrangian originating from (7.52) reads

$$\mathcal{L}_{G_{PS}vv} = G_{PS}\epsilon^{\mu\nu\rho\sigma}\mathrm{tr}\left[k_1^{v^{(m)}v^{(n)}}\partial_\mu v_\nu^{(m)}\partial_\rho v_\sigma^{(n)}\right], \tag{10.45}$$

with

$$k_1^{v^1v^1} = 19.6184 N_c^{-1}\lambda^{-1/2}M_{\mathrm{KK}}^{-1} \tag{10.46}$$

and thus

$$|\mathcal{M}_{G_{PS}\to vv}|^2 = 2(k_1^{v^1v^1}M_{PS}^2\mathrm{tr}\,T_vT_v)^2\left(1-\frac{4m_v^2}{M_{PS}^2}\right), \tag{10.47}$$

for vector mesons with equal masses.

	$\Gamma^{WSS}_{G_E}$[MeV]	$\Gamma_{G_E(1865)}$[MeV]
$G_E \to \pi\pi$	72.2...95.7|84.9...113	169...224|175...231
$G_E \to KK$	-	176...233|273...362
$G_E \to \eta\eta$	-	45.9...64.6|69.8...92.5
$G_E \to \eta\eta'$	-	3.01...3.14|0
$G_E \to \rho\rho$	-	2.91...3.86
$G_E \to \omega\omega$	-	0.84...1.12
$G_E \to K^*K^*$	-	0.15...0.20
$G_E \to a_1\pi,\ \pi\pi\rho$	-	161...274
$G_E \to K^*K\pi$	-	19.3...33.9
$G_E \to$ Hadrons	72.2...95.7|84.9...113	558...803|680...964

Table 10.3.: Hadronic two-body decays of the exotic scalar glueball G_E with model mass of 855 MeV and extrapolated to $M = 1865$ MeV for the proposed fragmented scalar glueball in [45]. $\lambda = 16.63 \ldots 12.55$. In decays into two pseudoscalar mesons, the two sets of values correspond to $x = 0$ and $x = 1$ in the coupling to the quark mass term (10.7). Four-body decays have been found to be strongly suppressed [133] and are hence not listed. Partial decay widths much smaller than 1 MeV are left out but considered in the total hadronic decay rate.

	$\Gamma^{WSS}_{G_D}$[MeV]	$\Gamma_{G_D(1865)}$[MeV]
$G_D \to \pi\pi$	12.4...16.5|15.2...20.1	16.1...21.3|18.3...24.2
$G_D \to KK$	4.16...5.51|50.5...67.0	9.87...13.1|48.8...64.7
$G_D \to \eta\eta$	1.85...3.71|14.1...18.7	3.38...5.75|13.7...18.1
$G_D \to \eta\eta'$	-	4.19...4.38|0
$G_D \to \rho\rho$	-	90.1...119
$G_D \to \omega\omega$	-	28.7...38.1
$G_D \to K^*K^*$	-	42.6...56.4
$G_D \to a_1\pi,\ \pi\pi\rho$	0.84...1.48	5.32...8.55
$G_D \to K^*K\pi$	-	0.64...1.13
$G_D \to$ Hadrons	19.3...27.2|80.6...107	200...267|247...329

Table 10.4.: Hadronic two-body decays of the dilatonic scalar glueball G_D with WSS model mass and extrapolated to $M = 1865$ MeV for the proposed fragmented scalar glueball in [45]. $\lambda = 16.63 \ldots 12.55$. In decays into two pseudoscalar mesons, the two sets of values correspond to $x = 0$ and $x = 1$ in the coupling to the quark mass term (10.28). Four-body decays have been found to be strongly suppressed [133] and are hence not listed. Partial decay widths much smaller than 1 MeV are left out but considered in the total hadronic decay rate.

	$\Gamma_{G_{PS}^{\mathrm{WSS}}}$[MeV]	$\Gamma_{G_{PS}(2359)}$[MeV]	$\Gamma_{G_{PS}(2600)}$[MeV]
$G_{PS} \to \rho\rho$	36.8...45.0	150...195	190...248
$G_{PS} \to \omega\omega$	11.3...13.8	48.8...63.8	62.2...81.3
$G_{PS} \to K^*K^*$	2.69...1.81	83.3...195	188...246
$G_{PS} \to \phi\phi$	-	16.3...21.2	29.2...38.2
$G_{PS} \to$ Hadrons	50.6...60.6	349...455	470...613

Table 10.5.: Decays of the pseudoscalar glueball into two vector mesons $\lambda = 16.63 \ldots 12.55$. Besides the WSS model result for the pseudoscalar mass, $M_G = 1813 \pm 7$MeV, an extrapolation to 2600 MeV (motivated by lattice results) is considered. Partial decay widths much smaller than 1 MeV have been left out and can be found in [135].

Discussion

In Table 10.5 we show the hadronic decay rates into two vector mesons, which in Ref. [135] were found to be dominant compared to other decay channels, such as that into three pseudoscalars. This is in stark contrast to the analysis of Refs. [154, 155], where the three-body decay into $KK\pi$ is dominant and decays into (axial) vector mesons were assumed to be negligible. More recently, Ref. [141] carried out computations of decay rates of the pseudoscalar glueball using a Dilute Gas of Instantons (DGI). Comparing their results on $\Gamma(\tilde{G} \to K\overline{K}\pi) \approx 0.24$ GeV and $\Gamma(\tilde{G} \to \eta'\pi\pi) \approx 0.05$ GeV to the WSS model predictions of $\Gamma(\tilde{G} \to K\overline{K}\pi) \approx 0.5$ MeV and $\Gamma(\tilde{G} \to \eta'\pi\pi) \approx 0.002 \ldots 0.001$ MeV [135], the results disagree by three orders of magnitude. However, to some extent, a disagreement is to be expected since the 't Hooft instanton mechanism is different from the Witten-Veneziano mechanism. In a recent partial wave analysis of $J/\Psi \to K_S^0 K_S^0 \eta'$ decays [144], the BES III collaboration identified the state $X(2370)$ to be a pseudoscalar with mass and width of about 2395 MeV and 188 MeV, respectively. They found their results to be consistent with a lattice computation of the production of a pseudoscalar glueball in radiative J/Ψ decays [143]. Besides the model mass prediction of 1813 ± 7 MeV, with corrections through mixing included, we thus extrapolate to 2395 MeV and 2600 MeV, motivated by the recent analysis of Ref. [144] and lattice QCD [11, 12], respectively. The width of 188 MeV found by [144] is already saturated by decays into two ρ mesons. The extrapolation of M_{KK} for higher mass glueballs works quite well for the dilaton scalar and tensor glueball but seems insufficient for the pseudoscalar glueball. However, one needs to keep in mind that in the WSS model, the interactions with two vector mesons arise from a formal expansion in $\sqrt{N_f/N_c}$, which is not a small parameter in real QCD. Extrapolations of the results of Ref. [141] to 2395 MeV would be welcome and could offer valuable insights into the nature of the mixing between the pseudoscalar glueball and the η' meson. Due to the stark contrast between the DGI and WSS model results, experimental data could give a clue on which mechanism is more relevant

Die approbierte gedruckte Originalversion dieser Dissertation ist an der TU Wien Bibliothek verfügbar.
The approved original version of this doctoral thesis is available in print at TU Wien Bibliothek.
TU Bibliothek WIEN Your knowledge hub

10.2.2 Spin-1

To leading order, the interactions of the pseudovector glueball with ordinary mesons arise from the CS term of the D8-brane since those originating from the DBI action vanish due to taking the trace of commutator terms. As the CS term involves a formal sum over all the form fields in the Ramond-Ramond sector of the theory, a subtlety arises due to the duality relations between their field strengths. For the field strengths with $p > 4$ we have the non-dynamical twisted field strengths [156, 157]

$$F_{p+1} = \mathrm{d}C_p - H \wedge C_{p-2} = (-1)^{p(p-1)/2} \star F_{9-p}, \quad p > 4 \tag{10.48}$$

of the Ramond-Ramond form fields appearing in the CS term. Expanding (7.6) in B_2, C_3 and C_5, we obtain the contributions

$$\begin{aligned} S_{\mathrm{CS}}^{D8} &= T_8 \sum_p \int_{D8} \sqrt{\hat{A}(\mathcal{R})} \mathrm{Tr} \exp\left(2\pi\alpha' F + B\right) \wedge C_p \\ &\supset T_8 \int_{D8} \mathrm{Tr} \frac{(2\pi\alpha')^2}{2!} F \wedge F \wedge C_5 + \mathrm{Tr} \frac{(2\pi\alpha')^2}{2!} F \wedge F \wedge B_2 \wedge C_3, \end{aligned} \tag{10.49}$$

which can be rearranged via partial integration

$$F \wedge F \wedge C_5 = A \wedge F \wedge \mathrm{d}C_5 = A \wedge F \wedge \star \mathrm{d}C_3 \tag{10.50}$$

$$F \wedge F \wedge B_2 \wedge C_3 = A \wedge F \wedge B_2 \wedge F_4. \tag{10.51}$$

The D8-brane action extends over the S_4, which greatly restricts the index structure for non-vanishing results. In (10.50) the Hodge dual is used to fill the indices on the S_4. In (10.51), the F_4 field strength from the background (7.1) ensures a non-trivial result.

Pseudovector Glueball

For the pseudovector glueball, we obtain from (10.50)

$$\begin{aligned} A \wedge F \wedge \star \mathrm{d}C_3 &= \frac{1}{4!} \sqrt{-g} A_M F_{NO} F_4^{\tau MNO} \mathrm{d}^4x \mathrm{d}z \mathrm{d}\Omega_4 \\ &= \frac{1}{3! M_{PV}} \sqrt{-g} g^{zz} g^{\tau\tau} (A_z F_{\mu\nu} + 2A_\mu F_{\nu z}) F_{\tilde{V}}^{\mu\nu} \frac{3}{2g_s} z^2 c(z) \mathrm{d}^4x \mathrm{d}z \mathrm{d}\Omega_4, \end{aligned} \tag{10.52}$$

where we projected onto the physical spin-1 polarizations via $\tilde{B}_{\mu\nu} = \frac{1}{2\sqrt{\Box}}\epsilon_{\mu\nu}{}^{\rho\sigma}F^{\tilde{V}}_{\rho\sigma}$ and used

$$\begin{aligned}&\left(\partial_\mu \star F^V_{\nu\rho} + \partial_\nu \star F^V_{\rho\mu} + \partial_\rho \star F^V_{\mu\nu}\right) = -\frac{1}{2}\epsilon_{\mu\nu\rho\sigma}\epsilon^{\sigma\alpha\beta\gamma}\partial_\alpha \star F^V_{\beta\gamma}\\ &= -\frac{1}{4}\epsilon_{\mu\nu\rho\sigma}\epsilon^{\sigma\alpha\beta\gamma}\partial_\alpha\epsilon_{\beta\gamma\lambda\kappa}F_V^{\lambda\kappa} = -\epsilon_{\mu\nu\rho\sigma}\partial_\alpha F_V^{\alpha\sigma} = -\epsilon_{\mu\nu\rho\sigma}\Box V^\sigma.\end{aligned} \tag{10.53}$$

Additionally we obtain from (10.51)

$$A \wedge F \wedge B_2 \wedge F_4 = -\frac{c(z)}{2M_{PV}}(A_z F_{\mu\nu} + 2A_\mu F_{\nu z})F^{\tilde{V}}_{\mu\nu}\left(\frac{3R^3_{\mathrm{D4}}}{g_s}\right)\mathrm{d}^4x\mathrm{d}z\mathrm{d}\Omega_4. \tag{10.54}$$

Collecting all contributions, we have

$$\mathcal{L}_{G_{PV}\to\Pi v} = -\left(1-\frac{1}{3!}\right)\frac{1}{M_{PV}}b_1^m\mathrm{tr}\left(v_\mu^{(m)}\partial_\nu\Pi + \Pi\partial_\mu v_\nu^{(m)}\right)F^{\tilde{V}}_{\mu\nu}, \tag{10.55}$$

with $(H_{PV}(z) \equiv N_4(z)/\mathcal{N}_{PV})$

$$\begin{aligned}b_1^m &= T_8\frac{(2\pi\alpha')^2}{2!}\frac{3R^3_{\mathrm{D4}}}{g_s}\left(\frac{8\pi^2}{3}\right)\int \mathrm{d}z K^{-1/2}\psi_{2m-1}(z)H_{PV}(z)\\ &= \frac{27}{4}\sqrt{\frac{\kappa}{\pi}}\frac{1}{M^2_{\mathrm{KK}}R^3_{\mathrm{D4}}}\int\frac{\mathrm{d}z}{\sqrt{1+z^2}}\psi_{2m-1}(z)H_{PV}(z) = \frac{\{112.054,\ldots\}}{\sqrt{\lambda}N_c}.\end{aligned} \tag{10.56}$$

The first term in (10.55) was already obtained in Ref. [132], but the second term involving $-1/3!$, arising through the dualization of C_3, was only considered later in Ref. [124] .

Interactions between the pseudovector glueball, one axial vector, and one vector meson are given by

$$\mathcal{L}_{G_{PV}\to va} = -\frac{5}{6}\frac{1}{M_{PV}}b_3^{mn}\mathrm{tr}\left(v_\mu^{(m)}a_\nu^{(n)}\right)F^{\tilde{V}}_{\mu\nu} \tag{10.57}$$

with

$$\begin{aligned}b_3^{mn} =& \frac{27}{4}\frac{\kappa}{M_{\mathrm{KK}}R^3_{\mathrm{D4}}}\int\mathrm{d}z\sqrt{1+z^2}(\psi_{2m-1}(z)\psi'_{2n}(z) - \psi'_{2m-1}(z)\psi_{2n}(z))N_4(z)\\ =&\frac{\{118.66,\ldots\}M_{\mathrm{KK}}}{\sqrt{\lambda}N_c}.\end{aligned} \tag{10.58}$$

From (10.57) we obtain

$$\begin{aligned}|\mathcal{M}_{G_{PV}\to av}|^2 = \left(\frac{b_3\mathrm{tr}\,T_aT_v}{2M_{PV}m_am_v}\right)^2&\left(M^6_{PV} + 2\left(m_a^2 - m_v^2\right)^2\left(m_a^2+m_v^2\right)\right.\\ &\left.- M^2_{PV}\left(3m_a^4 + 10m_a^2m_v^2 + 3m_v^4\right)\right).\end{aligned} \tag{10.59}$$

Note that since $M_{PV} \propto M_{\text{KK}}$, (10.57) does not depend on the compactification scale. A similar argument holds for the vector glueball. When extrapolating their masses, we shall, therefore, restrict ourselves to giving ratios of decay rates instead of their absolute values. Three-body decays result from the interactions arising through the commutator terms of $F_{MN} = \partial_M A_N - \partial_N A_M - i\,[A_M, A_N]$ and are governed by

$$\mathcal{L}_{G_{PV}\Pi vv} = \frac{5}{6}\frac{i}{M_V} b_2^{mn} \mathrm{tr}\left(\Pi\left[v_\mu^{(m)}, v_\nu^{(n)}\right]\right) F_{\mu\nu}^{\tilde{V}}, \tag{10.60}$$

where[8]

$$b_2^{mn} = \frac{81}{8}\sqrt{\frac{\kappa}{\pi}}\frac{1}{M_{\text{KK}}^2 R_{\text{D4}}^3}\int \mathrm{d}z \psi_{2m-1}(z)\psi_{2n-1}(z)H_{PV}(z) = \frac{\{7257.92, \ldots\}}{\lambda N_c^{3/2}}, \tag{10.61}$$

from which we obtain

$$\begin{aligned}
|\mathcal{M}_{G_{PV}\to v_1 v_2 \Pi}|^2 = &\left(\frac{b_2\,\mathrm{tr}\,T_s[T_{v_1}, T_{v_2}]}{M_{PV} m_{v_1} m_{v_2}}\right)^2 \\
&\times\Big(M_{PV}^6 + M_{PV}^4(m_\Pi^2 + 2(m_{v_1}^2 + m_{v_2}^2 - s_{12} - s_{23})) \\
&\quad + M_{PV}^2(m_\Pi^2(m_{v_1}^2 + m_{v_2}^2 - s_{12} - s_{23}) \\
&\quad - m_{v_1}^2(11m_{v_2}^2 + 4s_{12} + s_{23}) \\
&\quad - m_{v_2}^2 s_{12} - 4m_{v_2}^2 s_{23} + s_{12}^2 + 3s_{12}s_{23} + s_{23}^2) \\
&\quad + s_{23}(s_{12}(m_\Pi^2 + m_{v_1}^2 + m_{v_2}^2) - (m_{v_2}^2(m_\Pi^2 + 3m_{v_1}^2)) - s_{12}^2) \\
&\quad + m_{v_1}^2(m_{v_2}^2(m_\Pi^2 + m_{v_1}^2 + m_{v_2}^2) - s_{12}(m_\Pi^2 + 3m_{v_2}^2) + 2s_{12}^2) \\
&\quad + s_{23}^2(2m_{v_2}^2 - s_{12})\Big),
\end{aligned} \tag{10.62}$$

where s_{ij} is the squared center of mass energy of the vector meson-pseudoscalar meson subsystem.

To leading order, there would also be interactions of the pseudovector glueball with one axial vector and two vector mesons. They are, however, above the mass threshold obtained by using model masses and are thus not considered here.

Discussion

In Table 10.6, we have collected the results for the various hadronic decay rates of the pseudovector glueball. Table 10.7 shows the decay patterns when the mass of the pseudovector glueball is raised to 2980 MeV, the value obtained from quenched lattice QCD [12]. The

---

[8] Our results for b_1^m and b_2^{mn} for $m = n = 1$ differ from the ones in [132] by factors of 2 and $2^{3/2}$, respectively, due to the different normalization of the $SU(N_f)$ generators.

	$\Gamma_{G_{PV}^{\mathrm{WSS}}}$ [MeV]
$G_{PV} \to \rho\pi$	585...775
$G_{PV} \to K^*K$	259...338
$G_{PV} \to \eta\omega$	83.2...141
$G_{PV} \to \eta\phi$	13.8...11.3
$G_{PV} \to \eta'\omega$	31.9...26.0
$G_{PV} \to \eta'\phi$	5.21...8.83
$G_{PV} \to a_1\rho,\, \rho\rho\pi$	433...751
$G_{PV} \to K_1(1270)K^*$	26.9...35.6
$G_{PV} \to K_1(1400)K^*$	1.72...2.82
$G_{PV} \to f_1\omega$	40.9...54.2
$G_{PV} \to f_1'\omega$	1.32...1.75
$G_{PV} \to K^*K^*\pi$	37.6...66.0
$G_{PV} \to K^*\rho K$	5.85...10.3
$G_{PV} \to K^*\omega K$	1.66...2.91
$G_{PV} \to$ Hadrons	1476...2162

Table 10.6.: Hadronic decays of the pseudovector glueball with WSS model mass of $M_{PV} = 2311$ MeV.

three-body decay rates $\Gamma_{G_{PV}\to\rho\rho\pi}$ again include the a_1 resonance contribution shown in the Feynman diagrams of Fig. 10.3 with width given by (7.47) and the pertinent Dalitz plots are displayed in Fig. 10.4. The interference effects amount to a reduction of the decay rate of about 30%. Decays into mesons involving strangeness, like the physical $K_1(1270)$ and $K_1(1400)$ as well as f_1 and f_1', which are all rather sharp resonances in real QCD, are not summed resonantly but displayed separately. Despite the negative interference with the a_1 meson as well as the reduced coupling constant due to the contribution of the dualized field strength in (10.50), the pseudovector glueball turns out to be the broadest resonance of the WSS model, making its experimental identification difficult. However, in Chapter 14 we explore its role as a soft exchange in the threshold region of photoproduction of heavy pseudoscalar mesons using a bottom-up holographic construction. This process has been argued to be sensitive to pseudovector glueball exchange [158–160].

Vector Glueball

As was the case for the pseudovector glueball, the interactions of the vector glueball are purely anomalous and originate from the CS term in (7.6). The expansion of the latter is again given by (10.49) since the pseudovector and vector glueball only differ by their polarizations of the respective fields B_2 and C_3.

	$\frac{\Gamma_{G^{\mathrm{WSS}}_{PV}\to\dots}}{\Gamma_{G^{\mathrm{WSS}}_{PV}\to\rho\pi}}$	$\frac{\Gamma_{G_{PV(2980}\to\dots}}{\Gamma_{G_{PV(2980)}\to\rho\pi}}$
$\rho\pi$	1	1
K^*K	0.55	0.75
$\omega\eta$	0.14...0.18	0.17...0.21
$\phi\eta$	0.02...0.01	0.04...0.03
$\omega\eta'$	0.05...0.03	0.09...0.06
$\phi\eta'$	0.009...0.01	0.04...0.05
$a_1\rho, \rho\rho\pi$	0.74...0.97	2.64...3.35
$K_1(1270)K^*$	0.05	0.16
$K_1(1400)K^*$	0.003	0.24
$f_1\omega$	0.07	0.16
$f_1'\omega$	0.002	0.015
$f_1\phi$	-	0.01
$f_1'\phi$	-	0.04
$K^*K^*\pi$	0.06...0.09	0.43...0.57
$K^*\rho K$	0.010...0.013	0.52...0.69
$K^*\omega K$	0.003...0.004	0.17...0.22
$K^*K^*\eta$	-	0.11...0.12
ϕK^*K	-	0.04...0.06

Table 10.7.: Hadronic decays of the pseudovector glueball with WSS model mass $M_{PV} = 2311$ MeV and the quenched lattice value of 2980 MeV.

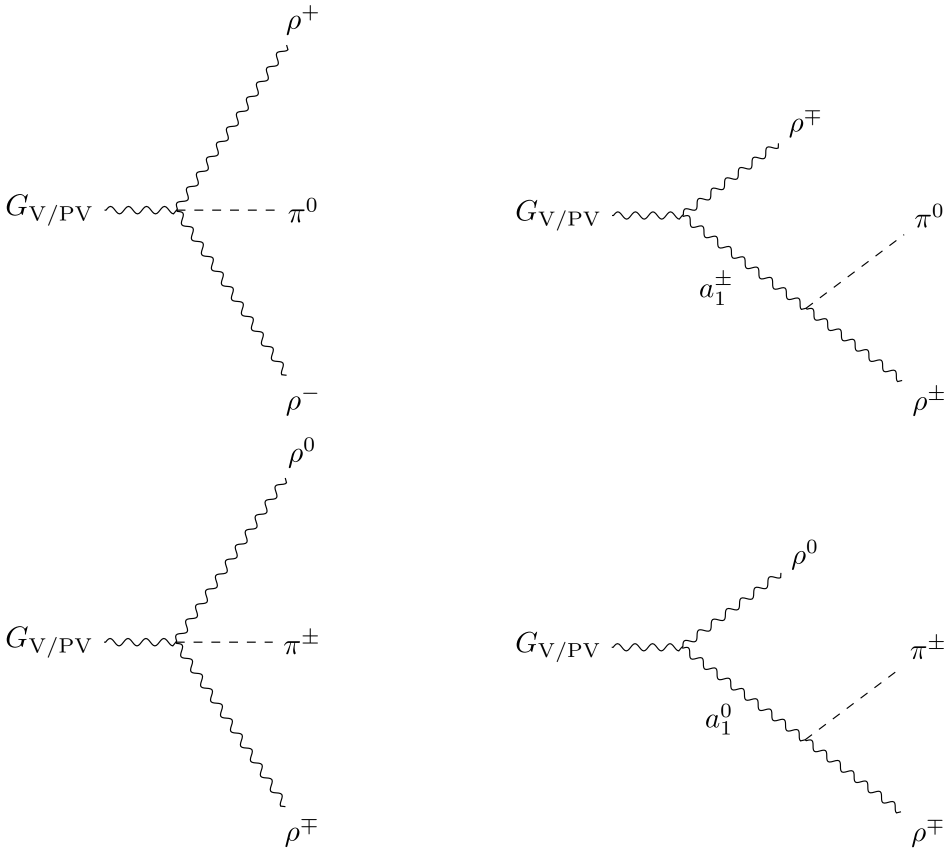
$G_{\mathrm{V/PV}}$
ρ^+
π^0
ρ^-
$G_{\mathrm{V/PV}}$
$\rho^\mp$
π^0
$a_1^\pm$
$\rho^\pm$
$G_{\mathrm{V/PV}}$
ρ^0
$\pi^\pm$
$\rho^\mp$
$G_{\mathrm{V/PV}}$
ρ^0
$\pi^\pm$
a_1^0
$\rho^\mp$

Fig. 10.3.: Feynman diagrams contributing to the hadronic three-body decay of the pseudovector and vector glueball into $\rho\rho\pi$.

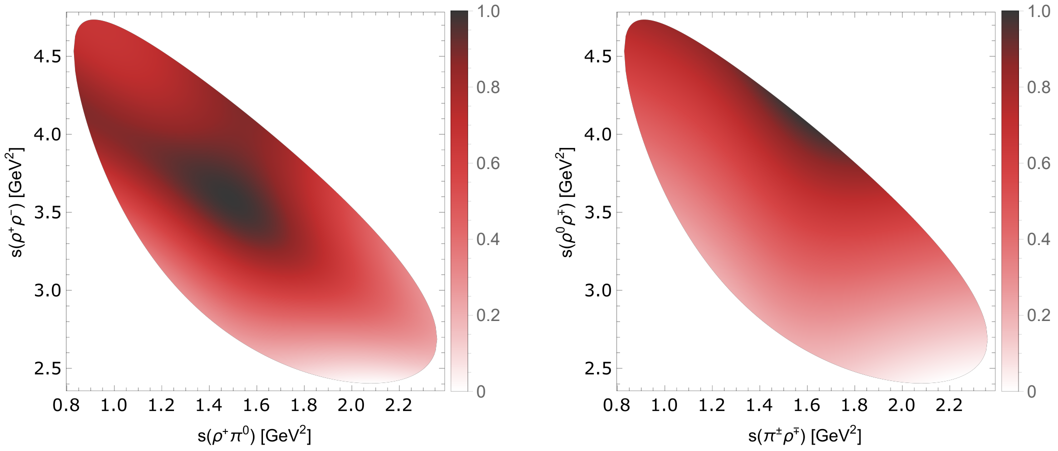

(a)

(b)

Fig. 10.4.: Dalitz plots for the three-body decay $G_{PV} \to \rho\rho\pi$ including a charged (a) and neutral (b) a_1 resonance.

.

Die approbierte gedruckte Originalversion dieser Dissertation ist an der TU Wien Bibliothek verfügbar.
The approved original version of this doctoral thesis is available in print at TU Wien Bibliothek.
TU Bibliothek, WIEN Your knowledge hub

From (10.50) we obtain

$$A \wedge F \wedge \star \mathrm{d}C_3 = \frac{\mathrm{d}^4x\mathrm{d}z\mathrm{d}\Omega_4}{6g_s}\sqrt{-g}g^{\tau\tau}\left(\frac{a(z)}{2}g^{\mu\kappa}g^{\nu\lambda}g^{\rho\delta}A_\mu F_{\nu\rho}\epsilon_{\kappa\lambda\delta\sigma}\sqrt{\Box}\eta^{\sigma\alpha}V_\alpha \right. \\ \left. -g^{zz}g^{\mu\kappa}g^{\nu\lambda}\left(A_z\partial_\mu A_\nu + A_\mu\partial_\nu A_z - A_\mu\partial_z A_\nu - \frac{3i}{2}A_z[A_\mu, A_\nu]\right)\partial_z\frac{a(z)}{\sqrt{\Box}}\star F^V_{\kappa\lambda}\right), \tag{10.63}$$

and from (10.51)

$$A \wedge F \wedge B_2 \wedge F_4 = \frac{a(z)}{z}\epsilon^{\mu\nu\rho\sigma}A_\mu F_{\nu\rho}\frac{1}{\sqrt{\Box}}V_\sigma\left(\frac{3R^3_{\mathrm{D4}}}{g_s}\right)\mathrm{d}^4x\mathrm{d}z\mathrm{d}\Omega_4, \tag{10.64}$$

where $\star F^V_{\mu\nu} = \sqrt{\Box}\tilde{C}_{\mu\nu}$.

The interaction Lagrangian coupling the vector glueball to pseudoscalar and vector mesons is thus given by

$$\mathcal{L}_{G_V\Pi v} = -\frac{1}{M_V}g_1^m \mathrm{tr}\,\left(\Pi\partial_\mu v_\nu^{(m)} + v_\mu^{(m)}\partial_\nu\Pi\right)\star F^V_{\mu\nu}, \tag{10.65}$$

where ($H_V(z) \equiv M_4(z)/\mathcal{N}_V$)

$$g_1^m = \frac{9}{16}\sqrt{\frac{\kappa}{\pi}}\frac{1}{M^2_{\mathrm{KK}}R^3_{\mathrm{D4}}}\int \mathrm{d}z\frac{1}{z}\psi_{2m-1}(z)\partial_z(zH_V(z)) = \frac{\{15.04,\dots\}}{\sqrt{\lambda}N_c}, \tag{10.66}$$

with the mass dependence explicitly given in the Lagrangian. The spin-averaged, squared amplitude is given by

$$|\mathcal{M}_{G_V\to v^m\Pi}|^2 = \frac{2}{3}\left(g_1^m M_V \mathrm{tr}\, T_s T_v\right)^2\left(1 - 2\frac{m^2_\Pi + m^2_v}{M^2_V} + \left(\frac{m^2_\Pi - m^2_v}{M^2_V}\right)^2\right) \tag{10.67}$$

Similarly, interactions with vector and axial vector mesons are governed by

$$\mathcal{L}_{G_V\to av} = \frac{1}{M_V}f_1^{mn}\epsilon^{\mu\nu\rho\sigma}\mathrm{tr}\,\left(v_\mu^m\partial_\nu a_\rho^n + a_\mu^n\partial_\nu v_\rho^m\right)V_\sigma + \frac{1}{M_V}f_2^{mn}\mathrm{tr}\,\left(v_\mu^m a_\nu^n\right)\star F_{\mu\nu}, \tag{10.68}$$

where

$$\begin{aligned} f_1^{mn} &= \frac{3}{8}\frac{\kappa}{M_{\mathrm{KK}}R_{\mathrm{D4}}^3}\int \mathrm{d}z\left(\frac{3}{2}(1+z^2)^{-1/3}\frac{M_V^2}{M_{\mathrm{KK}}^2}+36\right)\psi_{2m-1}(z)\psi_{2n}(z)H_V(z)\\ &= \frac{\{177.83,\dots\}M_{\mathrm{KK}}}{N_c\sqrt{\lambda}}\\ f_2^{mn} &= \frac{3}{8}\frac{\kappa}{M_{\mathrm{KK}}R_{\mathrm{D4}}^3}\int \mathrm{d}z\left(\frac{3}{2}\frac{1+z^2}{z}\right)\left(\psi_{2m-1}\psi'_{2n}-\psi'_{2m-1}\psi_{2n}\right)\partial_z(zH_V(z))\\ &= \frac{\{16.60,\dots\}M_{\mathrm{KK}}}{N_c\sqrt{\lambda}}. \end{aligned} \tag{10.69}$$

Note again that $M_V \propto M_{\mathrm{KK}}$ and hence (10.68) does not depend explicitly on the compactification scale. Carrying out the polarization sums and spin averaging, we obtain

$$\begin{aligned} |\mathcal{M}_{G_V\to av}|^2 =& \frac{1}{6}\left(\frac{\mathrm{tr}\, T_v T_a}{M_V^2 m_a m_v}\right)^2\Big[m_v^6\left(4f_1^2m_a^2+M_V^2(f_1-f_2)^2\right)\\ &+m_a^2(f_1+f_2)^2\left(M_V^3-M_V m_a^2\right)^2\\ &-m_v^4(M_V^2m_a^2(-15f_1^2+18f_1f_2+f_2^2)\\ &+8f_1^2m_a^4+2M_V^4(f_1-f_2)^2)\\ &+m_v^2\Big(4M_V^4m_a^2\left(2f_2^2-3f_1^2\right)+M_V^2m_a^4\left(15f_1^2+18f_1f_2-f_2^2\right)\\ &+4f_1^2m_a^6+M_V^6(f_1-f_2)^2\Big)\Big], \end{aligned} \tag{10.70}$$

We obtain the leading order quartic coupling to two vector mesons and one pseudoscalar meson from the commutator terms of the meson field strengths. Explicitly we have

$$\mathcal{L}_{G_V\to\Pi vv} = \frac{i}{M_V}g_1^{mn}\mathrm{tr}\left(\Pi\left[v_\mu^{(m)},v_\nu^{(n)}\right]\right)\star F_{\mu\nu}^V, \tag{10.71}$$

with

$$g_1^{mn} = \frac{9}{16}\sqrt{\frac{\kappa}{\pi}}\frac{1}{M_{\mathrm{KK}}^2R_{\mathrm{D4}}^3}\int\frac{3}{2}\mathrm{d}z\frac{1}{z}\psi_{2m-1}(z)\psi_{2n-1}(z)\partial_z(zH_V(z)) = \frac{\{1061,\dots\}}{\lambda N_c^{3/2}}, \tag{10.72}$$

TU Bibliothek Your knowledge hub WIEN
Die approbierte gedruckte Originalversion dieser Dissertation ist an der TU Wien Bibliothek verfügbar.
The approved original version of this doctoral thesis is available in print at TU Wien Bibliothek.

and the resulting spin-averaged squared amplitude, with resonance contributions neglected, is given by

$$
\begin{aligned}
|\mathcal{M}_{G_V\to v_1 v_2 \Pi}|^2 = {} & \frac{g_1^2}{m_{v_1}^2 m_{v_2}^2 M_V^2}(\mathrm{tr}T_s[T_{v_1},T_{v_2}])^2\Bigg[\\
& + m_\Pi^2\Bigg(m_{v_1}^2\left(m_{v_2}^2+M_V^2-s_{12}\right)+M_V^2\left(m_{v_2}^2-M_V^2+s_{12}\right) \\
& + s_{23}\left(M_V^2-m_{v_2}^2+s_{12}\right)\Bigg)+m_{v_2}^2 M_V^2\left(2M_V^2-s_{12}\right) \\
& + s_{23}\Bigg(m_{v_2}^2\left(s_{12}-4M_V^2\right)+s_{12}\left(M_V^2-s_{12}\right)\Bigg) \\
& + m_{v_1}^2\Bigg(m_{v_2}^2(17M_V^2-3(s_{12}+s_{23}))+m_{v_2}^4 \\
& + (M_V^2-s_{12})(2M_V^2-2s_{12}-s_{23})\Bigg) \\
& - m_\Pi^4-M_V^2+s_{23}^2\left(2m_{v_2}^2-s_{12}\right)+m_{v_1}^4 m_{v_2}^2\Bigg],
\end{aligned}
\tag{10.73}
$$

where s_{ij} is the center of mass energy of the vector meson and pseudoscalar subsystem. The interactions of the vector glueball with one axial vector and two vector mesons are close to the mass threshold when model masses are used. Hence, they will not be considered in the following.

Discussion

The resulting decay rates are collected in Table 10.8. Again, the a_1 meson is summed as a resonant contribution with width given by the WSS model prediction in (7.47). For the case of the vector glueball, we find almost maximal negative interference between the direct process and the resonant contribution. The decay $G_V \to a_1\rho$ would have a partial width of 822...1089 MeV, making it the dominant decay channel of the vector glueball. However, as a resonant contribution together with the direct interaction (see Fig. 10.3), the partial width of $G_V \to \rho\rho\pi$ is only about 60% of that. In the corresponding Dalitz plot of Fig. 10.5, the resonance is clearly visible and might help in experimental identification. We hope that the obtained Dalitz plots for decays into $\rho\rho\pi$ prove useful to experimentalists, although isolating the channel $G_V \to \rho\rho\pi \to 5\pi$ in, for example, J/Ψ decays, seems like a formidable task. When computing decays into axial vector mesons involving strangeness, the latter are again treated non-resonantly due to their small widths. When instead considered as resonant contributions using their experimental widths, the interference effects indeed turn out to be negligible. In Ref. [161], ratios of partial decay widths of the vector glueball were considered in the Extended Linear Sigma Model (eLSM) [42, 154, 155, 162]. The couplings obtained therein do not directly compare to

Die approbierte gedruckte Originalversion dieser Dissertation ist an der TU Wien Bibliothek verfügbar.
The approved original version of this doctoral thesis is available in print at TU Wien Bibliothek.
TU Bibliothek WIEN Your knowledge hub

	$\Gamma_{G_V^{\mathrm{WSS}}}$ [MeV]
$G_V \to \rho\pi$	34.3...45.4
$G_V \to K^*K$	37.8...50.1
$G_V \to \omega\eta$	5.78...9.80
$G_V \to \phi\eta$	3.45...2.81
$G_V \to \omega\eta'$	3.06...2.50
$G_V \to \phi\eta'$	3.22...5.46
$G_V \to a_1\rho,\, \rho\rho\pi$	339...417
$G_V \to K_1(1270)K^*$	185...246
$G_V \to K_1(1400)K^*$	320...424
$G_V \to f_1\omega$	212...281
$G_V \to f_1'\omega$	22.4...29.7
$G_V \to f_1\phi$	9.51...12.6
$G_V \to f_1'\phi$	47.8...63.3
$G_V \to K^*K^*\pi$	22.7...39.9
$G_V \to K^*\rho K$	30.3...53.2
$G_V \to K^*\omega K$	9.85...17.3
$G_V \to K^*K^*\eta$	7.77...12.1
$G_V \to \phi K^*K$	3.87...6.80
$G_V \to$ Hadrons	1301...1725

Table 10.8.: Hadronic decays of the vector glueball with WSS model mass $M_V = 2882$ MeV (mixing between vector glueball and singlet vector mesons neglected). Because of the large width of $a_1 \to \rho\pi$, the strongly interfering direct and resonant decays into $\rho\rho\pi$ have been combined.

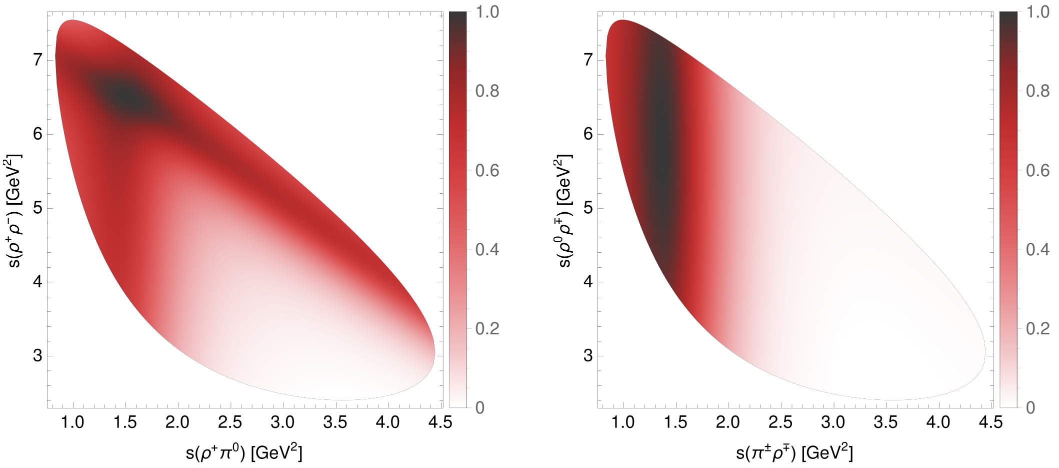

(a) (b)

Fig. 10.5.: Dalitz plots for the three-body decay $G_V \to \rho\rho\pi$ including a charged (a) and neutral (b) a_1 resonance.

	$\frac{\Gamma_{G_V^{\rm WSS}\to\ldots}}{\Gamma_{G_V^{\rm WSS}\to\rho\pi}}$	$\frac{\Gamma_{G_{V(3830)}\to\ldots}}{\Gamma_{G_{V(3830)}\to\rho\pi}}$	Ref. [161]
$\rho\pi$	1	1	1
K^*K	1.1	1.21	1.3
$\omega\eta$	0.17...0.22	0.18...0.23	0.16
$\phi\eta$	0.10...0.062	0.12...0.07	0.21
$\omega\eta'$	0.089...0.055	0.11...0.07	0.13
$\phi\eta'$	0.094...0.12	0.14...0.18	0.18
$a_1\rho,\ \rho\rho\pi$	9.88...9.18	17.0...15.3	1.8
$K_1(1270)K^*$	5.40	12.0	
$K_1(1400)K^*$	9.32	23.8	
$f_1\omega$	6.2	11.8	0.55
$f_1'\omega$	0.65	1.41	0.82
$f_1\phi$	0.28	0.83	
$f_1'\phi$	1.4	4.92	
$K^*K^*\pi$	0.66...0.88	1.92...2.54	
$K^*\rho K$	0.88...1.17	3.48...4.62	
$K^*\omega K$	0.29...0.38	1.14...4.62	
$K^*K^*\eta$	0.23...0.27	1.19...1.40	
ϕK^*K	0.11...0.15	0.70...0.93	

Table 10.9.: Relative branching ratios of the hadronic decays of the vector glueball with WSS model mass $M_V = 2882$ MeV and with quenched lattice QCD result [12] 3830 MeV, the latter for the sake of comparison with Ref. [161].

those obtained in the WSS model. In particular, there are two dimension-4 operators that are absent in our computations, which we thus interpret as subleading decay channels. On the other hand, there are terms in (10.68) that do not involve the dualized field strength, which are not reproduced by the eLSM computation. For comparison, we give in Table 10.9 the ratios obtained in [161] together with the results of the WSS model. While they agree on the dominant decay channel being $G_V \to a_1\pi$, the WSS model predicts a much more pronounced strength of these decays, differing even by an order of magnitude[9].

Implications for the $\rho\pi$ puzzle

The vector glueball is often quoted as a possible resolution to the long-standing $\rho\pi$ puzzle [163–168]. The latter is the experimental fact of a relative suppression of decays of $\psi' = \psi(2S) = \psi(3686)$ into $\rho\pi$ and K^*K, compared to the same decays of its radial ground state J/Ψ. Considering them as non-relativistic bound states of c and $\bar{c}$, one would instead expect a ratio that is roughly compatible with the ”12%” rule [134, 169]. A certain small mixing of J/Ψ with the vector glueball could explain this suppression by a resonant enhancement (cf. (9.46)) but requires a rather narrow vector glueball that is close in mass to that of J/Ψ. Unfortunately, the WSS model is unable to capture the behavior of $c\bar{c}$ states since they acquire most of their mass through their quark content, while the latter are massless in the WSS model. Our predictions also indicate a rather broad resonance, which is incompatible with the assumptions made in Ref. [165]. Another problem is the mass of the vector glueball, which in the WSS model is rather close to that of J/Ψ, but lattice computations predict a mass difference of about 700 MeV. On the other hand, in Section 9.4.3, we found a strong dependence of the mixing parameter on the mode number, so the situation for charmonia might be quite different from the computations presented above. Taking the decay patterns of Table 10.8 at face value, the vector glueball appears to be rather unsuitable for an explanation of the $\rho\pi$ puzzle due to the strong decays into $a_1\pi$ and $K_1(1400)K^*$, which have not been observed in the hadronic decays of J/ψ [9] .

---

[9] Again we take into account the negative interference with non-resonant $G_V \to \rho\rho\pi$ decays in the WSS model, whereas Ref. [161] considered only two-body decays.

10.2.3 Spin-2

Tensor Glueball

Except for the couplings from the pseudoscalar mass terms that vanish for traceless polarizations, the tensor glueball has the same interactions as the dilaton scalar glueball of Section 10.2.1. In particular, the coupling to two pseudoscalar mesons is given by

$$\mathcal{L}_{G_T\Pi\Pi} = t_1 \mathrm{tr}\,(\partial_\mu\Pi\partial_\nu\Pi)\, G_T^{\mu\nu}, \tag{10.74}$$

with ($H_T \equiv T_4/\mathcal{N}_T$)

$$t_1 = \frac{1}{\pi}\int \mathrm{d}z K^{-1} H_T = \frac{59.6729}{\sqrt{\lambda} M_{\mathrm{KK}} N_c} = 2\sqrt{3} d_1. \tag{10.75}$$

Averaging over the spin and carrying out the polarization sums, we obtain the partial decay width

$$\Gamma_{G_T\to\Pi\Pi} = \frac{|\mathbf{p}_\Pi|}{8\pi M_T^2}|\mathcal{M}_{G_T\to\Pi\Pi}|^2, \tag{10.76}$$

where

$$|\mathcal{M}_{G_T\to\Pi\Pi}|^2 = \frac{1}{5}\frac{t_1^2}{6M_T^4}\left(M_T^4 - 2M_T^2(m_{\Pi_1}^2 + m_{\Pi_2}^2) + (m_{\Pi_1}^2 - m_{\Pi_2})^2\right)^2. \tag{10.77}$$

Note that the factor of $1/5$ in (10.76) is due to averaging over the spin-2 polarization.

The coupling to two vector mesons is again obtained from the DBI part of (7.6)

$$\mathcal{L}_{G_T vv} = \mathrm{tr}\left[t_2 M_{\mathrm{KK}}^2 v_\mu^{(m)} v_\nu^{(n)} G_T^{\mu\nu} + t_3 F_{\mu\rho}^{(m)} F_\nu^{n\rho} G_T^{\mu\nu}\right], \tag{10.78}$$

with

$$\begin{aligned} t_2^{mn} &= \int \mathrm{d}z K \psi'_{2m-1} \psi'_{2n-1} H_T = 2\sqrt{3} d_2^{mn}, \\ t_3^{mn} &= \int \mathrm{d}z K^{-1/3} \psi_{2m-1} \psi_{2n-1} H_T = 2\sqrt{3} d_3^{mn}, \end{aligned} \tag{10.79}$$

and $d_{2,3}^{mn}$ given in (10.39). The spin-averaged squared amplitude is readily obtained as

$$\begin{aligned} \Gamma_{G_T\to vv} = \frac{1}{S}\bigg\{ &\frac{t_2^2}{120} \frac{M_{\mathrm{KK}}^4}{m_v^4} (M_T^4 + 12 m_v^2 M_T^2 + 56 m_v^4) \\ &+ \frac{2}{3} t_2 t_3 M_{\mathrm{KK}}^2 (M_T^2 - m_v^2) \\ &+ \frac{t_3^2}{10} (M_T^4 - 3 m_v^2 M_T^2 + 6 m_v^4) \bigg\} \frac{|\mathbf{p}_v|}{8\pi M_G^2}, \end{aligned}$$

where S is again the symmetry factor for identical particles.

There is also a coupling of the tensor glueball to one axial vector and one pseudoscalar meson,

$$\mathcal{L}_{G_T \Pi a} = -2 t_6^m M_{\mathrm{KK}} \mathrm{tr}\left(\partial_\mu \Pi a_\nu^{(m)}\right) G_T^{\mu\nu}, \tag{10.80}$$

with

$$t_6^m = \sqrt{\frac{\kappa}{\pi}} \int \mathrm{d}z \psi'_{2m} H_T = \frac{\{40.764, \dots\}}{M_{\mathrm{KK}} N_c \sqrt{\lambda}}, \tag{10.81}$$

and pertinent spin-averaged squared amplitude

$$\begin{aligned} |\mathcal{M}_{G_T\to a\Pi}|^2 = \frac{1}{5}\frac{1}{6} &\left(\frac{M_{\mathrm{KK}}^2 t_6^2 \mathrm{tr}\, T_s T_a}{M_T^2 m_a}\right)^2 (M_T - m_a - m_\Pi)(M_T + m_a - m_\Pi) \\ &\times (M_T - m_a + m_\Pi)(M_T + m_a + m_\Pi) \\ &\times (M_T^4 - 2 m_\Pi^2 (M_T^2 + m_a^2) + 8 M_T^2 m_a^2 + m_a^4 + m_\Pi^4). \end{aligned} \tag{10.82}$$

Three-body decays result from the Lagrangian

$$\mathcal{L}_{G_T \Pi\Pi v} = 2i\, \mathrm{tr}\; t_5^m \partial_\mu \Pi [\Pi, v_\nu^{(m)}] G_T^{\mu\nu}, \tag{10.83}$$

with coupling

$$t_5^m = \frac{1}{\pi} \int \mathrm{d}z K^{-1} \psi_{2m-1} H_T = \frac{\{724.367, \dots\}}{\lambda M_{\mathrm{KK}} N_c^{3/2}} = 2\sqrt{3} d_5^m. \tag{10.84}$$

From (10.83) we obtain

$$
\begin{aligned}
|\mathcal{M}_{G_T\to v\Pi_1\Pi_2}|^2 =& \frac{1}{5}\frac{t_5^2}{6M_T^4 m_v^2}\mathrm{tr}\, T_{s_1}[T_{s_2},v]^2 \\
&\times\left(M_T^4+M_T^2\left(8m_v^2-2s_{12}\right)+\left(m_v^2-s_{12}\right)^2\right) \\
&\times\left((M_T-m_v)^2-s_{12}\right)\left((M_T+m_v)^2-s_{12}\right),
\end{aligned}
\tag{10.85}
$$

where we neglected resonant contributions and s_{12} is the center of mass energy of the pseudoscalar meson subsystem

Discussion

Restricting ourselves to two- and three-body decays, the resulting partial decay widths are collected in Table 10.10 with ideal mixing in the $\omega\phi$ system assumed[10]. Again, we note that the corresponding decay rates into $a_1\pi$ in Ref. [98] are smaller by a factor of 1/3 since the charged contributions were not summed over. However, the conclusion therein is left unchanged. The eLSM computations of Ref. [145] do not give absolute values for the decay rates but similarly found dominating decays into pairs of vector mesons, although much more pronounced. For example, in the WSS model for a tensor glueball of mass 2000 and 2400 MeV, respectively, we obtain $\rho\rho : \pi\pi \sim 10-11$ whereas in Ref. [145] it varies between 60 and 50. Similarly, $\rho\rho : a_1\pi \sim 17-16$ whereas Ref. [145] quotes a result between 325 and 200. As was the case for the scalar glueballs, the decay $G_T \to a_1\pi$ is considered as a resonant contribution to decays into $G_T \to \rho\pi\pi$, as shown in the Feynman diagrams of Fig. 10.1. In Ref. [145], it was argued that the resonance $f_2(1950)$ is predominantly gluonic. For this resonance, the PDG quotes a width of about 464 MeV [9] , which is indeed in the right ballpark when compared to the WSS prediction for an unmixed tensor glueball of 2000 MeV.

10.3 Radiative Glueball Decays

Due to the absence of valence quarks, it is widely believed that radiative decay widths of glueballs are extremely small. Correspondingly, a sizeable radiative decay width of a given hadron is usually taken as evidence against its glueball nature[11]. As previously discussed in Section 7.2, and when confronted with experimental data in Section 7.3, the WSS model quite successfully reproduces numerous radiative decay widths of mesons. Through the

---

[10] See the discussion in Section 10.2.1 for non-ideal mixing.

[11] See for example the study by the BELLE collaboration [170] where it was argued that $f_0(1710)$ is not a glueball because of its sizeable two-photon width.

Die approbierte gedruckte Originalversion dieser Dissertation ist an der TU Wien Bibliothek verfügbar.
The approved original version of this doctoral thesis is available in print at TU Wien Bibliothek.
TU Bibliothek Your knowledge hub WIEN

	$\Gamma^{WSS}_{G_T}$[MeV]	$\Gamma_{G_T(2000)}$[MeV]	$\Gamma_{G_T(2400)}$[MeV]
$G_T \to \pi\pi$	19.9...26.3	27.7...36.8	33.8...44.7
$G_T \to KK$	6.66...8.83	19.2...25.4	29.2...38.6
$G_T \to \eta\eta$	1.02...1.35	3.97...5.26	6.48...8.58
$G_T \to \rho\rho$	-	270...358	382...507
$G_T \to \omega\omega$	-	88.2...117	127...169
$G_T \to K^* K^*$	-	240...318	417...552
$G_T \to f_1 \eta$	-	0.98...1.71	3.97...6.89
$G_T \to \eta' \eta'$	-	-	0.92...1.22
$G_T \to \phi\phi$	-	-	76.7...102
$G_T \to a_1 \pi,\ \rho\pi\pi$	2.34...3.79	14.2...18.6	25.1...32.8
$G_T \to K^* K \pi$	-	3.01...5.28	13.4...23.6
$G_T \to KK\rho$	-	-	3.26...5.72
$G_T \to$ Hadrons	29.9...40.1	666...883	1109...1474

Table 10.10.: Hadronic decays of the tensor glueball G_T with WSS model 1487 MeV mass and extrapolated to masses of 2000 and 2400 MeV, for $\lambda = 16.63 \ldots 12.55$. In decays involving f_1 we additionally vary $\theta_f = 20.4° \ldots 26.4°$. Partial decay widths much smaller than 1 MeV are left out.

couplings of glueballs to the (abelian) vector meson fields in Section 10.2, the relevant couplings to photons are obtained via VMD by substituting the vector fields with photon fields and their holographic wave functions by unity[12]. We shall now continue with our analysis of glueball decay patterns in order to make quantitative predictions for radiative decays.

10.3.1 Spin-0

Exotic Scalar Glueball

Decays into one vector meson and one photon are inherited from (10.14) and thus governed by

$$\mathcal{L}_{G_E v \mathcal{V}} = -\mathrm{tr}\left\{ c_3^{m\mathcal{V}} \left[2\eta^{\rho\sigma} F^{(m)}_{\mu\rho} F^{\mathcal{V}}_{\nu\sigma} \frac{\partial^\mu \partial^\nu}{M_E^2} G_E - \frac{1}{2} F^{(m)}_{\mu\nu} F^{\mathcal{V}\mu\nu} \left(1 + \frac{\Box}{M_E^2}\right) G_E \right] \right. \\ \left. + 3 c_4^{\mathcal{V}n} \frac{M_{\mathrm{KK}}^2}{M_E^2} v^{(n)}_\mu F^{\mathcal{V}\mu\nu} \partial_\nu G_E + \breve{c}_3^{m\mathcal{V}} F^{(m)}_{\mu\nu} F^{\mathcal{V}\mu\nu} G_E \right\}, \tag{10.86}$$

---

[12] For off-shell photons, one instead uses the bulk-to-boundary propagator in (7.69) to obtain transition form factors that encode the internal structure of bound states.

with

$$\begin{aligned}
c_3^{m\mathcal{V}} =&\kappa \int \mathrm{d}z K^{-1/3} \psi_{2m-1} \overline{H}_E = \frac{\{1.551, \ldots\}}{M_{\mathrm{KK}} N_c^{\frac{1}{2}}}, \\
c_4^{\mathcal{V}m} =&\kappa \int \mathrm{d}z \, \frac{20ZK}{(5K-2)^2} \psi'_{2m-1} H_E = \frac{\{-0.262, \ldots\}}{M_{\mathrm{KK}} N_c^{\frac{1}{2}}}, \\
\breve{c}_3^{m\mathcal{V}} =&\frac{\kappa}{4} \int \mathrm{d}z K^{-1/3} \psi_{2m-1} H_E = \frac{\{0.425, \ldots\}}{M_{\mathrm{KK}} N_c^{\frac{1}{2}}}.
\end{aligned} \tag{10.87}$$

The corresponding spin-averaged amplitude is given by

$$|\mathcal{M}_{G_E \to v\mathcal{V}}|^2 = \frac{\left(1 - \frac{m_v^2}{M_E^2}\right)^2}{2} \left[3c_4^{\mathcal{V}n} M_{\mathrm{KK}}^2 + 2\breve{c}_3^{m\mathcal{V}} M_E^2 + c_3^{m\mathcal{V}} \left(m_v^2 - M_E^2\right)\right]^2 \mathrm{tr}\, (eQT_{v^m})^2 . \tag{10.88}$$

The two-photon decay rate is obtained from interactions governed by

$$\begin{aligned}
\mathcal{L}_{G_E \mathcal{V}\mathcal{V}} =& - \mathrm{tr} \left\{ c_3^{\mathcal{V}\mathcal{V}} \left[F_{\mu\rho}^{\mathcal{V}} F_{\nu}^{\mathcal{V}\rho} \frac{\partial^\mu \partial^\nu}{M_E^2} G_E - \frac{1}{4} F_{\mu\nu}^{\mathcal{V}} F^{\mathcal{V}\mu\nu} \left(1 + \frac{\Box}{M_E^2}\right) G_E \right] \right. \\
&\left. + \frac{1}{2} \breve{c}_3^{\mathcal{V}\mathcal{V}} F_{\mu\nu}^{\mathcal{V}} F^{\mathcal{V}\mu\nu} G_E \right\},
\end{aligned} \tag{10.89}$$

with couplings

$$\begin{aligned}
c_3^{\mathcal{V}\mathcal{V}} &= \kappa \int \mathrm{d}z K^{-1/3} \overline{H}_E = 0.0355 \frac{\sqrt{\lambda}}{M_{\mathrm{KK}}}, \\
\breve{c}_3^{\mathcal{V}\mathcal{V}} &= \frac{\kappa}{4} \int \mathrm{d}z K^{-1/3} H_E = 0.0106 \frac{\sqrt{\lambda}}{M_{\mathrm{KK}}}.
\end{aligned} \tag{10.90}$$

From (10.89) we obtain

$$|\mathcal{M}_{G_E \to \mathcal{V}\mathcal{V}}|^2 = \frac{M_E^4}{2} \left(c_3^{\mathcal{V}\mathcal{V}} - 2\breve{c}_3^{\mathcal{V}\mathcal{V}}\right)^2 \mathrm{tr}\, \left(e^2 Q^2\right)^2 . \tag{10.91}$$

As mentioned in Section 10.2.1, the hadronic three-body decays are rather strongly suppressed. However, through VMD, the would-be suppression in λ and N_c is traded for an electric charge, and simultaneously, the phase space is enlarged. The corresponding Lagrangian describing interactions between the exotic scalar glueball, two pseudoscalars, and a photon follows from (10.23) and is given by

$$\begin{aligned}
\mathcal{L}_{G_E \Pi\Pi\mathcal{V}} =& 2ic_5^{\mathcal{V}} \left\{ \mathrm{tr}\, \partial_\mu \Pi [\Pi, \mathcal{V}_\nu] \frac{\partial_\mu \partial_\nu}{M_E^2} G_E + \frac{1}{2} \partial_\mu \Pi [\Pi, \mathcal{V}_\mu] \left(1 - \frac{\Box}{M_E^2}\right) G_E \right. \\
&\left. + 2i\breve{c}_5^{\mathcal{V}} \partial_\mu \Pi [\Pi, \mathcal{V}_\mu] G_E \right\},
\end{aligned} \tag{10.92}$$

Die approbierte gedruckte Originalversion dieser Dissertation ist an der TU Wien Bibliothek verfügbar.
The approved original version of this doctoral thesis is available in print at TU Wien Bibliothek.
TU Bibliothek Your knowledge hub WIEN

with couplings

$$c_5^{\mathcal{V}} = \int \mathrm{d}z \frac{\overline{H}_E}{\pi K} = \frac{62.6554}{\sqrt{\lambda} M_{\mathrm{KK}} N_c}, \qquad \breve{c}_5^{\mathcal{V}} = \int \mathrm{d}z \frac{H_E}{4\pi K} = \frac{16.39}{\sqrt{\lambda} M_{\mathrm{KK}} N_c}. \tag{10.93}$$

Carrying out the polarization sums, we obtain

$$\begin{aligned} |\mathcal{M}_{G_E \to \Pi_1 \Pi_2 \mathcal{V}}|^2 = &\left(\frac{4 m_A (c_5^{\mathcal{V}} + \breve{c}_5^{\mathcal{V}})\, e \,\mathrm{tr}\; T_s\,[T_s, Q]}{m_{\Pi_1}^2 + m_{\Pi_2}^2 - s_{13} - s_{23}} \right)^2 \Bigg(\left(m_{\Pi_1}^2 - s_{13} \right) \left(m_{\Pi_2}^2 - s_{23} \right) \\ &- \left(m_{\Pi_1}^2 + m_{\Pi_2}^2 - s_{13} - s_{23} \right) \left(m_{\Pi_1}^2 m_{\Pi_2}^2 - s_{13} s_{23} \right) \Bigg), \end{aligned} \tag{10.94}$$

with s_{ij} the center of mass energies of the pseudoscalar-photon subsystem. Note that due to the vanishing coupling of an axial vector meson to a pseudoscalar meson and a photon (cf. Section 7.3.3), there are no resonant axial vector contributions.

Discussion

In Table 10.11 the results for the partial widths for the radiative decays of the exotic scalar glueball are given. Again, these are evaluated for the mass of $f_0(1500)$ and $f_0(1710)$ with ideal mixing assumed for the $\omega\phi$ system[13]. With this assumption, we approach the ratios $9:1$ for $\rho\gamma$ and $\omega\gamma$ decays, but the $\omega\gamma$ and $\phi\gamma$ ratio deviates strongly from 2:1 due to the heavy mass of the ϕ meson. As was the case for the hadronic decays in Section 10.2, using a more realistic value for the $\omega\phi$ mixing angle $\theta_V \approx 28°$, the partial width for $\omega\gamma$ increases by about 17% while simultaneously decreasing $\phi\gamma$ by about 8.5%. This is also true for the corresponding computations in the following sections. As we will see shortly, the radiative widths of G_E are much smaller than those of G_D at equal mass; see Table 10.12. On the other hand, the three-body decays into $\pi\pi\gamma$ and $KK\gamma$, originally neglected in Ref. [98] , are the dominant radiative decay channels.

Dilaton Scalar Glueball

Using the interaction Lagrangian in (10.38), we obtain the coupling to one vector meson and one photon

$$\mathcal{L}_{G_D \mathcal{V} v} = 2 d_3^{m\mathcal{V}} \eta^{\rho\sigma} \mathrm{tr}\, \left(F_{\mu\rho}^{(m)} F_{\nu\sigma}^{\mathcal{V}} \right) \left(\eta^{\mu\nu} - \frac{\partial^\mu \partial^\nu}{\Box} \right) G_D, \tag{10.95}$$

---

[13] See the discussion in Section 10.2.1 for non-ideal mixing

	$\Gamma_{G_E(1506)}$[keV]	$\Gamma_{G_E(1712)}$[keV]
$G_E \to \rho\gamma$	13.4	20.7
$G_E \to \omega\gamma$	1.4	2.23
$G_E \to \phi\gamma$	0.30	0.98
$G_E \to \pi\pi\gamma$	114...151	134...177
$G_E \to KK\gamma$	14.5...19.2	29.8...39.5
$G_E \to \gamma\gamma$	0.076...0.058	0.087...0.066
$G_E \to$ Radiative	128...170	163...216

Table 10.11.: Radiative decays of the exotic scalar glueball G_E extrapolated to the masses of $f_0(1500)$, $f_0(1710)$.

with

$$d_3^{m\mathcal{V}} \equiv \kappa \int \mathrm{d}z\, K^{-1/3} \psi_{2m-1} H_D = \frac{\{0.46895, \dots\}}{M_{\mathrm{KK}}\sqrt{N_c}}. \tag{10.96}$$

The would-be coupling $d_2^{m\mathcal{V}}$ vanishes at zero virtuality due to the derivative acting on a constant bulk-to-boundary propagator. Nevertheless, it becomes important when computing transition form factors that may be used to estimate the contributions of the dilaton scalar glueball to hadronic light-by-light scattering [98] .

The spin-averaged squared amplitude is given by

$$|\mathcal{M}_{G_D \to v\mathcal{V}}|^2 = \frac{d_3^{m\mathcal{V}} \left(m_v^4 - 4m_v^2 M_D^2 + 3M_D^4\right)^2}{2M_D^4} \mathrm{tr}\, \left(eQT_v\right)^2 . \tag{10.97}$$

Replacing both vector mesons in (10.38) with photons by means of VMD, we obtain the 2γ interactions

$$\mathcal{L}_{G_D\mathcal{V}\mathcal{V}} = d_3^{\mathcal{V}\mathcal{V}} \eta^{\rho\sigma} \mathrm{tr}\, \left(F^{\mathcal{V}}_{\mu\rho} F^{\mathcal{V}}_{\nu\sigma}\right) \left(\eta^{\mu\nu} - \frac{\partial^\mu \partial^\nu}{\Box}\right) G_D, \tag{10.98}$$

with

$$d_3^{\mathcal{V}\mathcal{V}} \equiv \kappa \int \mathrm{d}z\, K^{-1/3} H_D = 0.0130195 \lambda^{1/2} M_{\mathrm{KK}}^{-1}, \tag{10.99}$$

and the amplitude

$$|\mathcal{M}_{G_D \to \mathcal{V}\mathcal{V}}|^2 = \frac{9}{2} \left(d_3^{\mathcal{V}\mathcal{V}} M_D^2 \mathrm{tr}\, (e^2 Q^2)\right)^2 . \tag{10.100}$$

Radiative three-body decays are seen to follow from

$$\mathcal{L}_{G_D\Pi\Pi\mathcal{V}} = 2i\,\mathrm{tr}\; d_5^{\mathcal{V}} \partial_\mu \Pi [\Pi, \mathcal{V}_\nu] \left(\eta_{\mu\nu} - \frac{\partial_\mu \partial_\nu}{M_D^2} \right) G_D, \tag{10.101}$$

with coupling

$$d_5^{\mathcal{V}} = \frac{1}{\pi} \int \mathrm{d}z K^{-1} H_D = \frac{17.2261}{\sqrt{\lambda} M_{\mathrm{KK}} N_c}, \tag{10.102}$$

and pertinent spin-averaged squared amplitude

$$\begin{aligned} |\mathcal{M}_{G_D\to\Pi\Pi\mathcal{V}}|^2 = &\left(\frac{4 d_5^{\mathcal{V}} e \mathrm{tr}\; S_1[S_2, Q]}{m_{\Pi_1}^2 + m_{\Pi_2}^2 - s_{13} - s_{23}} \right)^2 \\ &\times \Bigg(M_D^2 \left(m_{\Pi_1}^2 - s_{13} \right) \left(m_{\Pi_2}^2 - s_{23} \right) \\ &\quad - \left(m_{\Pi_1}^2 + m_{\Pi_2}^2 - s_{13} - s_{23} \right) \left(m_{\Pi_1}^2 m_{\Pi_2}^2 - s_{13} s_{23} \right) \Bigg), \end{aligned} \tag{10.103}$$

with s_{ij} the squared center of mass energy of the pseudoscalar-photon subsystem and again no contributions from resonant axial vector mesons.

Discussion

The results for the partial widths are displayed in Table 10.12, where the dilaton scalar glueball is alternatingly identified with $f_0(1500)$ and $f_0(1710)$ and again with assumed ideal mixing for ω and ϕ[14]. For both extrapolations, we find two-photon widths in the keV range, with dominating decays into $\rho\gamma$. Our predictions are somewhat in between the results of a few hundred eV to roughly up to 15 keV found in the literature [171, 172]. Interestingly, the decay rates into two-vector mesons obtained in Section 10.2.1 are comparable with the results of Ref. [150]. Unfortunately, no data for decays of $f_0(1710)$ involving a single photon appear to be available. The BELLE collaboration, however, reports a measurement for two-photon decays: $\Gamma_{\gamma\gamma}\mathcal{B}(K\bar{K}) = 12^{+3+227}_{-2-8}$ eV [170]. The conclusion therein is that due to its large two-photon width, $f_0(1710)$ is unlikely to be a glueball. On the contrary, the holographic prediction of the WSS model suggests an even larger branching fraction of $\Gamma_{\gamma\gamma}\mathcal{B}(K\bar{K}) \approx 690 \ldots 520$ eV that is about 2-3 sigma above the measurements quoted by BELLE. Another upper limit for this branching fraction is 480 eV from ARGUS [173]. BELLE obtains a central value for $\Gamma_{f_0(1710)\to\gamma\gamma}$ of a few tens of eV. This discrepancy with the WSS model prediction could be explained by $f_0(1710)$ containing a possibly large $s\bar{s}$ admixture, as, for example, found in the study of Ref. [174]. On the other hand, since the dilaton scalar glueball matches the hadronic decay patterns of $f_0(1710)$ remarkably well for $x \sim 1$, the BELLE result would seem to indicate that VMD

---

[14] See the discussion in Section 10.2.1 for non-ideal mixing.

	$\Gamma_{G_D(1506)}$ [keV]	$\Gamma_{G_D(1712)}$ [keV]
$G_D \to \rho\gamma$	184	276
$G_D \to \omega\gamma$	19.9	30.1
$G_D \to \phi\gamma$	14.1	29.4
$G_D \to \pi\pi\gamma$	8.17...10.8	9.59...12.7
$G_D \to KK\gamma$	1.04...1.38	2.14...2.83 5.67
$G_D \to \gamma\gamma$	1.74...1.32	1.98...1.50
$G_D \to$ Radiative	231...233	352...355

Table 10.12.: Radiative scalar glueball decay with G_D identified alternatively with $f_0(1500)$ and $f_0(1710)$ with masses 1506 MeV and 1712 MeV, respectively, for $\lambda = 16.63 \ldots 12.55$.

	$\Gamma_{G_E^{\text{WSS}}}$ [keV]	$\Gamma_{G_E(1865)}$ [keV]
$G_E \to \rho\gamma$	0.047	26.4
$G_E \to \omega\gamma$	0.003	2.86
$G_E \to \phi\gamma$	-	1.72
$G_E \to \pi\pi\gamma$	47.9...63.5	148...196
$G_E \to KK\gamma$	-	43.3...57.3
$G_E \to \gamma\gamma$	0.043...0.033	0.095...0.071
$G_E \to$ Radiative	47.9...63.5	191...253

Table 10.13.: Radiative decays of the exotic scalar glueball G_E with WSS model mass 855 MeV and extrapolated to the scalar glueball at 1865 MeV proposed in Ref. [45].

does not apply for radiative decays of $f_0(1710)$. A further complication not captured by the WSS is mixing with the novel $f_0(1770)$ resonance.

Fragmented Scalar Glueball

In Table 10.13, we show the resulting partial widths for the exotic scalar glueball with model mass as well as an extrapolation to the proposed fragmented scalar glueball of [45] with a mass of 1865 MeV. The radiative decay rates turn out to be negligible compared to the hadronic decays obtained in Section 10.2.1. For completeness, we also list the corresponding results for the dilaton scalar glueball in Table 10.14. They are again negligible compared to the hadronic decays computed in Section 10.2.1 with the conclusion that the exotics scalar glueball is a good fit for the fragmented scalar glueball, left unchanged.

	$\Gamma_{G_D^{\text{WSS}}}$ [keV]	$\Gamma_{G_D(1865)}$ [keV]
$G_D \to \rho\gamma$	175	346
$G_D \to \omega\gamma$	19.0	37.9
$G_D \to \phi\gamma$	12.9	42.8
$G_D \to \pi\pi\gamma$	8.03...10.6	10.6...14.1
$G_D \to KK\gamma$	0.96...1.27	3.11...4.12
$G_D \to \gamma\gamma$	1.72...1.30	2.16...1.63
$G_D \to$ Radiative	218...221	443...447

Table 10.14.: Radiative decays of the dilaton scalar glueball G_D with WSS model mass of 1487 MeV and extrapolated to the scalar glueball at 1865 MeV proposed in Ref. [45].

Pseudoscalar Glueball

From (10.45) one obtains couplings to one or two photons, respectively. They are given by

$$\mathcal{L}_{G_{PS} v \mathcal{V}} = G_{PS} \epsilon^{\mu\nu\rho\sigma} \operatorname{tr} \left[2 k_1^{v\mathcal{V}} \partial_\mu v_\nu \partial_\rho \mathcal{V}_\sigma \right], \tag{10.104}$$

where

$$k_1^{v^1\mathcal{V}} = 0.493557 N_c^{-1/2} M_{\text{KK}}^{-1}, \tag{10.105}$$

and

$$\mathcal{L}_{G_{PS} \mathcal{V}\mathcal{V}} = G_{PS} \epsilon^{\mu\nu\rho\sigma} \operatorname{tr} \left[k_1^{\mathcal{V}\mathcal{V}} \partial_\mu \mathcal{V}_\nu \partial_\rho \mathcal{V}_\sigma \right] \tag{10.106}$$

where

$$k_1^{\mathcal{V}\mathcal{V}} = 0.0145232 \lambda^{1/2} M_{\text{KK}}^{-1}. \tag{10.107}$$

The spin-averaged squared amplitudes following from (10.104) and (10.106) are given by

$$|\mathcal{M}_{G_{PS}\to v\mathcal{V}}|^2 = 2 \left(k_1^{v^1\mathcal{V}} e \operatorname{tr} T_v Q M_{PS}^2 \right)^2 \left(1 - \frac{m_v^2}{M_{PS}^2} \right)^2 \tag{10.108}$$

and

$$|\mathcal{M}_{G_{PS}\to \mathcal{V}\mathcal{V}}|^2 = 2 \left(k_1^{\mathcal{V}\mathcal{V}} e^2 \operatorname{tr} Q^2 M_{PS}^2 \right)^2 \tag{10.109}$$

respectively.

Discussion

In Table 10.15 we show the resulting partial decay widths for the WSS model mass of $1813 MeV \pm 7$ MeV together with two extrapolations to 2395 MeV, motivated by the study of [144], and the (quenched) lattice result of 2600 MeV. There appear to be no results for radiative decays of pseudoscalar glueball (candidates) with which we could compare.

	$\Gamma_{G_{PS}^{\text{WSS}}}$ [keV]	$\Gamma_{G_{PS}(2395)}$ [keV]	$\Gamma_{G_{PS}(2600)}$ [keV]
$G_{PS} \to \rho\gamma$	272...263	468...461	536...528
$G_{PS} \to \omega\gamma$	29.8...28.9	51.7...50.9	59.2...58.3
$G_{PS} \to \phi\gamma$	35.6...34.1	79.6...78.4	95.4...94.0
$G_{PS} \to \gamma\gamma$	1.75...1.30	2.30...1.71	2.49...1.86
$G_{PS} \to$ Radiative	339...328	602...592	693...682

Table 10.15.: Radiative pseudoscalar glueball decays for $\lambda = 16.63 \ldots 12.55$. Besides the WSS model result for the pseudoscalar mass, $M_G = 1813 \pm 7$MeV, extrapolations to X(2370) with mass 2395 MeV and 2600 MeV motivated by the analysis in [144] and lattice results, respectively, are considered.

10.3.2 Spin-1

Pseudovector Glueball

From (10.55) we obtain the couplings between the pseudovector glueball, a pseudoscalar meson, and a photon

$$\mathcal{L}_{G_{PV}\to\Pi\mathcal{V}} = -\frac{5}{6}\frac{1}{M_{PV}} b_1^{\mathcal{V}} \text{tr}\,\left(\mathcal{V}_\mu \partial_\nu \Pi + \Pi \partial_\mu \mathcal{V}_\nu\right) F_{\mu\nu}^{\tilde{\mathcal{V}}}, \tag{10.110}$$

where

$$b_1^{\mathcal{V}} = \frac{27}{4}\sqrt{\frac{\kappa}{\pi}} \frac{1}{M_{\text{KK}}^2 R_{\text{D4}}^3} \int \frac{\text{d}z}{\sqrt{1+z^2}} N_4(z) = \frac{2.70}{\sqrt{N_c}}. \tag{10.111}$$

Since the form field interactions originate from the non-gauge invariant CS term, care must be taken when evaluating photon polarization sums. Explicitly, we obtain

$$|\mathcal{M}_{G_{PV}\to\Pi\mathcal{V}}|^2 = 2\left(\frac{b_1^{\mathcal{V}}}{M_{PV}} e\, \text{tr}\, T_s Q m_\Pi^2\right)^2, \tag{10.112}$$

where we employed the photon polarization sum in axial gauge

$$\sum_\lambda \epsilon_\mu(k)\epsilon_\nu^*(k) = -g^{\mu\nu} - n^2 \frac{k^\mu k^\nu}{(k\cdot n)} + \frac{k^\mu n^\nu + k^\nu n^\mu}{k\cdot n} \tag{10.113}$$

to sum over the physical degrees of freedom. Note that n in (10.113) is an arbitrary auxiliary vector that is seen to drop out of the final result.

Equation (10.57) implies, via VMD, an interaction involving one axial vector meson and a photon

$$\mathcal{L}_{G_{PV}\to\mathcal{V}a} = -\frac{5}{6}\frac{1}{M_{PV}} b_3^{m\mathcal{V}} \text{tr}\,\left(\mathcal{V}_\mu a_\nu^{(m)}\right) F_{\mu\nu}^{\tilde{\mathcal{V}}} \tag{10.114}$$

with

$$b_3^{m\mathcal{V}} = \frac{27}{4}\frac{\kappa}{M_{\mathrm{KK}}R_{\mathrm{D4}}^3}\int \mathrm{d}z\sqrt{1+z^2}\,\psi_{2m-1}(z)\psi'_{2n}(z)N_4(z) = \frac{\{1.75,\ldots\}M_{\mathrm{KK}}}{\sqrt{N_c}}, \tag{10.115}$$

leading to

$$|\mathcal{M}_{G_{PV}\to a\mathcal{V}}|^2 = 2\left(\frac{b_3^{m\mathcal{V}}}{M_{PV}}m_a^2 e\,\mathrm{tr}\,T_a Q\right)^2\left(1-\frac{M_{PV}^2}{m_a^2}\right)^2, \tag{10.116}$$

Analogously, from (10.60), we derive the relevant interaction involving a photon, a pseudoscalar, and a vector meson

$$\mathcal{L}_{G_{PV}\Pi v\mathcal{V}} = \frac{5}{6}\frac{i}{M_V}2b_2^{m\mathcal{V}}\mathrm{tr}\left(\Pi\left[v_\mu^{(m)},\mathcal{V}_\nu\right]\right)F_{\mu\nu}^{\tilde{V}}, \tag{10.117}$$

where

$$b_2^{m\mathcal{V}} = \frac{\{168.081,\ldots\}}{\sqrt{\lambda}N_c}. \tag{10.118}$$

Disregarding resonance effects, the spin-averaged squared amplitude is expressed as

$$|\mathcal{M}_{G_{PV}\to\Pi v\mathcal{V}}|^2 = 2\left(\frac{b_2^{m\mathcal{V}}e\,\mathrm{tr}\,T_s[T_v,Q]}{M_{PV}m_v}\right)^2\left(\left(-m_\Pi^2+s_{12}+s_{23}\right)^2-4M_{PV}^2m_v^2\right). \tag{10.119}$$

Due to the appearance of a trace together with a commutator in the meson field strengths, there are no couplings to two photons.

Discussion

In Table 10.16 we collect the resulting radiative partial decay widths of the pseudovector glueball. For the three-body decays, we consider once more the a_1^0 meson as a resonant contribution as shown in Fig. 10.6, and its width is provided by (7.47). Similar to the hadronic decays discussed in Section 10.2.2, the radiative decays are found to be fairly significant. The primary radiative decay channels are into $\pi\rho\gamma$, exhibiting nearly maximal constructive interference between the resonant $a_1\gamma$ decay and the direct process.

Vector Glueball

The couplings to one photon and one pseudoscalar meson follow via VMD from (10.65)

$$\mathcal{L}_{G_V\Pi\mathcal{V}} = \frac{1}{M_V}g_1^{\mathcal{V}}\mathrm{tr}\,\left(\Pi\partial_\mu\mathcal{V}_\nu+\mathcal{V}_\mu\partial_\nu\Pi\right)\star F_{\mu\nu}^{V} \tag{10.120}$$

	$\Gamma_{G_{PV}^{\mathrm{WSS}}}$ [keV]
$G_{PV} \to \pi^0\gamma$	0.01
$G_{PV} \to \eta\gamma$	1.11...0.98
$G_{PV} \to \eta'\gamma$	0.59...1.62
$G_{PV} \to a_1\gamma, \rho\pi\gamma$	1395...1848
$G_{PV} \to f_1\gamma$	5.16
$G_{PV} \to f_1'\gamma$	1.40
$G_{PV} \to K^*K\gamma$	266...353
$G_{PV} \to X + \gamma$	1669...2209

Table 10.16.: Radiative decays of the pseudovector glueball with WSS model mass of $M_{PV} = 2311$ MeV.

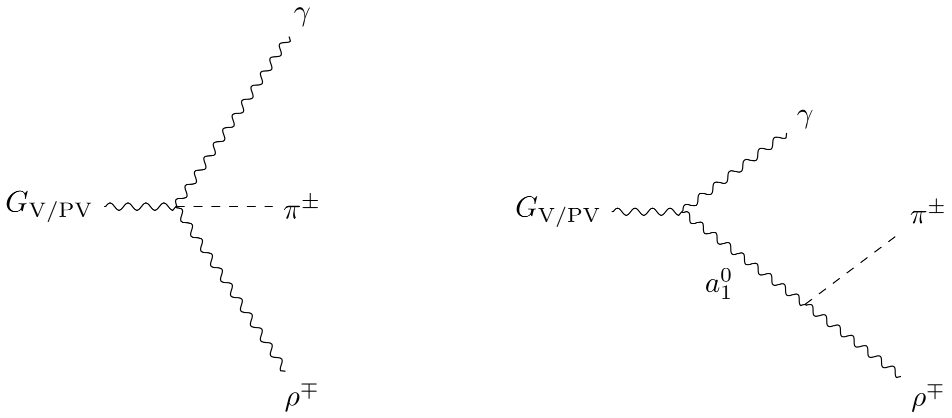
γ
$G_{\mathrm{V/PV}}$
$\pi^\pm$
$\rho^\mp$
γ
$G_{\mathrm{V/PV}}$
$\pi^\pm$
a_1^0
$\rho^\mp$

Fig. 10.6.: Feynman diagrams contributing to the radiative three-body decay of the (pseudo)vector glueball into $\pi\rho\gamma$.

where

$$g_1^{\mathcal{V}} = \frac{9}{16}\sqrt{\frac{\kappa}{\pi}}\frac{1}{M_{\mathrm{KK}}^2 R_{\mathrm{D4}}^3}\int \mathrm{d}z \frac{1}{z}\partial_z(zM_4(z)) = \frac{0.31}{\sqrt{N_c}}. \tag{10.121}$$

and the spin-averaged, squared amplitude is given by

$$|\mathcal{M}_{G_V\to\Pi\mathcal{V}}|^2 = \frac{2}{3}\left(eg_1^{\mathcal{V}}\mathrm{tr}\,T_sQ\right)^2 M_V^2\left(1-\frac{m_\Pi^2}{M_V^2}\right)^2. \tag{10.122}$$

Analogously, from (10.68) we obtain couplings of the vector glueball to an axial vector meson and one photon as

$$\mathcal{L}_{G_V a\mathcal{V}} = \frac{1}{M_V}f_1^{\mathcal{V}n}\epsilon^{\mu\nu\rho\sigma}\mathrm{tr}\left(\mathcal{V}_\mu\partial_\nu a_\rho^n + a_\mu^n\partial_\nu\mathcal{V}_\rho\right)V_\sigma + \frac{1}{M_V}f_2^{\mathcal{V}n}\epsilon^{\mu\nu\rho\sigma}\mathrm{tr}\left(\mathcal{V}_\mu\partial_\nu a_\rho^n - a_\mu^n\partial_\nu\mathcal{V}_\rho\right)V_\sigma, \tag{10.123}$$

where

$$\begin{aligned}
f_1^{\mathcal{V}n} &= \frac{3}{8}\frac{\kappa}{M_{\mathrm{KK}}R_{\mathrm{D4}}^3}\int \mathrm{d}z\left(\frac{3}{2}(1+z^2)^{-1/3}\frac{M_V^2}{M_{\mathrm{KK}}^2}+36\right)\psi_{2n}(z)M_4(z) = \frac{\{5.88,\ldots\}M_{\mathrm{KK}}}{\sqrt{N_c}}\\
f_2^{\mathcal{V}n} &= \frac{3}{8}\frac{\kappa}{M_{\mathrm{KK}}R_{\mathrm{D4}}^3}\int \mathrm{d}z\left(\frac{3}{2}\frac{1+z^2}{z}\right)\psi_{2n}'(z)\,\partial_z(zM_4(z)) = \frac{\{0.36,\ldots\}M_{\mathrm{KK}}}{\sqrt{N_c}}
\end{aligned} \tag{10.124}$$

and the pertinent spin-averaged squared amplitude

$$\begin{aligned}
|\mathcal{M}_{G_V\to a\mathcal{V}}|^2 = &\frac{1}{3\cdot 2}\left(\frac{\mathrm{tr}\,T_aQ^2}{m_aM_V^2}\right)^2\Big(-2M_V^2f_1^{n\mathcal{V}}f_2^{n\mathcal{V}}\left(-2m_a^2M_V^2-7m_a^4+M_V^4\right)\\
&+(f_1^{n\mathcal{V}})^2\left(9m_a^4M_V^2-6m_a^2M_V^4+4m_a^6+M_V^6\right)\\
&+M_V^2(f_2^{n\mathcal{V}})^2\left(6m_a^2M_V^2+m_a^4+M_V^4\right)\Big).
\end{aligned} \tag{10.125}$$

Note that the Lagrangian in (10.123) is again independent of the compactification scale.

Additionally, from (10.71) we get the quartic coupling including one photon

$$\mathcal{L}_{G_V\to\Pi v\mathcal{V}} = \frac{i}{M_V}g_1^{m\mathcal{V}}2\mathrm{tr}\left(\Pi\left[\mathcal{V}_\mu, v_\nu^{(m)}\right]\right)\star F_{\mu\nu}^V, \tag{10.126}$$

where

$$g_1^{m\mathcal{V}} = \frac{27}{32}\sqrt{\frac{\kappa}{\pi}}\frac{1}{M_{\mathrm{KK}}^2R_{\mathrm{D4}}^3}\int \mathrm{d}z\frac{1}{z}\psi_{2m-1}(z)\partial_z(zM_4(z)) = \frac{\{22.55,\ldots\}}{\sqrt{\lambda}N_c}. \tag{10.127}$$

Ignoring resonant contributions, the squared amplitude for the three-body decays resulting from (10.126) is given by

$$
\begin{aligned}
|\mathcal{M}_{G_V\to\Pi v^n\mathcal{V}}|^2 &= \frac{2(g_1^{m\mathcal{V}} e\mathrm{tr}\, T_s[Q,T_v])^2}{m_v^2 M_V^2 (M_V^2 - s_{12})^2} \\
&\times \Big(2m_v^2 M_V^2 \Big[(s_{12} - M_V^2)(m_\Pi^2 - 3M_V^2 + 2s_{12}) - s_{23}(M_V^2 + s_{12})\Big] \\
&\quad + (m_\Pi^2 - s_{12})^2 (M_V^2 - s_{12})^2 + 2s_{12}s_{23}(m_\Pi^2 - s_{12})(M_V^2 - s_{12}) \\
&+ 2m_v^4 M_V^4 + s_{23}^2 (M_V^4 + s_{12}^2)\Big).
\end{aligned}
\tag{10.128}
$$

To leading order, there are no three-body decays involving two photons due to the commutator terms in (10.126).

Decays into one pseudoscalar and two vector mesons are above the mass threshold. However, by replacing one of the external vector mesons with a photon, the phase space enlarges and allows for decays into one photon together with a vector and pseudoscalar meson

$$
\mathcal{L}_{G_V\to av\mathcal{V}} = -\frac{3i}{M_V} f_1^{mn} \epsilon^{\mu\nu\rho\sigma} \mathrm{tr} \mathcal{V}_\mu [v_\nu^m, a_\rho^n] V_\sigma
\tag{10.129}
$$

and f_1^{mn} given in (10.69). Interestingly enough, this coupling is absent for the pseudovector glueball of the previous section. Carrying out the polarization sums and spin-averaging, we obtain from (10.129)

$$
|\mathcal{M}_{G_V\to av\mathcal{V}}|^2 = 3\left(\frac{f_1 e\mathrm{tr}\, Q[T_v,T_a]}{2m_a m_v M_V\,(M_V^2 - s_{12})}\right)^2 \left(2|\tilde{\mathcal{M}}^T_{G_V\to av\mathcal{V}}|^2 + |\tilde{\mathcal{M}}^L_{G_V\to av\mathcal{V}}|^2\right),
\tag{10.130}
$$

with the transverse

$$
\begin{aligned}
|\tilde{\mathcal{M}}^T_{G_V\to av\mathcal{V}}|^2 &= m_a^4 \left(M_V^2 - s_{12}\right)\left(M_V^2 + 4m_v^2 - s_{12} - 4s_{13}\right) \\
&- 2m_a^2 \Big(M_V^4 \left(3m_v^2 + s_{12}\right) - 2M_V^2 s_{12}\left(m_v^2 + s_{12} + 2s_{13}\right) \\
&+ s_{12}\left(2m_v^4 - m_v^2(s_{12} + 4s_{13}) + s_{12}^2 + 4s_{12}s_{13} + 2s_{13}^2\right)\Big) \\
&- \left(m_v^2 - s_{12}\right)\Big(M_V^4 \left(3m_v^2 + s_{12}\right) \\
&+ M_V^2 \left(4m_v^4 - 2m_v^2(s_{12} + 2s_{13}) - 2s_{12}(s_{12} + 2s_{13})\right) \\
&+ s_{12}\left((s_{12} + 2s_{13})^2 - m_v^2(s_{12} + 4s_{13})\right)\Big),
\end{aligned}
\tag{10.131}
$$

Die approbierte gedruckte Originalversion dieser Dissertation ist an der TU Wien Bibliothek verfügbar.
The approved original version of this doctoral thesis is available in print at TU Wien Bibliothek.
TU Bibliothek Your knowledge hub WIEN

and longitudinal

$$
\begin{aligned}
|\tilde{\mathcal{M}}^{L}_{G_V\to av\mathcal{V}}|^2 &= 2m_a^6\left(M_V^2-s_{12}\right)\left(M_V^2+2m_v^2-s_{12}-2s_{13}\right)\\
&-2m_a^4\biggl[M_V^4\left(m_v^2+2(s_{12}+s_{13})\right)+2M_V^2\left(m_v^4+m_v^2(s_{12}+s_{13})-2(s_{12}+s_{13})^2\right)\\
&+s_{12}\left(2\left(s_{12}^2+3s_{12}s_{13}+3s_{13}^2\right)-3m_v^2(s_{12}+2s_{13})\right)\biggr]\\
&-m_a^2\biggl[M_V^6\left(11m_v^2+s_{13}\right)+M_V^4\biggl(4m_v^4-m_v^2(25s_{12}+4s_{13})\\
&-(s_{12}+2s_{13})(2s_{12}+3s_{13})\biggr)\\
&+M_V^2\biggl(m_v^2\left(13s_{12}^2+4s_{13}^2\right)-8m_v^4(s_{12}+s_{13})+4s_{12}^3\\
&+15s_{12}^2s_{13}+20s_{12}s_{13}^2+4s_{13}^3\biggr)\\
&+s_{12}\left(m_v^2\left(s_{12}^2+12s_{12}s_{13}+12s_{13}^2\right)-2s_{12}^3-9s_{12}^2s_{13}-18s_{12}s_{13}^2-12s_{13}^3\right)\biggr]\\
&+M_V^8m_v^2+M_V^6\left(3m_v^4+m_v^2(s_{13}-s_{12})+s_{12}s_{13}\right)\\
&+M_V^4\left(4m_v^6-2m_v^4s_{12}-m_v^2(s_{12}+2s_{13})(s_{12}+3s_{13})-s_{12}s_{13}(3s_{12}+5s_{13})\right)\\
&+M_V^2\biggl(m_v^2(s_{12}+2s_{13})\left(s_{12}^2+s_{12}s_{13}+2s_{13}^2\right)-\left(m_v^4\left(s_{12}^2+8s_{12}s_{13}+4s_{13}^2\right)\right)\\
&+s_{12}s_{13}(s_{12}+2s_{13})(3s_{12}+4s_{13})\biggr)\\
&+s_{12}s_{13}\left(m_v^2\left(s_{12}^2+6s_{12}s_{13}+4s_{13}^2\right)-(s_{12}+s_{13})(s_{12}+2s_{13})^2\right)
\end{aligned}
\tag{10.132}
$$

contributions of the vector glueball polarizations, respectively. The squared center of mass energy s_{12} is that of the axial and vector meson subsystem and s_{13} that of the vector meson-photon subsystem, respectively.

Discussion

Restricting ourselves to two- and three-body decays, we display the results for the partial widths in Table 10.17. As depicted in Fig. 10.6, the a_1^0 meson is summed resonantly together with the direct process into $\rho\pi\gamma$, although in this case, the interference is less significant than in the hadronic decay. Due to the large mass of the vector glueball, we find quite sizeable radiative widths, but still smaller than those of the pseudovector glueball, despite being about 500 MeV heavier in the WSS model. Again, the radiative widths are negligible compared to the hadronic decays obtained in Section 10.2.2.

	$\Gamma_{G_V}^{\mathrm{WSS}}$ [keV]
$G_V \to \pi^0\gamma$	27.8
$G_V \to \eta\gamma$	7.85...6.96
$G_V \to \eta'\gamma$	0.40...1.10
$G_V \to a_1\gamma, \rho\pi\gamma$	358...361
$G_V \to f_1\gamma$	41.5
$G_V \to f_1'\gamma$	11.4
$G_V \to K^*K\gamma$	78.2...104
$G_V \to a_1\rho\gamma$	338...447
$G_V \to K_1(1270)K^*\gamma$	47.2...62.6
$G_V \to K_1(1400)K^*\gamma$	47.3...62.7
$G_V \to X + \gamma$	958...1126

Table 10.17.: Radiative decays of the vector glueball with WSS model mass $M_V = 2882$ MeV.

10.3.3 Spin-2

Tensor Glueball

Couplings of the tensor glueball to photons are of particular importance in high-energy scattering processes like lepto- and photoproduction, where the tensor glueball may be identified with the leading state on the Pomeron trajectory (see III). Restricting the discussion, for now, to just the tensor glueball, we obtain its coupling to one photon and one vector meson from (10.78) as

$$\mathcal{L}_{G_T v^n \mathcal{V}} = 2 t_3^{\mathcal{V}n} G_T^{\mu\nu} \eta^{\rho\sigma} \operatorname{tr}\left(F^{\mathcal{V}}_{\mu\rho} F^{(n)}_{\nu\sigma}\right), \tag{10.133}$$

with

$$t_3^{\mathcal{V}n} = \int \mathrm{d}z K^{-1/3} \psi_{2n-1} H_T = 2\sqrt{3} d_3^{\mathcal{V}n}, \tag{10.134}$$

$d_3^{\mathcal{V}n}$ as given in (10.96) and the spin-averaged, squared amplitude follows as

$$|\mathcal{M}_{G_T \to v\gamma}|^2 = \frac{1}{5}\frac{1}{3M_T^4}\left(e \operatorname{tr} Q T_v \left(M_T^2 - m_v^2\right)\right)^2 \left(6M_T^4 + 3M_T^2 m_v^2 + 2m_v^4\right). \tag{10.135}$$

In a similar fashion, we obtain from (10.78)

$$\mathcal{L}_{G_T \mathcal{V}\mathcal{V}} = t_3^{\mathcal{V}\mathcal{V}} G_T^{\mu\nu} \eta^{\rho\sigma} \operatorname{tr}\left(F^{\mathcal{V}}_{\mu\rho} F^{\mathcal{V}}_{\nu\sigma}\right), \tag{10.136}$$

	$\Gamma_{G_T^{\mathrm{WSS}}}$ [keV]	$\Gamma_{G_T(2000)}$ [keV]	$\Gamma_{G_T(2400)}$ [keV]
$G_T \to \rho\gamma$	260	522	716
$G_T \to \omega\gamma$	28.3	57.5	79.1
$G_T \to \phi\gamma$	24.7	81.1	127
$G_T \to \pi\pi\gamma$	8.31...11.0	12.4...16.4	15.49...20.5
$G_T \to KK\gamma$	0.57...0.75	3.03...4.02	5.77...7.65
$G_T \to \gamma\gamma$	1.84...1.39	2.47...1.86	2.97...2.24
$G_T \to$ Radiative	324...327	681...685	949...955

Table 10.18.: Radiative tensor glueball decays for $\lambda = 16.63 \ldots 12.55$. Besides the pristine results for the WSS model mass of 1487 MeV, their extrapolations to glueball masses of 2000 and 2400 MeV are given.

with

$$t_3^{\mathcal{V}\mathcal{V}} = \int \mathrm{d}z K^{-1/3} H_T = 2\sqrt{3} d_3^{\mathcal{V}\mathcal{V}} \tag{10.137}$$

$d_3^{\mathcal{V}\mathcal{V}}$ as given in (10.99). Carrying out the polarization sums and averaging over the spin, (10.136) leads to

$$|\mathcal{M}_{G_T\to\gamma\gamma}|^2 = \frac{1}{5}\left[t_3^{\mathcal{V}\mathcal{V}} M_G^2 \mathrm{tr}\left(e^2 Q^2\right)\right]^2 . \tag{10.138}$$

Discussion

In Table 10.18 we list the resulting partial decay widths for a tensor glueball of the WSS model mass 1487 MeV together with extrapolations to 2000 MeV, motivated by Pomeron physics [36], as well as 2400 MeV motivated by lattice QCD [12]. The vector meson sector is again assumed to be ideally mixed[15]. The radiative decay widths of the tensor glueball are comparable with those of the dilaton scalar glueball in Table 10.12. Surprisingly, Ref. [172] obtained single photon decay widths that agree with ours, despite the large discrepancy in decays into two vector mesons pointed out previously in Section 10.2.3. The two-photon width of 2-3 keV is about an order of magnitude larger than the one obtained in Ref. [171] but comparable to those obtained in Refs. [172, 175] (1.72-0.96 keV).

---

[15] See the discussion in Section 10.2.1 for a more realistic mixing angle.

Part III

Reggeons, Pomeron, and Odderon

Introduction

11

> *Getretener Quark wird breit, nicht stark"*
>
> — **Johann Wolfgang von Goethe**
> *Westöstlicher Divan*

The calculations in Part II have indicated that, according to the WSS model, glueballs are broad resonances, making their experimental identification challenging. Although we have narrowed down the search area, it is prudent to explore different areas, such as high-energy scattering. Regge theory is a sophisticated framework that provides crucial insights into high-energy scattering processes and the fundamental nature of the scattered particles. Developed in the late 1950s by Tullio Regge [20], this theory has deepened our understanding of scattering amplitudes and their connections to bound states and resonances. Central to Regge theory is the concept of complex angular momentum. Normally, angular momentum is treated as a discrete quantum number. However, Regge demonstrated that allowing angular momentum to take complex values unveils profound structures and relationships within scattering amplitudes. In particular, the theory identifies specific complex values of angular momentum, known as Regge poles, where the scattering amplitude exhibits pole-like behavior. These poles correspond to families of particles with the same quantum numbers but different spins. Later, Chew and Frautschi [21, 22] indeed found that squared masses of baryons and mesons, when plotted against their spin, fall on trajectories that can be linearly approximated. The connections between these poles are traced by Regge trajectories, which are curves in the complex angular momentum plane and, in good approximation, parametrized by

$$J(t) = \alpha(0) + \alpha'|t| \tag{11.1}$$

where $\alpha(0)$ is the intercept, α' is the slope parameter, and t is the Mandelstam variable parametrizing the momentum transfer between the scattered particles, respectively. The poles are located at discrete values of spin, thus relating it to its mass

$$J_n = \alpha(0) + \alpha' m_n^2, \tag{11.2}$$

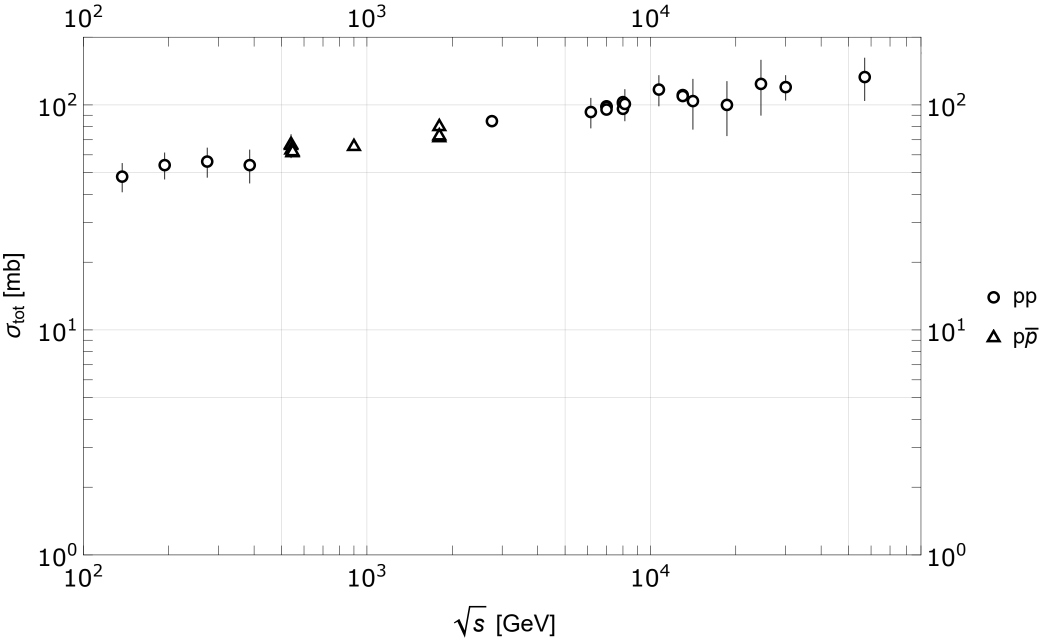

Fig. 11.1.: High-energy total cross sections from various experiments. Displayed is the combined data set of the PDG [9] .

where $J_n,\ m_n$ are the spin and mass of the n-th bound state, respectively. The properties of these trajectories, such as their slopes and intercepts, encode valuable information about the underlying dynamics of particle interactions and the exchanged trajectory is referred to as Reggeon. Regge theory provides a systematic way to analyze the high-energy behavior of scattering amplitudes. In particular, one finds for sufficiently high energies

$$\sigma_{tot}(s) \sim (\alpha' s)^{\alpha(0)-1}. \tag{11.3}$$

At very high center of mass energies $\sqrt{s}$, the experimental total cross sections σ_{tot} for pp and $p\bar{p}$ scattering shown in Fig. 11.1, can no longer be described by exchanges of ordinary meson trajectories with intercept below or at 1. These observations led to the proposal of the Pomeron, the Regge trajectory with the highest intercept and vacuum quantum numbers [176]. Experimentally, one finds $\alpha_{\mathbb{P}}(0) \approx 1.08$, a value seemingly incompatible with unitarity constraints. However, as will also be shown in the holographic computations below, the strong shadowing brought about by multiple Pomeron exchanges leads to a depletion of $\sigma_{tot}(s)$ for $s \to \infty$. The Pomeron Glueball Hypothesis (PGH) asserts that at low momentum transfers, the Pomeron is a glueball trajectory, with the lowest state identified with the tensor glueball. In Perturbative QCD (pQCD), it is obtained by resumming the rapidity ordered collinear gluon emissions, also known as Balitskii-Fadin-Kuraev-Lipatov (BFKL) ladder [177–180]. A more subtle contribution to high-energy pp and $p\bar{p}$ scattering is due to the Odderon. In pQCD it is parametrized by a C-odd exchange with intercept at, or slightly below, 1, corresponding to the Janik-Wosiek (JW) [181] and Bartels-Lipatov-Vacca (BLV) [182] solutions of the Bartels-Kwiecinski-Praszalowicz (BKP) equation [183, 184], respectively. The Odderon arises as the C-odd resummation of two (Lipatov rung) and three gluon ladder diagrams in perturbative QCD. For completeness, we note that the Pomeron and Odderon are also established concepts in the framework of the Color Glass Condensate (CGC) [185–187] (see Ref. [188] for a review). Reggeons with positive signature add in pp and $p\bar{p}$ scattering, while odd signature Reggeons subtract in the latter. At high energies, differences in observables of pp and $p\bar{p}$ scattering are thus attributed to the presence of Odderon exchanges. Indeed, a recent publication by the TOTEM and D∅ collaboration claims to have discovered the Odderon [189], though it is not fully undisputed [190]. In this part, we will address this claim by using a holographic bottom-up construction. Further, we will consider the 1^{+-} pseudovector glueball exchange, which has been argued to play a central role in diffractive photoproduction of heavy pseudoscalar mesons and at the high center of mass energies transmutes into one of the two branches of the holographic Odderon [191].

For reviews on the physics of the Pomeron and Odderon, see Refs. [36, 192–194].

The computations and discussion laid out in this part are based on Refs. [123, 195].

This part is structured as follows. In Chapter 12 we will formally introduce the concept of the Pomeron and Odderon in Gauge/Gravity duality. Next, we will consider general bottom-up model building in holographic QCD in Chapter 12.1. In Chapter 13, we will construct such a model to address the recently claimed Odderon observation at the LHC and Tevatron within a holographic framework. Lastly, we will turn to threshold production of heavy pseudoscalar mesons, a process that is argued to be sensitive to the exchange of a pseudovector glueball, in Chapter 14.

Die approbierte gedruckte Originalversion dieser Dissertation ist an der TU Wien Bibliothek verfügbar.
The approved original version of this doctoral thesis is available in print at TU Wien Bibliothek.
TU Bibliothek, WIEN Your knowledge hub

Pomeron and Odderon in Gauge/Gravity Duality

12

In the context of gauge/gravity duality, initial investigations into the Pomeron and Odderon were conducted in a series of seminal works focusing on the conformal limit in Refs. [191, 196–198]. Therein, the leading state on the Pomeron trajectory was identified with a 2^{++} graviton in the dual gravitational theory, while the leading state on the Odderon trajectory is associated with a $1^{\pm-}$ Kalb-Ramond field exchange. According to the holographic principle, the bulk fields thus couple to the corresponding QCD boundary operators [191]

$$\begin{aligned} h^{\mu\nu}[2^{++}] &: G^{a\mu\alpha}G^{a\nu}_{\alpha} \\ B^{\mu\nu}[1^{+-}] &: d^{abc}G^{a\alpha\beta}G^{b}_{\alpha\beta}G^{c\mu\nu} \\ C^{\mu\nu}[1^{--}] &: d^{abc}G^{a\alpha\beta}G^{b}_{\alpha\beta}\tilde{G}^{c\mu\nu}, \end{aligned} \tag{12.1}$$

with all traces subtracted. Consequently, the Pomeron and Odderon are sourced by the analytically continued spin-j boundary operators

$$\begin{aligned} h^{\mu\nu}_{j}[(2+j)^{++}] &: G^{a\mu\alpha}D_{\alpha_1}...D_{\alpha_j}G^{a\nu}_{\alpha} \\ B^{\mu\nu}_{j}[(1+j)^{+-}] &: d^{abc}G^{a\alpha\beta}D_{\alpha_1}...D_{\alpha_j}G^{b}_{\alpha\beta}G^{c\mu\nu} \\ C^{\mu\nu}_{j}[(1+j)^{--}] &: d^{abc}G^{a\alpha\beta}D_{\alpha_1}...D_{\alpha_j}G^{b}_{\alpha\beta}\tilde{G}^{c\mu\nu}, \end{aligned} \tag{12.2}$$

with the proper symmetrization assumed. The conformal dimensions and twist thus follow as $\Delta_h = 4 + j$ and $\tau_h = 2 + j$ for h_j, and $\Delta_b = 6 + j$ and $\tau_b = 5 + j$ for B_j and C_j, respectively.

Using type IIB supergravity on $AdS_5 \times S_5$, the strong coupling expansions of the Pomeron (+) and Odderon (-) intercept for a conformal theory were to leading order in λ found to be [191, 196]

$$j_0^{(+)} = 2 - \frac{2}{\sqrt{\lambda}}, \qquad j_{0,(i)}^{(-)} = 1 - \frac{m^2_{\text{AdS},(i)}}{2\sqrt{\lambda}}, \tag{12.3}$$

where

$$m^2_{\text{AdS},(1)} = (k+4)^2, \qquad m^2_{\text{AdS},(2)} = k^2, \qquad k \in \mathbb{N}_0 \tag{12.4}$$

is the squared AdS mass of the two possible solutions for the equations of motion of the Kalb-Ramond field, and the integer k corresponds to the mode number of the spherical harmonics on the S_5. For $\lambda \to \infty$, the intercepts correspond to that of a pure spin-2 and spin-1 exchange, respectively. As demonstrated in Ref. [196], this shift in the intercept away from integer values can be understood in the bulk theory in terms of diffusion in the transverse space with diffusion constant $\mathcal{D} = 1/(2\sqrt{\lambda})$. Consider for example the product space $\mathrm{AdS}_5 \times S_5$ with metric

$$\mathrm{d}s^2 = \left(\frac{r}{R_{\mathrm{D3}}}\right)^2 \eta_{\mu\nu}\mathrm{d}x^\mu \mathrm{d}x^\nu + \left(\frac{R_{\mathrm{D3}}}{r}\right)^2 \mathrm{d}r^2 + \mathrm{d}s^2_{S_5}, \tag{12.5}$$

and r identified with some energy scale. The curved background in (12.5) leads to an effective slope parameter since the Mandelstam variables are red-shifted

$$\tilde{s} = \left(\frac{R_{\mathrm{D3}}}{r}\right)^2 s, \qquad \tilde{t} = \left(\frac{R_{\mathrm{D3}}}{r}\right)^2 t \tag{12.6}$$

and we may thus identify

$$\alpha'_{eff}(r) = \left(\frac{R_{\mathrm{D3}}}{r}\right)^2 \alpha'. \tag{12.7}$$

Hence, the higher-dimensional nature of the Pomeron and Odderon gives rise to a continuum of their four-dimensional counterparts for each value of r. At high center of mass energies s and for $t > 0$, the dominant trajectory in a scattering amplitude of the form

$$\mathcal{A}(s,t) \sim \left(\frac{s}{s_0}\right)^{j_\pm + \frac{\alpha'_{eff}}{2}t} \tag{12.8}$$

is the one with minimal value of r and thus determined by the confinement scale r_0, highlighting the connection to glueballs. The situation is reversed for $t < 0$, where large values of r dominate and the effective slope in (12.7) vanishes. We further note that for $k = 0$, the strong coupling results in (12.3) already bear a striking resemblance to the pQCD picture, where, to leading order, the weak coupling expansion is found to be [181, 182, 199]

$$j_0^{(+)} = 1 + \frac{\lambda}{\pi^2}\ln 2, \qquad j_{0,(1)}^{(-)} = 1 - \frac{\lambda}{\pi}0.247, \qquad j_{0,(1)}^{(-)} = 1. \tag{12.9}$$

Interestingly enough, the Odderon solutions with intercept at $j = 1$ persist even for higher order expansions in λ, both at strong and weak coupling [182, 198]. This connection between the "hard" and "soft" Pomeron, dominating above or below the confinement scale, respectively, is not accidental. Using Gauge/String duality, Ref. [196] found the remarkable result that a running coupling leads to a transition between the soft and hard Pomeron in certain kinematical ranges of s and t and demonstrated that the curved

Die approbierte gedruckte Originalversion dieser Dissertation ist an der TU Wien Bibliothek verfügbar.
The approved original version of this doctoral thesis is available in print at TU Wien Bibliothek.
TU Bibliothek Your knowledge hub WIEN

geometry leads to the expected power law behavior of amplitudes expected in gauge theories, instead of the exponential suppression found from string scattering in flat space [200]. In Refs. [201, 202] this formalism was used to compute structure functions of Deep Inelastic Scattering (DIS) and confronted with measurements from HERA in the range of $0.1\ \text{GeV}^2 < Q^2 < 650\ \text{GeV}^2$. Upon identifying the virtuality Q^2 with the holographic coordinate $r^2 \simeq Q^2$, they were able to show that the observed running of the Pomeron intercept in ZEUS data [203] can be attributed to diffusion effects in AdS for large Q^2 and confinement effects at low virtualities.

Even though it has been heuristically demonstrated in Refs. [191, 196] that the Reggeon "form factors"

$$\left(\frac{s}{s_0}\right)^{\alpha' t/2} \tag{12.10}$$

arise from string scattering in AdS, the confining hard-wall model based on type IIB supergravity on $\text{AdS}_5 \times S_5$ considered therein does not display this behavior. This is because the appearance of (12.10) in a scattering amplitude crucially depends on the detailed nature of the confinement. In Chapter 13 we shall thus construct a holographic model that successfully reproduces this behavior while simultaneously incorporating all the features described above.

For additional important developments relevant for this part, see Refs. [200–202, 204–207].

12.1 Top-Down vs. Bottom-Up

Top-down holographic constructions, like the WSS model, which has been extensively discussed in Part II in the context of glueball physics, only partly lend themselves to Regge phenomenology. This is mostly due to the mass spectra not scaling linearly width mode number (c.f. (11.2)), but also due to their complexity. Nevertheless, they were with partial success applied to pp scattering [208, 209] and central production of $\eta,\ \eta'$ [210, 211] as well as f_1 [212] and J/Ψ production near threshold [213]. For an attempt to describe DIS in the Regge regime within the WSS model, see Appendix E. In contrast, bottom-up models are simplified versions of top-down constructions, retaining only the essential ingredients to describe specific phenomena. This simplification facilitates calculations and allows for a more realistic Ultraviolet (UV) behavior of certain observables, albeit at the expense of theoretical rigor. Early attempts related to glueball physics within bottom-up models can be found in Refs. [125–131]. For bottom-up holographic Regge phenomenology see Refs. [214, 215]. In the following chapters, we will employ the soft-wall model [216] together with a slight variation thereof, referred to as the repulsive-wall model, to address Pomeron and Odderon physics within a holographic framework.

Holographic Odderon at TOTEM?

13

In this chapter, we investigate the potential role of the Odderon in diffractive pp and $p\bar{p}$ elastic scattering, building upon the recently claimed observation of the Odderon reported by the D0 and TOTEM collaborations [189] in the data shown in Fig. 13.1. The plot shows a distinctive diffractive pattern with a bump-to-dip ratio that appears to decrease with $\sqrt{s}$ for the pp data and about constant for the $p\bar{p}$ data. A feature usually attributed to the presence of an Odderon exchange. Our approach utilizes a dual gravity formulation of QCD, incorporating a repulsive wall to account for confinement, which turned out to be a crucial ingredient in achieving Reggeization together with Gribov diffusion. Previous work has partially examined the Odderon's contribution in pp and $p\bar{p}$ scattering using effective string theory and AdS/CFT in the conformal limit, as discussed in Refs. [218, 219].

In Fig. 13.2 we show the pertinent Reggeized glueball exchanges for diffractive pp and $p\bar{p}$ scattering. As stated above, the C-even and -odd contributions add in the elastic pp scattering amplitude and subtract in the crossed $p\bar{p}$ amplitude

$$\begin{aligned} \mathcal{A}_{pp} &= \mathcal{A}_{pp}^{\mathbb{P}} + \mathcal{A}_{pp}^{\mathbb{O}} \\ \mathcal{A}_{p\bar{p}} &= \mathcal{A}_{pp}^{\mathbb{P}} - \mathcal{A}_{pp}^{\mathbb{O}}. \end{aligned} \tag{13.1}$$

To analyze (13.1), we set up a holographic bottom-up model.

13.1 The Repulsive-Wall Model

As shown in Appendix F, the soft-wall model fails to capture Gribov diffusion, which is necessary to describe the data in the off-forward region. In a sense, the soft-wall model with metric

$$\begin{aligned} ds^2 &= e^{2A(z)}(\mathrm{d}z^2 + \eta_{\mu\nu}\mathrm{d}x^\mu \mathrm{d}x^\nu), \\ e^{2A(z)} &= \left(\frac{R}{z}\right)^2 e^{a\kappa^2 z^2}, \end{aligned} \tag{13.2}$$

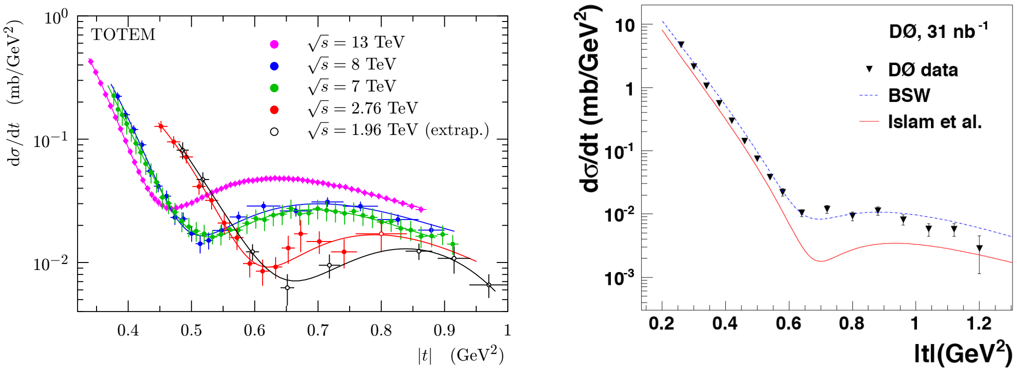

(a) (b)

Fig. 13.1.: Differential cross sections at different center of mass energies for pp scattering from the TOTEM collaboration (a) and for $p\bar{p}$ scattering from the DØ collaboration (b) [189, 217]

.

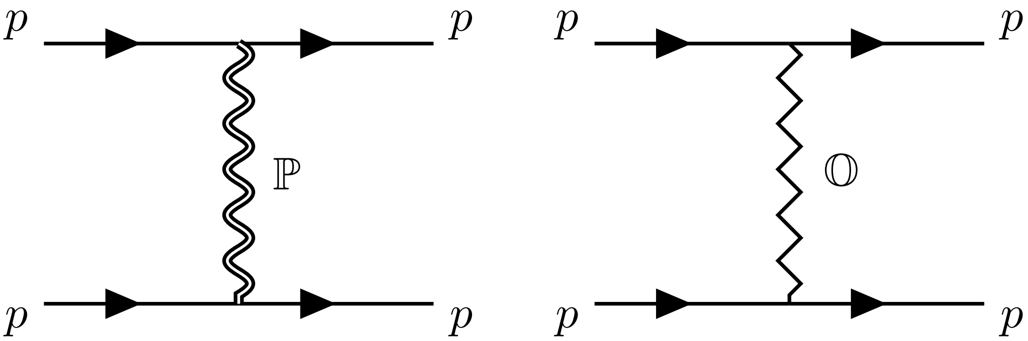

(a) (b)

Fig. 13.2.: Feynman diagrams for diffractive pp scattering through (a) Pomeron and (b) Odderon exchange

is too confining to capture the diffusive behavior in AdS. We will thus linearize the bulk equations of motion in the dilaton, which has been absorbed into the metric. The constant prefactor a serves to discriminate between open $|a| = 1^2$ and closed $|a| = 2^2$ string fluctuations as well as attractive $a < 0$ and repulsive $a > 0$ dilaton. The parameter R will be matched using the duality between type IIB supergravity on $\mathrm{AdS}_5 \times S_5$ and $\mathcal{N} = 4$ super Yang-Mills theory

$$R^2 \equiv R_{\mathrm{D3}}^2 = \sqrt{\lambda}\alpha', \tag{13.3}$$

with $R = 1$ in the following.

13.2 Reggeization of the Even and Odd Spin-j Exchanges

13.2.1 Even Spin-j

The even spin-j exchanges arise through the Reggeization of the transverse-traceless spin-2 graviton $\epsilon_{\mu\nu}^{TT} h_{j=2}$ with equations of motions following by linearizing the Einstein-Hilbert action and anomalous dimension of

$$\Delta_g(j = 2) = 2 + \sqrt{4 + m_5^2 R^2} \tag{13.4}$$

where $m_5^2 R^2 = 0$. To resum the even spin-j exchanges, we deform the anomalous dimension

$$\Delta_g(j) = 2 + \sqrt{4 + m_5^2 R^2 + m_j^2 R^2} \tag{13.5}$$

by using the quantized mass spectrum of the closed string

$$j = 2 + \frac{1}{2}\alpha' m_j^2. \tag{13.6}$$

The anomalous dimension (13.5) is thus given by

$$\Delta_g(j) = 2 + \sqrt{2\sqrt{\lambda}(j - j_{\mathbb{P}})} \tag{13.7}$$

with

$$j_{\mathbb{P}} = 2 - \frac{4}{2\sqrt{\lambda}}. \tag{13.8}$$

For completeness, we note that in Ref. [198] higher order corrections in $1/\sqrt{\lambda}$ to the Pomeron intercept have been computed. Based on the original BFKL analysis, we assume that j is the Mellin inverse of the squared center of mass energy s. The holographic

Pomeron Kernel $G_2(j,t,z,z')$ will be computed using the bulk equations of motion for a scalar field analytically continued to spin-j by (13.5). To obtain the bulk-to-bulk propagator $G_2(s,t,z,z')$, we resum the entire tower of even signature spin-j contributions by performing a Mellin transform together with a Sommerfeld-Watson transform

$$G_2(s,t,z,z') = \oint \frac{\mathrm{d}j}{4\pi i} \frac{(\alpha' s)^{j-2} + (-\alpha' s)^{j-2}}{\sin \pi(j-2)} G_2(j,t,z,z'). \tag{13.9}$$

In (13.9) we have performed a shift in j such that the leading state on the Pomeron trajectory corresponds to a spin-2 exchange. The distinction between $G_2(j,t,z,z')$ and its even signature Mellin transform $G_2(s,t,z,z')$ is made through its argument. The rightmost part of the contour in (13.9) is determined by the branch point of $G_2(j,t,z,z')$. In order to resum the trajectory, we will close the contour to the left. The poles to the right of the branch point, at non-negative integers, correspond to glueball modes.

13.2.2 Odd Spin-j

Similarly to the even signature contributions, the anomalous dimension for C-odd vector exchange is given by [215]

$$\Delta_g(j=1) = 2 + \sqrt{4 + m_5^2 R^2} \tag{13.10}$$

with $m_5^2 R^2 = -4 + m_k^2$ and where we identified the physical polarizations of the $C_2 \sim \star dC$ Ramond-Ramond field with the gauge field C[1]. Note that we added $m_k^2 = k^2,\ (4+k)^2$ with $k \in \mathbb{N}_0$, corresponding to the two branches of the holographic Odderon [191]. The branch with $m_k^2 = k^2$ has been argued to be unphysical since it does not correspond to propagating degrees of freedom. However, as was already argued in Ref. [191], upon analytically continuing to spin-j, they become physical, as can be seen by explicitly computing the bare type IIB B_2 propagator (see (3.23) in [218]). On the other hand, this branch sources the boundary operator $\mathcal{O}_k^{(16)} \sim \mathrm{tr}\, F_+ X^{k+1}$ and is thus more sensitive to the adjoint scalars of the supersymmetry theory. In contrast, the $m_k^2 = (4+k)^2$ branch sources $\mathcal{O}_k^{(16)} \sim \mathrm{tr}\, F_+ F_-^2 X^k$, in accordance with (12.1-12)[2]. The C-odd closed string exchange of C_j gauge fields is thus again resummed by shifting its anomalous dimension

$$\Delta_g(j) = 2 + \sqrt{4 + m_5^2 R^2 + \tilde{m}_j^2 R^2} \tag{13.11}$$

---

[1] The B_2 and C_2 fields of type IIB supergravity mix, similarly to the case of B_2 and C_3 in the type IIA computations of Part II

[2] See for example Table 7 of Ref. [220].

by the quantized mass spectrum of the closed string

$$j = 1 + \frac{1}{2}\alpha' \tilde{m}_j^2. \tag{13.12}$$

The anomalous dimension (13.11) is hence given by

$$\Delta_g(j) = 2 + \sqrt{2\sqrt{\lambda}(j - j_{\mathbb{O}})} \tag{13.13}$$

with

$$j_{\mathbb{O}} = 1 - \frac{m_k^2}{2\sqrt{\lambda}}. \tag{13.14}$$

The higher-order corrections considered in Ref. [198] showed that, in accordance with the JW and BLV solutions of pQCD and (13.14), the Odderon has one solution with intercept precisely at 1 and another solution with intercept slightly below 1. We proceed in a similar fashion as for the Pomeron. Reggeizing the Kalb-Ramond field via Mellin transform and pertinent projection onto odd-signature exchanges via Sommerfeld-Watson transform, we have

$$G_1(s,t,z,z') = \int \frac{\mathrm{d}j}{4\pi i} \frac{(\alpha' s)^{j-1} + (-\alpha' s)^{j-1}}{\sin \pi (j-1)} G_1(j,t,z,z'). \tag{13.15}$$

We shifted the trajectory so that the leading state on the Odderon trajectory corresponds to a spin-1 exchange.

To summarize, the even and odd signature exchanges can be Reggeized by

$$G_{j\pm}(s,t,z,z') = \oint \frac{\mathrm{d}j}{4\pi i} \frac{(\alpha' s)^{j-j_\pm} + (-\alpha' s)^{j-j_\pm}}{\sin \pi (j-j_\pm)} G_{j\pm}(j,t,z,z'), \tag{13.16}$$

with $j_+ = 2$ and $j_- = 1$.

13.2.3 Resummed Bulk-to-Bulk Propagator

In a holographic scattering amplitude, states with four-dimensional spin σ contribute an extra factor of p^σ compared to four-dimensional scalars, where $p \sim e^{A(z)}$ is the red-shifted four-dimensional energy [200]. Thus, the analytically continued spin-2 and spin-0 bulk-to-bulk propagator are related by

$$G_2(j,t,z,z') = e^{-(j-2)(A(z)+A(z'))}\, G_0(j,t,z,z') \tag{13.17}$$

where the scalar propagator obeys the Sturm-Liouville equation

$$L_z G_0(z,z') = \frac{\delta(z-z')}{w(z)} \tag{13.18}$$

with

$$L_z = \frac{1}{w(z)}\, d_z(w(x)\, p_0(z)\, d_z) + p_2(z). \tag{13.19}$$

The two linearly independent solutions, one regular and one singular, of the homogeneous equation (13.18)

$$L_z\, y_{1,2}(z) = 0 \tag{13.20}$$

can be utilized to obtain the Green's function as

$$G(z,z') = \frac{1}{wp_0\mathbb{W}} y_1(z_<)y_2(z_>), \tag{13.21}$$

with the Wronskian given by $\mathbb{W} = (y_1'y_2 - y_2'y_1)$. Note that the combination $wp_0\mathbb{W}$ is a constant independent of z, z', and that (13.21) is symmetric in z, z'. This becomes more evident when we employ the solutions derived from the eigenvalue problem $L_z y_n = \lambda_n y_n$, with

$$G(z,z') = \sum_n \frac{y_n(z)y_n^*(z')}{\lambda_n}, \tag{13.22}$$

and the normalizations

$$\int \mathrm{d}z\, w(z)y_n^*(z)y_m(z) = \delta_{nm}, \tag{13.23}$$

following from the hermiticity of $L_z = L_z^\dagger$ in $\mathbb{R}$.

For the particular background in (13.2), the weights are given by

$$\begin{aligned} w(z) &= \sqrt{g} \\ p_0(z) &= -g^{zz}(z) \\ p_2(z) &= S_j - tz^2, \end{aligned} \tag{13.24}$$

where $S_j = m_5^2R^2 + m_j^2R^2$. To solve (13.19), we employ a rescaling of the form

$$G_0(j,t,z,z') \to (zz')^{\frac{3}{2}} e^{\frac{3}{4}\kappa^2(z^2+z'^2)}\, G_0(j,t,v,v') \tag{13.25}$$

with $v = 3/2\kappa^2z^2$. Upon expansion of the dilaton to linear order $e^{2av/3} = 1 + 2av/3$, this leads to the Whittaker equation

$$K_0''(v) + \left(-\frac{S_j(1+\frac{2}{3}v)}{4v^2} + \frac{v(2-v)-3}{4v^2} + \frac{t/a}{2v}\right) K_0(v) = \frac{\delta(v-v')}{\sqrt{6}a\kappa}. \tag{13.26}$$

The homogeneous solutions of (13.26) are readily obtained

$$
\begin{aligned}
K_1(v) &= e^{-\frac{v}{2}} v^{\frac{1}{2}+\alpha}\, \mathbb{M}\left(\frac{1}{2}+\alpha-\beta, 1+2\alpha, v\right) \\
K_2(v) &= e^{-\frac{v}{2}} v^{\frac{1}{2}+\alpha}\, \mathbb{U}\left(\frac{1}{2}+\alpha-\beta, 1+2\alpha, v\right)
\end{aligned}
\tag{13.27}
$$

with the Kummer function $\mathbb{M}$, regular at the origin, and the Tricomi function $\mathbb{U}$, irregular and with a branch cut at the origin, and where

$$
\alpha = \frac{\Delta_g(j)-2}{2}, \; \beta = \frac{3-S_j-m_5^2+3\tilde{t}/a}{6}. \tag{13.28}
$$

To obtain the inhomogeneous solution to (13.26), we glue together the regular and irregular solution

$$
\begin{aligned}
K_0(v,v') &= \frac{1}{2}\mathcal{A}\, K_2(v)K_1(v') \qquad v > v' \\
K_0(v,v') &= \frac{1}{2}\mathcal{A}\, K_1(v)K_2(v') \qquad v < v',
\end{aligned}
\tag{13.29}
$$

and fix the normalization by the Wronskian

$$
\mathcal{A}^{-1} = -\sqrt{6}a\kappa \mathcal{W}(K_2,K_1) = -\frac{\sqrt{6}a\kappa\Gamma(1+2\alpha)}{\Gamma\left(\frac{1}{2}+\alpha-\beta\right)}. \tag{13.30}
$$

By linearizing the dilaton, the conformal intercept resulting from the gamma function is shifted

$$
j_{\mathbb{P}}(t) = j_+ - \frac{3}{2\sqrt{\lambda}} + \frac{\alpha'}{2}t, \tag{13.31}
$$

where we identified $5a\kappa^2R^2 = 2$. The intercept is shifted slightly below what one would obtain for the soft-wall model or pure AdS (see Appendix F). The positive root of the argument of the gamma function gives a pole with higher intercept

$$
j_{\mathbb{P}}(t) = j_+ + \frac{6}{\sqrt{\lambda}} + \frac{\alpha'}{2}t \tag{13.32}
$$

that is outside the contour of the Sommerfeld-Watson transform in Fig. 13.3. Reverting to the original coordinates and functions, we obtain the analytically continued scalar bulk-to-bulk propagator

$$
G_0(j,t,z,z') = -\frac{(zz')^2}{2}(3a\kappa^2zz'/2)^{\Delta_g(j)-2}\frac{\Gamma(\frac{3\Delta_g(j)+S_j-6+3\tilde{t}/a}{6})}{\Gamma(\Delta_g(j)-1)}\mathbb{M}(z)\mathbb{U}(z'), \tag{13.33}
$$

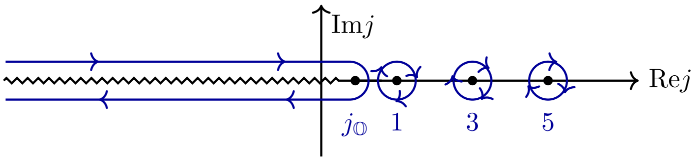

Fig. 13.3.: Complex j-plane structure for the odd spin-j bulk-to-bulk propagator. The poles give rise to the vector glueball spectrum, and the cut gives rise to the Odderon.

where the shorthand

$$\mathbb{M}(z) = \mathbb{M}\left(\frac{S_j + 3\Delta_g(j) - 6 - 3\tilde{t}/a}{6}, \Delta_g(j) - 1, a\kappa^2 z^2\right) \tag{13.34}$$

and similarly for $\mathbb{U}(z)$, was introduced. The branch cut of

$$\Gamma\left(\frac{1}{2} + \alpha - \beta\right) = \Gamma(iy) \approx e^{-i\gamma_E y}/iy \tag{13.35}$$

is chosen to the left of the integration contour, along the negative real axis as shown in Fig. 13.3. In the Regge limit of large s and small t, the integral is dominated by the saddle point. Recalling that $m_5^2 = 0$ for the Pomeron, we evaluate (13.16) by a saddle point approximation with the fully symmetric result

$$G_2(s,t,z,z') = -\frac{3}{5} f^+(\lambda) \sqrt{\frac{3\mathcal{D}}{5\pi\tau}} \frac{(zz')^2}{2} e^{-\frac{a}{2}(j_{\mathbb{P}}(t)-2)\kappa^2(z^2+z'^2)} (3a\kappa^2 zz'/2) e^{(j_{\mathbb{P}}(t)-2)\tau}, \tag{13.36}$$

with $\tau = \ln(\alpha' s z z') = \chi + \ln zz'$ and $\chi = \ln(\alpha' s)$ the rapidity. For the evaluation we used $\mathbb{M}(0,0,z) = \mathbb{U}(0,0,z) = 1$ and defined the signature factor

$$f^+(\lambda) = i + \frac{4\sqrt{\lambda}}{3\pi} - \frac{\pi}{4\sqrt{\lambda}}. \tag{13.37}$$

For the Odderon, we continue analogously. By relating the analytically continued spin-1 and spin-0 by

$$G_1(j,t,z,z') = e^{-(j-1)(A(z)+A(z'))} \tilde{G}_0(j,t,z,z') \tag{13.38}$$

with the rescaled scalar field

$$\tilde{G}_0(j,t,z,z') = (zz')^{-1} G_0(j,t,z,z'), \tag{13.39}$$

and

$$\Delta_g(j) = 2 + \sqrt{4 + S_j} = 2 + m_k, \tag{13.40}$$

Die approbierte gedruckte Originalversion dieser Dissertation ist an der TU Wien Bibliothek verfügbar.
The approved original version of this doctoral thesis is available in print at TU Wien Bibliothek.
TU Bibliothek
WIEN Your knowledge hub

we obtain

$$j_{\mathbb{O}}(t) = j_- - \frac{m_k^2 - 1}{2\sqrt{\lambda}} + \frac{\alpha'}{2} t. \tag{13.41}$$

The JW and BLV solutions of perturbative QCD are also reflected in the two branches of the holographic Odderon with $m_k^2 = k^2$ and $m_k^2 = (k+4)^2$ obtained from type IIB supergravity. For $k = 0$, the intercept in (13.41) is either greater than 1, and hence outside the contour of Fig. 13.3, or subleading. The solution with $k = 1$ has an intercept precisely at 1 and is thus the leading branch cut that will be picked up when evaluating (13.16) via saddle-point approximation. Note that the top-down construction of Ref. [218] found a similar intercept, though their solution only captures the forward behavior. Carrying out the integration of (13.16) along the contour in Fig. 13.3 in the saddle-point approximation and by using (13.38) and (13.41), the Odderon bulk-to-bulk propagator is given by

$$G_1(s,t,z,z') = -\frac{3}{5} f^-(\lambda) \sqrt{\frac{3\mathcal{D}}{5\pi\tau} \frac{(zz')}{2}}\, e^{-\frac{a}{2}(j_{\mathbb{O}}(t)-1)\kappa^2(z^2+z'^2)} (3a\kappa^2 zz'/2) e^{(j_{\mathbb{O}}(t)-1)\tau}, \tag{13.42}$$

with the odd signature factor

$$f^-(\lambda) = i + \frac{4\sqrt{\lambda}}{(m_k^2 - 1)\pi} - \frac{(m_k^2 - 1)\pi}{12\sqrt{\lambda}}. \tag{13.43}$$

Note that there is a pole at $k = 1$, which is apparent from the form of (13.16). This pole is in the literature referred to as maximal Odderon and may be regulated by constructing an amplitude whose numerator has a 0 at $j = 1$. Unfortunately, in our case it is not regulated. A different geometry might be able to cure the problem and allow for a study of the maximal holographic Odderon. Interestingly enough, the $k = 2$ branch of (13.37) and (13.43) coincide for large λ.

13.2.4 Conformal Limit

The conformal limit of (13.18) is obtained by taking $\kappa \to 0$

$$-\frac{\mathrm{d}^2}{\mathrm{d}z^2} G_0 + \left(\frac{S_j + \frac{15}{4}}{z^2} - t \right) G_0(z) = \delta(z - z') \tag{13.44}$$

where we rescaled the bulk-to-bulk propagator as

$$G_0(j,t,z,z') \to (zz')^{3/2} G_0(j,t,z,z'). \tag{13.45}$$

The two independent homogeneous solutions to (13.44) are given by the regular and singular Bessel functions J and Y, respectively. Explicitly we have

$$\begin{aligned} G_1(z) &= \sqrt{z}\, J_{-\sqrt{S_j+4}}(\sqrt{t}z) \\ G_2(z) &= \sqrt{z}\, Y_{-\sqrt{S_j+4}}(\sqrt{t}z), \end{aligned} \tag{13.46}$$

and hence

$$\begin{aligned} G_0(j,t,z,z') &= \mathcal{A}(zz')^2 J_{-\nu}(\sqrt{t}z_<), Y_{-\nu}(\sqrt{t}z_>) \\ \nu &= \Delta_g(j) - 2, \end{aligned} \tag{13.47}$$

with the normalization fixed by the Wronskian

$$\mathcal{A}^{-1} = \mathcal{W}(G_1(z), G_2(z)) = \frac{2}{\pi}. \tag{13.48}$$

Reverting the rescaling, we obtain the scalar AdS bulk-to-bulk propagator

$$G_0(j,t,z,z') = \frac{\pi}{2}(zz')^{j_\pm}\, J_{2-\Delta_g(j)}(\sqrt{t}z_<)\, Y_{2-\Delta_g(j)}(\sqrt{t}z_>). \tag{13.49}$$

In the Regge limit $x = \sqrt{t}\, z \ll 1$ the Bessel functions simplify

$$\begin{aligned} J_{-\nu}(x) &\approx \frac{1}{\Gamma(1-\nu)}\left(\frac{x}{2}\right)^{-\nu}, \\ Y_{-\nu}(x) &\approx -\frac{1}{\pi}\cos(\nu\pi)\,\Gamma(\nu)\left(\frac{x}{2}\right)^{-\nu}. \end{aligned} \tag{13.50}$$

The Sommerfeld-Watson transform (13.16) thus reduces to

$$\begin{aligned} G_{j_\pm}(s,t,z,z') = -\int \frac{\mathrm{d}j}{4\pi i}\, &\frac{1+e^{-i\pi(j-j_\pm)}}{\sin\pi(j-j_\pm)}\,\frac{\cos\pi(\Delta_g(j)-2)}{\Gamma(3-\Delta_g(j))}\Gamma(2-\Delta_g(j)) \\ \times &\left(\frac{tzz'}{4}\right)^{2-\Delta_g(j)} (\alpha' szz')^{j-j_\pm} \end{aligned} \tag{13.51}$$

We proceed to evaluate (13.51) in the saddle point approximation. The branch cut of $\Gamma(2-\Delta_g(j)) = \Gamma(iy) \approx e^{-i\gamma_E y}/iy$ at $\Delta_g(j) - 2 = -iy =$ is chosen to the left of the integration contour, along the negative real axis. In the Regge limit, the integral is dominated by the saddle point located at

$$\Delta_g(j) - 2 = \left(\frac{\ln(zz'|t|)}{2\mathcal{D}\chi}\right)^2 \to 0, \tag{13.52}$$

which we can use to approximate

$$G_{j_\pm}(j,t,z,z') = f^{\pm}(\lambda)\sqrt{\frac{\mathcal{D}}{4\pi\chi}}\frac{(zz')^{j_\pm}}{2}(\alpha' szz')^{j_{\mathbb{P}/\mathbb{O}}-j_\pm}e^{-\frac{\ln(zz'|t|)^2}{4\mathcal{D}\chi}} \tag{13.53}$$

for fixed but large rapidity χ, and with $j_{\mathbb{P}/\mathbb{O}}$ given by (13.8-13.14). The signature factors are now given by

$$f^{+}(\lambda) = i + \frac{\sqrt{\lambda}}{\pi} - \frac{\pi}{3\sqrt{\lambda}} \tag{13.54}$$

and

$$f^{-}(\lambda) = i + \frac{4\sqrt{\lambda}}{\pi m_k^2} - \frac{m_k^2\pi}{12\sqrt{\lambda}}\,. \tag{13.55}$$

Once more, the signature factor for the $k=2$ branch coincides with that of the Pomeron. As with the repulsive-wall scenario, the presence of the pole prevents fixing the intercept at 1 with $m_k^2 = 0$. In the AdS limit, diffusion becomes logarithmic in z, where the latter may be identified with the size of the transverse dipoles or strings composing the exchanged Pomeron/Odderon.

Forward Region

Restricting to the forward region, the solution to (13.44) is given by a superposition of conformal plane waves

$$G_0(j,0,z,z') = \int \frac{d\nu}{2\pi}\frac{e^{i\nu(\rho-\rho')}}{4\nu^2+4+m_\pm^2} \tag{13.56}$$

with $z = e^{-\frac{\rho}{2}}$ and $m_+^2 = m_j^2R^2$, $m_-^2 = m_k^2R^2 + m_j^2R^2$. Inserting (13.56) into (13.16) yields

$$G_{j_\pm}(s,0,z,z') = \sqrt{\frac{\mathcal{D}}{4\pi\chi}}(zz')^{j_\pm}(\alpha' szz')^{j_{\mathbb{O}/\mathbb{P}}-j_\pm}\ e^{-\frac{(\rho-\rho')^2}{4\mathcal{D}\chi}}, \tag{13.57}$$

with the shifted Pomeron $j_{\mathbb{P}}$ and Odderon $j_{\mathbb{O}}$ intercepts. The shift of the intercept is seen to follow from the diffusion in rapidity in AdS space

$$\tau = \ln(\alpha' szz') \sim \chi = \ln(\alpha' s) \tag{13.58}$$

with diffusion constant

$$\mathcal{D} = \frac{1}{2\sqrt{\lambda}}, \tag{13.59}$$

in agreement with the original analysis in [191, 196].

Finite Impact Parameter

The bulk-to-bulk propagator for forward scattering may alternatively be derived from its representation in impact parameter space. To demonstrate this, consider the Fourier inverse of (13.44)

$$\left(-\frac{1}{\sqrt{-g}}\partial_z\, g^{zz}\sqrt{-g}\,\partial_z - z^2\partial_\perp^2 + S_j\right)\tilde{G}_0(j,b,z,b',z') = \frac{\delta(z-z')}{\sqrt{-g}}\delta^2(b_\perp - b'_\perp) \quad (13.60)$$

For the sake of simplicity, our discussion will focus on the Odderon propagator; the Pomeron propagator can be derived in a similar manner. The solution to (13.60) is given by

$$\tilde{G}_0(j,b,z,b',z') = \frac{1}{4\pi zz'}\,\frac{e^{-\sqrt{S_j}\xi}}{\sinh\xi} \quad (13.61)$$

with ξ fixed by the chordal distance in AdS

$$\cosh\xi = 1 + \frac{(z-z')^2 + (b-b')^2}{2zz'} \quad (13.62)$$

Recall that $S_j = 2\sqrt{\lambda}(j - j_{\mathbb{O}})$ develops a branch point at $j = j_{\mathbb{O}}$ as displayed in Fig. 13.3. The Sommerfeld-Watson transform (13.16) of the solution (13.61) is given by

$$G_1(s,t,z,z') = \int \mathrm{d}^2 b_\perp\, e^{iq\cdot b_\perp}\int\frac{\mathrm{d}j}{4\pi i}\left(\frac{s^{j-1}+(-s)^{j-1}}{\sin(\pi(j-1))}\right)(\alpha' zz')^{j-1}\,\tilde{G}_0(j,b_\perp,z,b'_\perp,z'), \quad (13.63)$$

and integrated along the contour in Fig. 13.3. In the forward limit, we may transform from $b_\perp$ to ξ using (13.62) and

$$\mathrm{d}^2 b_\perp = 2\pi zz' \sinh\xi\,\mathrm{d}\xi, \quad (13.64)$$

to obtain

$$G_1(s,0,z,z') = \int_{\xi_0}^{\infty} 2\pi zz'\mathrm{d}\xi\int_{\mathcal{C}_L}\frac{\mathrm{d}j}{4\pi i}\left(\frac{1-e^{-i\pi(j-1)}}{\sin(\pi(j-1))}\right)(\alpha' szz')^{j-1}\,\frac{e^{(2-\Delta_g(j))\xi}}{4\pi}, \quad (13.65)$$

with $\xi_0 = |\ln z/z'|$. In the double limit of large rapidities $\tau = \ln(\alpha' szz') \gg 1$, and strong coupling $\sqrt{\lambda} \gg 1$, the j-integration can be evaluated to leading order in $\sqrt{\lambda}/\tau \ll 1$ by following the original arguments presented in Ref. [197]. The resulting expression is

$$G_1(s,0,z,z') \approx \frac{zz'}{4}\,(\alpha' szz')^{j_{\mathbb{O}}-1} f^{-}(\lambda)\left(\frac{\sqrt{\lambda}}{2\pi}\right)^{\frac{1}{2}}\int_{\xi_0}^{\infty} d\xi\,\xi\,\frac{e^{-\frac{\xi^2}{4D\tau}}}{\tau^{\frac{3}{2}}}. \quad (13.66)$$

The remaining Gaussian integral is readily carried out with the result

$$G_1(s,0,z,z') \approx f^-(\lambda)\ (\alpha' s z z')^{j_{\mathbb{O}}-1}\ \frac{zz'}{2}\sqrt{\frac{\mathcal{D}}{4\pi\tau}}\, e^{-\frac{\xi_0^2}{4D\tau}}\,. \tag{13.67}$$

Following the analogous steps for the Pomeron, we obtain

$$G_2(s,0,z,z') \approx f^+(\lambda)\,(\alpha' s z z')^{j_{\mathbb{P}}-2}\,\frac{(zz')^2}{2}\sqrt{\frac{\mathcal{D}}{4\pi\tau}}\, e^{-\frac{\xi_0^2}{4D\tau}} \tag{13.68}$$

in agreement with (13.57).

13.3 Bulk Dirac Fields

We identify the proton and its antiparticle with bulk Dirac fermions. The nucleon is described by the chiral spinor pair $\Psi_{1,2}$, where the index $1,2$ refers to the boundary chirality $1,2=\pm=R,L$. The bulk fields source the QCD boundary operators $\mathcal{O}_\pm$ with anomalous dimension $\pm M=\pm(\Delta-2)=\pm(\tau-3/2)$ and where τ is the twist. The bulk fermion action is given by

$$S_F=\frac{1}{g_5^2}\int \mathrm{d}^5x\sqrt{g}\left(\frac{i}{2}\overline{\Psi}_{1,2}e^M_{\hat{M}}\Gamma^{\hat{M}}\overleftrightarrow{D}_M\Psi_{1,2}-(\pm M)\,\overline{\Psi}_{1,2}\Psi_{1,2}\right), \tag{13.69}$$

with $\frac{1}{2}\ln g(z)=2A(z)=2\ln\frac{R}{z}+a\kappa^2z^2$ and covariant derivative

$$D_M=\partial_M+\frac{1}{8}\omega_M^{AB}\left[\Gamma_A,\Gamma_A\right]. \tag{13.70}$$

Index contractions involving the (flat) gamma matrix algebra

$$\Gamma^{\hat{M}}=(\gamma^\mu,-i\gamma^5),\ \left\{\Gamma^{\hat{M}},\Gamma^{\hat{N}}\right\}=2\eta^{\hat{M}\hat{N}} \tag{13.71}$$

are performed by using the tetrads

$$e^M_{\hat{M}}=e^{-A(z)}\delta^M_{\hat{M}}. \tag{13.72}$$

Using the above relations, (13.69) reduces to

$$S_F=\frac{1}{g_5^2}\int \mathrm{d}^4x\mathrm{d}z e^{4A(z)}\left\{-\frac{i}{2}\overline{\Psi}_{1,2}\left[\not{\partial}-2i\gamma_5A'(z)-i\gamma_5\partial_z\right]\Psi_{1,2}+e^{A(z)}M\overline{\Psi}_{1,2}\Psi_{1,2}\right\}. \tag{13.73}$$

We eliminate the metric factors in the kinetic term by redefining the field

$$\Psi \to g_5 e^{-2A(z)} \Psi \tag{13.74}$$

and arrive at

$$S_F = \int \mathrm{d}^4x \mathrm{d}z \left\{ -\frac{i}{2} \overline{\Psi}_{1,2} \left[\not{\partial} - i\gamma_5 \partial_z \right] \Psi_{1,2} + e^{A(z)} M \overline{\Psi}_{1,2} \Psi_{1,2} + h.c. \right\}. \tag{13.75}$$

The equations of motion following from (13.75) are given by

$$\left[-i\not{\partial} - \gamma_5 \partial_z + M e^{A(z)} \right] \Psi = 0. \tag{13.76}$$

By performing a chiral Kaluza-Klein decomposition

$$\begin{aligned} \Psi_1(p, z; n) &= \psi_R(z; n) \Psi_R^0(p) + \psi_L(z; n) \Psi_L^0(p) \\ \Psi_2(p, z; n) &= \psi_R(z; n) \Psi_L^0(p) + \psi_L(z; n) \Psi_R^0(p), \end{aligned} \tag{13.77}$$

with

$$\Psi_{L/R}^0 = \sum_n e^{ik_n x} \frac{1 \mp \gamma_5}{2} u_s(k) f_{L/R}(z), \tag{13.78}$$

their respective chiral projections, they reduce to a coupled differential equation for the mode functions

$$\left(\partial_z \pm M e^{A(z)} \right) f_{L/R} = \pm m_n f_{R/L} \tag{13.79}$$

which is decoupled by iteration

$$\left(\partial_z^2 \pm M A'(z) e^{A(z)} - M^2 e^{2A(z)} \right) f_{L/R}(z) = m_n^2 f_{L/R}(z). \tag{13.80}$$

As in Section 13.2, we linearize the dilaton $e^{2A(z)} \approx \left(\frac{R}{z}\right)^2 \left(1 + a\kappa_N^2 z^2\right)$, in (13.80) to get

$$\left(-\partial_z^2 + \frac{M(M \pm 1)}{z^2} + a^2 \kappa_N^4 z^2 - \tilde{m}_n^2 \right) f_{L/R}(z) = 0, \tag{13.81}$$

where $\tilde{m}_n^2 = m_n^2 + M(M \pm 1) a \kappa_N^2$. Note that we did not expand $e^{A(z)}$ since this would result in a chirally antisymmetric mass spectrum. Further, we introduced a new mass scale κ_N to account for the different Regge trajectories of the baryon and the glueball spectrum. Transforming coordinates

$$u = a\kappa_N^2 z^2, \tag{13.82}$$

and performing one final field redefinition

$$f_{L/R}(u) = e^{-\frac{u}{2}} u^{\frac{1+\sqrt{1+4M(M\pm1)}}{4}} f_{L/R}(u), \tag{13.83}$$

we obtain the Sturm-Liouville normal form for the associated Laguerre polynomials $L_n^\alpha(u)$

$$uf''_{L/R}(u) + (\alpha + 1 - u)f'_{L/R}(u) + nf_{L/R}(u) = 0, \tag{13.84}$$

where

$$\begin{aligned} \alpha &= \frac{1}{2}\sqrt{1 + 4M(M \pm 1)} \\ n &= \frac{\tilde{m}_n^2}{4a\kappa_N^2} - \frac{2 + \sqrt{1 + 4M(M \pm 1)}}{4}. \end{aligned} \tag{13.85}$$

The mass eigenvalues are thus given by

$$m_n^2 = 4a\kappa_N^2 \left(n + \frac{1}{2} - \frac{M(M \pm 1/2) + \sqrt{1 + 4M(M \pm 1)}}{4}\right). \tag{13.86}$$

Choosing the positive parity solution with $M = \Delta - \frac{d}{2}$, $\tau = 3$ and $\Delta = \tau + \frac{1}{2}$, we obtain

$$m_n^2 = 4a\kappa_N^2 \left(n + \frac{3}{4}\right), \qquad \alpha = \frac{2 \pm 1}{2}, \tag{13.87}$$

Reverting the rescalings and coordinate transformations, the holographic chiral baryon wave functions are given by

$$\begin{aligned} \psi_L(n, z) &= n_L a\kappa_N^2 z^4 e^{-\frac{3}{2}a\kappa_N^2 z^2} L_n^{3/2}(a\kappa_N^2 z^2) \\ \psi_R(n, z) &= n_R a\kappa_N^2 z^4 e^{-\frac{3}{2}a\kappa_N^2 z^2} L_n^{1/2}(a\kappa_N^2 z^2), \end{aligned} \tag{13.88}$$

with the normalization fixed by

$$\int \mathrm{d}z n_{L/R} n_{L/R}{}^* f_{L/R}^n(z) f_{L/R}^m(z) = \delta_{mn}, \tag{13.89}$$

and thus

$$n_L = \sqrt{\frac{2\sqrt{a\kappa} n!}{\Gamma(n + 5/2)}}, \qquad n_R = n_L^n \sqrt{n + 3/2}. \tag{13.90}$$

Positivity of the squared mass eigenvalues restricts the background to the repulsive-wall with $a > 0$. The squared mass eigenvalues display the anticipated Regge behavior, scaling linearly with the mode number. The non-normalizable solutions of (13.81) are given in terms of Kummer functions

$$\begin{aligned} \tilde{\psi}_R(n, z) &= N_R\, U\Big(-n, 3/2, a\kappa_N^2 z^2\Big), \\ \tilde{\psi}_L(n, z) &= N_L\, U\Big(-n, 1/2, a\kappa_N^2 z^2\Big), \end{aligned} \tag{13.91}$$

which can be recast as a sum over Regge poles

$$\begin{aligned}\tilde{\psi}_R(p,z) &= \sum_{n=0}^{\infty} \frac{f_n p \tilde{\psi}_R(n,z)}{p^2-m^2} \\ \tilde{\psi}_L(p,z) &= \sum_{n=0}^{\infty} \frac{f_n m_n \tilde{\psi}_R(n,z)}{p^2-m^2},\end{aligned} \tag{13.92}$$

with $f_n = \kappa_N / n_R$. Performing the Lehmann–Symanzik–Zimmermann (LSZ) reduction of the amplitude will project out the pertinent external states, thus effectively reducing the bulk-to-boundary propagator to

$$\tilde{\psi}_{L/R}(p,z) = f_0\, m_p \psi_{L/R}(0,z) \tag{13.93}$$

13.4 Diffractive pp and $p\bar{p}$ Scattering

Fig. 13.2 illustrates the Feynman graphs for elastic pp and $p\bar{p}$ scattering. In the Regge limit, they involve an exchange of a Pomeron $\mathbb{P}$ and Odderon $\mathbb{O}$. In the framework of dual gravity, these Feynman graphs are replaced by the Witten diagrams depicted in Fig. 13.4, where the Pomeron and Odderon propagators are replaced by the bulk-to-bulk propagators $G_2(s,t,z,z')$ and $G_1(s,t,z,z')$, respectively. Building on our previous analysis in Section 13.2, the Pomeron is associated with a summation of massive even-spin glueballs, while the Odderon corresponds to a sum of massive odd-spin glueballs. The solid lines denote the bulk-to-boundary Dirac fermion propagator originating from the chiral Kaluza-Klein modes of the bulk Dirac fermions discussed earlier in Section 13.3.

The even and odd spin-j contributions to Fig. 13.2 are

$$\begin{aligned}\mathcal{A}_{pp\to pp}(s,t) &= \sum_{j=2,4,..} \mathcal{A}_{\mathbb{P}}(j,s,t) + \sum_{j=1,3,..} \mathcal{A}_{\mathbb{O}}(j,s,t), \\ \mathcal{A}_{p\bar{p}\to p\bar{p}}(s,t) &= \sum_{j=2,4,..} \mathcal{A}_{\mathbb{P}}(j,s,t) - \sum_{j=1,3,..} \mathcal{A}_{\mathbb{O}}(j,s,t),\end{aligned} \tag{13.94}$$

which we will now set up.

13.4.1 Even Spin-j

The even spin-j contribution to diffractive pp scattering in Fig. 13.4a may be factorized into

$$i\mathcal{A}_{\mathbb{P}}(j,s,t) = (-i)\mathcal{V}^{\mu\nu}_{j\Psi\Psi}(q_1,q_2,k,m_n)\tilde{G}_{\mu\nu,\alpha\beta}(k)(-i)\mathcal{V}^{\alpha\beta}_{j\Psi\Psi}(p_1,p_2,k,m_n). \tag{13.95}$$

with the bulk Pomeron-nucleon vertex for the repulsive-wall given by

$$\mathcal{V}^{\alpha\beta}_{\mathbb{P}\Psi\Psi}(p_1, p_2, k, m_n) = -\frac{1}{2}\sqrt{2\kappa^2}\int \mathrm{d}z\sqrt{g}e^{-3A(z)}\,\overline{\Psi}(p_2, z)\gamma^\alpha p^\beta \Psi(p_1, z)\,J_h(m_n, z)). \tag{13.96}$$

The coupling is dictated by the holographic principle, where the graviton couples to the QCD energy momentum tensor. The functions $J_h(m_n, z)$ follow from a decomposition of the Pomeron bulk-to-bulk propagator $G_2(s, t, z, z')$ into pieces depending on z using

$$J_h(m_n, z) \equiv \sqrt{\frac{3}{4}}a\kappa z^3 e^{-(j_{\mathbb{P}}(t)-2)a\kappa^2 z^2/2}, \tag{13.97}$$

and a Pomeron propagator

$$\tilde{G}_{\mu\nu,\alpha\beta}(m_n k) = -\frac{3}{5}f^+(\lambda)\sqrt{\frac{3\mathcal{D}}{5\pi\tau}}e^{(j_{\mathbb{P}}(t)-2)\tau}(-i)\,P_{\mu\nu,\alpha\beta}(k), \tag{13.98}$$

where the relevant flat 4-dimensional spin-2 propagator is

$$P_{\mu\nu,\alpha\beta}(k) = \frac{1}{2}\left(P_{\mu\alpha}P_{\nu\beta} + P_{\mu\beta}P_{\nu\alpha} - \frac{2}{3}P_{\mu\nu}P_{\alpha\beta}\right)(k), \quad P_{\mu\nu}(k) = -\eta_{\mu\nu} + \frac{k_\mu k_\nu}{k^2}. \tag{13.99}$$

The 5-dimensional Pomeron exchange is given by

$$\begin{aligned} G_{\mu\nu,\alpha\beta}(m_n, k, z, z') &= G_2(s, t, z, z')P_{\mu\nu,\alpha\beta}(k) \\ &= J_h(m_n, z)\tilde{G}_{\mu\nu,\alpha\beta}(m_n(j), k)J_h(m_n, z'). \end{aligned} \tag{13.100}$$

In the Regge limit, we may utilize the high-energy relation for spinor products

$$\overline{u}(p_2)\gamma^\mu u(p_1) = (p_1 + p_2)^\mu \delta_{s_1 s_2} \tag{13.101}$$

and after reducing the chiral bulk spinors to 4D, the amplitude reduces to

$$\begin{aligned} \mathcal{A}_{\mathbb{P}}(s, t) &= \frac{3}{5}f^+(\lambda)\sqrt{\frac{3\mathcal{D}}{5\pi\tau}}\frac{\kappa^2}{2}g^2_{\mathbb{P}\overline{\Psi}\Psi}4s^2\left(1 + \frac{t - 4m_p^2}{s}\right)e^{(j_{\mathbb{P}}(t)-2)\tau}\delta_{s_1 s_2}\delta_{s_1' s_2'} \\ &\equiv \mathcal{N}f^+(\lambda)e^{(j_{\mathbb{P}}(t)-2)\tau}\mathcal{V}_{\mathbb{P}}(s, t), \end{aligned} \tag{13.102}$$

where

$$g_{\mathbb{P}\overline{\Psi}\Psi} = \frac{729 f_0 m_p \kappa_N^4 \kappa(n_L^2 + n_R^2)}{4(3\kappa_N^2 + 8(j_{\mathbb{P}}(0) - 2)\kappa^2)^5}, \qquad \mathcal{N} = \frac{3}{5}\sqrt{\frac{3\mathcal{D}}{5\pi\tau}}\frac{\kappa^2}{2}. \tag{13.103}$$

Note that we used $a = 4$ for the closed string exchange and $a = 1$ for the baryon, which originates from the open string sector.

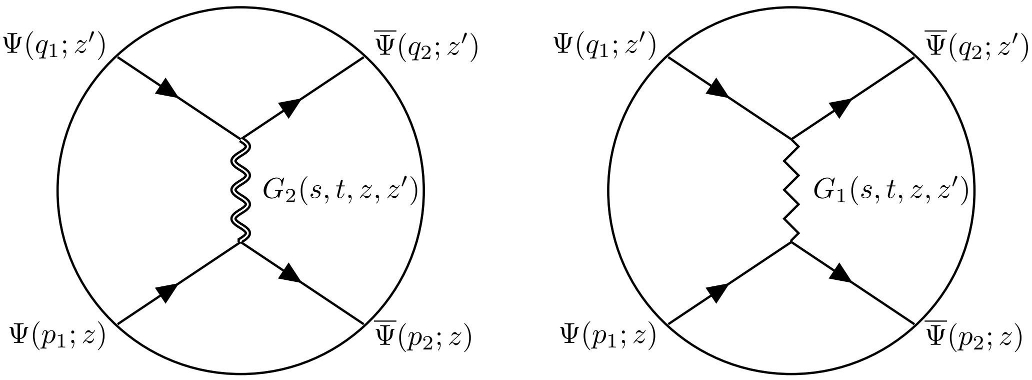

(a) (b)

Fig. 13.4.: Witten diagrams for diffractive pp elastic scattering through (a) Pomeron and (b) Odderon exchange

13.4.2 Odd Spin-j

For the odd spin-j contributions, we proceed similarly. We decompose the Odderon bulk-to-bulk propagator into functions depending on z and a Regge propagator with pertinent 4-dimensional Lorentz structure. The amplitude for diffractive pp scattering is thus given by

$$i\mathcal{A}_{\mathbb{O}}(s,t) = \sum_{m\leq n} (-i)\mathcal{V}^{(n)\mu}_{j\Psi\Psi}(q_1,q_2,k,m_n)\tilde{H}_{\mu\nu}(m_n,k)(-i)\mathcal{V}^{(m)\nu}_{j\Psi\Psi}(p_1,p_2,k,m_n) \tag{13.104}$$

where

$$\begin{aligned}\mathcal{V}^{(1)\beta}_{\mathbb{O}\Psi\Psi}(p_1,p_2,k,m_n) &= +\sqrt{2\kappa^2}\frac{1}{2}\int \mathrm{d}z\sqrt{g}\,e^{-2A(z)}\,\overline{\Psi}(p_2,z)\sigma^{\alpha\beta}\gamma^5\Psi(p_1,z)k_\alpha\,J_h(m_n,z))\\ \mathcal{V}^{(2)\beta}_{\mathbb{O}\Psi\Psi}(p_1,p_2,k,m_n) &= -\sqrt{2\kappa^2}\frac{1}{2}\int \mathrm{d}z\sqrt{g}\,e^{-2A(z)}\,\overline{\Psi}(p_2,z)\gamma^\beta\gamma^5\Psi(p_1,z)\,J_h(m_n,z)),\end{aligned} \tag{13.105}$$

with

$$J_h(m_n,z) = \sqrt{\frac{3}{4}a\kappa z^2}e^{-(j_{\mathbb{O}}(t)-1)a\kappa^2 z^2/2}, \tag{13.106}$$

are now the bulk Odderon-nucleon vertices. They follow from an assumed minimal coupling of the boundary sources B_{MN} and C_{MN} in (12.1) to the chiral Dirac fermion current

$$\overline{\Psi}\sigma^{AB}\Psi, \qquad \sigma^{AB} = \frac{i}{2}\left[\Gamma^A,\Gamma^B\right]. \tag{13.107}$$

The reduced Odderon exchange is given by

$$H_{\mu\nu}(m_n,k,z,z') = J_h(m_n,z)\tilde{H}_{\mu\nu}(k,z,z')J_h(m_n,z'), \tag{13.108}$$

where

$$\tilde{H}_{\mu\nu}(k,z,z') = -\frac{3}{5}f^{-}(\lambda)\sqrt{\frac{3\mathcal{D}}{5\pi\tau}}e^{(j_{\mathbb{O}}(t)-1)\tau}(-i)\,P_{\mu\nu}(k). \tag{13.109}$$

As was the case for the spin-1 glueballs in Part II, the equations of motion of the Kalb-Ramond B_2 and Ramond-Ramond fields $C_2,\ C_3$ are tied through a topological mass term that originates from a Chern-Simons type interaction (c.f. (7.4) for type IIA supergravity). In particular, the fluctuations $C_{\mu\nu}$ and $B_{\mu z}$ form the 1^{--} vector glueball, which transmutes into the Odderon upon Reggeization. To project onto the physical degrees of freedom for a vector exchange, we utilize $C_{\mu\nu} \sim \epsilon_{\mu\nu\rho\sigma}F^{\rho\sigma}$, up to factors depending on the particular string theoretic origin of this coupling. In the forward limit, only the 5-dimensional axial Dirac coupling will survive and thus encodes contributions to the total cross sections, as well as their difference $\Delta\sigma_{tot} = \sigma_{tot}^{pp} - \sigma_{tot}^{p\overline{p}}$. Recall that in pQCD, the BKP Odderon is a Reggeized 1^{--} exchange arising from the resummation of the soft, collinear, and rapidity ordered gluon emissions. As such, it corresponds to the $(\frac{1}{2},\frac{1}{2})$ representation of the complexified Lorentz group $SO(3,1)$. This coupling of the Kalb-Ramond and Ramond-Ramond fields is absent in type II supergravity actions[3], which makes a direct comparison between pQCD and top-down holography difficult. Of course, if the assumed holographic principle holds, there should be a clear relation between them. Ref. [218] first encountered this problem and obtained a baryon coupling on the light-cone through the polarization B_{+z} on $\mathrm{AdS}_5 \times S_5$, which furnishes a $(0,1)$ representation of the complex $SO(3,1)$. One way to determine a vector-like coupling in top-down holographic QCD would be to use the WSS model of Part I where baryons are represented by instanton configurations of the flavor gauge fields [222], which naturally couple to the vector glueball through the CS term.

We again reduce the chiral bulk Dirac spinors to 4D and utilize the LSZ formula to obtain

$$\begin{aligned}
g^{(1)}_{\mathbb{O}\overline{\Psi}\Psi} &= \int \mathrm{d}z\sqrt{g}\,e^{-2A(z)}\,\left(\psi_L(z)^2+\psi_R(z)^2\right)\,J_h(m_n,z) = \frac{7776 f_0 m_p \kappa_N^4 \kappa (n_L^2+n_R^2)}{(9\kappa_N^2+32(j_{\mathbb{O}}(0)-1)\kappa^2)^4}\\
g^{(2)}_{\mathbb{O}\overline{\Psi}\Psi} &= \int \mathrm{d}z\sqrt{g}\,e^{-2A(z)}\,2\psi_L(z)\psi_R(z)\,J_h(m_n,z) = \frac{15552 f_0 m_p \sqrt{3\pi}\kappa\kappa_N^4 n_L n_R}{(9\kappa_N^2+32(j_{\mathbb{O}}(0)-1)\kappa^2)^4}
\end{aligned} \tag{13.110}$$

---

[3] See for example Ref. [220] or the Appendix of Ref. [221]

Die approbierte gedruckte Originalversion dieser Dissertation ist an der TU Wien Bibliothek verfügbar.
The approved original version of this doctoral thesis is available in print at TU Wien Bibliothek.
TU Bibliothek Your knowledge hub WIEN

In the Regge limit, the amplitude is given by

$$\begin{aligned}\mathcal{A}_{\mathbb{O}}(s,t) =&\frac{3}{5}f^{-}(\lambda)\sqrt{\frac{3\mathcal{D}}{5\pi\tau}}e^{(j_{\mathbb{O}}(t)-1)\tau}\frac{\kappa^2}{2}\\ &\times\Bigg[g^{(1)2}_{\mathbb{O}\overline{\Psi}\Psi}4k_\mu k_\alpha\overline{u}(p_2)\sigma^{\mu\nu}u(p_1)P_{\nu\beta}(k)\overline{u}(q_2)\sigma^{\alpha\beta}u(q_1)\\ &\quad+g^{(2)2}_{\mathbb{O}\overline{\Psi}\Psi}(p_1+p_2)^\mu P_{\mu\nu}(k)(q_1+q_2)^\nu\delta_{s_1s_2}\delta_{s_1's_2'}\\ &\quad+ig^{(1)}_{\mathbb{O}\overline{\Psi}\Psi}g^{(2)}_{\mathbb{O}\overline{\Psi}\Psi}\Big(k_\alpha\overline{u}(q_2)\sigma^{\alpha\beta}u(q_1)P_{\beta\nu}(p_1+p_2)^\nu\delta_{s_1s_2}\\ &\quad+k_\mu\overline{u}(p_2)\sigma^{\mu\nu}u(p_1)P_{\nu\beta}(k)(q_1+q_2)^\beta\delta_{s_1's_2'}\Big)\Bigg]\\ \equiv&\mathcal{N}f^{-}(\lambda)e^{(j_{\mathbb{O}}(t)-1)\tau}\mathcal{V}_{\mathbb{O}}(s,t),\end{aligned}\tag{13.111}$$

where we once more used $\overline{u}(p_2)\gamma^\mu u(p_1)=(p_1+p_2)^\mu\delta_{s_1s_2}$ for $s\to\infty$. In particular, the forward limit of the amplitude is given by

$$\mathcal{A}_{\mathbb{O}}(s,0)=\mathcal{N}f^{-}(\lambda)\left(g^{(2)}_{\mathbb{O}\overline{\Psi}\Psi}\right)^2e^{(j_{\mathbb{O}}(t)-1)\tau}2s\left(1-\frac{4m_p^2}{2s}\right).\tag{13.112}$$

13.4.3 Total Cross Sections

Recall that, after evaluating the Sommerfeld-Watson transform via saddle point approximation, the signature factors are given by

$$f^{+}(\lambda)=i+\frac{4\sqrt{\lambda}}{3\pi}-\frac{\pi}{4\sqrt{\lambda}},\qquad f^{-}(\lambda)=i+\frac{4\sqrt{\lambda}}{(m_k^2-1)\pi}-\frac{(m_k^2-1)\pi}{12\sqrt{\lambda}}.\tag{13.113}$$

For the following analytical computations, we will work strictly in the limit of large ’t Hooft coupling λ and drop everything subleading. We will, however, keep the subleading piece in the numerical analysis. By utilizing the optical theorem, we obtain the total cross sections for pp and $p\overline{p}$ scattering

$$\sigma_{\pm}(s)=\frac{1}{s}\mathrm{Im}(\mathcal{A}_{\mathbb{P}}(s,0)\pm\mathcal{A}_{\mathbb{O}}(s,0)).\tag{13.114}$$

Explicitly, using (13.102) and (13.112) for large s and at $t = 0$, we obtain

$$\begin{aligned}\sigma_{\pm}(s) &= \frac{6}{5}\sqrt{\frac{2\mathcal{D}}{5\pi\tau}}\,\frac{\kappa^2}{2}\left(2g^2_{\mathbb{P}\overline{\Psi}\Psi}\, e^{(j_{\mathbb{P}}(0)-1)\tau}\left(1-\frac{4m_p^2}{s}\right) \pm g^{(1)2}_{\mathbb{O}\overline{\Psi}\Psi}\, e^{(j_{\mathbb{O}}(0)-1)\tau}\left(1-\frac{4m_p^2}{2s}\right)\right)\\ &= 2\mathcal{N}e^{(j_{\mathbb{P}}(0)-1)\tau}\left(g^2_{\mathbb{P}\overline{\Psi}\Psi}\left(1-\frac{4m_p^2}{s}\right) \pm g^{(1)2}_{\mathbb{O}\overline{\Psi}\Psi}\, e^{(j_{\mathbb{O}}(0)-j_{\mathbb{P}}(0))\tau}\left(1-\frac{4m_p^2}{2s}\right)\right).\end{aligned} \tag{13.115}$$

The rho-parameters are given by

$$\begin{aligned}\rho_{\pm}(s) &= \frac{\mathrm{Re}\mathcal{A}_{\pm}(s,0)}{\mathrm{Im}\mathcal{A}_{\pm}(s,0)}\\ &= \frac{\frac{4\sqrt{\lambda}}{3\pi}(1-\frac{4m_p^2}{s})g^2_{\mathbb{P}\overline{\Psi}\Psi}\, e^{(j_{\mathbb{P}}(0)-1)\tau} \pm \frac{4\sqrt{\lambda}}{(m_k^2-1)\pi}(1-\frac{4m_p^2}{2s})g^2_{\mathbb{O}\overline{\Psi}\Psi}\, e^{(j_{\mathbb{O}}(0)-1)\tau}}{(1-\frac{4m_p^2}{s})g^2_{\mathbb{P}\overline{\Psi}\Psi}\, e^{(j_{\mathbb{P}}(0)-1)\tau} \pm (1-\frac{4m_p^2}{2s})g^2_{\mathbb{O}\overline{\Psi}\Psi}\, e^{(j_{\mathbb{O}}(0)-1)\tau}},\end{aligned} \tag{13.116}$$

which approaches the constant

$$\frac{4\sqrt{\lambda}}{3\pi} \tag{13.117}$$

in the large rapidity limit. This constant is incompatible with data from high-energy scattering [9] , which instead suggests $\rho(s) \sim 0.1$ for $\sqrt{s} \geq 100$ GeV [223] (and references therein). In Section 13.5 we will show that, by resumming multi Reggeon exchange in the eikonal limit, the strong shadowing brought about by the Reggeons decreases the rho parameter to 0, in accordance with expectations from experiment.

13.4.4 Elastic Differential Cross sections

Carrying out the spin and polarization sums, we obtain the squared amplitude for elastic scattering of pp and $p\overline{p}$ as

$$\begin{aligned}\left|\mathcal{A}_E^{\pm}(s,t)\right|^2 = \frac{s^2}{4g_5^2}\Bigg[& e^{2j_{\mathbb{P}}(t)\tau} g^4_{\mathbb{P}\overline{\Psi}\Psi}\left(1+\frac{2t-8m_p^2}{s}+\frac{21}{16}\left(\frac{t}{s}\right)^2-\frac{10m_p^2 t}{s^2}\right)\\ &+4e^{2j_{\mathbb{O}}(t)\tau}\frac{\left(g^{(2)}_{\mathbb{O}\overline{\Psi}\Psi}\right)^4}{s^2} \pm \frac{4}{s}(g_{\mathbb{P}\overline{\Psi}\Psi}g^{(2)}_{\mathbb{O}\overline{\Psi}\Psi})^2 e^{(j_{\mathbb{P}}(t)+j_{\mathbb{O}}(t))\tau} + 64e^{2j_{\mathbb{O}}(t)\tau}\left(g^{(1)}_{\mathbb{O}\overline{\Psi}\Psi}\right)^4\left(\frac{t}{s}\right)^2\Bigg].\end{aligned} \tag{13.118}$$

The interference between the Pomeron and Odderon exchange is highly suppressed in the strict Regge limit but is still parametrically more important than the Odderon exchange on its own. The elastic differential cross sections are given by

$$\frac{d\sigma_\pm}{dt} = \frac{1}{16\pi s^2}|\mathcal{A}_\pm(s,t)|^2. \tag{13.119}$$

This allows us to determine the elastic slope parameter at large rapidity

$$B_\pm(s,t=0) = \frac{d}{dt}\left(\ln\frac{d\sigma_\pm}{dt}(s,t)\right)_{t=0} \to 2\tau\left(\frac{d}{dt}j_{\mathbb{P}}(t)\right)_{t=0} = \alpha'\tau, \tag{13.120}$$

and matches the logarithmic value usually found in the literature [223]

$$B(s,t=0) = 1\,\mathrm{GeV}^{-2}\ln\left(\frac{s}{1\ \mathrm{GeV}^2}\right) \tag{13.121}$$

for both the Pomeron and the Odderon with $\alpha' = 1\,\mathrm{GeV}^{-2}$.

13.5 Eikonal Elastic Scattering

It is well known that single Pomeron exchange leads to a violation of the Froissart-Martin bound [224, 225]

$$\sigma_{tot} \lesssim \ln\left(\frac{s}{s_0}\right)^2, \tag{13.122}$$

and thus unitarity. A simple way to address this issue in the Regge limit is through the resummation of all t-channel exchanges, a process known as eikonalization [192]. Following Ref. [205], we rewrite the respective total cross sections for Pomeron and Odderon exchange as

$$\sigma_{\mathbb{R}}(s) = \frac{1}{s}\int \mathrm{d}^2b_\perp \mathrm{d}z\mathrm{d}z'\left(\sqrt{g(z)}\psi_{12}(j_{\mathbb{R}},z)\right)\left(\sqrt{g(z')}\psi_{34}(j_{\mathbb{R}},z')\right)2s\ \mathrm{Im}\,\chi(j_{\mathbb{R}},s,b_\perp,z,z'). \tag{13.123}$$

The vertex and metric factors $e^{-3A(z)}$ and $e^{-2A(z)}$, $e^{-A(z)}$ for the Pomeron and Odderon, respectively, are left implicit. The eikonal phase $\chi(j_{\mathbb{R}},s,b_\perp,z,z')$ for the Reggeon $\mathbb{R} = \mathbb{P},\mathbb{O}$, follows from the truncated Born amplitude

$$\chi(j_{\mathbb{R}},s,b_\perp,z,z') = s^{j_\pm-1}G(j_{\mathbb{R}},s,b_\perp,z,z') \tag{13.124}$$

Die approbierte gedruckte Originalversion dieser Dissertation ist an der TU Wien Bibliothek verfügbar.
The approved original version of this doctoral thesis is available in print at TU Wien Bibliothek.
TU Bibliothek Your knowledge hub WIEN

with $j_\pm = 2, 1$ for the Pomeron and Odderon, respectively. To ease up on notation, we introduce the shorthand $\chi_\mathbb{R} \equiv \chi(j_\mathbb{R}, s, b_\perp, z, z')$. After Fourier transforming to impact parameter space with coordinates $b_\perp$, we obtain from (13.36) and (13.42)

$$\begin{aligned} s^1\, G_2 &= \frac{3}{5} f^+(\lambda) \sqrt{\frac{3\mathcal{D}}{5\pi\tau}} \frac{(zz')^2}{2} e^{-\frac{a}{2}(j_\mathbb{P}(0)-2)\kappa^2(z^2+z'^2)} (3a\kappa^2 zz'/2) e^{(j_\mathbb{P}(0)-1)\tau}\, e^{-\frac{b_\perp^2}{2\alpha'\tilde{\tau}}} \frac{4\pi}{\alpha'\tilde{\tau}} \\ s^0\, G_1 &= \frac{3}{5} f^-(\lambda) \sqrt{\frac{3\mathcal{D}}{5\pi\tau}} \frac{(zz')}{2} e^{-\frac{a}{2}(j_\mathbb{O}(0)-1)\kappa^2(z^2+z'^2)} (3a\kappa^2 zz'/2) e^{(j_\mathbb{O}(0)-1)\tau}\, e^{-\frac{b_\perp^2}{2\alpha'\tilde{\tau}}} \frac{4\pi}{\alpha'\tilde{\tau}}, \end{aligned} \tag{13.125}$$

with

$$\tilde{\tau} = \tau\left(1 - \frac{1}{5\tau}\frac{z^2+z'^2}{R^2}\right), \tag{13.126}$$

and $G_2 = G(j_\mathbb{P}, s, b_\perp, z, z')$, $G_1 = G(j_\mathbb{O}, s, b_\perp, z, z')$. Notably, the exponent in (13.125) displays the celebrated Gribov diffusion in impact parameter. After carrying out the eikonalization, the *pp* and *p$\bar{p}$* scattering amplitudes are given by

$$\begin{aligned} \mathcal{A}_{pp}(s, b_\perp, z, z') &= -2is\left(e^{i(\chi_\mathbb{P}+\chi_\mathbb{O})} - 1\right) \\ \mathcal{A}_{p\bar{p}}(s, b_\perp, z, z') &= -2is\left(e^{i(\chi_\mathbb{P}-\chi_\mathbb{O})} - 1\right). \end{aligned} \tag{13.127}$$

The transformation back to momentum space yields the eikonalized amplitudes

$$\begin{aligned} \mathcal{A}_{pp}(s, t) &= -2is \int \mathrm{d}^2 b_\perp\, e^{-iq_\perp \cdot b_\perp} \left(e^{i(\chi_\mathbb{P}+\chi_\mathbb{O})} - 1\right) \\ \mathcal{A}_{p\bar{p}}(s, t) &= -2is \int \mathrm{d}^2 b_\perp\, e^{-iq_\perp \cdot b_\perp} \left(e^{i(\chi_\mathbb{P}-\chi_\mathbb{O})} - 1\right) \end{aligned} \tag{13.128}$$

To further ease up on notation, we introduce

$$\begin{aligned} \chi_\mathbb{R}(s, b_\perp, z, z') = a_\mathbb{R} e^{-\frac{b_\perp^2}{2\alpha'\tilde{\tau}}} & \\ a_\mathbb{P} &= \tilde{\mathcal{N}} f^+(\lambda) 3a\kappa^2 \frac{(zz')^3}{2} e^{-\frac{a}{2}(j_\mathbb{P}(0)-2)\kappa^2(z^2+z'^2)} e^{(j_\mathbb{P}(0)-1)\tau} s^{-j_+} \mathcal{V}_\mathbb{P}(s, t, z, z') \\ a_\mathbb{O} &= \tilde{\mathcal{N}} f^-(\lambda) 3a\kappa^2 \frac{(zz')^2}{2} e^{-\frac{a}{2}(j_\mathbb{O}(0)-1)\kappa^2(z^2+z'^2)} e^{(j_\mathbb{O}(0)-1)\tau} s^{-j_-} \mathcal{V}_\mathbb{O}(s, t, z, z') \\ \tilde{\mathcal{N}} &= \frac{6}{5\alpha'} \sqrt{\frac{3\pi\mathcal{D}}{5\tau^3}} \\ a_\pm &= a_\mathbb{P} \pm a_\mathbb{O} \end{aligned} \tag{13.129}$$

with $\mathbb{R} = \mathbb{P}, \mathbb{O}$ and $\mathcal{V}_{\mathbb{P}}(s,t,z,z'),\ \mathcal{V}_{\mathbb{O}}(s,t,z,z')$ given in (13.102) and (13.111), respectively. After carrying out the angular integration, we can proceed to integrate over b to get

$$\mathcal{A}_\pm(s,t,z,z') = -4is\pi \int bdbJ_0(qb) \sum_{n=1}^{\infty} \frac{(ia_\pm)^n}{n!} e^{-\frac{nb^2}{2\alpha'\tilde{\tau}}} = -4i\pi s\alpha'\tilde{\tau} \sum_{n=1}^{\infty} \frac{(ia_\pm)^n}{n\,n!}\, e^{-\frac{\alpha'}{2n}q^2\tilde{\tau}}. \tag{13.130}$$

However, for the numerical evaluation later on, it proved better to work with (13.128) instead and carry out the integration numerically, rather than the sum in (13.130).

13.5.1 Eikonalized Cross Sections

For forward scattering, the sum in (13.130) may be carried out analytically

$$\sum_n \frac{(ia_\pm)^n}{n \cdot n!} = -\left(\ln(-ia_\pm) + \gamma_E + \Gamma(0, -ia_\pm) \right), \tag{13.131}$$

where $\Gamma(a,b)$ is the incomplete Gamma function. Working at fixed z, z', we obtain the forward amplitude

$$\mathcal{A}_\pm(s,0,z,z') = 4i\pi\alpha' s\tilde{\tau} \left(\ln(-ia_\pm) + \gamma_E + \mathcal{O}(e^{ia_\pm}) \right), \tag{13.132}$$

with the incomplete Gamma function strongly suppressed at large rapidities. From (13.132) and (13.123) we readily obtain the eikonalized total cross sections

$$\sigma_\pm(s) = \left\langle \frac{1}{s}\ \mathrm{Im}\left(\mathcal{A}_{\mathbb{P}}(s,0,z,z') \pm \mathcal{A}_{\mathbb{O}}(s,0,z,z') \right). \right\rangle \tag{13.133}$$

The averaging over the external states in (13.133) for each exchanged Reggeon $\mathbb{R} = \mathbb{P}, \mathbb{O}$ is carried out via

$$\int \mathrm{d}z\mathrm{d}z' \left(\sqrt{g(z)}\psi_{12}(j_{\mathbb{R}}, z)\right)\left(\sqrt{g(z')}\psi_{34}(j_{\mathbb{R}}, z')\right), \tag{13.134}$$

which amounts to

$$\langle a_\pm \rangle = \tilde{\mathcal{N}} \left(e^{(j_{\mathbb{P}}(0)-1)\tau} f^+(\lambda) s^{-j_+} \mathcal{V}_{\mathbb{P}}(s,t) \pm e^{(j_{\mathbb{O}}(0)-1)\tau} f^-(\lambda) s^{-j_-} \mathcal{V}_{\mathbb{O}}(s,t) \right). \tag{13.135}$$

The eikonalized total cross sections are thus given by

$$\sigma_\pm(s) = 4\pi\alpha'\tilde{\tau}\ \mathrm{Re}\left(\ln(-i\,\langle a_\pm \rangle) + \gamma_E + \mathcal{O}(e^{i\langle a_\pm \rangle}) \right), \tag{13.136}$$

or, more explicitly

$$\sigma_\pm(s) = 4\pi\alpha'\tau\Big((j_{\mathbb{P}}(0)-1)\tau-\frac{3}{2}\ln\tau+\ln\big|h_+\pm h_-\,e^{(j_{\mathbb{O}}(0)-j_{\mathbb{P}}(0))\tau}\big|+\gamma_E+\mathcal{O}\Big), \tag{13.137}$$

with

$$h_\pm = s^{-j_\pm}\mathcal{V}_{\mathbb{R}}(s,0)\,f^\pm(\lambda)\equiv\bar{h}_\pm\,f^\pm(\lambda) \tag{13.138}$$

At large rapidities (13.136) asymptotes to the Froissart-Martin bound (13.122)

$$\sigma_\pm(s)\to 4\pi\alpha'\,(j_{\mathbb{P}}(0)-1)\,\tau^2, \tag{13.139}$$

and thus, unitarity is restored. Note that the proportionality constant in (13.136) is solely fixed by the Pomeron intercept.

The difference between the $p\bar{p}$ and pp cross sections, becomes exponentially small at large rapidities

$$\begin{aligned}\Delta\sigma =&\sigma_+-\sigma_- = 4\pi\alpha'\tau\ \ln\left|\frac{1+\frac{h_-}{h_+}e^{(j_{\mathbb{O}}-j_{\mathbb{P}})\tau}}{1-\frac{h_-}{h_+}e^{(j_{\mathbb{O}}-j_{\mathbb{P}})\tau}}\right|\\ &\to 8\pi\alpha'\tau\,\frac{1+\frac{16\lambda}{3(m_k^2-1)\pi^2}}{1+\frac{16\lambda}{9\pi}}\ \frac{\bar{h}_-}{\bar{h}_+}\ e^{(j_{\mathbb{O}}(0)-j_{\mathbb{P}}(0))\tau}.\end{aligned} \tag{13.140}$$

$\Delta\sigma$ is negative for the Odderon branch $m_k^2=k^2\to 0$, corresponding to an intercept of $j_{\mathbb{O}}(0)=1+\frac{1}{2\sqrt{\lambda}}$. However, this branch is not picked up by the contour $\mathcal{C}_L$ in Fig. 13.3. The leading contribution without a pole in the signature factor (13.43) is from $k=2$, which gives $\Delta\sigma>0$. The same holds true for higher values of k, as well as for all values of k for the $m_k^2=(4+k)^2$ branch. This is in qualitative agreement with Ref. [218][4], who traced this result back to the geometry and polarization $B_{\mu z}$, which we also used. Unfortunately, no pp and $p\bar{p}$ measurements or extrapolations at the same center of mass energy exist to check the above results.

13.5.2 rho and B Parameters

The rho parameters for pp and $p\bar{p}$ scattering are readily obtained by using (13.132)

$$\rho_\pm(s)=\frac{\mathrm{Re}\,\mathcal{A}_\pm(s,0)}{\mathrm{Im}\,\mathcal{A}_\pm(s,0)}=\frac{-\frac{1}{2}\mathrm{Im}\ln(-i\,\langle a_\pm\rangle\,/+i\,\langle a_\pm\rangle^*)}{\mathrm{Re}\ln|\,\langle a_\pm\rangle\,|+\gamma_E+\mathcal{O}}. \tag{13.141}$$

---

[4] Note that they defined $\Delta\sigma$ with an opposite sign.

$g^{(2)}_{\mathbb{O}\overline{\Psi}\Psi}$	α' (GeV^{-2})	$g_{\mathbb{P}\overline{\Psi}\Psi}$	$\mathcal{N}_\sigma$	$\mathcal{N}_\rho$
0	1.098(2)	2.1856(40)	$4.6 \cdot 10^{-3}(07)$	0.787(190)
15	1.098(2)	2.1856(40)	$4.6 \cdot 10^{-3}(07)$	0.787(190)
25	1.098(2)	2.1857(40)	$4.6 \cdot 10^{-3}(07)$	0.787(190)

Table 13.1.: Best-fit parameters for forward quantitites in pp and $p\bar{p}$ scattering for different input values of $g^{(2)}_{\mathbb{O}\overline{\Psi}\Psi}$.

At large rapidities, this reduces to

$$\begin{aligned} \rho_+(s) &\to \frac{\frac{\pi}{2}(1+\mathcal{O}(\frac{1}{\sqrt{\lambda}}))}{(j_{\mathbb{P}}(0)-1)\,\tau} \\ \rho_-(s) &\to \frac{\mathcal{O}(\frac{1}{\sqrt{\lambda}})}{(j_{\mathbb{P}}(0)-1)\,\tau}. \end{aligned} \tag{13.142}$$

The strong shadowing caused by the eikonalization of the Born amplitude for a single Pomeron exchange depletes both quantities to zero, in accordance with expectations from experiment. Note that the eikonalization does not change the B parameter in (13.120).

For the numerical evaluation, we fix the ’t Hooft coupling to the Lüscher contribution obtained by using the (time-like) Nambu-Goto string estimate in Ref. [226]

$$2 - \frac{3}{2\sqrt{\lambda}} = 1 + \frac{1}{6}. \tag{13.143}$$

The value for the Pomeron intercept is thus close to the phenomenological Donnachie-Landshoff intercept of 1.08 [227]. The pole of the signature factor $f^-(\lambda)$ in (13.43) prevents us from exploring the physics of the maximal Odderon. Thus, there is only a subtle dependence on $g^{(2)}_{\mathbb{O}\overline{\Psi}\Psi}$ and we refrain from fitting it to the data. Instead, we will use it as input in the following fits to obtain an upper bound on this coupling. We perform a global fit to the total cross sections in (13.136), rho parameters in (13.141) and slope parameter $B(s, t = 0)$ in (13.120) for the available pp and $p\bar{p}$ scattering data with $\sqrt{s} \geq 1$ TeV [228–235]. The results are collected in Table 13.1. Besides fitting α', $g_{\mathbb{P}\overline{\Psi}\Psi}$ we introduced overall scale factors for the total cross section $\mathcal{N}_\sigma$ and rho parameter $\mathcal{N}_\rho$. The results confirm the very subtle dependence on $g^{(2)}_{\mathbb{O}\overline{\Psi}\Psi}$, which are almost independent in the range of $0 \leq g^{(2)}_{\mathbb{O}\overline{\Psi}\Psi} \leq 25$. In Fig. 13.5, Fig. 13.6a and Fig. 13.6b, we show plots of the fitted quantities for $g^{(2)}_{\mathbb{O}\overline{\Psi}\Psi} = 15$, which showed the fastest convergence, together with the empirical data.

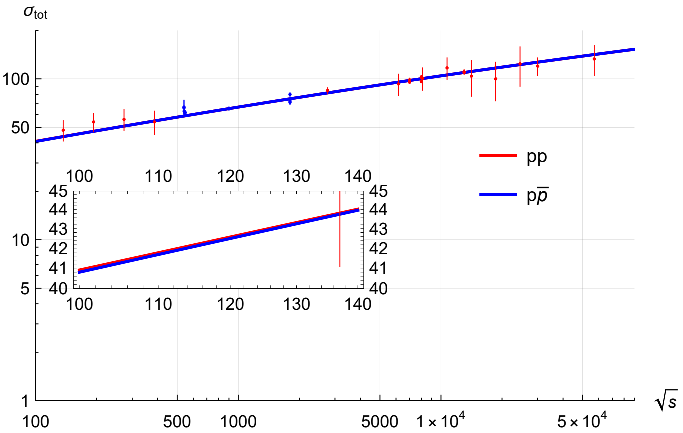

Fig. 13.5.: Total cross sections for pp and $p\bar{p}$ scattering, with the parameters given in Table 13.1 for $g^{(2)}_{\mathbb{O}\overline{\Psi}\Psi} = 15$.

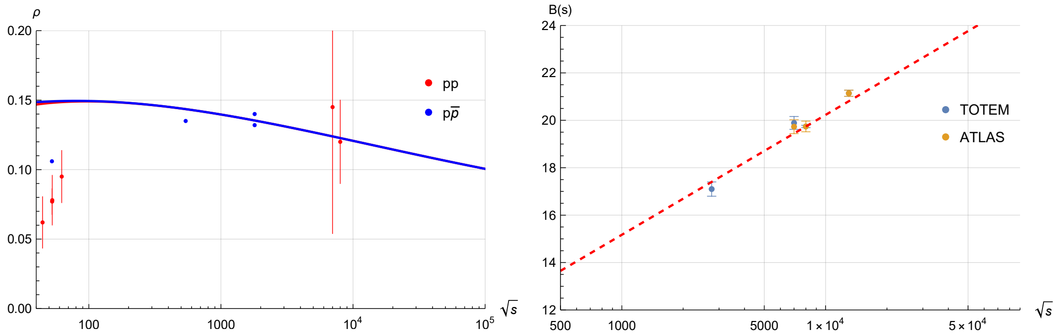

(a) (b)

Fig. 13.6.: Results for the rho (a) and slope (b) parameters versus $\sqrt{s}$ with the parameters given in Table 13.1 for $g^{(2)}_{\mathbb{O}\overline{\Psi}\Psi} = 15$.

13.5.3 Elastic Differential Cross Sections

Using the eikonalized amplitudes (13.130), the spin-averaged elastic differential cross sections are given by

$$\frac{d\sigma_\pm(s,t)}{dt} = \frac{1}{16\pi s^2}\langle|\mathcal{A}_\pm(s,t,z,z')|^2\rangle, \tag{13.144}$$

where averaging is performed using (13.134). In particular, at large rapidities we have

$$\begin{aligned}\frac{d\sigma_\pm(s,t)}{dt} &= \frac{(2\pi\alpha'\tilde\tau)^2}{16\pi s^2}\sum_{m,n=1}^{\infty}\frac{\langle g_\pm^m\, a_\pm^{*n}\rangle}{m\,n\,m!\,n!}\,e^{\frac{\alpha' t\tilde\tau}{2}(\frac{1}{m}+\frac{1}{n})}\\ &\to \frac{(2\pi\alpha'\tilde\tau)^2}{16\pi s^2}\,\langle|a_\pm|^2\rangle\,e^{\alpha' t\tau}.\end{aligned} \tag{13.145}$$

The diffractive nature of the differential cross section (13.144) is best understood in impact parameter space

$$\frac{d\sigma_\pm(s,t)}{dt} = \frac{1}{4\pi}\left\langle\left|\int \mathrm{d}^2b_\perp\, e^{-iq_\perp\cdot b_\perp}\big(1-e^{i(\chi_{\mathbb{P}}\pm\chi_{\mathbb{O}})}\big)(s,b_\perp,z,z')\right|^2\right\rangle \tag{13.146}$$

with $t=-q_\perp^2$. At large rapidities, the Froissart-Martin (13.139) is saturated, and the T-matrix in (13.146) approaches the black disc limit to wit

$$\begin{aligned}\langle\,\mathrm{Re}\mathcal{T}_\pm(s,b_\perp)\rangle =& \langle\,\mathrm{Re}(1-e^{i(\chi_{\mathbb{P}}\pm\chi_{\mathbb{O}})})(s,b_\perp)\rangle\\ &\to \theta(b(s)-|b_\perp|),\end{aligned} \tag{13.147}$$

with radius proportional to rapidity τ

$$b(s) = \sqrt{2\alpha'(j_{\mathbb{P}}(0)-1)}\tau, \tag{13.148}$$

for both pp and $p\bar p$. Fig. 13.7a illustrates the behavior of the T-matrix as a function of $b_\perp$ for fixed $\sqrt{s}$, and with vertex factors set to unity. Notably, the black-disc limit is reached at $\sqrt{s}\sim 1$ PeV. The parameters employed in this analysis are those listed in Table 13.2, with $g_{\mathbb{O}\overline{\Psi}\Psi}=15$. These values were obtained by a global fit to the empirical differential cross sections provided by TOTEM [236–240] and DØ [217]. The ratio $\tau/\sqrt{\lambda}$, which we previously argued to be large for the validity of the saddle point approximation, ranges between 4.2 and 5.3 for the datasets used in the fits. To further test the validity of this approximation, data at higher center of mass energies would be welcome.

Similarly, in Fig. 13.7b we illustrate the behavior of the differential cross section

$$\frac{d\sigma_+}{\mathrm{d}^2b_\perp} = 2\langle\mathrm{Re}\mathcal{T}_+(s,b_\perp)\rangle \tag{13.149}$$

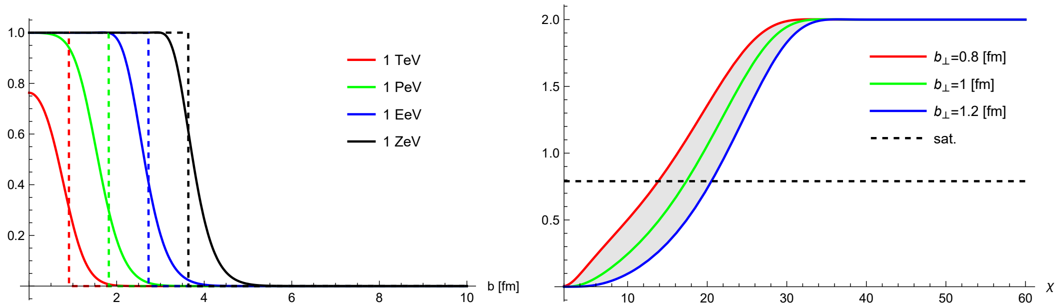

(a) (b)

Fig. 13.7.: (a) The real part of the pp T-matrix approaches a step function at large rapidities and large λ. (b) The differential pp cross section in (13.149) crosses the saturation (dashed) line at large rapidities and fixed $b_\perp$ for pp.

for different impact parameters values $b_\perp = 0.8, 1, 1.2$ fm and over $\chi = \ln s$. The (dashed) saturation line follows from the condition

$$\left.\frac{\mathrm{d}\sigma_+}{\mathrm{d}^2 b_\perp}\right|_S = 2(1 - e^{-\frac{1}{2}}) = 0.79. \tag{13.150}$$

For $b_\perp = 0.8,\ 1,$ and 1.2fm, the crossing occurs within the rapidity range $\chi_S = 14 - 20$, aligning with a recent estimate derived using the standard Nambu-Goto string model (see Figure 2 in Ref. [241]).

Asymptotically, we obtain from (13.147) and (13.146)

$$\frac{d\sigma_\pm(s,t)}{dt} \to \pi b^2(s)\, \frac{J_1^2(\sqrt{|t|}\, b(s))}{|t|}, \tag{13.151}$$

with the expected diffractive patterns. In the black-disc limit, the first diffractive minimum is located at

$$t_{\text{ min}}(s) \approx \frac{14.67}{b^2(s)}. \tag{13.152}$$

For increasing $\sqrt{s}$ it decreases, in accordance with the measurements shown in Fig. 13.1. Again, (13.151) saturates the Froissart-Martin bound (13.139), in accordance with unitarity. The total cross sections $\sigma_\pm(s)$ are directly related to the elastic differential cross section

$$\sigma_\pm(s) = \left(\frac{16\pi}{1+\rho_\pm^2(s)}\left(\frac{d\sigma_\pm(s,t)}{dt}\right)\right)^{\frac{1}{2}}_{t=0} \to 2\pi b^2(s). \tag{13.153}$$

The rightmost result is only valid in the large rapidity limit, where the rho parameter (13.142) depletes to zero.

Die approbierte gedruckte Originalversion dieser Dissertation ist an der TU Wien Bibliothek verfügbar.
The approved original version of this doctoral thesis is available in print at TU Wien Bibliothek.
TU Bibliothek Your knowledge hub WIEN

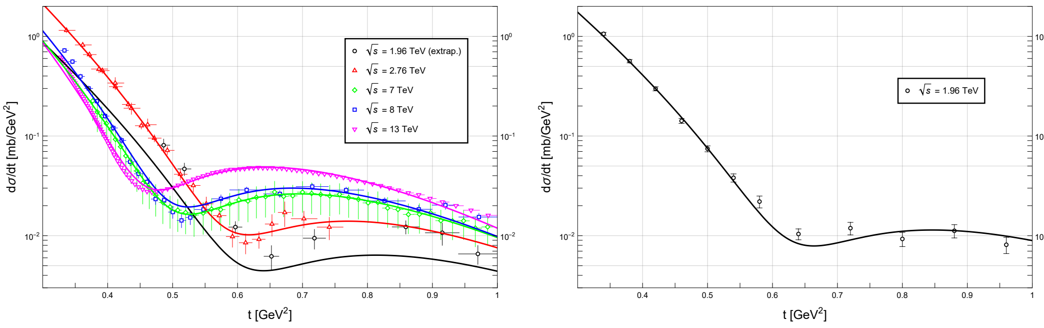

(a) (b)

Fig. 13.8.: (a) Results for the differential pp cross section (13.146), together with a weighted linear extrapolation of the results to $\sqrt{s} = 1.96$ TeV and a comparison to the corresponding TOTEM data and extrapolation [236–240]. (b) Results for the differential $p\bar{p}$ cross section (13.146) compared to the data from DØ [217].

$\sqrt{s}$	α' [GeV^{-2}]	$g_{\mathbb{P}\overline{\Psi}\Psi}$	$\mathcal{N}_{\mathrm{d}\sigma}$
1.96 TeV	0.640(21)	1.071(15)	0.003
2.76 TeV	0.715(27)	1.009(3)	0.007
7 TeV	0.607(5)	1.089(3)	0.002
8 TeV	0.626(15)	1.046(9)	0.003
13 TeV	0.587(5)	1.0782(3)	0.002

Table 13.2.: Best fit parameters for the differential cross section data from TOTEM [236–240] and DØ [217] with a fixed Odderon coupling of $g^{(2)}_{\mathbb{O}\overline{\Psi}\Psi} = 15$. The standard error on $\mathcal{N}_{\mathrm{d}\sigma}$ is negligible.

Fig. 13.8a displays the fit results for the holographic eikonalized elastic differential pp cross-section at center-of-mass energies of $\sqrt{s} = 2.76,\ 7,\ 8,$ and 13 TeV, using data from [236–240]. Additionally, a linear extrapolation of the fit parameters from Table 13.2 with weighted errors is shown for $\sqrt{s} = 1.96$ TeV, in qualitative agreement with Fig. 13.1. The diffractive tail is accurately reproduced for scattering data with $\sqrt{s} \geq 7$ TeV. Above this center of mass energy, the model parameters appear to converge. The bump-dip region is less pronounced and exhibits relatively large errors in the TOTEM data at $\sqrt{s} = 2.76$ TeV. Varying the input values for $g^{(2)}_{\mathbb{O}\overline{\Psi}\Psi}$ in the fit reveals that, due to the low intercept, the dependence on this coupling is even less pronounced than for the forward quantities in Table 13.1.

Our results for the holographic eikonalized elastic differential $p\bar{p}$ cross section at $\sqrt{s} = 1.96$ TeV, shown in Fig. 13.8b, are compared to those reported by the DØ collaboration. The diffractive peak is nearly absent in this channel and at this energy. Fig. 13.9 presents extrapolations of the $p\bar{p}$ differential cross section to $\sqrt{s} = 2.76,\ 7,\ 8,$ and 13 TeV, with the diffractive pattern still evident. Further data to test our predictions at these higher energies would be desirable.

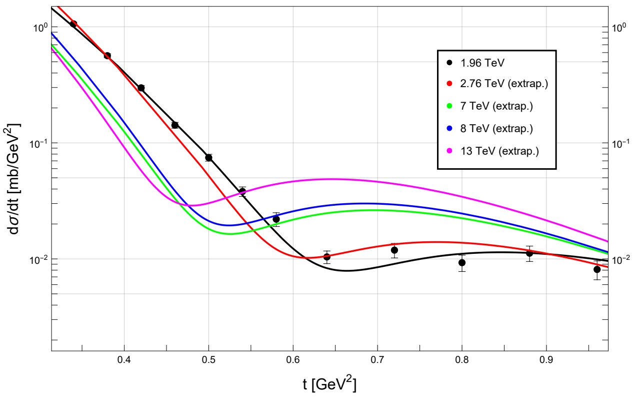

Fig. 13.9.: Extrapolated differential $p\bar{p}$ cross section

Conclusions

We have constructed the elastic pp and $p\overline{p}$ scattering amplitudes in a Gauge/Gravity dual approach and confronted them with experimental data. Our construction is based on Reggeized exchanges of a graviton and Kalb-Ramond field coupled to Dirac fermions in the bulk using a repulsive-wall background. The graviton is coupled to the baryon through its energy momentum tensor, while the Kalb-Ramond field couples through a five-dimensional Pauli coupling.

Upon eikonalization of the leading Witten diagrams, we successfully reproduced the forward quantities ρ, B and σ_{tot} as well as the differential cross sections measurements and extrapolations reported by TOTEM and DØ. Instead of fitting the gravity dual parameters α', λ and g_5 to the glueball mass spectrum, we have instead fitted the couplings to experimental data and obtained an upper bound for the Dirac coupling of a non-maximal Odderon. However, the first diffractive oscillation in the differential cross section is very well reproduced by solely using an eikonalized Pomeron exchange. At $\sqrt{s} = 1.96$ TeV, the diffractive pattern is absent for both pp and $p\overline{p}$ scattering.

Based on our model, we extracted the proton saturation rapidity and found it to be in the range $14 < \chi_S < 20$. This suggests a parton-x saturation of $x_S < 10^{-6}$, which poses a challenging task for future colliders.

Although our holographic results for pp and $p\overline{p}$ elastic cross sections at high energies align with the reported TOTEM data, they do not definitively support the contributions of both a Pomeron and an Odderon exchange. This is primarily due to the inability to fix the Odderon intercept at 1, which prevents us from studying the strongest contribution the Odderon might make.

Threshold Photoproduction of Heavy Pseudoscalar Mesons

14

The holographic computations on pp and $p\overline{p}$ scattering in the previous chapter showed that there is no significant contribution from Odderon exchange with intercept below 1 in the data from TOTEM and DØ. Another process that has been argued to be sensitive to Odderon exchange is threshold photoproduction of heavy pseudoscalar mesons like η_c and η_b. In this chapter, we examine this process via the exchange of a pseudovector glueball in the reaction $\gamma p \to \eta_{c,b} p$, as depicted in Fig. 13.2b. At threshold and for intermediate energies, the amplitude is thought to be dominated by a gluon rich 1^{+-} exchange with a subleading contribution from a nearly on-shell photon, called the Primakoff effect (see Fig. 14.1b). Whether the pseudovector exchange is discernable from the Primakoff exchange is an open question that we now try to address using holographic QCD. Additionally, previous studies usually found that the differential and total cross sections are in the picobarn range [159, 160, 242–244], posing a challenging task for experimentalists. To shed light on this issue, we will set up a holographic framework to compute the corresponding Witten diagrams in Fig. 14.2.

As in the previous chapter, we follow Ref. [191] and identify the gluonic boundary operators with dimension $\Delta = 6$

$$\begin{aligned} B^{\mu\nu} &\to d^{abc} G^{a\alpha\beta} G^{b}_{\alpha\beta} G^{c\mu\nu} \\ \tilde{B}^{\mu\nu} &\to d^{abc} G^{a\alpha\beta} G^{b}_{\alpha\beta} \tilde{G}^{c\mu\nu}. \end{aligned} \tag{14.1}$$

They are interpreted as C-odd twist-5 operators on the light front. In pQCD, on the other hand, factorization arguments show that the leading contribution to this process stems from a C-odd local twist-3 operator [245]

$$d^{abc} G^{a\alpha +} G^{b+}_{\alpha} G^{c+\nu}. \tag{14.2}$$

We will work with the standard soft-wall model with metric

$$\mathrm{d}s^2 = \left(\frac{1}{z}\right)^2 (\eta_{\mu\nu}\mathrm{d}x^\mu \mathrm{d}x^\nu - \mathrm{d}z^2) = e^{2A(z)}(\eta_{\mu\nu}\mathrm{d}x^\mu \mathrm{d}x^\nu - \mathrm{d}z^2), \tag{14.3}$$

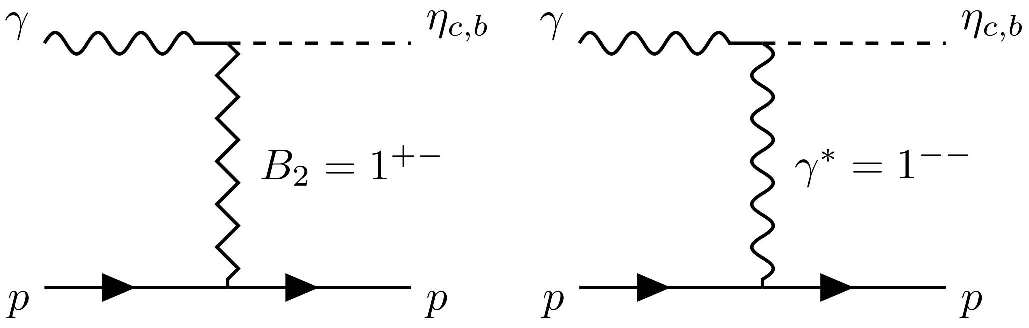

γ
$\eta_{c,b}$
$B_2 = 1^{+-}$
p
p
γ
$\eta_{c,b}$
$\gamma^* = 1^{--}$
p
p

(a)

(b)

Fig. 14.1.: Threshold photoproduction of $\eta_{c,b}$ through (a) s-wave pseudovector glueball exchange and (b) p-wave photon exchange.

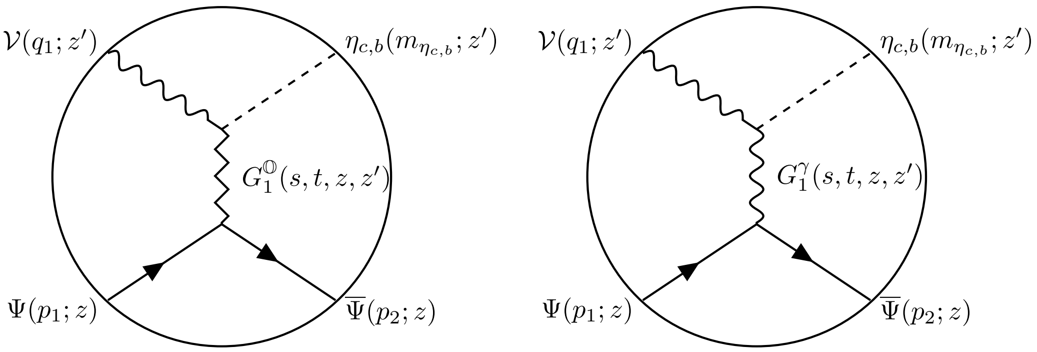

$\mathcal{V}(q_1; z')$
$\eta_{c,b}(m_{\eta_{c,b}}; z')$
$G_1^{\mathbb{O}}(s,t,z,z')$
$\Psi(p_1; z)$
$\overline{\Psi}(p_2; z)$
$\mathcal{V}(q_1; z')$
$\eta_{c,b}(m_{\eta_{c,b}}; z')$
$G_1^{\gamma}(s,t,z,z')$
$\Psi(p_1; z)$
$\overline{\Psi}(p_2; z)$

(a)

(b)

Fig. 14.2.: Witten diagrams for threshold production of $\eta_{c,b}$ through (a) Odderon and (b) photon exchange.

and dilaton $\phi(z) = \kappa^2 z^2$. Consequently, we obtain from (14.3) the tetrads $e^M_{\hat{M}} = z\delta^M_{\hat{M}}$. To proceed with the computation of the holographic amplitudes, we need to define the field content, determine the mass spectrum, and specify interaction terms.

14.1 Bulk Action and Fields

14.1.1 Bulk Pseudoscalar Fields

In the original soft-wall model [216], the massive tower of physical pseudoscalar mesons arises through chiral symmetry breaking induced by a bifundamental scalar field together with a mixing of the longitudinal components of the axial vector meson fields. Focusing on heavy pseudoscalar mesons, we will simplify our analysis by approximating them with the fluctuations of the singlet part of $A_z = \frac{1}{\sqrt{N_f}}\eta$, with[1] $N_f = 1+2$ of the 5-dimensional gauge field A_M with quadratic action given by

$$S_A = -\int \mathrm{d}^5x \, \sqrt{g} e^{-\phi} \frac{1}{4g_5^2} F^{MN} F_{MN} \tag{14.4}$$

and ensuing equations of motion

$$\partial_M \left(\sqrt{g} e^{-\phi} F^{MN} \right) = 0. \tag{14.5}$$

After performing a Kaluza-Klein decomposition with respect to the 4-dimensional and holographic coordinate, the bulk wave function is seen to solve

$$\begin{aligned} \Box A^\mu + z e^{\phi} \partial_z \left(e^{-\phi} \frac{1}{z} \partial_z A^\mu \right) &= 0, \\ \Box A_z - \partial_z \left(\partial_\mu A^\mu \right) &= 0, \end{aligned} \tag{14.6}$$

subject to the gauge condition

$$\partial_\mu A^\mu + z e^{\phi} \partial_z \left(e^{-\phi} \frac{1}{z} A_z \right) = 0. \tag{14.7}$$

The normalizable modes are readily obtained

$$\phi_n(z) = c_n \kappa z L_n(\kappa^2 z^2), \tag{14.8}$$

and their normalization is fixed by

$$\int \sqrt{g} e^{-\phi} e^{-4A(z)} \phi_m(z) \phi_n(z) = \delta_{mn}, \tag{14.9}$$

giving $c_n = \frac{1}{2}$. The mass spectrum displays the anticipated Regge behavior

$$m_n^2 = 4\kappa^2(n+1). \tag{14.10}$$

Note that we obtain a divergent decay constant at $z' = 0$ given by

$$F_n = \frac{1}{g_5} \left(e^{-\phi} \frac{1}{z'} \partial_{z'} \phi_n(z') \right) \Big|_{z'=0}. \tag{14.11}$$

---

[1] The notation 1+2 refers to one heavy and two light flavor branes.

Assuming that the UV boundary condition is set at $z' \sim \frac{1}{m_c}$, where m_c is the charm quark mass[2], the result is finite. The bulk wavefunction is thus given by

$$\phi_n(z) = -\frac{f_n}{m_n} \times 4g_5(n+1)\kappa z L_n(\kappa^2 z^2), \tag{14.12}$$

with $f_n = -F_n/m_n$ fixed by experiment later on.

14.1.2 Bulk Dirac Fields

We obtain similar formulas for the bulk Dirac fields as in Section 13.3. In particular, the dynamics of the bulk Dirac fields follow from the action in Section 13.69 but with the dilaton now explicit

$$S_F = \frac{1}{2g_5^2} \int \mathrm{d}^5 x e^{-\phi(z)} \sqrt{g} \left(\frac{i}{2} \overline{\Psi}_{1,2} e_A^N \Gamma^A \left(\overrightarrow{D}_N^{L,R} - \overleftarrow{D}_N^{L/R} \right) \Psi_{1,2} - (\pm M + V(z)) \overline{\Psi}_{1,2} \Psi_{1,2} \right), \tag{14.13}$$

with $V(z) = \kappa_N^2 z^2$, $\omega_{\mu\nu z} = -1/z\eta_{\mu\nu}$ and

$$\begin{aligned} \overrightarrow{D}_N^{L,R} &= \overrightarrow{\partial}_N + \frac{1}{8}\omega_{NAB} \left[\Gamma^A, \Gamma^B\right] - iA_N^a T^a \\ \overleftarrow{D}_N^{L,R} &= \overleftarrow{\partial}_N + \frac{1}{8}\omega_{NAB} \left[\Gamma^A, \Gamma^B\right] + iA_N^a T^a. \end{aligned} \tag{14.14}$$

The equations of motion following from (14.13) are given by

$$\left(i e_A^N \Gamma^A D_N^{L,R} - \frac{i}{2}(\partial_N \phi) e_A^N \Gamma^A - (\pm M + V(z)) \right) \Psi_{1,2} = 0, \tag{14.15}$$

and their normalizable solutions are

$$\begin{aligned} \Psi_1(p, z; n) &= \psi_R(z; n) \Psi_R^0(p) + \psi_L(z; n) \Psi_L^0(p) \\ \Psi_2(p, z; n) &= \psi_R(z; n) \Psi_L^0(p) + \psi_L(z; n) \Psi_R^0(p), \end{aligned} \tag{14.16}$$

where

$$\begin{aligned} \psi_R(z; n) &= z^\Delta \times \tilde{\psi}_R(z; n) = z^\Delta \times \left(n_R\, \xi_N^{\tau - \frac{3}{2}} L_n^{(\tau-2)}(\xi_N) \right) \\ \psi_L(z; n) &= z^\Delta \times \tilde{\psi}_L(z; n) = z^\Delta \times \left(n_L\, \xi_N^{\tau - 1} L_n^{(\tau-1)}(\xi_N) \right), \end{aligned} \tag{14.17}$$

---

[2] Note that in the case of a bifundamental scalar field, m_c should be properly introduced via its non-normalizable mode.

with $L_n^{(\alpha)}(\xi_N)$ the generalized Laguerre polynomials and we introduced the shorthand $\xi_N = \kappa_N^2 z^2$. The free boundary spinors are normalized such that

$$\overline{u}(p)u(p) = 2M_N, \tag{14.18}$$

whereas the bulk fields $\tilde{\psi}_{L,R}$ satisfy

$$\int \mathrm{d}z\, e^{-\kappa_N^2 z^2} \, \frac{1}{z^{2\tau-3}} \, \tilde{\psi}_{L,R}(z;n)\tilde{\psi}_{L,R}(z;n') = \delta_{nn'}, \tag{14.19}$$

giving

$$\begin{aligned} n_R &= n_L \sqrt{\tau - 1 + n}, \\ n_L &= \frac{1}{\kappa_N{}^{(\tau-2)}} \left(\frac{2\Gamma(n+1)}{\Gamma(\tau+n)} \right)^{\frac{1}{2}}. \end{aligned} \tag{14.20}$$

The fermionic mass spectrum Reggeizes, and we obtain

$$m_n^2 = 4\kappa_N^2 (n + \tau - 1). \tag{14.21}$$

The bulk-to-boundary propagator is obtained from the non-normalizable solutions to (14.15) in terms of Kummer functions

$$\begin{aligned} \tilde{\psi}_R(p,z) &= N_R \, U\left(-\frac{p^2}{4\kappa_N^2}, 3-\tau, \xi_N \right), \\ \tilde{\psi}_L(p,z) &= N_L \, U\left(-\frac{p^2}{4\kappa_N^2}, 2-\tau, \xi_N \right), \end{aligned} \tag{14.22}$$

with $N_R/N_L = p/2\kappa_N$ and

$$N_L = \frac{\Gamma\left(\tau - 1 - \frac{p^2}{4\kappa_N^2}\right)}{\Gamma(\tau - 1)}. \tag{14.23}$$

The bulk-to-boundary propagator in (14.22) can be rewritten as a sum over Regge poles

$$\begin{aligned} \tilde{\psi}_R(p,z) &= \sum_{n=0}^{\infty} \frac{f_n p \, \tilde{\psi}_R(n;z)}{p^2 - m_n^2} \\ \tilde{\psi}_L(p,z) &= \sum_{n=0}^{\infty} \frac{f_n m_n \, \tilde{\psi}_L(n;z)}{p^2 - m_n^2} \end{aligned} \tag{14.24}$$

with decay constant $f_n = 2\kappa_N/(n_R \Gamma(\tau-1)) = -F_n/m_n$.

14.1.3 Bulk Spin-1 Fields

Soft-Wall

The pseudovector glueball previously considered in Section 9.2.1 arises as fluctuation of the Kalb-Ramond B_2 field with an admixture of the Ramond-Ramond field C_3 through the topological mass term. For simplicity, we consider only the part of the action

$$S_B = -\int \mathrm{d}^5x\,\sqrt{g}\frac{1}{12\tilde{g}_5^2}e^{-2\phi}H^{MNO}H_{MNO}, \tag{14.25}$$

which is seen to reduce to that of a massive spin-1 field in 5d as given in (14.4). Note that the axial gauge field $\tilde{V}_M = (0, V_\mu)$ is obtained through the projection $B_{\mu\nu} = 1/\sqrt{-\partial^2}\epsilon_{\mu\nu\rho\sigma}\partial^\rho\tilde{V}^\sigma$ onto the three physical degrees of freedom of a massive spin-1 field and also gives a correct kinetic term in (14.25). As in 7.2, the photon field follows via VMD from the polarizations along the 4-dimensional subspace A_μ with open-string coupling κ_γ fixed by the rho meson pole in the time-like bulk-to-boundary propagator. Thus, the following formulas hold equally for the pseudovector glueball and the photon field and only differ by the respective string couplings. In the following, quantities associated with a pseudovector glueball will be denoted by an index b. Following [246], we obtain the normalizable solutions

$$\phi_n(z) = c_n\kappa^2z^2L_n^1(\kappa^2z^2) \equiv J(m_n, z), \tag{14.26}$$

with the coupling of the closed string sector given by twice that of the open string sector. The dilaton is thus given by $\phi = \kappa_b^2z^2 = (2\kappa_\gamma)^2z^2 = (2\kappa)^2z^2$ for the corresponding pseudovector glueball quantities. The normalization is fixed by

$$\int \mathrm{d}z\sqrt{g}e^{-\phi}e^{-4A(z)}\phi_m(z)\phi_n(z) = \delta_{mn}, \tag{14.27}$$

giving $c_n = \sqrt{2/(n+1)}$ and the resulting decay constant is

$$F_n = \frac{1}{g_5}\left(e^{-\phi}\frac{1}{z'}\partial_{z'}\phi_n(z')\right)\bigg|_{z'=0} = -\frac{2}{g_5}c_n(n+1)\kappa^2. \tag{14.28}$$

The fermionic mass spectrum Reggeizes, and we obtain

$$m_n^2 = 4\kappa^2(n+1). \tag{14.29}$$

We now proceed to fix the mass scale of the spin-1 sector through the rho meson mass of $m_\rho = 0.775$ GeV [9] giving

$$\kappa_\gamma = 0.3875 \text{ GeV}^{-1}, \qquad \kappa_b = 2\kappa_\gamma = 0.775 \text{ GeV}^{-1}. \tag{14.30}$$

The bulk wave function may thus be rewritten as

$$\phi_n(z) = \frac{f_n}{m_n} \times 2g_5\kappa^2 z^2 L_n^1(\kappa^2 z^2), \tag{14.31}$$

where $f_n = -F_n/m_n$. The bulk-to-bulk propagator in Fig. 14.2a can be simplified for threshold production. In particular, the mode sum representation

$$G_1(z, z') = \sum_n \frac{\phi_n(z)\phi_n(z')}{k^2 - m_n^2} \tag{14.32}$$

reduces to

$$\begin{aligned} G_1(z \to 0, z') &\approx \frac{\phi_n(z \to 0)}{-g_5 F_n} \sum_n \frac{-g_5 F_n \phi_n(z')}{k^2 - m_n^2} \\ &= \frac{z^2}{2} \times V(k, z'). \end{aligned} \tag{14.33}$$

For spacelike momenta $k^2 = -K^2$, the bulk-to-bulk pseudovector propagator in Fig. 14.2a with one leg at the boundary is thus given by

$$G_1(z \to 0, z') \approx \frac{z^2}{2} \sum_n \frac{g_5 F_n \phi_n(z')}{K^2 + m_n^2} = \frac{z^2}{2} \times \mathcal{V}_b(K, z'), \tag{14.34}$$

with

$$\begin{aligned} \mathcal{V}_b(K, z) &= \kappa_b^2 z^2 \Gamma(1 + a_K)\mathcal{U}(1 + a_K, 2, \kappa_b^2 z^2) \\ &= \kappa_b^2 z^2 \int_0^1 \frac{dx}{(1-x)^2} x^{a_K} \exp\left[-\frac{x}{1-x}\kappa_b^2 z^2\right], \qquad \mathcal{V}_b(0, z) = \mathcal{V}_b(K, 0) = 1, \end{aligned} \tag{14.35}$$

where $a_K = K^2/4\kappa_b^2$ and $\mathcal{U}(a, b, c)$ is the confluent hypergeometric function of the second kind. Analogous formulas hold for the Primakoff exchange.

Hard-Wall

The expansion in (14.34) will lead to divergent z integrals in some couplings. Additionally, the dilaton, which acts as a regulator in the soft-wall model, is absent in interactions arising from the Chern-Simons term. We will thus utilize a hard-wall[3] cut-off for said quantities to only integrate up to a physically reasonable value of z. In the bulk, the normalizable solutions following from (14.6) with $\phi = 0$ are given in terms of Bessel functions of the first kind

$$\phi_n(z) = c_n z J_1(m_n z), \tag{14.36}$$

where $c_n = \sqrt{2}/z_0 J_1(m_n z_0)$. The position of the hard-wall z_0, and thus the mass spectrum, is fixed by the roots of the Bessel function

$$J_0(m_n z_0) = 0. \tag{14.37}$$

Again, we fix it by rho meson mass and obtain $z_0 = 3.103\ \text{GeV}^{-1}$. This will serve as a hard-wall cut-off for divergent integrals in the Chern-Simons term.

14.1.4 Interactions

The Kalb-Ramond field couples to the flavor branes through the Chern-Simons term in (7.6). In particular, when reduced to a 5-dimensional theory, we have

$$S_{CS} = T_8 \int \operatorname{Tr}\Big(e^{\mathcal{F}} \wedge \sum_j C_{2j+1}\Big) \to \tilde{T}_8 \int \mathrm{d}^5 x \epsilon^{MNOPQ} \operatorname{Tr}(A_M F_{NO} B_{PQ}), \tag{14.38}$$

where we absorbed constant factors arising from the integration in $\tilde{T}_8$ and with $\mathcal{F} = 2\pi\alpha' F + B$. We will assume that a similar coupling holds for heavy pseudoscalar mesons like $\eta_{c,b}$, as well as assume a coupling to fermions through their magnetic moment. The interaction terms of the Kalb-Ramond field with bulk pseudoscalars and Dirac fermions are thus given by

$$\begin{aligned} S_B = \int \mathrm{d}^5 x \sqrt{g} \Big(& \frac{1}{2} g_{CS} \ \operatorname{Tr} \epsilon^{MNOP} A_z F_{MN} B_{OP} \\ & + e^{-\phi} g_{B\psi} \sum_{1,2} (\pm) \overline{\Psi}_{1,2} e^M_{\hat{M}} e^N_{\hat{N}} \sigma^{\hat{M}\hat{N}} \Psi_{1,2} \, B_{MN} \Big) . \end{aligned} \tag{14.39}$$

---

[3] The formulas for the hard-wall model are equivalent to those of the soft-wall model but with a vanishing dilaton ($\kappa \to 0$). Though this limit must sometimes be taken with care.

Similarly, we obtain for the $U(1)$ gauge fields

$$\begin{aligned} S_A = \int \mathrm{d}^5x\,\sqrt{g}\Big(& e^{-\phi}\sum_{1,2}\frac{i}{2g_5^2}\overline{\Psi}_{1,2}e^{M}_{\hat{M}}\Gamma^{\hat{M}}\Psi_{1,2}A_M \\ & + \frac{1}{2}g_{CS}\,\mathrm{Tr}\,\epsilon^{MNOP}A_zF_{MN}F_{OP} \\ & + e^{-\phi}\eta_P\sum_{1,2}(\pm)\overline{\Psi}_{1,2}e^{M}_{\hat{M}}e^{N}_{\hat{N}}\sigma^{\hat{M}\hat{N}}\Psi_{1,2}\,F_{MN}\Big), \end{aligned} \tag{14.40}$$

which, through VMD, will lead to photon couplings. The couplings g_{CS} and the 5D Newton constant are given by $g_{CS} = \frac{N_c}{24\pi^2}$ and $\tilde{g_5}^2 = 2\kappa^2 = 16\pi G_N = 8\pi^2/N_c^2$, respectively. The Pauli parameter η_P will be fixed by matching the Pauli form factor to its experimental value. The trace runs over the flavors and selects the pertinent charges for charmonia $e_c = 2/3\;e$ or bottomonia $e_b = -1/3\;e$ production, respectively.

14.2 Holographic Photoproduction of η_c and η_b

The amplitude displayed in Fig. 14.2 following from the interactions given in (14.39-14.40) for the production of η_c is given by

$$\begin{aligned} i\mathcal{A}(s,t)_{\gamma p\to\eta p} &= \sum_n i\tilde{\mathcal{A}}_{\gamma p\to\eta p}(m_n,s,t) \qquad (14.41) \\ i\tilde{\mathcal{A}}_{\gamma p\to\eta p}(m_n,s,t) &= (-i)V^{\mu}_{\mathbb{O}\gamma\eta}(q_1,q_2,k,m_n)\,\tilde{P}_{\mu\nu}(m_n^{\mathbb{O}},\Delta)\,(-i)V^{\nu}_{\mathbb{O}\overline{\Psi}\Psi}(p_1,p_2,k,m_n) \\ &\quad + (-i)V^{\mu}_{\gamma\gamma^*\eta}(q_1,q_2,k,m_n)\,\tilde{P}_{\mu\nu}(m_n^{\gamma},\Delta)\,(-i)V^{\nu}_{\gamma*\overline{\Psi}\Psi}(p_1,p_2,k,m_n), \end{aligned}$$

where we defined the bulk vertices

$$\begin{aligned} V^{\mu}_{\mathbb{O}\gamma\eta}(q_1,q_2,k) &= g_{CS}\frac{e_{c,b}}{2\sqrt{N_fK^2}}\int \mathrm{d}z\phi(z)J_b(m_n,z)\epsilon^{\mu\nu\rho\sigma}k_\nu F_{\rho\sigma} \\ V^{\sigma}_{\mathbb{O}\overline{\Psi}\Psi}(p_1,p_2,k) &= \frac{\epsilon_{\mu\nu\rho\lambda}k^\rho\eta^{\lambda\sigma}}{2\sqrt{K^2}}\int \mathrm{d}z\sqrt{g}e^{-\phi}\sum_{1,2}(\pm)\overline{\Psi}_{1,2}(p_2,z)\sigma^{\mu\nu}\Psi_{1,2}(p_1,z)J_b(m_n,z). \end{aligned} \tag{14.42}$$

The field strength $F_{\rho\sigma} = iq_\rho\epsilon_\sigma(q) - iq_\sigma\epsilon_\rho(q)$ is now to be understood in terms of the polarizations $\epsilon_\mu(q)$ of the external photon with momentum q and the reduced spin-1 bulk propagator following from (14.32) is

$$\begin{aligned} G_1(m_n,t,z,z')_{\mu\nu} &= J_b(m_n,z)\tilde{P}_{\mu\nu}J_b(m_n,z'), \\ \tilde{P}_{\mu\nu}(m_n,k) &= \frac{-i}{k^2-m_n^2}P_{\mu\nu}(k), \quad P_{\mu\nu}(k) = \eta^{\mu\nu} - \frac{k^\mu k^\nu}{k^2}. \end{aligned} \tag{14.43}$$

The photon vertices follow in a similar fashion as

$$\begin{aligned}
V^{\mu}_{\gamma^\star\gamma\eta}(q_1,q_2,K) &= \frac{e^2_{c,b}}{2\sqrt{N_f}}\int \mathrm{d}z\phi(z)\times\frac{z^2}{2}\epsilon^{\mu\nu\rho\sigma}F_{\mu\nu}F_{\rho\sigma}\\
V^{\nu(1)}_{\gamma^\star\overline{\Psi}\Psi}(p_1,p_2,K) &= \frac{e_{c,b}}{2g_5^2}\int \mathrm{d}z\sqrt{g}e^{-\phi}\sum_{1,2}\overline{\Psi}_\pm(p_2,z)\gamma^\nu\Psi_\pm(p_1,z)J(m_n,z)\\
V^{\nu(2)}_{\gamma^\star\overline{\Psi}\Psi}(p_1,p_2,K) &= \eta_P\frac{e}{2}\int \mathrm{d}z\sqrt{g}e^{-\phi}\sum_{1,2}(\pm)\overline{\Psi}_\pm(p_2,z)\sigma^{\mu\nu}\Psi_\pm(p_1,z)K_\mu J(m_n,z)\\
V^{\nu(3)}_{\gamma^\star\overline{\Psi}\Psi}(p_1,p_2,K) &= \eta_P\frac{e}{2}\int \mathrm{d}z\sqrt{g}e^{-\phi}\sum_{1,2}\overline{\Psi}_\pm(p_2,z)\gamma^\nu i\gamma^5\Psi_\pm(p_1,z)\partial_z J(m_n,z).
\end{aligned}$$

The bulk couplings to $\eta_{c,b}$ in (14.42) and (14.44) originate from the Chern-Simons term in (14.38) and neither include metric nor dilaton factors to regulate the integrals over the radial coordinate. On the other hand, the couplings to baryons arise from the DBI part of the action since they are identified with instanton configurations of the flavor gauge fields and are thus finite[4].

With the holographic pseudoscalar wave functions localized at the boundary, we may take $z' \to 0$ and for spacelike momenta $t = -K^2$ we can use (14.34) in (14.41) to obtain

$$\begin{aligned}
i\mathcal{A}(s,t)_{\gamma p\to\eta p} =& i\tilde{\mathcal{A}}_{\gamma p\to\eta p}(s,t)\\
i\tilde{\mathcal{A}}_{\gamma p\to\eta p}(s,t) = & (-i)\mathcal{V}^{\mu}_{\mathbb{O}\gamma\eta}(q_1,q_2,k)\times P_{\mu\nu}(\Delta)\times(-i)\mathcal{V}^{\nu}_{\mathbb{O}\overline{\Psi}\Psi}(p_1,p_2,k)\\
&+(-i)\mathcal{V}^{\mu}_{\gamma\gamma^*\eta}(q_1,q_2,k)\times P_{\mu\nu}(\Delta)\times(-i)\mathcal{V}^{\nu}_{\gamma*\overline{\Psi}\Psi}(p_1,p_2,k)
\end{aligned}\tag{14.44}$$

The normalizable modes in (14.42) are now to be substituted with their non-normalizable counterparts $\mathcal{V}(Q,z)$. For spacelike momenta, we thus get

$$\begin{aligned}
\mathcal{V}^{\mu}_{\mathbb{O}\gamma\eta}(q_1,q_2,K) &= g_{CS}\frac{e_{c,b}}{2\sqrt{N_f}}\int \mathrm{d}z\varphi(z)\times\frac{z^2}{2}\epsilon^{\mu\nu\rho\sigma}k_\nu F_{\rho\sigma},\\
\mathcal{V}^{\sigma}_{\mathbb{O}\overline{\Psi}\Psi}(p_1,p_2,K) &= \frac{g_{B\Psi}}{2\sqrt{K^2}}\int \mathrm{d}z\sqrt{g}e^{-\phi}2\psi_L(z)\psi_R(z)\mathcal{V}_b(K,z)\overline{u}(p_2)\gamma^5\sigma_{\rho\lambda}u(p_1)K^\rho\eta^{\lambda\sigma}.
\end{aligned}\tag{14.45}$$

---

[4] Though they receive $1/N_c$ corrections from the Chern-Simons term that stabilize them at finite size [222].

Analogous vertices follow for the Primakoff exchange

$$\begin{aligned}
\mathcal{V}^{\mu}_{\gamma^\star\gamma\eta}(q_1,q_2,K) &= \frac{e^2_{c,b}}{2\sqrt{N_f}}\int \mathrm{d}z\varphi(z)\times\frac{z^2}{2}\epsilon^{\mu\nu\rho\sigma}\eta F_{\mu\nu}F_{\rho\sigma},\\
\mathcal{V}^{\nu(1)}_{\gamma^\star\overline{\Psi}\Psi}(p_1,p_2,K) &= \frac{e}{2g_5^2}\int \mathrm{d}z\sqrt{g}e^{-\phi}z\left(\psi_R^2(z)+\psi_L^2(z)\right)\mathcal{V}(K,z)\overline{u}(p_2)\gamma^\nu u(p_1),\\
\mathcal{V}^{\nu(2)}_{\gamma^\star\overline{\Psi}\Psi}(p_1,p_2,K) &= \eta_P\frac{e}{2}\int \mathrm{d}z\sqrt{g}e^{-\phi}\left(2\psi_L(z)\psi_R(z)\right)\mathcal{V}(K,z)\overline{u}(p_2)\sigma^{\mu\nu}u(p_1)K_\mu,\\
\mathcal{V}^{\nu(3)}_{\gamma^\star\overline{\Psi}\Psi}(p_1,p_2,K) &= \eta_P\frac{e}{2}\int \mathrm{d}z\sqrt{g}e^{-\phi}z\left(\psi_L^2(z)-\psi_R^2(z)\right)\mathcal{V}(K,z)\overline{u}(p_2)\gamma^\nu u(p_1).
\end{aligned} \tag{14.46}$$

14.2.1 Form Factors

As in Section 10.3, for an off-shell photon we obtain transition form factors that describe the internal structure of composite particles. After projecting the chiral bulk spinors to 4D and performing the relevant LSZ reduction of the 3-point functions, we obtain, for example, the Dirac form factor that arises through the current associated with the covariant derivative

$$W^\mu(K^2)^{EM}_{Dirac} = \overline{u}(p_2)\gamma^\mu u(p_1)\times e_N\times C_1(K)\equiv\frac{1}{F_N(p_2)F_N(p_1)}\frac{\delta S^{EM}_{Dirac}}{\delta\epsilon_\mu}, \tag{14.47}$$

with e_N the electric charge of the nucleon, $F_N(p) = \langle 0|\,\mathcal{O}_N(0)\,|N(p)\rangle$ the nucleon source constant and

$$\begin{aligned}
C_1(K) =& \frac{1}{2}\int e^{-\kappa^2z^2}z^{3-2\tau}(\tilde{\psi}_L^2+\tilde{\psi}_R^2)\mathcal{V}(Q,z)\\
=&\frac{(a_K+2\tau)\Gamma(a_K+1)\Gamma(\tau)}{2\Gamma(a_K+\tau+1)}.
\end{aligned} \tag{14.48}$$

From

$$\langle N(p_2)|J^\mu_{EM}(0)|N(p_1)\rangle = \overline{u}(p_2)\left(F_1(K)\gamma^\mu + F_2(K)\frac{i\sigma^{\mu\nu}}{2M_N}k_\nu\right)u(p_1) \tag{14.49}$$

we obtain the electromagnetic Dirac and Pauli form factors

$$\begin{aligned}
F_1(Q) &= C_1(K)+\eta_P C_2(K)\\
F_2(Q) &= \eta_P C_3(K)
\end{aligned} \tag{14.50}$$

where

$$\begin{aligned} C_2(K) &= \frac{1}{2}\int e^{-\kappa^2 z^2} z^{3-2\tau}(\tilde{\psi}_L^2 - \tilde{\psi}_R^2) z\partial_z \mathcal{V}(K,z) \\ &= \frac{a_K(a_K(\tau-1)-1)\Gamma(a_K+1)\Gamma(\tau)}{\Gamma(a_K+\tau+2)}, \end{aligned} \tag{14.51}$$

and

$$\begin{aligned} C_3(K) &= 2M_N \int e^{-\kappa^2 z^2} z^{3-2\tau}\tilde{\psi}_L\tilde{\psi}_R z\mathcal{V}(Q,z) \\ &= \frac{4(\tau-1)\tau\Gamma(a_K+1)\Gamma(\tau)}{\Gamma(a_K+\tau+1)}. \end{aligned} \tag{14.52}$$

For details we refer the reader to Ref. [247]. Note that the 5-dimensional Pauli term $\sigma^{\mu z}$ in (14.40) leads to an additional contribution to $F_1(Q)$. Fixing these form factors to their experimental values in units of the nuclear magneton

$$F_1(0) = 1, \qquad F_2(0) = (\mu_p - 1) = 1.7928, \qquad \mu_p = 2.7928 \tag{14.53}$$

we obtain

$$\eta_P = 1.7928/C_3(0) = 1.7928/4(\tau-1), \tag{14.54}$$

Analogously, we obtain the C-odd gluonic form factor via the exchange of a Kalb-Ramond field

$$\begin{aligned} F_b(K) &= \int \mathrm{d}z z^{-2\tau+3} e^{-\phi} 2M_N \tilde{\psi}_R\tilde{\psi}_L \mathcal{V}_b(K,z) \\ &= 16(\tau-1)\Gamma(\tau+1)\Gamma\left(a_K+1\right) \times {}_2\tilde{F}_1\left(\tau+1, a_K+1; \tau+a_K+1; -3\right), \end{aligned} \tag{14.55}$$

with a factor of $2M_N$ pulled out in analogy with the electromagnetic Pauli form factor and ${}_p\tilde{F}_q$ is the regularized hypergeometric function. We fix $F_b(K)$ through the nucleon tensor charge, which is a measure for the net transverse spin of the quark content of the nucleus at a given energy scale. It is defined through

$$\langle P\, S|\bar{\psi} i\sigma^{\mu\nu}\gamma^5\psi|P\, S\rangle = 2\delta q(P^\mu S^\nu - P^\nu S^\mu), \tag{14.56}$$

where P and S refer to the momentum and spin of the nucleon, respectively. The nucleon tensor charge, and thus also its intrinsic spin, is deeply related to the $U(1)_A$ anomaly

$$\langle P\, S|\bar{\psi} i\gamma^\mu\gamma^5\psi|P\, S\rangle = 2M_N\Sigma(0)S^\mu, \tag{14.57}$$

where $\Sigma(0)$ is the net quark helicity of the u, d and s quarks[5]. On the lattice, one obtains [249]

$$\delta q = \delta u + \delta d \approx 0.839 - 0.231 = 0.608, \tag{14.58}$$

which we use to fix the normalization

$$F_b(0) = 0.608. \tag{14.59}$$

The C-odd charge radius is obtained from

$$\langle r^2 \rangle = -6 \left(\frac{\mathrm{d} \ln F_b(K)}{\mathrm{d}K^2} \right)_{K^2=0}, \tag{14.60}$$

and explicitly given by

$$\begin{aligned} \langle r^2 \rangle =& \frac{3}{2\kappa_b^2} \Big(\gamma_E - 4\Gamma(\tau+1) \\ & \times \Big({}_2F_1^{(0,0,1,0)}(1,\tau+1,\tau+1,-3) + {}_2F_1^{(1,0,0,0)}(1,\tau+1,\tau+1,-3) \Big) \Big), \end{aligned} \tag{14.61}$$

where $\gamma_E = 0.5772...$ is the Euler-Mascheroni constant, and the superscript indices denote derivatives with respect to the argument. Using $\tau = 3$ and $\kappa_\gamma = 0.3875$ GeV we obtain

$$\sqrt{\langle r^2 \rangle} = 2.733 \text{ GeV}^{-1} = 0.540 \text{ fm}, \tag{14.62}$$

Comparisons with the existing literature are in order. The 1^{+-} nucleon form factor without Reggeization in Ref. [242] is assumed to be monopole-like and normalized to unity. The dipole analysis of Ref. [159] with a Reggeized pseudovector glueball exchange fixes this form factor to the leading twist quark Generalized PDF (GPD), also normalized to unity. These analyses, as well as ours, are in stark contrast to the relatively large value obtained in Ref. [158] that even displays a sign change near the origin.

In Fig. 14.3 we display the various form factors after fixing them as described above. The open string couplings obey the relations $\phi(z) = \kappa_N^2 z^2 = \kappa_\gamma^2 z^2 = \kappa^2 z^2$, and for the closed string sector, we recall that $\phi = \kappa_b^2 z^2 = 4\kappa^2 z^2$. As mentioned above, the remaining coupling κ is fixed by the rho meson mass, which gives

$$(\kappa_b, \kappa_\gamma, \kappa_N) = (0.775, 0.3875, 0.3875) \text{ GeV}. \tag{14.63}$$

---

[5] At this point it is worth mentioning the famous result of the EMC which implies $\Sigma(3.5 - 29.5 \text{ GeV}^2) = 0.14(3)(10)$ [248]. This result is consistent with 0 and led to the proton spin crisis. It might be argued that this crisis is resolved since current theoretical predictions agree with the most recent measurements. However, the exact spin decomposition and its energy dependence are still open problems.

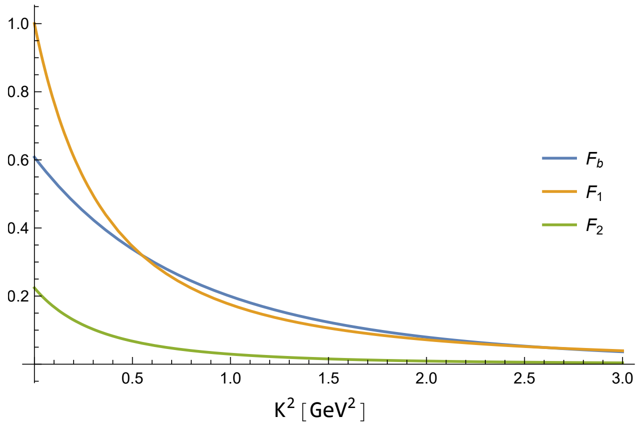

Fig. 14.3.: C-even and C-odd nucleon form factors in the approximation $\kappa_N = \kappa_\gamma$ with the normalization fixed by the charge, magnetic moment and (14.59).

Notably, at intermediate K^2, the dominant form factor is F_1, in analogy to the Primakoff effect. At larger momentum transfer, the C-odd form factor $F_b(K^2)$ becomes slightly more dominant. Additionally, the corresponding part of the action in (14.39) leads to a kinematical enhancement of this contribution, in agreement with pQCD [159, 160].

14.2.2 Threshold Vertices

For space-like momentum transfers, the vertex between the pseudovector glueball, $\eta_{c,b}$ and a photon is given by

$$\mathcal{V}_{\mathbb{O}\eta\gamma}(K) = \frac{e_{c,b}}{2\sqrt{N_f}} \int \mathrm{d}z \varphi(z) \times \frac{z^2}{2}. \tag{14.64}$$

Amputation of the amplitude effectively leads to a substitution of the bulk-to-boundary propagator by

$$\varphi(q,z) \to \phi_n(z) = g_5 c_n \kappa z L_n(\kappa^2 z^2) - \frac{f_n}{m_n} \times 4 g_5 (n+1) \kappa z L_n(\kappa^2 z^2), \tag{14.65}$$

and thus (14.64) reduces to

$$\mathcal{V}_{\mathbb{O}\eta\gamma}(K) \approx \frac{e_{c,b}}{2\sqrt{N_f}} \int \mathrm{d}z \phi_n(z) \times \frac{z^2}{2} \equiv e_{c,b} \left(\frac{f_{\eta_{c,b}}}{M_{\eta_{c,b}}} \right) \mathbb{V}_{\mathbb{O}\eta\gamma}. \tag{14.66}$$

Since we approximated the full bulk-to-bulk propagator for small z, the limit in (14.34) leads to a divergent integral for the coupling in (14.66). To obtain a rough estimate for this coupling, we cut off the integral at a physically reasonable value z_0 determined by the hard-wall mass spectrum in (14.37) with which we obtain

$$\mathbb{V}_{\mathbb{O}\eta\gamma} = -\frac{g_5}{\sqrt{N_f}}\kappa_\gamma z_0^4/4. \tag{14.67}$$

Analogously, we obtain for the vertex involving a photon instead of a glueball

$$\mathcal{V}_{\eta\gamma\gamma^*}(K) = \frac{e_{c,b}^2}{2\sqrt{N_f}}\int \mathrm{d}z\varphi_n(z)\times\frac{z^2}{2}, \tag{14.68}$$

with the same vertex as in (14.66)

$$\begin{aligned}\mathcal{V}_{\eta\gamma\gamma^*}(K) &\approx \frac{e_{c,b}^2}{2\sqrt{N_f}}\int \mathrm{d}z\phi_n(z)\times\frac{z^2}{2}\\ &\equiv e_{c,b}^2\left(\frac{f_{\eta_{c,b}}}{M_{\eta_{c,b}}}\right)\mathbb{V}_{\gamma\gamma\eta},\end{aligned} \tag{14.69}$$

and

$$\mathbb{V}_{\gamma\gamma\eta} = -\frac{g_5}{\sqrt{N_f}}\frac{\kappa_\gamma z_0^4}{4}. \tag{14.70}$$

To proceed with the numerical analysis, we fix f_{η_c} by the leading value obtained from pQCD [250]

$$\Gamma_{\eta\to\gamma\gamma} = 4\pi Q_c^4\alpha^2\frac{f_{\eta_c}^2}{M_{\eta_c}}, \tag{14.71}$$

with Q_c the charm quark charge. The PDG quotes the η_c two-photon decay width as $\Gamma_{\eta_c\to\gamma\gamma} = 5.376\times 10^{-6}$ GeV [9] from which one obtains

$$f_{\eta_c} = 0.327\ \mathrm{GeV}, \tag{14.72}$$

where we used $M_{\eta_c} = 2.9839$ GeV. No experimental result is available for the equivalent quantity involving η_b. However, we can fix this constant by using heavy quark symmetry

$$\frac{f_{\eta_b}}{f_{\eta_c}} = \sqrt{\frac{M_{\eta_c}}{M_{\eta_b}}}, \tag{14.73}$$

which amounts to

$$f_{\eta_b} = 0.184\ \mathrm{GeV}, \tag{14.74}$$

where $M_{\eta_b} = 9.3897$ GeV was used.

14.3 Differential Cross Section

Averaging over the initial state spins and polarizations and summing over those of the outgoing states, we obtain the differential cross section from

$$\frac{\mathrm{d}\sigma}{\mathrm{d}t} = \frac{1}{16\pi(s-M_N^2)^2}\frac{1}{2}\sum_{\mathrm{pol}}\frac{1}{2}\sum_{\mathrm{spin}}|\mathcal{A}(s,t)_{\gamma p\to\eta p}|^2 \,. \tag{14.75}$$

and the cross sections from

$$\sigma(s) = \int_{-t\,\mathrm{min}}^{-t\,\mathrm{max}} \frac{\mathrm{d}\sigma}{\mathrm{d}t}, \tag{14.76}$$

with the kinematical bounds $t_{min/max}$ fixed as in Appendix D.3. Explicitly we obtain

$$\frac{\mathrm{d}\sigma}{\mathrm{d}t} = \frac{2e^2 e_{c,b}^2 g_{CS}^2}{16\pi(s-M_N^2)^2} \times \left(\frac{f_X}{M_X}\right)^2 \times \Big(F_{\mathbb{O}}(s,t) + F_\gamma(s,t) + F_{\mathbb{O}\gamma}(s,t)\Big), \tag{14.77}$$

with the C-odd $F_{\mathbb{O}}$, photon F_γ, and mixed $F_{\mathbb{O}\gamma}$ contributions

$$\begin{aligned}
F_{\mathbb{O}}(s,t) =& -\frac{F_b(K)^2 g_{B\psi}^2 \mathbb{V}_{\mathbb{O}\gamma\eta}^2}{K^2 M_N^2} \\
&\times \Big(M_N^2 K^2(M_X^2 - M_N^2) + M_X^4 - K^2 s^2 \\
&+ K^2 s(K^2 + 2M_N^2 + M_X^2)\Big), \\
F_\gamma(s,t) =& e^4 e_X^2 \mathbb{V}_{\gamma\gamma\eta}^2 \\
&\times \Big[F_2(K)^2 K^2 \Big(\frac{-K^2 s(K^2 + 2M_N^2 + M_X^2) + K^2 s^2}{M_N^2} \\
&+ (K^2(2K^2 + M_N^2) + 3K^2 M_X^2 + M_X^4)\Big) \\
&+ 4F_2(K)F_1(K)K^2(K^2 + M_X^2)^2 \\
&+ 2F_1(K)^2\Big(K^6 + 2K^4(M_X^2 - s) - 2M_N^2 M_X^4 \\
&+ K^2(-2M_N^2(M_X^2 + 2s) + 2M_N^4 - 2sM_X^2 + M_X^4 + 2s^2)\Big)\Big], \\
F_{\mathbb{O}\gamma}(s,t) =& 0,
\end{aligned} \tag{14.78}$$

respectively.

14.3.1 Estimate of $g_{B\psi}$

The overall scale of the cross section in (14.76) is dictated by $g_{B\psi}$, the strength of the coupling of the Odderon to the nucleon. As a closed string exchange in $\mathrm{AdS}_5 \times S_5$, one would expect $g_{B\psi} \sim \sqrt{g_s}$ with $g_s = \lambda/4\pi N_c$. In holographic models, one typically encounters 't Hoof couplings around $\lambda \sim 10$, yielding $g_{B\psi} \sim 0.5$. Alternatively, one could estimate this coupling via the boundary operator in (14.1) using instantons [251]

$$\langle P'S|d^{abc}G^{a\alpha\beta}G^{b}_{\alpha\beta}G^{c\mu\nu}|PS\rangle \sim \frac{\kappa^2_{I+\bar{I}}}{\rho^3}\, f(q\rho)\, \langle P'S|\overline{\psi}\sigma^{\mu\nu}\psi|PS\rangle, \tag{14.79}$$

where $f(q\rho)$ represents the form factor induced by an instanton of size ρ. Within the relevant kinematic range for threshold production of η_c and η_b, we have $\rho\sqrt{|t_{\mathrm{min}}|} \sim 1$ and $f(q_{\,\mathrm{min}}\rho) \sim 1$. Notably, for a dense instanton ensemble as described in Ref. [252], the packing fraction of instantons is $\kappa_{I+\bar{I}} \sim 0.7$, with a mean instanton size of $\rho \sim \frac{1}{3}$ fm. This leads to an estimate for the dual coupling of $g_{B\psi} \sim \kappa^2_{I+\bar{I}} \sim 0.5$, which aligns with the string estimate.

14.3.2 Numerical Results

As discussed above, we shall consider the range $g_{B\psi} = \{1, 0.5\}$ where the first value corresponds to the pure soft-wall coupling and the second value encodes a possible suppression due to its stringy origin. Additionally, we have fixed κ to the rho meson mass, as is required by VMD, and the closed string couplings to twice that of the open string sector. Fig. 14.4a displays the various contributions to the differential cross section for threshold production of η_c at $W = 4.3\text{GeV}$ as well as the sum of all contributions. In Fig. 14.4b we compare our results to Ref. [160] (open-blue-dots), which are comparable in magnitude. The latter analysis is dominated by the Primakoff photon exchange, which, in our model, starts to take over only for higher momentum transfers. The integrated cross section is $\sigma(W = 4.3 \text{ GeV}) = \{10.3,\ 2.76\}$ pb, which is in line with previous estimates found in the literature [159, 160, 242–244]. Fig. 14.5a displays the same quantity but at a higher center of mass energy of $W = 10$ GeV. At this energy, the non-Reggeized Odderon exchange is dominant for the whole kinematically allowed range, and the integrated cross section is given by $\sigma(W = 10 \text{ GeV}) = \{202,\ 50\}$ pb. In Fig. 14.5b, we compare with the dipole approximation of Ref. [159], which considered Odderon (red-triangle) as well as photon (green-diamond) exchange and their coherent sum (black-diamond). At $t = t_{min}$, the magnitude of both models seems to agree but deviates at larger momentum transfers, with the model of Ref. [159] depleting much sooner. Note that the photon contributions are of different nature, since the model of Ref. [159] displays the Primakoff effect, which is

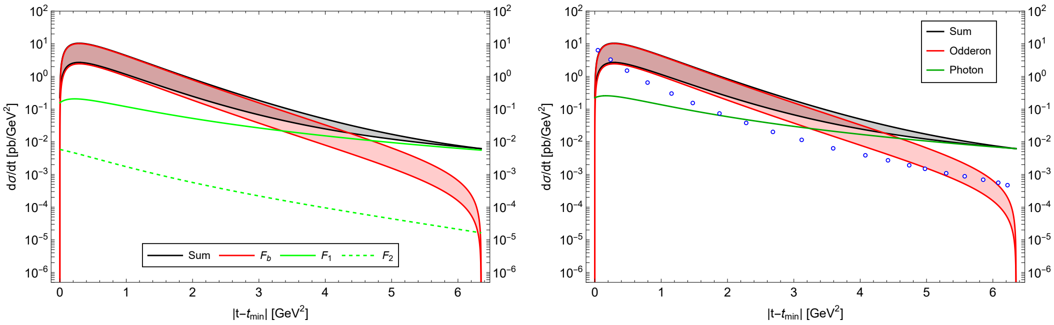

(a)

(b)

Fig. 14.4.: (a) Holographic differential cross section for threshold photoproduction of η_c at $W = 4.3$ GeV. The solid and dotted green lines correspond to the Dirac and Pauli contributions of p-wave photon exchange, respectively. The solid red line corresponds to the non-Reggeized Odderon exchange with $g_{B\psi} = \{1, 0.5\}$ and the solid black line to the sum of all contributions. (b) Holographic differential cross section as in (a) but with the photon contribution summed. The data points are from the Primakoff photon exchange estimate (open blue circles) in Ref. [160].

absent in VMD-like models. In Fig. 14.6 we show the differential cross section relevant for the future Electron-Ion Collider (EIC) [253, 254] at $W = 50$ GeV. At this energy, the cross section is given by $\sigma(W = 50\text{ GeV}) = \{242,\ 59\}$ pb. At higher center of mass energies, say, at $W = 300$ GeV, the integrated cross section starts to diverge, and one would need to Reggeize the Odderon exchange. Nevertheless, in Fig. 14.7a we show the holographic results for the different contributions to η_c productions as well as their sum. In Fig. 14.7b we compare with the pQCD analysis of Ref. [160], which considered photon exchange (open blue circles) and the Odderon models of Ref. [244] (green triangles) and Ref. [243] (orange diamonds). They are comparable in magnitude and UV behavior, though the model of Ref. [244] displays a cusp due to the sign change in their Odderon-nucleon form factor. Moving on to the production of η_b, we display in Fig. 14.8a the differential cross section at the kinematical threshold of $W = 11$ GeV. Again, the p-wave photon exchange corresponds to the green line (Dirac: solid, Pauli: dotted), a solid red line denotes the pseudovector glueball exchange, and the solid black line gives their sum. The differential cross section integrates to $\sigma(W = 11\text{ GeV}) = \{0.002,\ 0.001\}$. Interestingly, for the kinematical range allowed for η_b production, the photon contribution crosses the Odderon contribution twice for $g_{B\psi} = 0.5$.

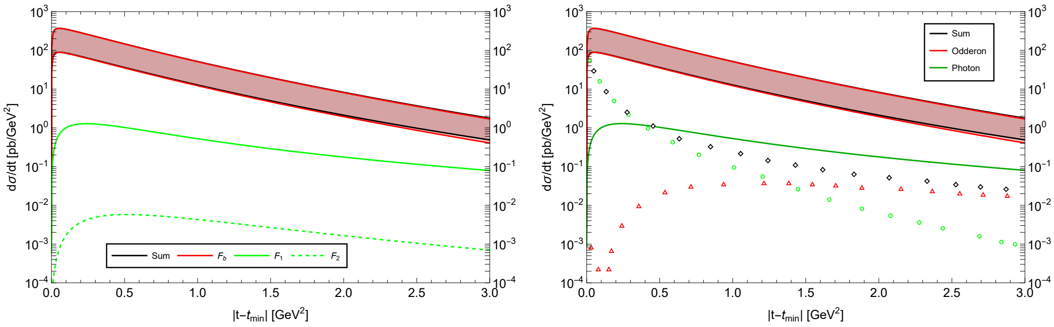

(a) (b)

Fig. 14.5.: (a) Holographic differential cross section for threshold photoproduction of η_c at $W = 10$ GeV with the same color coding as in Fig. 14.4a.
(b) Holographic differential cross section as in (a) but with the photon contribution summed. The data points correspond to the Primakoff photon exchange (green diamonds) and Odderon exchange (red triangles), as well as their sum (black diamonds) of Ref. [159].

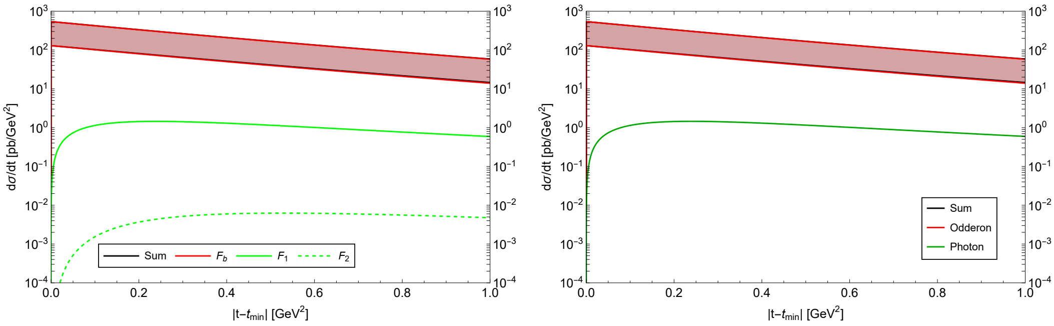

(a) (b)

Fig. 14.6.: (a) Holographic differential cross section for threshold photoproduction of η_c at $W = 50$ GeV with the same color coding as in Fig. 14.4a.
(b) Holographic differential cross section as in (a) but with the photon contribution summed.

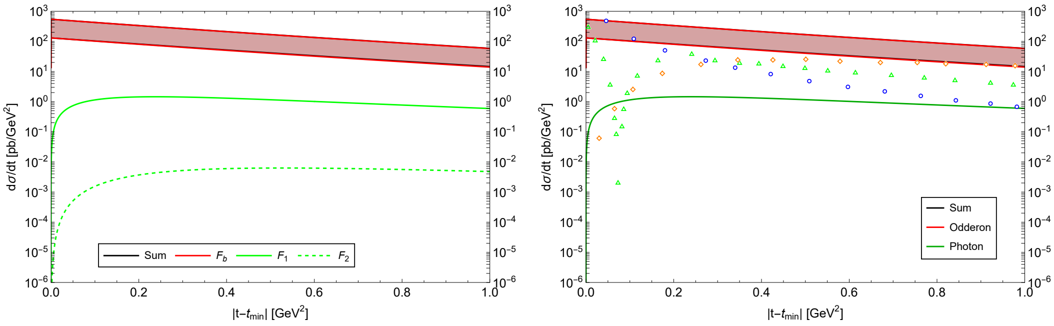

(a) (b)

Fig. 14.7.: (a) Holographic differential cross section for threshold photoproduction of η_c at $W = 300$ GeV with the same color coding as in Fig. 14.4a.
(b) Holographic differential cross section as in (a) but with the photon contribution summed. The data points correspond to the Primakoff photon exchange (blue open circles) from Ref. [160] and the Odderon models of Ref. [243] (orange diamonds) and of Ref. [244] (green-triangles).

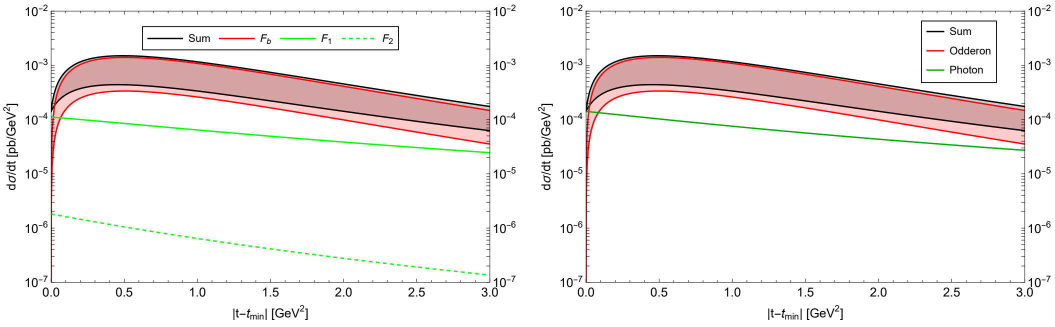

(a)

(b)

Fig. 14.8.: (a) Holographic differential cross section for threshold photoproduction of η_b at $W = 11$ GeV with the same color coding as in Fig. 14.4a. (b) Holographic differential cross section as in (a) but with the photon contribution summed.

A similar process involving Pomeron exchange is the production of vector mesons like J/Ψ and Υ, through which one might extract the gravitational form factor of the proton. We thus compare in Fig. 14.9 our holographic computations for η_c production with the holographic computations of J/Ψ production (blue) of Ref. [215] for different center of mass energies: (a) $W = 4.58$ GeV, (b) $W = 4.30$ GeV, (c) $W = 10$ GeV, (d) $W = 50$ GeV and (e) $W = 300$ GeV. In Fig. 14.9f we show the integrated cross sections for η_c and J/Ψ for different center of mass energies W. The data points correspond to measurements from SLAC [255] and Cornell [256]. The differential and integrated photoproduction cross sections for η_c are well below those for J/Ψ for the whole kinematical range considered. While measuring this process poses a challenging task for experimentalists, extracting the C-odd gluonic form factor $F_b(K)$, which probes the nucleon spin budget, from the data and comparing it to our prediction would be interesting.

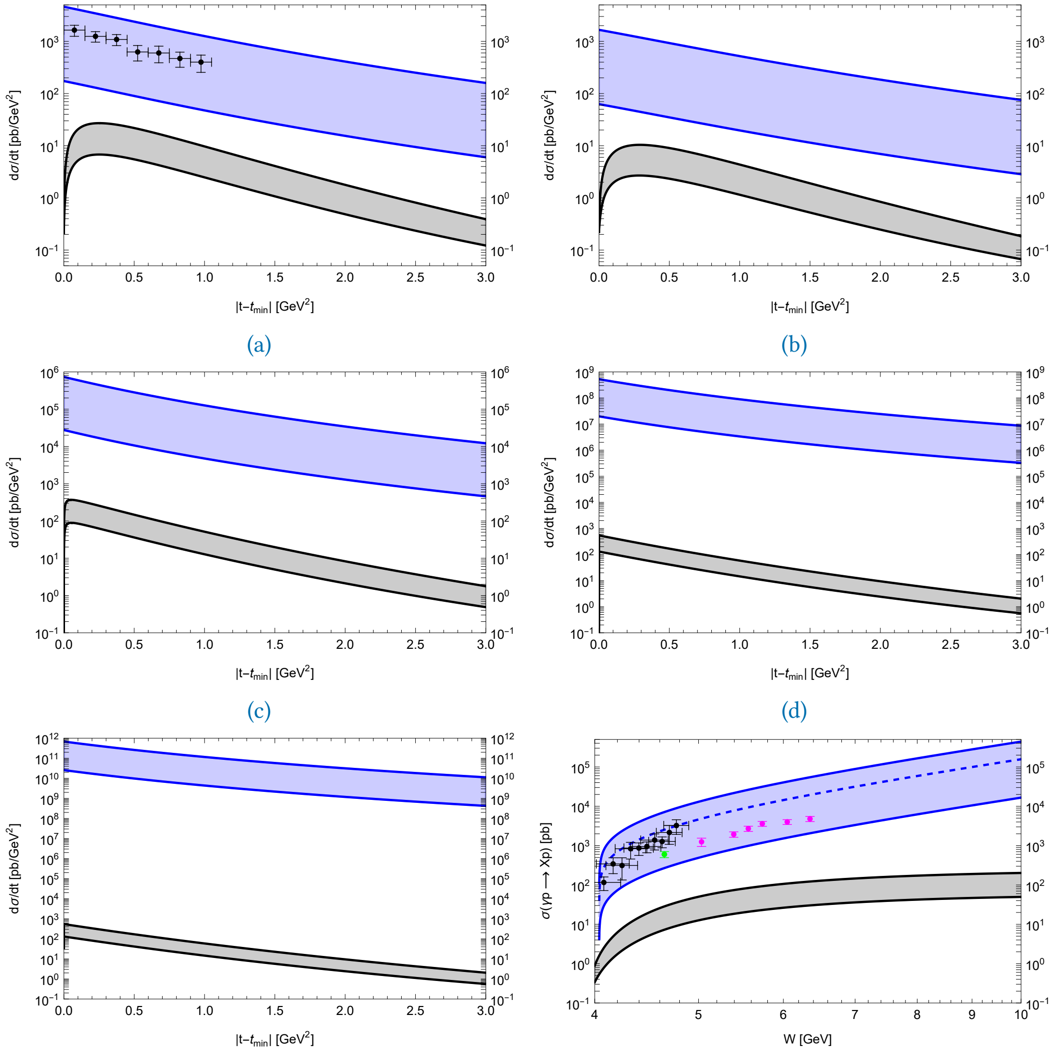

(a) (b) (c) (d) (e) (f)

Fig. 14.9.: Holographic differential and total cross sections for threshold photoproduction of J/Ψ (shaded blue) [215], and the present results for η_c (shaded black with $g_{B\psi} = \{1, 0.5\}$) at $W = 4.58$ GeV (a), $W = 4.30$ GeV (b), $W = 10$ GeV (c), $W = 50$ GeV (d) and $W = 300$ GeV (e). (f) Integrated holographic cross sections for threshold photoproduction of η_c (shaded black) and J/Ψ (shaded blue) [215]. The data points are from GlueX [257] (black), SLAC [255] (magenta) and Cornell [256] (green), respectively.

Conclusions and Final Remarks

In the first part of this thesis, we considered the Witten-Sakai-Sugimoto model to compute hadronic and radiative decay rates of various glueballs. Overall, they turned out to be rather broad resonances with surprisingly large radiative decay widths in the keV range. The latter is usually taken as evidence against the glueball nature of a resonance. A comparison of our model predictions with measurements reported by the PDG [9] showed that the resonance $f_0(1710)$ fits a glueball identification rather well once identified with the dilaton scalar glueball. Unfortunately, since the scalar meson nonet is absent in the WSS model, we cannot comment in more detail on the scenario of the fragmented scalar glueball, which is a resonance mixing strongly with the scalar isoscalar mesons. However, the reported mass and width computed in Ref. [45] seem to fit rather well when the fragmented scalar glueball is identified with the lightest, exotic scalar glueball of the WSS model once its mass is suitably adjusted. The pseudoscalar glueball inherits its interactions through mixing with the singlet η_0 meson and plays a prominent role in the realization of the Witten-Veneziano mechanism. When compared to the glueball candidate $X(2370)$, we found that the hadronic decays into two rho mesons already saturate the recently extracted width by the BES III collaboration [144]. On the other hand, the interactions of the pseudoscalar glueball with ordinary mesons arise through a formal expansion in N_f/N_c, which is not a small parameter in QCD. Already to this order, there may be significant corrections through the backreaction of the flavor branes on the original geometry or higher order effects, which the WSS model may not capture. The pseudovector glueball turned out to be the broadest resonance within the framework of the WSS model. Identifying it in experiment may thus prove extremely difficult, to say the least. A more promising candidate might be the vector glueball, which transpired to possess a rather peculiar enhancement of decays into a pair of an axial vector and vector meson. Upon adjusting the mass of the highest-spin state allowed by the supergravity limit, the decay pattern of the tensor glueball was found to be compatible with that of $f_2(1950)$.

To further look for evidence of glueballs, we turned to Regge physics in Part III. Therein, we identified the C-even Pomeron with a Reggeized tensor glueball trajectory and its C-odd counterpart, the Odderon, with a Reggeized spin-1 glueball trajectory. In the framework of holography, these states arise from the Reggeization of the exchange of a graviton and Kalb-Ramond field, respectively. We developed the repulsive wall model, a holographic bottom-up model capturing the essential features of Regge phenomenology, including Gribov diffusion, to formally address the physics of the Pomeron and Odderon. We assumed a coupling of the graviton to the QCD energy momentum tensor and coupled the Kalb-Ramond field through a 5-dimensional Pauli coupling to the Baryon. The resulting pp and $p\bar{p}$ (differential) cross sections and various forward quantities were confronted with numerous experimental measurements. While there may be a maximal Odderon contribution to these processes, we found that the current experimental data is very well described by using an eikonalized Pomeron exchange, without significant admixtures of an Odderon with intercept below 1. This is opposed to the conclusion by TOTEM and DØ [189], which attributes the diffractive pattern to an underlying Odderon exchange, but in line with the findings of Ref. [190]. We aim to develop a suitable holographic model for the maximal Odderon with intercept at 1 to further elucidate this issue in future research.

Finally, we considered diffractive photoproduction of heavy pseudoscalar mesons, which is argued to be sensitive to soft gluon exchanges in the threshold region. We have set up a holographic soft wall model for the Kalb-Ramond field and assumed a minimal 5-dimensional Pauli coupling to baryons. After fixing the C-odd gluonic form factor at the optical point to the nucleon tensor charge, we found that at center of mass energies above 10 GeV, the contribution from photon exchange is overtaken by a non-Reggeized Odderon: the pseudovector glueball. The resulting differential and integrated cross sections were found to be in the pb range, thus posing a formidable challenge for experimentalists.

While this thesis presents only a small step in the arduous journey to discovering the long anticipated but still elusive glueballs, it has successfully refined the parameter space for future investigations. The decay patterns computed in Part II suggest a significant gluonic content of the resonances $f_0(1710)$ and $f_2(1950)$. Additionally, the analysis in Part III suggests that the field of low-x physics at intermediate energies, where the Pomeron contribution does not obscure that of the Odderon, might be a suitable area for future investigations. In that regard, studying processes with polarized beams or targets are particularly promising since one can extract observables insensitive to C-even exchanges and thus provide a cleaner environment for Odderon physics. The study of these processes may also shed light on the gluonic contribution to the spin of the proton, as well as the observed single spin asymmetries, which are encoded in Generalized Parton Distribution Functions (GPDs) and Transverse Momentum Distributions (TMDs). The future EIC [253], which is currently under construction at BNL, is poised to be an exceptional tool for probing these phenomena with unprecedented detail.

Appendices

A

M-Theory Lift and Dimensional Reduction

The lift of a type IIA string-frame metric to 11-dimensional supergravity is given by the relation [79]

$$\begin{aligned} \mathrm{d}s^2 &= G_{AB}\mathrm{d}x^A\mathrm{d}x^B \\ &= e^{-2\phi/3} g_{MN}\mathrm{d}x^M\mathrm{d}x^N + e^{4\phi/3}\left(\mathrm{d}x^{11} + C_M\mathrm{d}x^M\right)^2 , \end{aligned} \tag{A.1}$$

with $M, N = 0, \ldots 9$, omitting the 11th index and $A, B = 0, \ldots 10$. The tetrads following from the decomposition in (A.1) are related via

$$E_A^{\hat{A}} = \begin{pmatrix} e^{-\phi/3} e_M^{\hat{M}} & 0 \\ e^{2\phi/3} C_M & e^{2\phi/3} \end{pmatrix} \tag{A.2}$$

By introducing the radial coordinate r related to U by $U = \frac{r^2}{2L}$, one obtains the lifted metric

$$\mathrm{d}s^2 = \frac{r^2}{L^2}\left[f(r)\mathrm{d}x_4^2 + \eta_{\mu\nu}\mathrm{d}x^\mu\mathrm{d}x^\nu + \mathrm{d}x_{11}^2\right] + \frac{L^2}{r^2}\frac{\mathrm{d}r^2}{f(r)} + \frac{L^2}{4}\mathrm{d}\Omega_4^2, \tag{A.3}$$

with $f(r) = 1 - r_{\mathrm{KK}}^6/r^6$. In the limit $r \to \infty$, this geometry reduces to the of pure $\mathrm{AdS}_7 \times S_4$. The 4-form flux of the background (7.1) is now given by

$$F_4 = \frac{6}{L}\epsilon_4. \tag{A.4}$$

Depending on whether the indices pertain to the 10-dimensional subspace or the compactified direction $x_{11} \simeq x_{11} + 2\pi R_{11}$ with $R_{11} = g_s l_s$, the form field decomposes into

$$A_{MNO} = C_{MNO}, \qquad A_{MN11} = B_{MN} \tag{A.5}$$

and its field strength into

$$F^{(11)}_{MNOP} = F_{MNOP}, \qquad F_{MNO11} = H_{MNO}. \tag{A.6}$$

Since the metric in (A.1) is non-diagonal, we obtain the twisted field strength

$$\begin{aligned} F_{\hat{M}\hat{N}\hat{O}\hat{P}} &= e^{4\phi/3}\left(F_{\hat{M}\hat{N}\hat{O}\hat{P}} + 4C_{[\hat{M}}H_{\hat{N}\hat{O}\hat{P}]}\right), \\ F_{\hat{M}\hat{N}\hat{O}1\hat{1}} &= e^{\phi/3}H_{\hat{M}\hat{N}\hat{O}}, \end{aligned} \tag{A.7}$$

where we used flat indices to simplify the computations. For easier reference, we give (6.4) again

$$S_{11} = \frac{1}{2\kappa_{11}^2}\int \mathrm{d}x\sqrt{-G}\left(R - \frac{1}{2}|F_4|^2\right) - \frac{1}{3!}\int A_3 \wedge F_4 \wedge F_4,$$

where $2\kappa_{11} = (2\pi)^7 l_P^8$, $l_P = g_s^{1/3} l_s$. Using (A.1) and (A.7), the 11-dimensional supergravity action (6.4) reduces to

$$\begin{aligned} S_{IIA} &= S_{NS} + S_R + S_{CS}, \\ S_{NS} &= \frac{1}{2\kappa_{10}^2}\int \mathrm{d}^{10}x\sqrt{-g}e^{-2\phi}\left(R + 4\nabla_M\phi\nabla^M\phi - \frac{1}{2}|H_3|^2\right), \\ S_R &= \frac{1}{2\kappa_{10}^2}\int \mathrm{d}^{10}x\sqrt{-g}\left(-\frac{1}{2}|F_2|^2 - \frac{1}{2}|\tilde{F}_4|^2\right), \\ S_{CS} &= -\frac{1}{2\kappa_{10}^2}\int \mathrm{d}^{10}x\frac{1}{2}B_2 \wedge F_4 \wedge F_4, \end{aligned}$$

as already given in (7.4).

B

Type IIA Supergravity Equations of Motion

The equations of motion following from (7.4) are given by

$$
\begin{aligned}
R_{MN} + 2\nabla_M \nabla_N \phi - \frac{1}{2} H_M{}^{OP} H_{NOP} - \frac{e^{2\phi}}{2}\left(\tilde{F}_M^{\,O} \tilde{F}_{NO} - \frac{1}{2}|F_2|^2\right)& \\
-\frac{e^{2\phi}}{2}\left(\frac{4}{3!} F_M{}^{OPQ} F_{NOPQ} - \frac{1}{2} g_{MN} |F_4|^2\right) &= 0, \\
R + 4\nabla_M \nabla^M \phi - 4\nabla_M \phi \nabla^M \phi - \frac{1}{2}|H_3|^2 &= 0, \\
\nabla_M \tilde{F}^{MN} - \frac{1}{3!} \tilde{F}^{NO_1O_2O_3} H_{O_1O_2O_3} &= 0, \\
\nabla_O\left(e^{-2\phi} H^{OMN} + C_P \tilde{F}^{OPMN}\right) - \frac{1}{2! \cdot (4!)^2 \sqrt{-g}} \epsilon^{MNO_1 \ldots O_8} F_{O_1 \ldots O_4} F_{O_5 \ldots O_8} &= 0 \\
\nabla_P \tilde{F}^{PMNO} - \frac{1}{3! \cdot 4! \sqrt{-g}} \epsilon^{MNOP_1 \ldots P_7} H_{P_1P_2P_3} \hat{F}_{P_4 \ldots P_7} &= 0.
\end{aligned}
\tag{B.1}
$$

Linearizing these equations with respect to the fluctuations of $g_{MN}, \phi,\ C_1,\ B_2, C_3$, and taking into account that neither C_1 nor B_2 are sourced by the D4-branes, one obtains

$$
\begin{aligned}
R_{MN} + 2\nabla_M \nabla_N \phi - \frac{e^{2\phi}}{2}\left(\frac{4}{3!} F_M{}^{OPQ} F_{NOPQ} - \frac{1}{2}|F_4|^2\right) g_{MN} &= 0, \\
R + 4\nabla_M \nabla^M \phi - 4\nabla_M \phi \nabla^M \phi &= 0, \\
\nabla_M F^{MN} &= 0, \\
\nabla_O\left(e^{-2\phi} H^{OMN}\right) - \frac{3R^3 \sqrt{\hat{g}_{S_4}}}{2! \cdot 4! \sqrt{-g} g_s} \epsilon^{MNO_1 \ldots O_4} F_{O_1 \ldots O_4} &= 0, \\
\nabla_P F^{PMNO} - \frac{3R^3 \sqrt{\hat{g}_{S_4}}}{3! \cdot \sqrt{-g} g_s} \epsilon^{MNOP_1 \ldots P_3} H_{P_1P_2P_3} &= 0.
\end{aligned}
\tag{B.2}
$$

TU Bibliothek, WIEN Your knowledge hub

C

Towards the Unquenched Glueball Spectrum from Holographic QCD

Lattice QCD calculations of the glueball spectrum often employ the quenched approximation, neglecting the dynamic effects of sea quarks [11, 134]. However, going beyond this approximation poses significant challenges due to computationally costly simulations and large uncertainties. While some progress on computing the unquenched glueball spectrum on the lattice has been made, results remain inconclusive, though they suggest minimal changes to the mass spectrum [13, 14, 35, 258]. In this appendix, we address this problem using holographic QCD, where only recently the first steps towards the unquenched glueball spectrum have been made [259].

The WSS model considered in Chapter 7 is formulated in the probe approximation, where the flavor branes do not backreact on the original geometry induced by the color branes. To leading order in N_f/N_c, the backreacted geometry has been worked out for localized branes in Ref. [76] and for smeared branes, where the branes are homogeneously smeared out over the compactified τ direction, in Ref. [77]. Limiting to the τ-odd fluctuation $h_{M\tau}$, for which the computations are somewhat less complex, Ref. [259] carried out the first computations of the unquenched glueball spectrum utilizing the smeared approximation. As a first step towards the full unquenched glueball spectrum for states with even τ parity, we will also consider the smeared approximation and partly use the formalism developed in [259].

The closed string action in (7.4) is no longer sufficient when backreaction effects are taken into account. This is due to the D8 branes coupling to a 9-form potential C_9, whose dual field strength is a constant. This introduces a term in the equations of motion that is amenable to a cosmological constant and a mass term for the Kalb-Ramond field B_2.

The consistent action that includes this potential is that of Romans massive type IIA supergravity [260]. Its bosonic part is given by [79]

$$\begin{aligned}
S^M_{IIA} &= S_{NS} + S_R + S_{CS} + S_M \\
S_{NS} &= \frac{1}{2\kappa^2_{10}} \int \mathrm{d}^{10}x\sqrt{-g}e^{-2\phi}\left(R + 4\nabla_M\phi\nabla^M\phi - \frac{1}{2}|H_3|^2\right) \\
S_R &= \frac{1}{2\kappa^2_{10}} \int \mathrm{d}^{10}x\sqrt{-g}\left(-\frac{1}{2}|\tilde{F}_2|^2 - \frac{1}{2}|\tilde{F}_4|^2\right) \\
S_{CS} &= -\frac{1}{2\kappa^2_{10}} \int \mathrm{d}^{10}x\frac{1}{2}B_2 \wedge \hat{F}_4 \wedge \hat{F}_4 \\
S_M &= -\frac{1}{2\kappa^2_{10}} \int \mathrm{d}^{10}x\sqrt{-g}\frac{1}{2}M_R^2 + \frac{1}{2\kappa^2_{10}} \int M_R F_{10},
\end{aligned} \tag{C.1}$$

where

$$\begin{aligned}
&\tilde{F}_2 = F_2 + M_R B_2, \quad F_2 = dC_1 \\
&\hat{F}_4 = F_4 + \frac{1}{2}M_R B_2 \wedge B_2, \quad F_4 = dC_3 \\
&\tilde{F}_4 = F_4 - C_1 \wedge H_3 + \frac{1}{2}M_R B_2 \wedge B_2., \quad H_3 = dB_2.
\end{aligned} \tag{C.2}$$

and

$$M_R = \pm\frac{N_f}{4\pi l_s} \tag{C.3}$$

is the Romans mass. The signs refer to the charge of the D8 and $\overline{\text{D8}}$ branes, respectively. From (C.2) we see that F_2 can be completely reabsorbed into B_2 when $M_R \neq 0$, introducing a Higgs-like effect where C_1 corresponds to the longitudinal mode of B_2.

The field equations following from (C.1) are given by

$$\begin{aligned}
&R_{MN} + 2\nabla_M \nabla_N \phi - \frac{1}{2} H_M{}^{OP} H_{NOP} - \frac{e^{2\phi}}{2} \left(\tilde{F}_M^{\ O} \tilde{F}_{NO} - \frac{1}{2} |F_2|^2 \right) \\
&\qquad - \frac{e^{2\phi}}{2} \left(\frac{4}{3!} F_M{}^{OPQ} F_{NOPQ} - \frac{1}{2} g_{MN} |F_4|^2 \right) + \frac{1}{2} e^{2\phi} M_R^2 g_{MN} = 0, \\
&R + 4\nabla_M \nabla^M \phi - 4\nabla_M \phi \nabla^M \phi - \frac{1}{2} |H_3|^2 = 0, \\
&\nabla_O \left(e^{-2\phi} H^{OMN} + C_P \tilde{F}^{OPMN} \right) - \frac{1}{2! \cdot (4!)^2 \sqrt{-g}} \epsilon^{MNO_1 \ldots O_8} F_{O_1 \ldots O_4} F_{O_5 \ldots O_8} \\
&\qquad - M_R \tilde{F}^{MN} - \frac{1}{2} M_R B_{OP} \tilde{F}^{OPMN} \\
&\qquad - \frac{M_R \sqrt{-g}^{-1}}{2 \cdot 2! \cdot 4!} \epsilon^{MNO_1 \ldots O_8} B_{O_1 O_2} B_{O_3 O_4} \hat{F}_{O_5 \ldots O_8} = 0, \\
&\nabla_M \tilde{F}^{MN} - \frac{1}{3!} \tilde{F}^{NO_1 O_2 O_3} H_{O_1 O_2 O_3} = 0, \\
&\nabla_P \tilde{F}^{PMNO} - \frac{1}{3! \cdot 4! \sqrt{-g}} \epsilon^{MNOP_1 \ldots P_7} H_{P_1 P_2 P_3} \hat{F}_{P_4 \ldots P_7} \\
&\qquad - \frac{M_R}{4! \sqrt{-g}} \epsilon^{MNOP_1 \ldots P_7} B_{P_1 P_2} B_{P_3 P_4} H_{P_5 P_6 P_7} = 0, \\
&\star F_{10} - \frac{1}{2} B_{MN} \tilde{F}^{MN} - \frac{3}{4!} B_{MN} B_{OP} \tilde{F}^{MNOP} \\
&\qquad - \frac{3 \sqrt{-g}^{-1}}{2! (4!)^2} \epsilon^{M_1 \ldots M_{10}} B_{M_1 M_2} B_{M_3 M_4} B_{M_5 M_6} F_{M_7 \ldots M_8} - M_R = 0, \\
&\mathrm{d}M = 0.
\end{aligned} \tag{C.4}$$

Working to first order in N_f/N_c, we see from (C.4) that C_9 does not modify the equations of motion for the dilaton and metric. Additionally, we need to take the contributions from the DBI action into account, which, in the smeared approximation, reads

$$S_{DBI} = -\frac{N_f T_8 M_{\mathrm{KK}}}{\pi} \int \mathrm{d}^{10}x \frac{\sqrt{-g}}{\sqrt{g_{44}}} e^{-\phi}, \tag{C.5}$$

where the integration region now extends over the full spacetime. For simplicity, we adopt the notation of Ref. [77] and write the line element as

$$\mathrm{d}s^2 = \left(\frac{U_{\mathrm{KK}}}{R_{\mathrm{D4}}} \right)^{3/2} \left[e^{2\lambda} \eta_{\mu\nu} \mathrm{d}x^\mu \mathrm{d}x^\nu + e^{2\tilde{\lambda}} \mathrm{d}x_4^2 \right] + R_{\mathrm{D4}}^{3/2} U_{\mathrm{KK}}^{1/2} \left[e^{-2\varphi} dr^2 + e^{2\nu} \mathrm{d}\Omega_4^2 \right], \tag{C.6}$$

with all constant factors explicit. The functions

$$\lambda(r), \quad \tilde{\lambda}(r), \quad \varphi(r), \quad \nu(r) \tag{C.7}$$

only depend on the radial coordinate, which is related to the standard WSS coordinate as[1]

$$e^{-3r} = 1 - \frac{U_{\mathrm{KK}}}{U}^{3} \tag{C.8}$$

They are given in terms of a series expansion in N_f/N_c as

$$\Psi(u) = \Psi_0(u) + \epsilon_F \psi_1(u) + \mathcal{O}(\epsilon_F^2), \tag{C.9}$$

with the effective expansion parameter given by

$$\epsilon_F = \frac{\lambda^2}{12\pi^3}\frac{N_f}{N_c}. \tag{C.10}$$

The backreacted solutions $\Psi_1(u)$ are given in terms of hypergeometric functions, and their complete expressions can be found in Ref. [77]. Before turning to the glueball modes, we will set up the formalism using the meson spectrum.

C.1 Spin-1 Mesons

The (axial) vector mesons again arise as fluctuations of the gauge fields living on the D8 brane. Pulling out the constant parts we have

$$\begin{aligned} S_{DBI} \supset & -T_8 \int \mathrm{d}^9x e^{-\phi}\sqrt{-g_8}\left[1 + \frac{1}{4}(2\pi\alpha'^2)g^{MN}g^{OP}F_{MO}F_{NP}\right] \\ = & -\kappa \int \mathrm{d}^4x\mathrm{d}z \left[\frac{1}{2}\frac{e^{\epsilon_F(-\varphi_1+4\nu_1-\phi_1)}}{(1+z^2)^{1/3}}F_{\mu\nu}^2 + \frac{9}{4}\frac{U_{\mathrm{KK}}}{R_{\mathrm{D4}}^3}e^{\epsilon_F(\varphi_1+4\nu_1+2\lambda_1-\phi_1)}(1+z^2)F_{\mu z}^2\right], \end{aligned} \tag{C.11}$$

where we performed the substitutions

$$r = -\frac{1}{3}\log\frac{z^2}{1+z^2}, \qquad \mathrm{d}r = -\frac{2}{3Z}\frac{1}{1+z^2}dZ. \tag{C.12}$$

This reduces to the familiar DBI action of the WSS model when evaluated at $\epsilon_F = 0$

$$S_{DBI} = -\kappa \int \mathrm{d}^4x\mathrm{d}z\left[\frac{1}{2}K^{-1/3}F_{\mu\nu}^2 + KM_{\mathrm{KK}}^2F_{\mu z}^2\right], \qquad K = 1 + z^2. \tag{C.13}$$

---

[1] And not to be confused with the radial coordinate of the Witten model $r^2 = 2UL$.

Following Ref. [259] we define

$$\begin{aligned} a(z) &= \frac{e^{\epsilon_F(-\varphi_1+4\nu_1-\phi_1)}}{(1+z^2)^{1/3}} \\ b(z) &= e^{\epsilon_F(\varphi_1+4\nu_1+2\lambda_1-\phi_1)}(1+z^2) \end{aligned} \tag{C.14}$$

to write

$$-\kappa\int \mathrm{d}^4x\mathrm{d}z\left[\frac{1}{2}a(z)F_{\mu\nu}^2+\frac{9}{4}\frac{U_{\mathrm{KK}}}{R_{\mathrm{D4}}^3}b(z)F_{\mu z}^2\right], \tag{C.15}$$

and expand the vector meson fields as

$$A_\mu(x^\mu,z)=\sum_n\frac{\psi_n(z)}{\sqrt{a(z)}}B_\mu(x^\mu). \tag{C.16}$$

This leads to the trivial normalization condition of the vector meson fields

$$\kappa\int \mathrm{d}z\psi_n(z)\psi_m(z)=\delta_{nm}. \tag{C.17}$$

Plugging this ansatz into the action and partially integrating the potential term gives

$$\int \mathrm{d}^4x\mathrm{d}z\sum_n\left[-\frac{1}{2}\left(F_{\mu\nu}^{(n)}\right)^2+\frac{1}{2}\lambda_n M_{\mathrm{KK}}^2\left(B_\mu^{(n)}\right)^2\right], \tag{C.18}$$

where the eigenvalue λ_n is obtained from the Hamiltonian

$$\hat{H}_\psi\psi_n(z)=-\frac{1}{\sqrt{a(z)}}\partial_Z\left[b(z)\partial_Z\left(\frac{\psi_n(z)}{\sqrt{a(z)}}\right)\right]=\lambda_n\psi_n(z) \tag{C.19}$$

Expanding all functions as

$$\chi(z)=\chi^{(0)}(z)+\epsilon_F\chi^{(1)}(z) \tag{C.20}$$

we obtain the correction to the mass by numerically solving

$$\hat{H}_\psi^{(0)}\psi_n^{(0)}(z)=-\frac{1}{\sqrt{a_0(z)}}\partial_Z\left[b_0(z)\partial_Z\left(\frac{\psi_n(z)}{\sqrt{a_0(z)}}\right)\right]=\lambda_n^{(0)}\psi_n^{(0)}(z), \tag{C.21}$$

and then perturbatively calculating

$$\lambda_n=\lambda_n^{(0)}+\epsilon_F\delta\lambda_n=\lambda_n^{(0)}+\epsilon_F\left\langle n\right|\delta\hat{H}_\psi^{(0)}\left|n\right\rangle_0 \tag{C.22}$$

We can easily compute the overlap integral by implementing a shooting method for the first five vector meson modes. In Table C.1 we show the results for the first five modes. The ratio of masses between vector and axial vector mesons is decreasing compared to

n	λ_ψ^{2n-1}	$\delta\lambda_\psi^{2n-1}$	λ_ψ^{2n}	$\delta\lambda_\psi^{2n}$
1	0.669	+0.181	1.569	-0.197
2	2.874	-0.333	4.546	-0.825
3	6.581	-1.080	9.008	-1.786
4	11.797	-4.443	14.958	-3.627
5	18.491	-5.878	22.397	-5.279

Table C.1.: Numerical results for vector meson masses.

the quenched approximation. For $\epsilon_F = 0.02$, the ratio of masses between $m_{a_1}^2/m_\rho^2 = (2.346, 2.327)$ is further away from its experimental value of 2.519. However, the mass ratio $m_{\rho(1450)}^2/m_\rho^2 = (4.302, 4.268)$ is closer to its experimental value of 3.573. The bold extrapolation to $N_f = 2$ would match this, though it needs to be taken with a grain of salt. However, one must be cautious when comparing with experimental data since the smearing approximation breaks $U(N_f) \to U(1)^{N_f}$. Thus, it can only be considered the first mode in a Kaluza-Klein expansion of the backreaction of the localized brane solution of Ref. [76].

C.2 Dilaton Scalar Glueball

The equation of motion for the dilaton following from (C.4) and (C.5) is given by

$$R + 4\nabla_M\nabla^M\phi - 4\nabla_M\phi\nabla^M\phi - \frac{\lambda}{8\pi^3}\frac{N_f}{N_c}\frac{1}{l_s^2}e^{\phi-\tilde{\lambda}} = 0. \tag{C.23}$$

Linearizing this expression, we obtain the dilaton equation of motion

$$4\nabla_M\nabla^M\tilde{\phi} - 8\nabla_M\phi\nabla^M\tilde{\phi} - \frac{\lambda}{8\pi^3}\frac{N_f}{N_c}\frac{1}{l_s^2}e^{\phi-\tilde{\lambda}} = 0, \tag{C.24}$$

where $\tilde{\phi}$ denotes the fluctuation and ϕ the background value. Decomposing the dilaton fluctuation into a holographic and 4-dimensional mode, we obtain

$$-D_4''(r) - \frac{R_{\mathrm{D4}}^3}{U_{\mathrm{KK}}}e^{-2\lambda-2\varphi}M_D^2 D_4(r) + \frac{1}{8}\epsilon_F e^{\phi-\tilde{\lambda}-2\varphi}D_4(r) = 0. \tag{C.25}$$

Treating ϵ_F as a parameter, we expand (C.61) to first order in ϵ_F and solve it using a shooting method. To compactify the interval, we transform using[2]

$$r = -\frac{2}{3}\log\sin(x) \tag{C.26}$$

---

[2] This is equivalent to $z = \tan(x)$ used in the main text.

Die approbierte gedruckte Originalversion dieser Dissertation ist an der TU Wien Bibliothek verfügbar.
The approved original version of this doctoral thesis is available in print at TU Wien Bibliothek.
TU Bibliothek WIEN Your knowledge hub

After checking that the solutions scale linear in ϵ_F, we can extract the mass correction as

$$M_D^2 = \lambda_D M_{\text{KK}}^2, \qquad \lambda_D = \lambda_D^{(0)} + \epsilon_F \lambda_D^{(1)} \tag{C.27}$$

where

$$\lambda_D^{(0)} = 2.455165, \qquad \lambda_D^{(1)} = -50.1073 \cdot 10^{-6}. \tag{C.28}$$

The mass correction is negative, which does not fit the change in mass of either scalar glueball in [13]. The reason for this could be that the dilaton and exotic scalar glueball, which are already difficult to disentangle when the closed string sector alone is considered, are no longer diagonal when flavor-brane effects are taken into account. Unfortunately, we have not yet succeeded in diagonalizing the scalar sector of the backreacted Lagrangian. We leave this topic for future work.

C.3 Pseudovector Glueball

Since the 1^{+-} nonet of ordinary mesons is absent in the WSS model, it is sufficient to consider the linearized equations of motion for the pseudovector glueball. Taking into account that even with the backreaction included, only C_3 is sourced by the background, the relevant equations in (C.4) reduce to

$$\begin{aligned} \nabla_O \left(e^{-2\phi} H^{OMN} \right) - \frac{1}{2! \cdot (4!)^2 \sqrt{-g}} \epsilon^{MNO_1 \ldots O_8} F_{O_1 \ldots O_4} F_{O_5 \ldots O_8} &= 0, \\ \sqrt{-g} \nabla_P F^{PMNO} - \frac{1}{3! \cdot 4!} \epsilon^{MNOP_1 \ldots P_7} H_{P_1 P_2 P_3} F_{P_4 \ldots P_7} &= 0. \end{aligned} \tag{C.29}$$

They are solved by using the ansatz

$$\begin{aligned} B_{\mu\nu} &= a(r) \tilde{B}_{\mu\nu}(x^\mu), \\ C_{\nu\tau r} &= \frac{3a(r)}{2 g_s M^2} e^{\tilde{\lambda} - \varphi - 4\nu} \epsilon_\nu{}^{\mu\rho\sigma} \partial_\mu \tilde{B}_{\rho\sigma}(x^\mu), \end{aligned} \tag{C.30}$$

where $\tilde{B}_{\mu\nu}$ denotes the polarization and the x^μ dependence is implicitly understood in the following. From the bulk Lagrangian, we obtain

$$a''(r) - 4\lambda' a'(r) + \frac{R_{\text{D4}}^3}{U_{\text{KK}}} M^2 e^{-2\varphi - 2\lambda} a(r) - 9 e^{8\lambda + 2\tilde{\lambda} - 2\phi} a(r) = 0, \tag{C.31}$$

and the contribution from the DBI action is given by

$$S_{D8} \supset -T_8 N_f \int \mathrm{d}^9 x\, e^{-\phi} \frac{\sqrt{-g_8}}{4} g^{MN} g^{OP} B_{MO} B_{NP}. \tag{C.32}$$

Die approbierte gedruckte Originalversion dieser Dissertation ist an der TU Wien Bibliothek verfügbar.
The approved original version of this doctoral thesis is available in print at TU Wien Bibliothek.
TU Bibliothek Your knowledge hub WIEN

The full mode equation is thus

$$a''(r) - 4\lambda' a'(r) + \frac{R_{\mathrm{D4}}^3}{U_{\mathrm{KK}}} M^2 e^{-2\varphi - 2\lambda} a(r) - 9 e^{8\lambda + 2\tilde{\lambda} - 2\phi} a(r) - \epsilon_F e^{\phi - \tilde{\lambda} - 2\varphi} a(r) = 0. \tag{C.33}$$

For the numerical solution, it is prudent to rescale $a(r)$ using

$$a(r) \to \frac{e^{3r/2}}{\sqrt{e^{3r} - 1}} N_4(r). \tag{C.34}$$

To obtain the mass correction, we again expand in terms of

$$M_{PV}^2 = \lambda_{PV} M_{\mathrm{KK}}^2, \qquad \lambda_{PV} = \lambda_{PV}^{(0)} + \epsilon_F \lambda_{PV}^{(1)} \tag{C.35}$$

where

$$\lambda_{PV}^{(0)} = 5.930777, \qquad \lambda_{PV}^{(1)} = -138 \cdot 10^{-6}. \tag{C.36}$$

The mass correction is again negative, in disagreement with Ref. [13].

C.4 Vector Glueball

Employing the same procedure as was used for the spin-1 mesons to the bulk Lagrangian for the vector glueball, we obtain

$$\begin{aligned} \mathcal{L}_{bulk}^V = & \frac{\lambda N_c^2}{32\pi^2 M_{\mathrm{KK}}^4 R_{\mathrm{D4}}^6} \int \mathrm{d}^4 x \mathrm{d}z) \left[-\frac{1}{4} c(z) \left(F_{\mu\nu}^V \right)^2 M_4(z)^2 \right. \\ & \left. -\frac{1}{2} \eta^{\mu\nu} V_\mu V_\nu M_{\mathrm{KK}}^2 \left(-z\partial_z \left(e(z) \partial_z (z M_4(z)) \right) M_4(z) + d(z) M_4(z)^2 \right) \right] \end{aligned} \tag{C.37}$$

where

$$\begin{aligned} e(z) = & \frac{1 + z^2}{z} e^{\epsilon_F (\varphi_1 - \tilde{\lambda}_1 + 4\nu_1)} \\ d(z) = & 4z e^{\epsilon_F (2\phi_1 - \tilde{\lambda}_1 - \varphi_1 - 4\nu_1)} \\ c(z) = & \frac{z}{(1 + z^2)^{1/3}} e^{\epsilon_F (-2\lambda_1 - \tilde{\lambda}_1 - \varphi_1 + 4\nu_1)} \end{aligned} \tag{C.38}$$

Expanding the DBI action to second order in B_2, the correction to the mass from the D8-branes is given by

$$-\frac{2\kappa \lambda^2 N_f}{(2\pi)^2 R^6} \int \mathrm{d}^4 x \mathrm{d}z \frac{9}{16} g(z) \frac{1}{2} M_4(z)^2 \eta^{\mu\nu} V_\mu V_\nu, \tag{C.39}$$

where

$$g(z) = \frac{16}{9}\frac{(1+z^2)}{\Box}e^{\epsilon_F(2\lambda-2\tilde{\lambda}-4\nu+3\phi-\varphi)}. \tag{C.40}$$

Similarly, as in Section 9.4, the mixing contribution is now given by

$$-\frac{\kappa\lambda}{2\pi}\frac{M_{\mathrm{KK}}}{R_{\mathrm{D4}}^3}\mathrm{tr}\int_0^\infty \mathrm{d}^4x\mathrm{d}z\frac{3}{2}h(z)M_4(z)\eta^{\mu\nu}\partial_z A_\mu(z)V_\nu(x^\mu), \tag{C.41}$$

with

$$h(z) = \frac{2}{3}\frac{(1+z^2)}{\sqrt{\Box}}e^{\epsilon_F(2\lambda+\phi-\tilde{\lambda})} \tag{C.42}$$

Note that both corrections are already present in the original WSS model, as discussed in Section 9.4.3. Rescaling the wave function via

$$M_4(z) = \sqrt{\frac{4}{27\pi N_c}}M_{\mathrm{KK}}^2R_{\mathrm{D4}}^3\frac{\tilde{M}_4(z)}{\sqrt{c(z)}}, \tag{C.43}$$

the vector glueball mode has a trivial normalization condition, and we obtain

$$\begin{aligned}\mathcal{L}_{bulk} =& \kappa\int \mathrm{d}^4x\mathrm{d}z\Big\{-\frac{1}{2}\eta^{\mu\nu}V_\mu V_\nu M_{\mathrm{KK}}^2\Big[-z\partial_z\Big(e(z)\partial_z\Big(z\frac{\tilde{M}_4(z)}{\sqrt{c(z)}}\Big)\Big)\frac{\tilde{M}_4(z)}{\sqrt{c(z)}} \\ &+d(z)\frac{\tilde{M}_4^2(z)}{c(z)}\Big]-\frac{1}{4}\left(F_{\mu\nu}^V\right)^2\tilde{M}_4(z)^2\Big\} \\ =& \int \mathrm{d}^4x\mathrm{d}z\left[-\frac{1}{4}\left(F_{\mu\nu}^V\right)^2\tilde{M}_4(z)^2-\frac{1}{2}\lambda_{(n)V}M_{\mathrm{KK}}^2\tilde{M}_4(z)^2\eta^{\mu\nu}V_\mu V_\nu\right].\end{aligned} \tag{C.44}$$

The mass eigenvalues are obtained from the Hamiltonian

$$\hat{H}_V\tilde{M}_4(z) = -\frac{z}{\sqrt{c(z)}}\partial_z\left[e(z)\partial_z\left(z\frac{\tilde{M}_4(z)}{\sqrt{c(z)}}\right)\right]+\frac{d(z)}{c(z)}\tilde{M}_4(z) = \lambda_{(n)V}\tilde{M}_4(z) \tag{C.45}$$

Pulling out the factors of M_{KK} contained in $\Box V(x^\mu)$, we can further simplify the DBI contributions to

$$S_{DBI}^{V^2} = -\epsilon_F M_{\mathrm{KK}}^2\kappa\int \mathrm{d}^4x\mathrm{d}z\frac{g(z)}{c(z)}\frac{1}{2}\tilde{M}_4(z)^2\eta^{\mu\nu}V_\mu V_\nu, \tag{C.46}$$

and

$$S_{DBI}^{vV} = -\sqrt{\epsilon_F}M_{\mathrm{KK}}^2\kappa\int_0^\infty \mathrm{d}^4x\mathrm{d}z\frac{h(z)}{\sqrt{c(z)}}\partial_z\left(\frac{\psi_n(z)}{\sqrt{a(z)}}\right)\tilde{M}_4(z), \tag{C.47}$$

where we used $\operatorname{tr} T^0 = \sqrt{N_f/2}$. The quadratic action is now given by

$$\begin{aligned}
S_V^{(2)} =& \kappa \int \mathrm{d}^4x \mathrm{d}z \sum_n \Bigg[-\frac{1}{4} \left(F^{(n)}_{\mu\nu} \right)^2 - \frac{1}{2} m_n^2 \left(B^{(n)}_\mu \right)^2 \\
& -\frac{1}{4} \left(F^{V(n)}_{\mu\nu} \right)^2 - \frac{1}{2} \eta^{\mu\nu} V^{(n)}_\mu V^{(n)}_\nu M_{\mathrm{KK}}^2 \left(\lambda_{V(n)} + \epsilon_F \frac{g(z)}{c(z)} \right) \Bigg] \\
=& \int \mathrm{d}^4x \sum_n \Bigg[-\frac{1}{4} \left(F^{(n)}_{\mu\nu} \right)^2 - \frac{1}{2} m_n^2 \left(B^{(n)}_\mu \right)^2 \\
& -\frac{1}{4} \left(F^{V(n)}_{\mu\nu} \right)^2 - \frac{1}{2} \eta^{\mu\nu} V^{(n)}_\mu V^{(n)}_\nu M_{\mathrm{KK}}^2 \left(\lambda_{V(n)} + \epsilon_F \delta\lambda^{DBI}_{V(n)} \right) \Bigg],
\end{aligned} \tag{C.48}$$

and the mixing term

$$\begin{aligned}
S_{mixing} &= \kappa \int \mathrm{d}^4x \mathrm{d}z \sum_{m,n} \sqrt{\epsilon_F} M_{\mathrm{KK}}^2 \frac{h(z)}{\sqrt{c(z)}} \partial_z \left(\frac{\psi_m(z)}{\sqrt{a(z)}} \right) \tilde{M}_4^{(n)}(z) \eta^{\mu\nu} v^{(m)}_\mu V^{(n)}_\nu \\
&= -\int \mathrm{d}^4x \sum_{m,n} \sqrt{\epsilon_F} \xi_1^{mn} \eta^{\mu\nu} v^{(m)}_\mu V^{(n)}_\nu,
\end{aligned} \tag{C.49}$$

where we defined

$$\delta\lambda^{DBI}_{V(n)} \equiv \left\langle n \left| \frac{g(z)}{c(z)} \right| n \right\rangle, \qquad \xi_1^{mn} \equiv -M_{\mathrm{KK}}^2 \left\langle n \left| \frac{h(z)}{\sqrt{c(z)}} \partial_z \frac{1}{\sqrt{a(z)}} \right| \psi_m \right\rangle, \tag{C.50}$$

and generalized the action to include the higher radial modes as well. Note that it is sufficient to take the original background for the corrections arising from the DBI action on the D8-branes.

As in Section 9.4.3, the action is diagonalized by

$$\begin{aligned}
V_\mu &\to V_\mu \cos\theta - v_\mu \sin\theta, \\
v_\mu &\to V_\mu \sin\theta + v_\mu \cos\theta,
\end{aligned} \tag{C.51}$$

with the squared masses now given by

$$\begin{aligned}
\tilde{m}^2 &= m^2 \left(\cos\theta^2 + \frac{M_V^2}{m^2} \sin\theta^2 - \frac{2\xi_1}{m^2} \sin\theta\cos\theta \right), \\
\tilde{M}_V^2 &= M_V^2 \left(\cos\theta^2 + \frac{m^2}{M_V^2} \sin\theta^2 + \frac{2\xi_1}{M_V^2} \sin\theta\cos\theta \right).
\end{aligned} \tag{C.52}$$

Using

$$\begin{aligned}
M_V &= M_{\mathrm{KK}}^2 \left(\lambda_V^{(0)} + \epsilon_F \delta\lambda_V^{(1)} + \epsilon_F \delta\lambda_V^{DBI} \right) \\
m &= M_{\mathrm{KK}}^2 \left(\lambda^{(0)} + \epsilon_F \delta\lambda^{(1)} \right)
\end{aligned} \tag{C.53}$$

n	λ_ψ^{2n-1}	$\delta\lambda_\psi^{2n-1}$	λ_V^n	$\delta\lambda_V^n$	$\delta\lambda_{V(n)}^{DBI}$
1	0.669	+0.181	9.227	-2.533	+0.867
2	2.874	-0.333	15.954	-4.837	+1.234
3	6.581	-1.064	24.155	-7.429	+1.737
4	11.797	-4.316	33.837	-9.288	+2.353
5	18.491	-5.644	45.001	-10.79	+3.072

Table C.2.: Numerical results for vector meson and vector glueball masses.

and (9.46), as well as the the mixing contribution from (C.50) for $n = 1$, we obtain the mixing angle

$$|\theta| = 2.76 \ldots 2.55^\circ \tag{C.54}$$

and the corrected masses

$$\begin{aligned}\tilde{m}^2 &= 0.798 \ldots 0.7422 M_{\text{KK}}^2 = (845 \ldots 818)^2 \,\text{MeV}^2 \\ \tilde{M}_V^2 &= 7.995 \ldots 8.526 M_{\text{KK}}^2 = (2684 \ldots 2771)^2 \,\text{MeV}^2\end{aligned} \tag{C.55}$$

where we expanded to linear order in ϵ_F.

The results for the mass corrections are collected in Table C.2. They are consistent with the observations in Ref. [259] that glueball masses are corrected downwards. The correction from the DBI action, however, is positive. The general statement that the total mass correction is always negative is thus not true (see Section C.5) The mixing term in (C.50) for and $1 \leq m, n \leq 5$ is given by

$$\xi_1 = M_{\text{KK}}^2 \begin{pmatrix} -0.346849 & -0.242167 & 0.0611645 & -0.00716388 & 0.00148879 \\ 0.403661 & -0.427151 & -0.669275 & 0.0811266 & -0.018741 \\ -0.517088 & 0.779097 & -0.019303 & -0.00195332 & 0.147257 \\ 0.563727 & -1.21228 & 0.584095 & -1.63627 & -0.126371 \\ -0.638369 & 1.46602 & -1.36052 & 1.49765 & -1.85748 \end{pmatrix} \tag{C.56}$$

The overlap integrals involving the mode $m = 5$ are relatively large, signaling that this mode is already beyond a perturbative approach. In principle, one would need to carry out a full diagonalization of this system, including the higher modes in n and up to $m = 4$. We leave this for future work. While there exists no result from unquenched lattice QCD for the vector glueball, the corrections for states where they have been computed are of the order of 10% for almost all states [13]. We view the numerical smallness of the perturbations in Table C.2 as a further indication that unquenching effects on the glueball mass spectrum remain small. Furthermore, the overlap integral that generates mixing between the vector glueball and singlet vector mesons is small, signaling a mostly unmixed vector glueball.

C.5 Tensor Glueball

Linearizing the bulk equations of motion (C.4) with the DBI contribution in (C.5) in terms of metric fluctuations, we obtain

$$\begin{aligned}&\frac{1}{2}\left(\nabla^O\nabla_M h_{ON}+\nabla^O\nabla_N h_{MO}\right)-\frac{1}{2}\nabla^2 h_{MN}-\frac{1}{2}\nabla_M\nabla_N h\\&-\left(\nabla_M h_N{}^O+\nabla_N h_M{}^O-\nabla^O h_{MN}\right)\nabla_O\bar{\phi}\\&+\left[\frac{9}{4}\left(U_{\mathrm{KK}}R_{\mathrm{D4}}^3\right)^{-1/2}e^{2\bar{\phi}-8\nu}+\frac{\lambda}{16\pi^3 l_s^2}\frac{N_f}{N_c}e^{\phi-\tilde{\lambda}}\right]h_{MN}=0.\end{aligned} \tag{C.57}$$

The ansatz for the tensor mode is given by

$$h_{\mu\nu}=\left(\frac{U_{\mathrm{KK}}}{R_{\mathrm{D4}}}\right)^{3/2}e^{2\lambda}T_4(r)T_{\mu\nu}e^{ikx},\quad k^2=-M_T^2\quad T_{\mu\nu}T^{\mu\nu}=1\text{ wrt }\eta_{\mu\nu} \tag{C.58}$$

and seen to solve the mode equation

$$T_4''(r)+\left(\frac{R_{\mathrm{D4}}^3}{U_{\mathrm{KK}}}M_T^2e^{-2\lambda-2\varphi}-\frac{9}{2}e^{2\phi-8\nu-2\varphi}+2\lambda''\right)T_4(r)=\frac{9}{8}\epsilon_F T_4(r)e^{\phi-\tilde{\lambda}-2\varphi}. \tag{C.59}$$

We can simplify this further by utilizing the equation of motion for λ, which, in our convention with all constant factors explicit, reads

$$\lambda''(r)=\frac{9}{4}e^{2\phi-8\nu-2\varphi}+\frac{\epsilon_F}{4}e^{\phi-\tilde{\lambda}-2\varphi}, \tag{C.60}$$

to get

$$T_4''(r)+\frac{R_{\mathrm{D4}}^3}{U_{\mathrm{KK}}}M^2e^{-2\lambda-2\varphi}T_4(r)=\frac{5}{8}\epsilon_F e^{\phi-\tilde{\lambda}-2\varphi}T_4(r). \tag{C.61}$$

We solve (C.61) by using a shooting method for various values of ϵ_F. After checking that the results scale linear in ϵ_F, we can extract the mass correction as

$$M_T^2=\lambda_T M_{\mathrm{KK}}^2,\qquad \lambda_T=\lambda_T^{(0)}+\epsilon_F\lambda_T^{(1)} \tag{C.62}$$

where

$$\lambda_T^{(0)}=2.455165,\qquad \lambda_T^{(1)}=15.0609\cdot 10^{-6}. \tag{C.63}$$

The mass correction for the tensor glueball is positive, in agreement with expectations from lattice QCD [13]. Comparing (C.57) and (C.25), we see that they obey a Schrödinger-type equation with slightly different potentials

$$-H''(r) + V(r)H(r) = 0, \quad V(r) = -\frac{R^3}{U_{\text{KK}}} e^{-2\lambda - 2\varphi} M^2_{D/T} + \begin{cases} \frac{1}{8}\epsilon_F e^{\phi - \tilde{\lambda} - 2\varphi} & \text{Dilaton} \\ \frac{5}{8}\epsilon_F e^{\phi - \tilde{\lambda} - 2\varphi} & \text{Tensor}, \end{cases} \tag{C.64}$$

The degeneracy, which originally arose through the isometries of the background, is seen to be lifted in the backreacted case, even in the smeared approximation. We further note that the potentials in (C.64) become strictly positive for $M^2 < 0$, which excludes a tachyonic glueball state. The backreaction reinforces this behavior even further.

Kinematics

D

D.1 Two-Body Decay

Consider the reaction

$$A \to 1 + 2 \tag{D.1}$$

which is depicted in Fig. D.1. The scattering direction is chosen to be in the z-direction

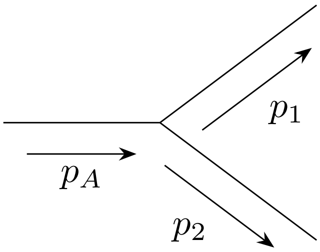

Fig. D.1.: Kinematics of the two-body decay.

such that the momenta are given by $p_A^\mu = (m_A, 0, 0, 0)$, $p_1^\mu = (k_1, 0, 0, p)$ and $p_2^\mu = (k_2, 0, 0, -p)$ with

$$\begin{aligned} k_{1,2} =& \frac{m_A^2 - m_{2,1}^2 + m_{1,2}^2}{2m_A} \\ p =& \frac{\sqrt{(m_A^2 - (m_1 + m_2)^2)(m_A^2 - (m_1 - m_2)^2)}}{2m_A} \end{aligned} \tag{D.2}$$

satisfying $p_1 + p_2 = p_A$ and $p_i^2 = -m_i^2$. The corresponding polarization vectors read $q_{A,1,2}^{(m=1)\mu} = -\frac{1}{\sqrt{2}}(0, 1, i, 0)$, $q_{A,1,2}^{(m=-1)\mu} = \frac{1}{\sqrt{2}}(0, 1, -i, 0)$, $q_{1,2}^{(m=0)\mu} = \frac{1}{m_{1,2}}(p, 0, 0, k_{1,2})$

and $q_A^{(m=0)\mu} = (0,0,0,1)$. For massless particles, we drop the $(m=0)$ polarization. For spin-2 particles, we define the polarization tensors by

$$\begin{aligned}
q_i^{(m=2)\mu\nu} &= q_i^{(m=1)\mu} q_i^{(m=1)\nu} \\
q_i^{(m=1)\mu\nu} &= \frac{1}{\sqrt{2}} \left(q_i^{(m=1)\mu} q_i^{(m=0)\nu} + q_i^{(m=0)\mu} q_i^{(m=1)\nu} \right) \\
q_i^{(m=0)\mu\nu} &= \frac{1}{\sqrt{6}} \left(q_i^{(m=1)\mu} q_i^{(m=-1)\nu} + 2 q_i^{(m=0)\mu} q_i^{(m=0)\nu} + q_i^{(m=-1)\mu} q_i^{(m=1)\nu} \right) \\
q_i^{(m=-1)\mu\nu} &= \frac{1}{\sqrt{2}} \left(q_i^{(m=-1)\mu} q_i^{(m=0)\nu} + q_i^{(m=0)\mu} q_i^{(m=-1)\nu} \right) \\
q_i^{(m=-2)\mu\nu} &= q_i^{(m=-1)\mu} q_i^{(m=-1)\nu},
\end{aligned}$$

which amounts to replacing the spin-2 polarization sums by

$$\sum_{m=-2}^{2} q_i^{(m)\mu\nu} \left(q_i^{(m)\rho\sigma} \right)^\star \to \frac{1}{2} \left(P^{\mu\rho}(k_i) P^{\nu\sigma}(k_i) + P^{\mu\sigma}(k_i) P^{\nu\rho}(k_i) - \frac{2}{3} (P^{\mu\nu}(k_i) P^{\rho\sigma}(k_i) \right) \tag{D.3}$$

where $P^{\mu\nu}(k_i) = -\eta^{\mu\nu} + \frac{k_i^\mu k_i^\nu}{k_i^2}$. Note the different normalization from [133] by a factor of 2: $\left(q_i^{(m)} \right)^2 = 1$.

To obtain the decay rate, one needs to integrate over the two-body phase space

$$\Gamma_{A \to 1\,2} = \frac{(2\pi)^4}{2 m_A} \int \frac{\mathrm{d}^3 p_1}{(2\pi)^3 2 k_1} \frac{\mathrm{d}^3 p_2}{(2\pi)^3 2 k_2} |\mathcal{M}_{A \to 1\,2}|^2, \tag{D.4}$$

which can be carried out analytically, with the result

$$\Gamma_{A \to 1\,2} = \frac{|p|}{8\pi} |\mathcal{M}_{A \to 1\,2}|^2, \tag{D.5}$$

since the on-shell relations fix all angles.

D.2 Three-Body Decay

Following [261] (see also [9]), we consider the reaction

$$A \to 1 + 2 + 3 \tag{D.6}$$

which is depicted in Fig. D.2. Working in the rest frame of the decaying particle, the

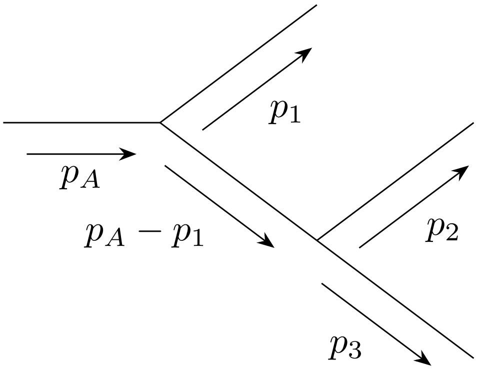

Fig. D.2.: Kinematics of the three-body decay.

three-body decay width is given by

$$\begin{aligned} \mathrm{d}\Gamma &= \frac{1}{2m_A}\frac{\mathrm{d}^3p_1}{(2\pi)^3}\frac{\mathrm{d}^3p_2}{(2\pi)^3}\frac{\mathrm{d}^3p_3}{(2\pi)^3}\frac{|\mathcal{M}|^2}{2E_1 2E_2 2E_3}(2\pi)^4\delta^4(p_A - p_1 - p_2 - p_3) \\ &= \frac{1}{(2\pi)^5}\frac{|\mathcal{M}|^2}{2m_A}\frac{\mathrm{d}^3p_1}{2E_1}\frac{\vec{p_2}^2}{2E_2}\frac{\mathrm{d}|\vec{p_2}|\mathrm{d}\cos\theta_{12}\mathrm{d}\phi_{12}}{2E_3}\delta(m_A - E_1 - E_2 - E_3). \end{aligned} \tag{D.7}$$

Using $\vec{p_3} = -\vec{p_1} - \vec{p_2}$ we can rewrite E_3 as

$$E_3^2 = m_3^2 + \vec{p_1}^2 + \vec{p_2}^2 + 2|\vec{p_1}||\vec{p_2}|\cos\theta_{12} \tag{D.8}$$

to obtain

$$E_3\mathrm{d}E_3 = |\vec{p_1}||\vec{p_2}|\mathrm{d}\cos\theta_{12}, \tag{D.9}$$

which can be used to integrate over the energy-conserving delta function. Furthermore, we can also carry out the integration over ϕ_{12}

$$\mathrm{d}\Gamma = \frac{1}{(2\pi)^4}\frac{|\mathcal{M}|^2}{2m_A}\frac{|\vec{p_1}|\mathrm{d}|\vec{p_1}|}{2E_1}\frac{|\vec{p_2}|\mathrm{d}|\vec{p_2}|}{2E_2}\mathrm{d}\cos\theta_1\mathrm{d}\phi_1. \tag{D.10}$$

Integrating over the remaining angles, we obtain

$$\mathrm{d}\Gamma = \frac{1}{(2\pi)^3}\frac{|\mathcal{M}|^2}{2m_A}\frac{|\vec{p_1}|\mathrm{d}|\vec{p_1}|}{2E_1}\frac{|\vec{p_2}|\mathrm{d}|\vec{p_2}|}{2E_2}. \tag{D.11}$$

Using $E_i\mathrm{d}E_i = |\vec{p_i}|\mathrm{d}|\vec{p_i}|$ we are left with

$$\mathrm{d}\Gamma = \frac{1}{(2\pi)^3}\frac{|\mathcal{M}|^2}{2m_A}\mathrm{d}E_1\mathrm{d}E_2. \tag{D.12}$$

It is now convenient to define the center of mass energies of the subsystems as

$$\begin{aligned} s_{ij} = -(p_i + p_j)^2, \quad E_i = \frac{m_A^2 + m_i^2 - s_{jk}}{2m_A} \\ m_A^2 + m_1^2 + m_2^2 + m_3^2 = s_{12} + s_{23} + s_{13} \end{aligned} \tag{D.13}$$

with which we finally arrive at

$$\mathrm{d}\Gamma = \frac{1}{(2\pi)^3} \frac{|\mathcal{M}|^2}{32 m_A^3} \mathrm{d}s_{ij} \mathrm{d}s_{jk}, \tag{D.14}$$

where the integration region is bounded by

$$\begin{aligned} (m_1 + m_2)^2 \leq & s_{12} \leq (m_A - m_3)^2, \\ (E_{23}^*)^2 - (k_2^* + k_3^*)^2 \leq & s_{23} \leq (E_{23}^*)^2 - (k_2^* - k_3^*)^2 \\ E_{23}^* \equiv & E_2^* + E_3^* \\ \vec{k}_i^* = & \sqrt{(E_i^*)^2 - m_i^2}. \end{aligned} \tag{D.15}$$

Note the dependence of s_{23} on s_{12} through the energies of the particles in the s_{12} rest frame

$$E_2^* = \frac{s_{12} - m_1^2 + m_2^2}{2\sqrt{s_{12}}}, \quad E_3^* = \frac{m_A^2 - s_{12} - m_3^2}{2\sqrt{s_{12}}}. \tag{D.16}$$

A plot of (D.14) over s_{ij} and s_{jk} with the proper kinematical bounds in (D.15) is known as Dalitz plot. The kinematics are fixed by the on-shell relations

$$\begin{aligned} p_A^2 = -m_A^2, \quad p_i^2 = -m_i^2, \quad s_{ij} = -(p_i - p_j)^2 \\ p_i \cdot p_j = \frac{1}{2}(m_i^2 + m_j^2 - s_{ij}) \quad p_A \cdot p_i = \frac{1}{2}(s_{jk} - m_A^2 - m_i^2), \end{aligned} \tag{D.17}$$

and the momenta

$$\begin{aligned} |\vec{p}_i| &= \frac{\sqrt{\lambda(m_A^2, m_i^2, s_{jk})}}{2m_A}, & E_i &= \frac{m_A^2 + m_i^2 - 2_{jk}}{2m_A}, \\ p_{1,2} &= (E_{1,2}, p_{1,2}\cos\theta_{1,2}, p_{1,2}\sin\theta_{1,2}, 0), & q_{1,2}^{(1)} &= (0, 0, 0, 1), \\ q_{1,2}^{(2)} &= (0, -\sin\theta_{1,2}, -\cos\theta_{1,2}, 0), & q_{1,2}^{(3)} &= 1/m_{1,2}(|\vec{p}_{1,2}|, E_{1,2}\cos\theta_{1,2}, E_{1,2}\sin\theta_{1,2}, 0) \\ p_3 &= (E_3, p_3, 0, 0), & q_3^{(1)} &= (0, 0, 0, 1) \\ q_3^{(2)} &= (0, 0, 1, 0), & q_3^{(3)} &= 1/m_3(|\vec{p}_3|, E_3, 0, 0), \end{aligned} \tag{D.18}$$

Die approbierte gedruckte Originalversion dieser Dissertation ist an der TU Wien Bibliothek verfügbar.
The approved original version of this doctoral thesis is available in print at TU Wien Bibliothek.
TU Bibliothek WIEN Your knowledge hub

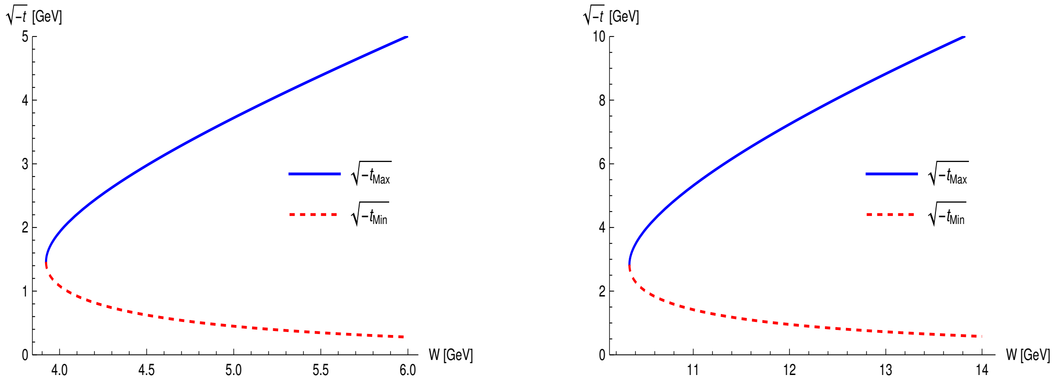

(a) (b)

Fig. D.3.: Minimal and maximal transverse momentum transfer t_{min}, t_{max} in the physical region for η_c (a) and η_b (b) versus $W = \sqrt{s}$. The photon momentum is taken to be at the optical point $q^2 = -Q^2 = 0$, and the hadron masses are given by $M_N = 0.938$ GeV, $M_{\eta_b} = 2.984$ GeV and $M_{\eta_b} = 9.399$ GeV.

given in the rest frame of the decaying particle with the reaction plane aligned by particle A and 3 and where $\lambda(a,b,c) = a^2 + b^2 + c^2 - 2ab - 2ac - 2bc$ is the Källén function. Momentum conservation then implies

$$\cos\theta_i = \frac{|\vec{p}_j|^2 - |\vec{p}_i|^2 - |\vec{p}_3|^2}{2|\vec{p}_i||\vec{p}_3|}. \tag{D.19}$$

D.3 Photoproduction at Threshold

The meson photoproduction process is characterized by two Lorentz-invariant quantities, s and t. The Mandelstam variable s is defined as the square of the total center-of-mass energy $s = (q_1 + p_1)^2$, and is related to the center-of-mass energy by $W = \sqrt{s}$. The variable $t = \Delta^2$ is the square of the four-momentum transfer, where $\Delta^\mu = (p_2 - p_1)^\mu$. For photoproduction, the virtuality of the photon is zero $Q^2 = 0$, while leptoproduction, which involves a virtual photon, can also be studied with slight modifications of the following formulas. The external states are fixed by the on-shell conditions[1]

$$p_1^2 = p_2^2 = M_N^2 \,, \qquad q_1^2 = 0 \,, \qquad q_2^2 = M_X^2 .$$

---

[1] This time with the metric in mostly minus convention.

With these conditions, one may parametrize the four-momenta in the center of mass frame as

$$q_1 = \left(\frac{s - M_N^2}{2\sqrt{s}},\ 0,\ -\frac{s - M_N^2}{2\sqrt{s}} \right) \tag{D.20}$$

$$q_2 = \left(\frac{s + M_X^2 - M_N^2}{2\sqrt{s}},\ -|\vec{p}_X| \sin\theta,\ -|\vec{p}_X| \cos\theta \right)$$

$$p_1 = \left(\frac{s + M_N^2}{2\sqrt{s}},\ 0,\ \frac{s - M_N^2}{2\sqrt{s}} \right)$$

$$p_2 = \left(\frac{s - M_X^2 + M_N^2}{2\sqrt{s}}, |\vec{p}_X| \sin\theta,\ |\vec{p}_X| \cos\theta \right)$$

where M_N is the nucleon mass, M_X is the mass of the produced meson, and θ is the scattering angle in the center of mass frame. The magnitude of the outgoing three-momentum reads

$$|\vec{p}_X| = \left(\frac{[s - (M_X + M_N)^2][s - (M_X - M_N)^2]}{4s} \right)^{1/2}, \tag{D.21}$$

and the scattering angle is fixed by

$$\cos\theta = \frac{2st + (s - M_N^2)^2 - M_X^2(s + M_N^2)}{2\sqrt{s}|\vec{p}_X|(s - M_N^2)} \tag{D.22}$$

with $\bar{p}^\mu = \frac{1}{2}(p_1 + p_2)^\mu$. At threshold $\sqrt{s} \to M_N + M_X$ and the momentum transfer t is near the threshold value t_{th}

$$t_{th} = -\frac{M_N M_X^2}{M_N + M_X} \tag{D.23}$$

In Fig. D.3 we display the kinematically allowed region in $(W, \sqrt{-t})$ for threshold production of η_c and η_b, respectively. Near threshold $s \gtrsim (M_N + M_X)^2$ and the proton factorizes into parton degrees of freedom, provided the produced meson is heavy enough. In this limit, the incoming and outgoing nucleons are on the light cone, up to M_N^2/M_X^2 corrections. In this kinematical region, the outgoing meson has a skewness of order 1, leading to the suppression of higher-twist contributions [245, 262–264].

E

Deep Inelastic Scattering in the Witten-Sakai-Sugimoto Model

DIS is a cornerstone of high-energy physics, providing crucial insights into the fundamental structure of matter. In a DIS experiment, a target particle (typically a proton or neutron) is bombarded with a lepton beam (electrons, muons, or neutrinos), and the resulting scattering patterns are analyzed. This process is inelastic, meaning that the internal state of the target particle is altered, allowing for the investigation of its constituents. The term "deep" refers to the high energies involved, which enable probing the target at very small distance scales.

The parton model, a fundamental theoretical framework for understanding DIS, posits that the target particle is composed of point-like constituents called partons (quarks and gluons) [265]. DIS experiments have provided compelling evidence for the existence of these partons and their interactions [266].

The low-x regime, where the parton struck by the lepton carries a small fraction of the target's momentum, is of particular interest [267]. It is theorized that as x decreases, the density of gluons within the proton increases significantly. Understanding this high gluon density regime is essential for testing the limits of QCD. In the extreme low-x limit, gluon density saturation may occur [267, 268], potentially leading to novel phenomena that could offer insights into the fundamental nature of matter. Moreover, the low-x regime is relevant for interpreting the interactions of high-energy cosmic rays with atmospheric nuclei.

The HERA collider at DESY (Germany) was pivotal for investigating low-x DIS, colliding electrons or positrons with protons [269]. The data collected at HERA have significantly advanced our understanding of proton structure in this regime. Future experiments, such as the EIC at BNL (US), are poised to further explore the low-x frontier over a wide kinematical range [253, 254].

In this appendix, we explore to what extent a soft Pomeron exchange within the WSS model can describe the data gathered by HERA. To this end, we focus on low virtualities and thus describe the soft Pomeron as a Reggeized tensor glueball exchange coupled to

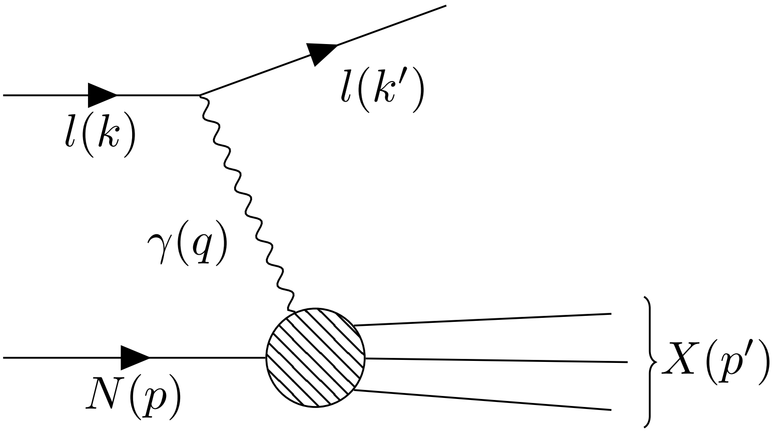

Fig. E.1.: Deep inelastic lepton-proton scattering into a collection of final states X.

baryons. The latter are modelled by a holographic fermion action that arises through quantization of the instanton moduli space of the flavor gauge fields [209, 222, 270–272].

E.1 Kinematics

The standard kinematical variables to describe the deep inelastic scattering of Fig. E.1 are given by[1] [266]

$$\begin{aligned} s &= -(p+k)^2, \\ q &= k - k', \\ q^2 &\equiv Q^2 \\ W^2 &= -p'^2 = -(p+q)^2, \\ \nu &= -\frac{p\cdot q}{m_p} = \frac{W^2+Q^2-m_p^2}{2m_p}, \\ x &= -\frac{Q^2}{2p\cdot q} = \frac{Q^2}{W^2+Q^2-m_p^2}, \\ y &= \frac{p\cdot q}{p\cdot k} = \frac{W^2+Q^2-m_p^2}{s-m_p^2}. \end{aligned} \tag{E.1}$$

Furthermore, we define the ratio of longitudinal and transverse polarization strengths of the virtual photon as [273]

$$\varepsilon = \frac{2(1-y)-y^2\delta(W^2,Q^2)}{1+(1-y)^2+y^2\delta(W^2,Q^2)}, \tag{E.2}$$

---

[1] Recall that we use the mostly plus convention of the metric

Die approbierte gedruckte Originalversion dieser Dissertation ist an der TU Wien Bibliothek verfügbar.
The approved original version of this doctoral thesis is available in print at TU Wien Bibliothek.
TU Bibliothek Your knowledge hub WIEN

where

$$\delta(W^2, Q^2) = \frac{2m_p^2 Q^2}{(W^2 + Q^2 - m_p^2)^2}. \tag{E.3}$$

E.2 Differential cross section

Following Ref. [274], the differential cross section is given by

$$\begin{aligned} \mathrm{d}\sigma &= \sum_X \int \frac{\mathrm{d}^3 k'}{(2\pi)^3 2E'} (2\pi)^4 \delta(k + p - k' - p') \frac{|\mathcal{M}|^2}{2E2M} \\ &= \sum_X \int \frac{\mathrm{d}^3 k'}{(2\pi)^3 2E'} \frac{(2\pi)^4 \delta(k + p - k' - p')}{2E2M} \frac{e^4}{q^4} \\ &\quad \times \langle p, \lambda | \, j_h^\mu(0) \, | X \rangle \langle X | \, j_h^\nu(0) \, | p, \lambda \rangle \langle k, s_l | \, j_{l\mu}(0) \, | k' \rangle \langle k' | \, j_{l\nu}(0) \, | k, s_l \rangle , \end{aligned} \tag{E.4}$$

where we sum over the collection of final states X. It can be decomposed into a leptonic tensor $l_{\mu\nu}$ defined by

$$l_{\mu\nu} = \sum_{s_l} \langle k, s_l | \, j_{l\mu}(0) \, | k' \rangle \langle k' | \, j_{l\nu}(0) \, | k, s_l \rangle , \tag{E.5}$$

and a hadronic tensor $W^{\mu\nu}$ defined by[2]

$$W^{\mu\nu}_{\lambda\lambda'}(p, q) = \frac{1}{4\pi} \int \mathrm{d}^4 x e^{iqx} \langle p, \lambda' | \, [j^{\mu\dagger}(x), j^\nu(0)] \, | p, \lambda \rangle \tag{E.6}$$

where λ, λ' are the helicities of the in- and outgoing proton, respectively, and $j^\mu(x)$ is the hadronic current. Inserting a complete set of states gives

$$\begin{aligned} W^{\mu\nu}_{\lambda\lambda'}(p, q) = \frac{1}{4\pi} \int \mathrm{d}^4 x e^{iqx} \Big[&\langle p, \lambda' | \, (j^{\mu\dagger}(x) \, | X \rangle \langle X | \, j^\nu(0)) \, | p, \lambda \rangle \\ &- \langle p, \lambda' | \, (j^\mu(x) \, | X \rangle \langle X | \, j^{\dagger\nu}(0)) \, | p, \lambda \rangle \Big] . \end{aligned} \tag{E.7}$$

Due to translational invariance, we have

$$\begin{aligned} \langle p, \lambda' | \, j^\mu(x) \, | X \rangle &= \langle p, \lambda' | \, j^\mu(0) \, | X \rangle \, e^{i(p - p')x} \\ \langle X | \, j^\mu(x) \, | p, \lambda' \rangle &= \langle p, \lambda' | \, j^\mu(0) \, | X \rangle \, e^{i(p' - p)x} . \end{aligned} \tag{E.8}$$

Energy conservation implies $p'_0 \geq p_0$ and since $q_0 > 0$ we obtain

$$W^{\mu\nu}_{\lambda\lambda'}(p, q) = \frac{1}{4\pi} \sum_X \left[(2\pi)^4 \delta(q + p - p') \langle p, \lambda' | \, j^\mu(0) \, | X \rangle \langle X | \, j^\nu(0) \, | p, \lambda \rangle \right] , \tag{E.9}$$

---

[2] There are different conventions including a factor of $1/m_p$ in the amplitude where the hadronic tensor has then a dimension of $[\text{mass}]^{-1}$. See e.g. [275]

Die approbierte gedruckte Originalversion dieser Dissertation ist an der TU Wien Bibliothek verfügbar.
The approved original version of this doctoral thesis is available in print at TU Wien Bibliothek.
TU Bibliothek, WIEN Your knowledge hub

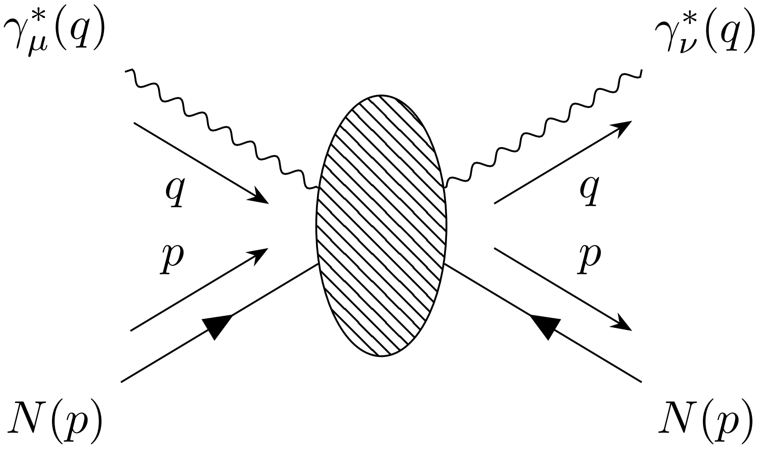

Fig. E.2.: Double virtual forward Compton scattering.

which corresponds to the term in (E.4) up to a factor of $1/(4\pi)$.

E.2.1 Relation to Forward Compton Scattering

The hadronic tensor is related to the absorptive part of the double virtual forward Compton process [274] as depicted in Fig. E.2. We thus consider the reaction

$$\gamma^*(q) + p(p,\lambda) \to \gamma^*(q) + p(p,\lambda'), \tag{E.10}$$

with the amplitude given by

$$T^{\mu\nu} = i\int \mathrm{d}^4 x e^{iqx} \langle p,\lambda'|\, \hat{T}(j^\mu(x) j^\nu(0)\, |p,\lambda\rangle\,. \tag{E.11}$$

Since $T^{\mu\nu}$ and $W^{\mu\nu}$ share the same symmetries, they have an equivalent Lorentz decomposition. Considering only the symmetric, spin independent part, we can write

$$T_{\mu\nu} = \tilde{F}_1(x,Q^2)\left(\eta^{\mu\nu} - \frac{q^\mu q^\nu}{Q^2}\right) + \frac{2x}{Q^2}\tilde{F}_2(x,Q^2)\left(p^\mu + \frac{q^\mu}{2x}\right)\left(p^\nu + \frac{q^\nu}{2x}\right). \tag{E.12}$$

By utilizing the optical theorem, the DIS cross section is obtained by integrating over the Lorentz Invariant Phase Space (LIPS) given by

$$\sum_X \int \mathrm{dLIPS}|\mathcal{M}_{\gamma p\to X}|^2 = 2\mathrm{Im}\mathcal{M}_{\gamma p\to\gamma p}(s,t=0), \tag{E.13}$$

from which we obtain the relations

$$2\mathrm{Im}T_{\mu\nu} = 4\pi W_{\mu\nu} \implies \mathrm{Im}\tilde{F}_1 = 2\pi F_1, \quad \mathrm{Im}\tilde{F}_2 = 2\pi . F_2 \tag{E.14}$$

We therefore find another equivalent definition of the hadronic tensor in terms of the (virtual) forward Compton scattering amplitude

$$W^{\mu\nu}_{\lambda\lambda'}(p,q) = \frac{i}{2\pi}\int \mathrm{d}^4x e^{iqx}\,\langle p,\lambda'|\,\hat{T}(j^\mu(x)j^\nu(0))\,|p,\lambda\rangle\,. \tag{E.15}$$

E.2.2 Hadronic Tensor

Averaging the absorptive part over the proton helicities gives the unpolarized hadronic tensor

$$W^{\mu\nu}(p,q) = \sum_{s,s'}\frac{1}{2}\delta_{ss'}\mathrm{Im}T^{\mu\nu}_{ss'}(p,q) = \frac{1}{2i}\left[T^{\mu\nu}_{ss}(p,q) - (T^{\nu\mu}_{ss}(p,q))^*\right] \tag{E.16}$$

Due to Lorentz invariance, the symmetric contributions of the hadronic tensor may be decomposed as

$$W^{\mu\nu} = \eta^{\mu\nu}W_1 - \frac{p^\mu p^\nu}{m_p^2}W_2 - \frac{q^\mu q^\nu}{m_p^2}W_4 - \frac{p^\mu q^\nu + p^\nu q^\mu}{m_p^2}W_5, \tag{E.17}$$

where current conservation implies

$$\begin{aligned} W_4 &= \frac{m_p^2}{Q^2}W_1 + \left(\frac{p\cdot q}{Q^2}\right)^2 W_2,\\ W_5 &= -\frac{p\cdot q}{Q^2}W_2, \end{aligned} \tag{E.18}$$

and hence

$$W^{\mu\nu}(p,q) = W_1(\nu,Q^2)\left(\eta^{\mu\nu} - \frac{q^\mu q^\nu}{Q^2}\right) - \frac{1}{m_p^2}W_2(\nu,Q^2)\left(p^\mu - \frac{p\cdot q}{Q^2}q^\mu\right)\left(p^\nu - \frac{p\cdot q}{Q^2}q^\nu\right). \tag{E.19}$$

Equivalently it may be written using the dimensionless structure functions F_1 and F_2

$$W^{\mu\nu}(p,q) = F_1(x,Q^2)\left(\eta^{\mu\nu} - \frac{q^\mu q^\nu}{Q^2}\right) + \frac{2x}{Q^2}F_2(x,Q^2)\left(p^\mu + \frac{q^\mu}{2x}\right)\left(p^\nu + \frac{q^\nu}{2x}\right), \tag{E.20}$$

where $F_1 = W_1$ and $F_2 = -(\nu/m_p)W_2$. [3]

---

[3] Note that in the other convention for the hadronic tensor this would be $F_1 = m_pW_1$ and $F_2 = \nu W_2$, which would also be dimensionless.

The total cross sections for the transversely and longitudinally polarized virtual photons are given by [266][4]

$$\begin{aligned}\sigma_T &= \frac{4\pi^2\alpha_{em}}{m_p\kappa_\gamma}F_1(Q^2,\nu)\\ \sigma_L &= \frac{4\pi^2\alpha_{em}}{m_p\kappa_\gamma}\left[-F_1(Q^2,\nu)+\frac{m_p}{\nu}\left(1+\frac{\nu^2}{Q^2}\right)F_2(Q^2,\nu)\right],\end{aligned} \tag{E.21}$$

with the flux factor κ_γ given by $\kappa_\gamma = \sqrt{\nu^2+Q^2}$ (Gilman convention), $\kappa_\gamma = \nu - Q^2/(2m_p)$ (Hand convention).

HERA measured the reduced cross section, which for a neutral current exchange is given by

$$\sigma_{red}^{NC}(Q^2,W^2,y) = \frac{q^4 x}{2\pi\alpha_{em}^2(1+(1-y)^2)}\frac{\mathrm{d}^2\sigma}{\mathrm{d}x\mathrm{d}Q^2}(e\,p\to e\,X)\,. \tag{E.22}$$

It can be expressed in terms of longitudinal σ_L and transverse σ_T cross section as [273]

$$\begin{aligned}\sigma_{red}^{NC}(Q^2,W^2,y) = &\frac{1+(1-y)^2+y^2\delta(W^2,Q^2)}{(1+(1-y)^2)(1+2\delta(W^2,Q^2))}\frac{Q^2}{4\pi^2\alpha_{em}}(1-x)\\ &\times\left[\sigma_T(W^2,Q^2)+\sigma_L(W^2,Q^2)-(1-\varepsilon)\sigma_L(W^2,Q^2)\right]\end{aligned} \tag{E.23}$$

The total photoproduction cross section can be extracted from

$$\sigma_{\gamma p}(W^2) = \sigma_T(W^2,0). \tag{E.24}$$

E.3 Low-Energy Couplings and Pomeron propagator

E.3.1 Tensor Glueball 2γ-couplings

The bulk-to-boundary propagator for an off-shell photon is obtained by solving (7.69) with the boundary condition $\mathcal{J}(0,z)=1$. Interactions between the tensor glueball and two virtual photons following from (10.78) are thus given by

$$\mathcal{L}_{G_T\mathcal{V}\mathcal{V}} = \mathrm{tr}\left[t_2^{\mathcal{V}^*\mathcal{V}^*}(Q_1,Q_2)\frac{Q_1^2Q_2^2}{M_{\mathrm{KK}}^2}\mathcal{V}_\mu\mathcal{V}_\nu G_T^{\mu\nu} + t_3^{\mathcal{V}*\mathcal{V}*}(Q_1,Q_2)G_T^{\mu\nu}\,\mathrm{tr}\left(F_{\mu\rho}^{\mathcal{V}}F_\nu^{\mathcal{V}\rho}\right)\right], \tag{E.25}$$

---

[4] This reference is missing a factor of $4\pi^2$ above Eq.(17).

with the double-virtual transition form factors

$$\begin{aligned} t_2^{\mathcal{V}^*\mathcal{V}^*}(Q_1,Q_2) &= \frac{M_{\text{KK}}^4}{Q_1^2Q_2^2}\kappa\int \mathrm{d}z K\mathcal{J}'(Q_1,z)\mathcal{J}'(Q_2,z)H_T, \\ t_3^{\mathcal{V}*\mathcal{V}*}(Q_1,Q_2) &= \kappa\int \mathrm{d}z K^{-1/3}\mathcal{J}(Q_1,z)\mathcal{J}(Q_2,z)H_T, \end{aligned} \tag{E.26}$$

where we pulled out a factor of $\frac{M_{\text{KK}}^4}{Q_1^2Q_2^2}$ for convenience.

E.3.2 Tensor Glueball Proton Coupling

As dictated by the holographic principle, the tensor glueball couples predominantly to the stress-energy tensor of QCD via

$$S_{int} = \lambda_P\int \mathrm{d}^4x\delta G_{\mu\nu}T^{\mu\nu}, \tag{E.27}$$

where the vertex structure is determined by the matrix element of $T^{\mu\nu}$ which, by current conservation, can be written as

$$\langle p',s'|\,T_{\mu\nu}(0)\,|p,s\rangle = \overline{u}\left[A(t)\gamma_{(\mu}P_{\nu)} + \frac{i}{2m_p}B(t)P_{(\mu}\sigma_{\nu)\rho}k^\rho + C(t)\frac{(k_\mu k_\nu - \eta_{\mu\nu}k^2)}{m_p}\right]u, \tag{E.28}$$

where

$$P = (p+p')/2, \quad k = p-p', \quad \overline{u}' = \overline{u}(p',s'), \quad u = \overline{u}(p,s) \tag{E.29}$$

and

$$T_{(\mu_1\ldots\mu_n)} = \frac{1}{n!}\sum_{\sigma\in S_n}T_{\mu_{\sigma_1}\ldots\mu_{\sigma_n}}, \qquad T_{[\mu_1\ldots\mu_n]} = \frac{1}{n!}\sum_{\sigma\in S_n}(-1)^{\text{sign}(\sigma)}T_{\mu_{\sigma_1}\ldots\mu_{\sigma_n}}, \tag{E.30}$$

denote symmetrization and antisymmetrization with respect to the indices in brackets, respectively. Following Refs. [209, 222, 271] we model baryons as charge one instantons of the $SU(2)$ gauge fields. Upon quantization of the moduli space, they are identified with spin $1/2$ fermions of mass

$$m_{\mathcal{B}}^{cl} = M_{\text{KK}}\left(8\pi^2\kappa + \sqrt{\frac{2^2}{6}+\frac{2}{15}N_c}\right) + \mathcal{O}(1/\lambda) \tag{E.31}$$

In curved spacetime, however, the mass is to be identified in terms of proper time as

$$S = \int m_5\mathrm{d}\tau, \tag{E.32}$$

Die approbierte gedruckte Originalversion dieser Dissertation ist an der TU Wien Bibliothek verfügbar.
The approved original version of this doctoral thesis is available in print at TU Wien Bibliothek.
TU Bibliothek Your knowledge hub WIEN

giving a radially dependent mass

$$m_5(U) = \frac{m^{cl}_{\mathcal{B}}}{\sqrt{-g_{00}}} = m^{cl}_{\mathcal{B}}\left(\frac{R_{\mathrm{D4}}}{U}\right)^{3/4}. \tag{E.33}$$

To simplify the further analysis, we bring the 5d metric into a conformally flat form

$$ds_5^2 = H(w)(\mathrm{d}w^2 + \eta_{\mu\nu}\mathrm{d}x^\mu \mathrm{d}x^\nu) \tag{E.34}$$

with $H(w) = (U(w)/R_{\mathrm{D4}})^{3/2}$ and

$$w(U) = \int_{U_{\mathrm{KK}}}^{U} \frac{R_{\mathrm{D4}}^{3/2}\mathrm{d}U'}{\sqrt{U'^3 - U_{\mathrm{KK}}^3}}. \tag{E.35}$$

Treating the instanton solution as an effective fermion field living on the D8 world volume, we can reduce the action to a 5-dimensional Lagrangian

$$S_f = -i\mathcal{N}\int \mathrm{d}^5x e^{-\phi}\mathrm{Vol}_{S_4}(U)\sqrt{g_5}\left[\overline{\psi}e^m_{\hat{a}}\Gamma^{\hat{a}}D_m\psi + m_5\overline{\psi}\psi\right], \tag{E.36}$$

where unhatted indices pertain to the 5d world volume, and hatted indices correspond to tangent space indices. The radially dependent S_4 volume is given by $\mathrm{Vol}_{S_4}(U) = R_{\mathrm{D4}}^3 U V_4$ and $\mathcal{N}$ denotes the prefactors that arise from dimensional reduction, which will later be absorbed into the normalization of the baryon wave function. Note that the covariant derivative in (E.36) also induces interactions between baryons and the 5-dimensional gauge fields [271]. Omitting these couplings for simplicity, the covariant derivative is given by

$$D_m\psi = \left(\partial_m - \frac{i}{4}\omega_m^{\hat{a}\hat{b}}\sigma_{\hat{a}\hat{b}}\right)\psi, \tag{E.37}$$

with

$$\sigma_{\hat{a}\hat{b}} = \frac{i}{2}\left[\Gamma_{\hat{a}}, \Gamma_{\hat{b}}\right], \quad \left[\Gamma_{\hat{a}}, \Gamma_{\hat{b}}\right] = 2\eta_{\hat{a}\hat{b}}. \tag{E.38}$$

From the tetrads

$$e^{\hat{a}} = H(w)^{1/2}\delta^{\hat{a}}_m \mathrm{d}x^m \tag{E.39}$$

the Cartan connections are readily obtained as

$$\omega^{\hat{\mu}}{}_{\hat{\nu}} = 0, \quad \omega^{\hat{\mu}}{}_{\hat{w}} = \frac{1}{2}\partial_w \ln H(w)\mathrm{d}x^\mu. \tag{E.40}$$

Identifying $\Gamma_{\hat{\mu}} = \gamma_\mu$ and $\Gamma_{\hat{w}} = \gamma_5$ we obtain

$$\begin{aligned} S_f = -i\mathcal{N}\int \mathrm{d}^4x\mathrm{d}w &\left(\mathrm{Vol}_{S_4}(w)e^{-\phi}\sqrt{g_5}H^{-5/2}\right)H^{-1/2}(w) \\ &\times\left(\overline{\psi}\left[\gamma^\mu\partial_\mu + \gamma^5\partial_w + \frac{\partial_w H}{H}\gamma^5\right]\psi + m_5(w)H^{1/2}\overline{\psi}\psi\right). \end{aligned} \tag{E.41}$$

The factors depending on w may be reabsorbed into ψ by

$$\psi = \frac{1}{H(w)}\mathcal{B}. \tag{E.42}$$

Without the contribution from the Chern-Simons term, the baryon wave function is localized at $w = 0$ ($U = U_{\mathrm{KK}}$) [222]. We can thus approximate the expression in the first brackets in (E.41) with its value at $w = 0$ and absorb all constants into the normalization of $\mathcal{B}$ to obtain

$$S_f - i\int \mathrm{d}^4x\mathrm{d}w \left[\overline{\mathcal{B}}\gamma^m\partial_m\mathcal{B} + m_{\mathcal{B}}(w)\overline{\mathcal{B}}\mathcal{B}\right], \tag{E.43}$$

where $m_{\mathcal{B}} = m_{\mathcal{B}}^{cl}\left(\frac{U(w)}{U_{\mathrm{KK}}}\right)$. For small w the mass gets a correction of $m_{\mathcal{B}} = m_{\mathcal{B}}^{cl}\left(1 + \frac{wM_{\mathrm{KK}}^2}{3}\right)$. We can rewrite this expression by symmetrizing the indices pertaining to Minkowski space to obtain

$$S_f \supset -\frac{i}{2}\int \mathrm{d}^4x\mathrm{d}w\overline{\mathcal{B}}\eta_{\mu\nu}(\gamma^\mu\partial^\nu + \gamma^\nu\partial^\mu)\mathcal{B} = -\frac{i}{2}\int \mathrm{d}^4x\mathrm{d}w\overline{\mathcal{B}}H^{-1}(w)g_{\mu\nu}(\gamma^\mu\partial^\nu + \gamma^\nu\partial^\mu)\mathcal{B}. \tag{E.44}$$

Identifying

$$T_{\mathcal{B}}^{\mu\nu} = -\frac{i}{2}\overline{\mathcal{B}}(\gamma^\mu\partial^\nu + \gamma^\nu\partial^\mu)\mathcal{B} \tag{E.45}$$

with the 5d fermionic stress-energy tensor and inducing fluctuations of the background metric, we find the linearized interaction Lagrangian

$$S_f^{lin} = \int \mathrm{d}^4x\mathrm{d}wH^{-1}(w)h_{\mu\nu}T_{\mathcal{B}}^{\mu\nu}. \tag{E.46}$$

By performing a chiral Kaluza-Klein decomposition, the equations of motion following from (E.43) are given by

$$(\pm\partial_w + m_{\mathcal{B}}(w))f_\pm = m_{\mathcal{N}}f_\mp. \tag{E.47}$$

To get a canonically normalized action, we impose the normalization condition

$$\int \mathrm{d}w|f_\pm(w)|^2 = 1, \tag{E.48}$$

In [271] it was shown that (E.47) can be decoupled and brought into the dimensionless form

$$\left[-\partial_{\tilde{w}}^2 - \frac{\lambda N_c}{27\pi}\partial_{\tilde{w}}\tilde{U}(\tilde{w}) + \left(\frac{\lambda N_c}{27\pi}\tilde{U}(\tilde{w}) + \sqrt{\frac{2}{15}}N_c\right)^2\right]f_-(\tilde{w}) = \left(\frac{m_{\mathcal{B}}}{M_{\mathrm{KK}}}\right)^2 f_-(\tilde{w}). \tag{E.49}$$

For large λN_c one encounters a steep potential with a minimum localized at $\tilde{w}_{\text{min}} \sim \mathcal{O}(1/\lambda N_c)$. Therefore, we approximate

$$|f_\pm(w)|^2 = \delta(w), \tag{E.50}$$

and thus

$$S_f^{lin} = \lambda_P \int \mathrm{d}^4 x q_{\mu\nu} T^{\mu\nu} \tag{E.51}$$

with

$$\lambda_P = \frac{1}{\mathcal{N}_T} \int \mathrm{d}w T(w)\delta(w) = \frac{1}{\mathcal{N}_T} = \frac{103.136}{M_{\text{KK}} N_c \sqrt{\lambda}} = 8.88 \text{ GeV}^{-1}. \tag{E.52}$$

where we used the boundary condition $T(U_{\text{KK}}) = 1$. Hence, we find the glueball proton vertex to be given by

$$\Gamma_{\mu\nu} = \lambda_P \left[A(t) \frac{\gamma_\mu P_\nu + \gamma_\nu P_\mu}{2} + B(t) \frac{i(P_\mu \sigma_{\nu\rho} + P_\nu \sigma_{\mu\rho})k^\rho}{4m_p} + C(t) \frac{(k_\mu k_\nu - \eta_{\mu\nu} k^2)}{m_p} \right], \tag{E.53}$$

where, again, $k = p' - p$, $P = (p + p')/2$ and $\lambda_P = 8.88$. This value differs from Ref. [211] by about 1.5%, which we attribute to numerical uncertainties. However, the value quoted in Ref. [209] is off by a factor of $\sqrt{2}$, which we believe stems from an inconsistent normalization of the glueball polarization. Matching this to a spin $1/2$ particle gives the constraints $A(0) = 1$, $B(0) = 0$. Note that since in the forward limit $k \to 0$, $B(t)$ and $C(t)$ will play no role in our analysis.

E.3.3 Reggeized Tensor Glueball Propagator

Following Ref. [208], we use the Pomeron propagator obtained by taking the Regge limit of the Virasoro-Shapiro amplitude. This amounts to the replacement

$$\frac{-i}{t - m_G^2} \to \frac{i\alpha'_g}{2} \frac{e^{-\frac{i\pi}{2}\alpha_g(t)} \Gamma[-\chi] \Gamma[1 - \frac{\alpha_g(t)}{2}]}{\Gamma[\frac{\alpha_g(t)}{2} - 1 - \chi]} \left(\frac{\alpha'_g s}{2} \right)^{\alpha_g(t) - 2}, \tag{E.54}$$

where $\alpha_g(t) = 1 + \epsilon_g + \alpha'_g t$ and $\chi = \alpha'_g(4m_p^2 - 3M_T^2)$. For the following numerical analysis, we shall fix to fit results obtained in Ref. [208] who obtained

$$\epsilon_g = 0.08, \qquad \alpha' = 0.3 \text{ GeV}^{-2}, \tag{E.55}$$

and use the mass of the tensor glueball obtained in the WSS model. Note that the data gathered by ZEUS [203] suggests a Pomeron intercept slowly varying with Q^2 but about constant below $Q^2 < 1 \text{ GeV}^2$, as is the case for the data used in the following section.

E.4 Structure Functions from Holographic QCD

Using the vertices (E.26), (E.53) and the Pomeron propagator (E.54) we find

$$\begin{aligned} T^{\mu\nu}_{\mathrm{WSS}}(p,q) =& \frac{(-i\alpha'_g W^2)^{\epsilon_g}}{2\pi W^2}\left(-\eta^{\mu\mu'}+\frac{q^\mu q^{\mu'}}{Q^2}\right)\left(-\eta^{\nu\nu'}+\frac{q^\nu q^{\nu'}}{Q^2}\right)\mathrm{tr}\,\mathcal{Q}^2 \\ & \times 2\left[\frac{t_2^{\mathcal{V}^*\mathcal{V}^*}}{M_{\mathrm{KK}}^2}q^4(\eta^{\mu'\sigma}\eta^{\nu'\rho}+\eta^{\mu'\rho}\eta^{\nu'\sigma}) - t_3^{\mathcal{V}\mathcal{V}}\Big(-Q^2\eta^{\mu'\sigma}\eta^{\nu'\rho}-Q^2\eta^{\mu'\rho}\eta^{\nu'\sigma}\right. \\ & \left. + q^{\mu'}q^\rho\eta^{\nu'\sigma}+q^{\nu'}q^\rho\eta^{\mu'\sigma}-2q^\rho q^\sigma\eta^{\mu'\nu'}+q^{\mu'}q^\sigma\eta^{\nu'\rho}+q^{\nu'}q^\sigma\eta^{\mu'\rho}\Big)\right] \\ & \times \frac{1}{2}(\eta^{\kappa\sigma}\eta^{\lambda\rho}+\eta^{\kappa\rho}\eta^{\lambda\sigma}-\frac{1}{2}\eta^{\kappa\lambda}\eta^{\rho\sigma})2\lambda_P A(t)p^\kappa p^\lambda \end{aligned} \tag{E.56}$$

From this, we obtain the structure functions

$$\begin{aligned} F_1 &= \mathcal{N}_P\left[t_3^{\mathcal{V}\mathcal{V}}\left((W^2+Q^2)^2+m_p^4-2m_p^2W^2\right)+t_2^{\mathcal{V}^*\mathcal{V}^*}m_p^2M_{\mathrm{KK}}^2\left(Q^2\right)^2\right], \\ F_2 &= \frac{\mathcal{N}_P}{2}4Q^2(W^2+Q^2-m_p^2)\left(t_3^{\mathcal{V}\mathcal{V}}+\frac{t_2^{\mathcal{V}^*\mathcal{V}^*}}{M_{\mathrm{KK}}^2}Q^2\right), \end{aligned} \tag{E.57}$$

or, equivalently,

$$\begin{aligned} W_1 &= \mathcal{N}_P\left[t_3^{\mathcal{V}\mathcal{V}}\left((W^2+Q^2)^2+m_p^4-2m_p^2W^2\right)+\frac{t_2^{\mathcal{V}^*\mathcal{V}^*}}{M_{\mathrm{KK}}^2}m_p^2\left(Q^2\right)^2\right], \\ W_2 &= \frac{\mathcal{N}_P}{2}\left(t_3^{\mathcal{V}\mathcal{V}}+\frac{t_2^{\mathcal{V}^*\mathcal{V}^*}}{M_{\mathrm{KK}}^2}Q^2\right)\left(-4Q^2\right), \end{aligned} \tag{E.58}$$

where we defined $\mathcal{N}_P \equiv \frac{\lambda_P}{2\pi W^2}\mathrm{tr}\,\mathcal{Q}^2\cos\left(\frac{\pi}{2}\epsilon_g\right)(\alpha'_g W^2)^{\epsilon_g}$.

E.5 Results

A direct comparison of our theoretical predictions with measurements from H1, ZEUS, FNAL and astroparticle data [269, 276–280] leads to a rather significant mismatch. The reasons for this are manifold. The predominant contributor is the rapid decrease of the transition form factors at high virtualities. This could be remedied by increasing M_{KK}, a procedure that is indeed favored when addressing glueball physics (see Chapter 10). However, the scale of the photon bulk-to-boundary propagator is unambiguously fixed by the rho meson mass, which enforces the standard value of $M_{\mathrm{KK}} = 0.949$ GeV. We will

Die approbierte gedruckte Originalversion dieser Dissertation ist an der TU Wien Bibliothek verfügbar.
The approved original version of this doctoral thesis is available in print at TU Wien Bibliothek.
TU Bibliothek WIEN Your knowledge hub

λ_P	$\bar{t}_2^{\mathcal{V}^*\mathcal{V}^*}$	$\bar{t}_3^{\mathcal{V}^*\mathcal{V}^*}$
9.38(9)[GeV^{-1}]	8.40(11)	2.13(4)

Table E.1.: Best fit results for a global fit of the photoproduction cross section, reduced cross section, and $F_2(Q^2, W)$ to the data of [269, 276–280] above $\sqrt{s} = 300$ GeV and for $Q^2 \leq 0.5$ GeV^2.

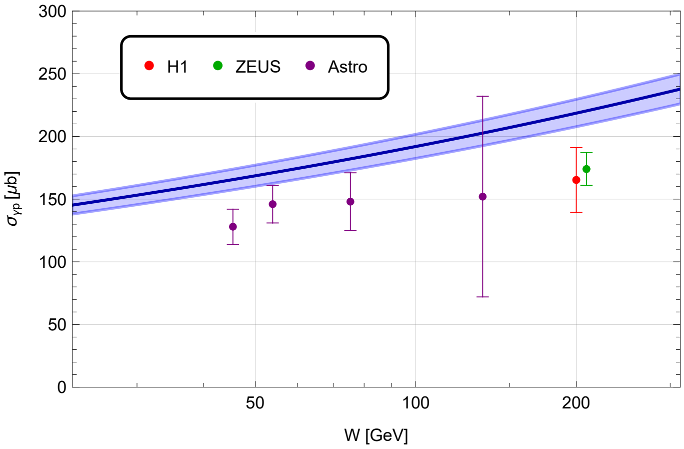

Fig. E.3.: Photoproduction cross section with the parameters from Table E.1 through exchange of a Reggeized tensor glueball compared to data from [278–280].

thus refrain from fitting this quantity[5] and instead only fit λ_P, $t_2^{\mathcal{V}^*\mathcal{V}^*}$ and $t_3^{\mathcal{V}^*\mathcal{V}^*}$. The other quantities are fixed by the top-down Pomeron analysis of [208] using CDF data. Explicitly they are given by $\alpha'_g = 0.3$ and $\epsilon_g = 0.086$ with resulting $\chi \approx -0.93$.

For the global fit, we use data in the range of $\sqrt{s} \geq 300$ GeV and $0 \leq Q^2 \leq 0.5\text{GeV}^2$. The fit results are displayed in Table E.1 where the values for $\bar{t}_2^{\mathcal{V}^*\mathcal{V}^*}$ and $\bar{t}_3^{\mathcal{V}^*\mathcal{V}^*}$ correspond to an increase in the scale of the pristine WSS results in (E.26), but with the Q^2 behavior fixed. In Fig. E.3 we show the photoproduction cross section (E.24) together with data from [278–280]. We note that the data is very well reproduced even when using the WSS model predictions but with the scale adjusted accordingly. Fig. E.4 displays the reduced cross section at $\sqrt{s} = 300$ GeV together with the corresponding data from [269, 276, 277] for various virtualities. At virtualities above $Q^2 \sim 0.35$ GeV^2 the predictions start to deviate, since the scale factors $\bar{t}_2^{\mathcal{V}^*\mathcal{V}^*}$ and $\bar{t}_3^{\mathcal{V}^*\mathcal{V}^*}$ can no longer compensate the UV behavior of the photon bulk-to-boundary propagator $\mathcal{J}(Q, z)$. In Fig. E.5 we show the reduced cross sections for various virtualities Q^2 at $\sqrt{s} = 318$ GeV and compare it to the data from [269, 276, 277]. At this slightly higher center of mass energy, the agreement is better even for virtualities above $Q^2 \sim 0.5$ GeV^2. The hadronic structure function $F_2(Q^2, W)$ together with data from [269, 276, 277] is shown in E.6. Unfortunately, no measurements for virtualities above $Q^2 = 0.25$ GeV^2 are reported. Below this value,

---

[5] Fitting M_{KK} gives a value of about 1.7 GeV and a resulting tensor glueball mass of roughly 2.6 GeV.

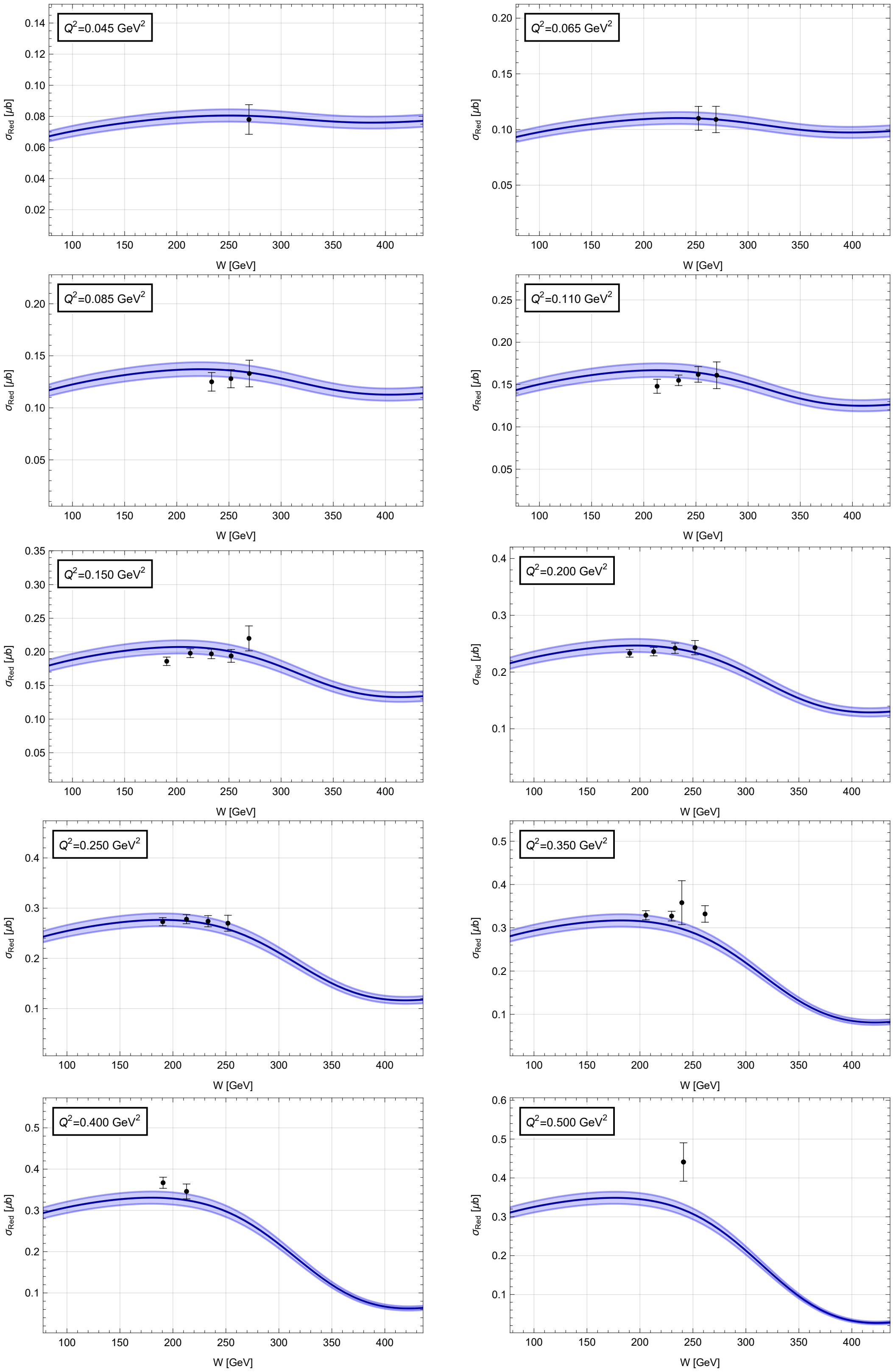

Fig. E.4.: Fit of the reduced cross sections within a 90% confidence interval compared to data from HERA [269, 276, 277] at a center of mass energy of $\sqrt{s} = 300$ GeV and $0.045\ \text{GeV}^2 \leq Q^2 \leq 0.40\ \text{GeV}^2$.

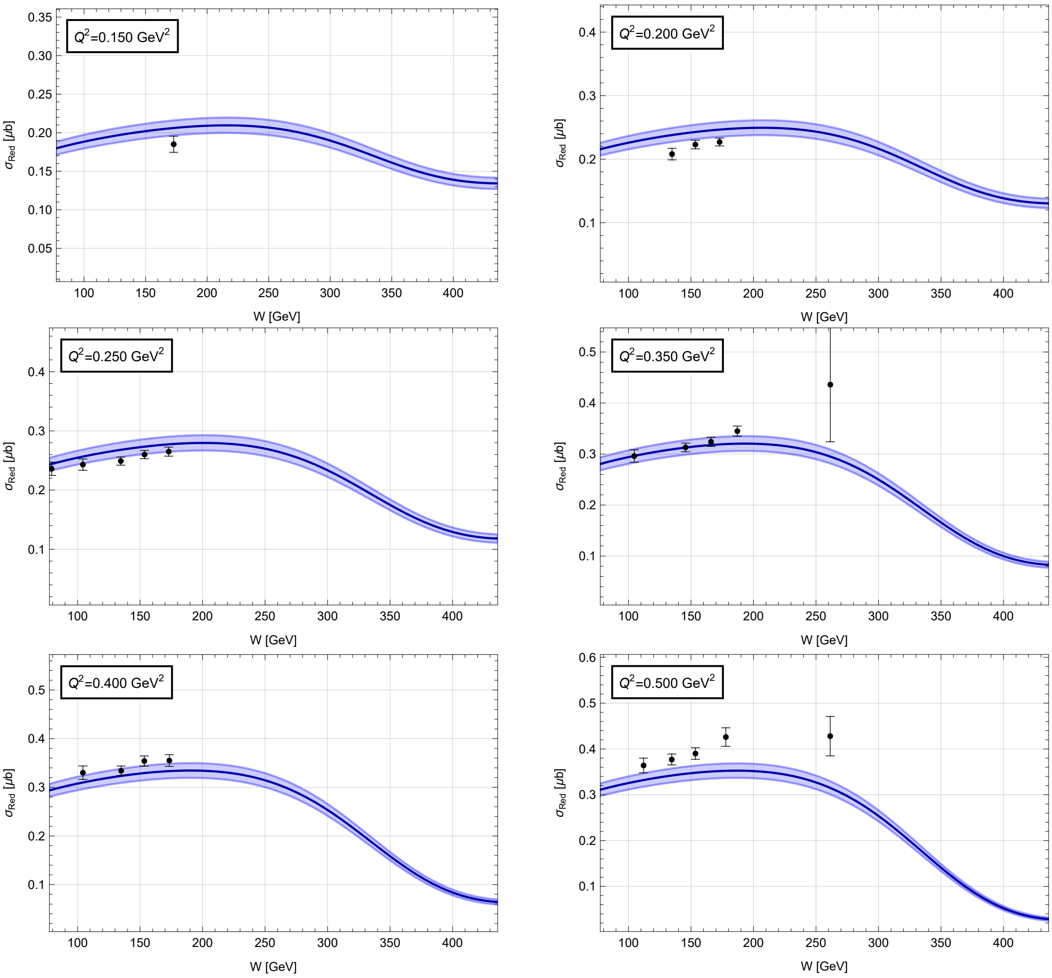

Fig. E.5.: Fit of the reduced cross sections within a 90% confidence interval compared to data from HERA [269, 276, 277] at a center of mass energy of $\sqrt{s} = 318$ GeV and $0.15\ \mathrm{GeV}^2 \leq Q^2 \leq 0.40\ \mathrm{GeV}^2$.

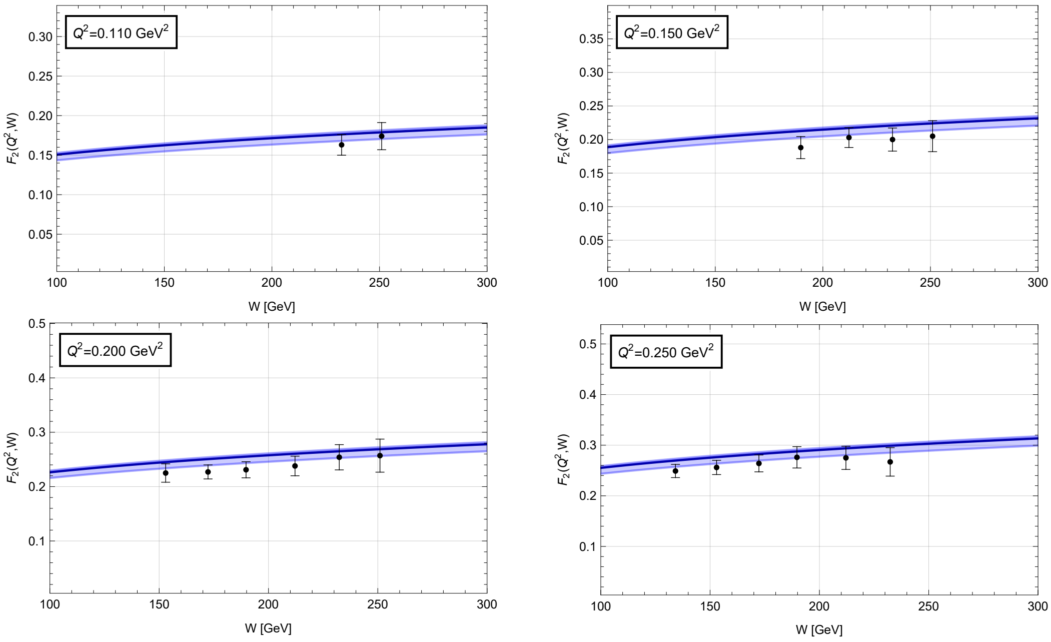

Fig. E.6.: Fit of the structure function $F_2(Q^2, W)$ within a 90% confidence interval compared to data from HERA [269, 276, 277] at a center of mass energy of $\sqrt{s} = 300$ GeV and $0.11\ \mathrm{GeV}^2 \leq Q^2 \leq 0.25\ \mathrm{GeV}^2$.

the fit reproduces the data well. The analysis laid out in this appendix shows that the WSS model is unfit to describe the low-x data by HERA. This was seen to be primarily due to the wrong UV behavior, which only to some extent could be compensated by increasing the couplings. The predictions deviate strongly from the data above virtualities of $0.5\ \mathrm{GeV}^2$. However, a similar behavior was found in the phenomenological Tensor Pomeron Model (TPM) [273, 281], which attributed this behavior to a transition from soft to hard Pomeron at these virtualities. The overall scale, effectively governed by the tensor glueball coupling to the proton, is too small, as seen from the photoproduction cross section results. Whether a complete computation using instantons could remedy this shortcoming would be interesting. Especially the Chern-Simons term yields corrections of $\mathcal{O}(1/N_c)$ and stabilizes the instanton at a finite size, which would yield a more substantial overlap with the holographic wave function of the tensor glueball in the corresponding integrals for the transition form factors. A more suitable avenue to describe the data would be to improve the UV behavior by constructing a soft-wall model (see [214] for an attempt) and use the WSS model to determine the Lorentz structure of the interactions as well as fix the couplings at $Q^2 = 0$.

F

Bulk-to-Bulk Propagator in the Soft-Wall Model

To contrast with the findings in the main text using a repulsive wall, we offer a thorough derivation of the bulk-to-bulk propagator within the soft-wall model. While numerous characteristics of the analogous computations using a repulsive wall reappear, Gribov diffusion is absent.

Consider the soft-wall model with dilaton $\phi(z) = (2\kappa z)^2$. The Reggeized scalar propagator is obtained by solving the Sturm-Liouville problem

$$L_z y(z) = \frac{\delta(z-z')}{w(z)} \tag{F.1}$$

with

$$L_z = \frac{1}{w(z)}\, d_z(w(x)\, p_0(z)\, d_z) + p_2(z), \tag{F.2}$$

and

$$\begin{aligned} w(z) &= \sqrt{g}e^{-\phi(z)} \\ p_0(z) &= -g^{zz}(z) \\ p_2(z) &= S_j - tz^2, \end{aligned} \tag{F.3}$$

where we recall that $S_j = m_5^2R^2 + m_j^2R^2$. Explicitly, we have

$$\left(-z^3e^{4\kappa^2z^2}\partial_z\left(\frac{1}{z^3}e^{-4\kappa^2z^2}\partial_z\right) - t + \frac{S_j}{z^2}\right)G_0(j,t,z,z') = z^3e^{4\kappa^2z^2}\delta(z-z') \tag{F.4}$$

with $t = K^2$. To simplify the differential equation (F.4), we rescale the spin-j propagator as

$$G_0(j,t,z,z') \to (zz')^{\frac{3}{2}}e^{\frac{3}{4}\kappa^2(z^2+z'^2)}\, G_0(j,t,u,u') \tag{F.5}$$

with $u = \kappa z$ and $\kappa^2 \to \frac{8}{3}\kappa^2$, which now solves

$$-\frac{\mathrm{d}^2}{\mathrm{d}u^2}G_0 + \left(\frac{S_j + \frac{15}{4}}{u^2} + \frac{9}{4}u^2 - \frac{t}{\kappa^2} + 3\right)G_0 = \frac{e^{\frac{3}{4}(u^2-u'^2)}}{\kappa}\left(\frac{u}{u'}\right)^{3/2}\delta(u-u') \tag{F.6}$$

Using the delta function, the right hand side evaluates to a constant, leading to a standard Green's function problem. Upon rescaling $u \to \sqrt{3}u$ and $\tilde{t} = t/3\kappa^2$, (F.6) now reads

$$-\frac{\mathrm{d}^2}{\mathrm{d}u^2} G_0 + \left(\frac{S_j + \frac{15}{4}}{u^2} + \frac{u^2}{4} - \tilde{t} + 1 \right) G_0 = \frac{1}{\sqrt{3}\kappa} \delta(u - u') \tag{F.7}$$

Performing one final coordinate transformation $v = \frac{1}{2}u^2$ and subsequently rescaling the propagator as

$$G_0(j, t, v, v') = \frac{1}{(vv')^{\frac{1}{4}}} K_0(j, t, v, v') \tag{F.8}$$

(13.18) reduces to the Whittaker equation

$$\frac{\mathrm{d}^2 K_0}{dv^2} + \left(\frac{\frac{1}{4} - \alpha^2}{v^2} + \frac{\beta}{v} - \frac{1}{4} \right) K_0 = -\frac{\delta(v - v')}{\sqrt{6}\kappa} \tag{F.9}$$

with

$$\alpha = \frac{1}{2}(\Delta_g(j) - 2) \qquad \beta = \frac{1}{2}(\tilde{t} - 1) \tag{F.10}$$

The independent homogeneous solutions to (F.9) are given by the Whittaker functions

$$\begin{aligned} K_1(v) &= e^{-\frac{v}{2}} v^{\frac{1}{2}+\alpha}\, \mathbb{M}\left(\frac{1}{2} + \alpha - \beta, 1 + 2\alpha, v \right) \\ K_2(v) &= e^{-\frac{v}{2}} v^{\frac{1}{2}+\alpha}\, \mathbb{U}\left(\frac{1}{2} + \alpha - \beta, 1 + 2\alpha, v \right) \end{aligned} \tag{F.11}$$

in terms of the regular Kummer $\mathbb{M}$ and irregular Tricomi $\mathbb{U}$ hypergeometric functions. The inhomogeneous solution to ((F.9)) is now obtained from

$$\begin{aligned} K_0(v, v') &= \frac{1}{2}\mathcal{A}\, K_2(v) K_1(v') \qquad v > v' \\ K_0(v, v') &= \frac{1}{2}\mathcal{A}\, K_1(v) K_2(v') \qquad v < v' \end{aligned} \tag{F.12}$$

with the normalization fixed by the Wronskian

$$\mathcal{A}^{-1} = -\sqrt{6}\kappa \mathcal{W}(K_2, K_1) = -\frac{4\kappa\Gamma(1 + 2\alpha)}{\Gamma\left(\frac{1}{2} + \alpha - \beta \right)}. \tag{F.13}$$

The confining bulk-to-bulk propagator is thus given by

$$G_0(j, t, z, z') = -(zz')^2 (4\kappa^2 zz')^{\Delta_g(j)-2} \frac{\Gamma(\frac{\Delta_g(j)-\tilde{t}}{2})}{\Gamma(\Delta_g(j) - 1)} \mathbb{M}(z)\mathbb{U}(z') \tag{F.14}$$

where we introduced the shorthand $\mathbb{M}(z) = \mathbb{M}(\frac{\Delta_g(j)-\tilde{t}}{2}, \Delta_g(j)-1, 4\kappa^2 z^2)$. Before we proceed to evaluate the Sommerfeld-Watson formula, we express the Whittaker function involving $\mathbb{U}$ in terms of $\mathbb{M}$ by using the identity

$$K_2(v) = e^{-\frac{v}{2}} v^{\frac{1}{2}+\alpha} \Bigg(\frac{\Gamma(-2\alpha)\mathbb{M}\left(\frac{1}{2}+\alpha-\beta, 1+2\alpha, v\right)}{\Gamma(\frac{1}{2}-\alpha-\beta)} \\ + \frac{\Gamma(2\alpha)\mathbb{M}\left(\frac{1}{2}-\alpha-\beta, 1-2\alpha, v\right)}{\Gamma(\frac{1}{2}+\alpha-\beta)} v^{-2\alpha} \Bigg). \tag{F.15}$$

The singular part in v is subleading when the integral is evaluated in the saddle-point approximation. We will thus drop it in the subsequent analysis. After reverting the rescalings and transforming to the original z coordinate, the bulk-to-bulk propagator is symmetric

$$G_0(j,t,z,z') = -(zz')^2 (4\kappa^2 zz')^{\Delta_g(j)-2} \frac{\Gamma(\frac{\Delta_g(j)-\tilde{t}}{2})\Gamma(2-\Delta_g(j))}{\Gamma(\frac{4-\tilde{t}-\Delta_g(j)}{2})\Gamma(\Delta_g(j)-1)} \mathbb{M}(z)\mathbb{M}(z'), \tag{F.16}$$

where we introduced the shorthand

$$\mathbb{M}(z) = \mathbb{M}\left(\frac{\Delta_g(j)-\tilde{t}}{2}, \Delta_g(j)-1, 4\kappa^2 z^2\right). \tag{F.17}$$

F.1 Conformal Limit

In the confining case considered above, the bulk-to-bulk propagator is given by

$$G_0(j,t,z,z') = -(zz')^2 (4\kappa^2 zz')^{b-1} \frac{\Gamma(a)\Gamma(1-b)}{\Gamma(1+a-b)\Gamma(b)} \\ \times \mathbb{M}(a,b,4\kappa^2 z^2)\mathbb{M}(a,b,4\kappa^2 z'^2) \tag{F.18}$$

where $a = \frac{\Delta_g(j)-\tilde{t}}{2}$ and $b = \Delta_g(j)-1$. Taking $\kappa \to 0$, and simultaneously $\tilde{t} = t/8\kappa^2 \to \infty$ we may use the identity

$$\lim_{a\to\infty} \mathbb{M}(a,b,-x/a) = \Gamma(b) x^{\frac{1-b}{2}} J_{b-1}(2\sqrt{x}), \tag{F.19}$$

where $x = |t|z^2/4$. To leading order in κ, we thus obtain

$$\begin{aligned} G_0(j,t,z,z') = -(zz')^2(4\kappa^2 zz')^{\Delta_g(j)-2}\frac{\Gamma(2-\Delta_g(j))}{\Gamma(\Delta_g(j)-1)}\left(\frac{|t|zz'}{2}\right)^{2-\Delta_g(j)} \\ \times J_{\Delta-2}\left(\sqrt{|t|}z\right) J_{\Delta-2}\left(\sqrt{|t|}z'\right) \end{aligned} \tag{F.20}$$

Resumming the Regge trajectory using a Sommerfeld-Watson transform

$$\begin{aligned} G_2(s,t,z,z') = -\,(zz')^2 \int \frac{\mathrm{d}j}{4\pi i}\Bigg[\frac{1+e^{-i\pi j}}{\sin \pi j}(\alpha' szz')^j(4\kappa^2 zz')^{\Delta_g(j)-2} \\ \times \frac{\Gamma(2-\Delta_g(j))}{\Gamma(\Delta_g(j)-1)}\left(\frac{|t|zz'}{2}\right)^{2-\Delta_g(j)} J_{\Delta-2}\left(\sqrt{|t|}z\right) J_{\Delta-2}\left(\sqrt{|t|}z'\right)\Bigg] \end{aligned} \tag{F.21}$$

we obtain

$$G_2(j,t,z,z') = -\frac{f^+(\lambda)}{2}\sqrt{\frac{\mathcal{D}}{4\pi\chi}}(zz')^2(\alpha' szz')^{j_{\mathbb{P}}} e^{-\frac{\log(zz'|t|)^2}{4\mathcal{D}\tau}} J_0\left(\sqrt{|t|}z\right) J_0\left(\sqrt{|t|}z'\right). \tag{F.22}$$

Upon taking the Regge limit, the Bessel functions become trivial at the saddle point, thus reproducing the conformal result presented in (13.53). Notably, the Regge limit must be applied after evaluating the Sommerfeld-Watson transform; otherwise, the dependence on t would vanish entirely, as evident in equation (13.50).

An ambiguity arises in the sign of α in (F.9) and (13.44), given that $\alpha = (\Delta-2)/2 = \sqrt{S_j+4}/2$, and both the Whittaker and Bessel equations are symmetric under $\alpha \to -\alpha$. However, this ambiguity is resolved in the saddle point approximation and the limit of small $\sqrt{\lambda}/\tau$. In this regime, the order of the Bessel function becomes integer, allowing the use of reflection formulas to establish the correct symmetry in z and z', a requirement for the Green's function of a self-adjoint operator. The Whittaker function $M_{\beta,\alpha}$, equivalent to K_1 in our analysis, is symmetric under $\alpha \to -\alpha$ for all values of α.

F.2 Mode Sum Representation

The spin-j bulk-to-bulk propagator may be decomposed as [282]

$$G_0(j,K,z,z') = -\sum_n \frac{\psi_n(j,z)\psi_n(j,z')}{K^2+m_n^2(j)}. \tag{F.23}$$

The normalizable modes $\psi_n(j,z)$ are given in terms of associated Laguerre polynomials $L_n^\alpha(y)$. Explicitly, they are given by

$$\psi_n(j,z) = c_n(j)\, z^{\Delta_g(j)} L_n^{\Delta_g(j)-2}(4\kappa^2 z^2), \tag{F.24}$$

where

$$\Delta_g(j) = 2 + \sqrt{2\sqrt{\lambda}(j - j_{\mathbb{P}})} \tag{F.25}$$

and the normalization is

$$c_n(j) = \left(\frac{2(4\kappa^2)^{\Delta_q(j)-1}\Gamma(n+1)}{\Gamma(n+\Delta_q(j)-1)} \right)^{\frac{1}{2}}. \tag{F.26}$$

The squared glueball mass spectrum is given by

$$m_n^2(j) = 16\kappa^2 \left(n + \frac{1}{2}\Delta_g(j) \right). \tag{F.27}$$

Decomposed in this way, the role of Regge poles is evident. However, the process of Reggeization necessitates a summation over the entirety of the Regge trajectory. The Sommerfeld-Watson transform of the bulk-to-bulk propagator in impact parameter space is given by

$$G_1(s,t,z,z') = \int \mathrm{d}^2 b_\perp e^{-iqb_\perp} \int_{\mathcal{C}_L} \frac{\mathrm{d}j}{4\pi i} \left(\frac{1 - e^{-i\pi(j-1)}}{\sin(\pi(j-1))} \right) (\alpha' s z z')^{j-1} \tilde{G}_0(j,b,z,z'). \tag{F.28}$$

Fourier transforming (F.23) by utilizing

$$\int \mathrm{d}^2 q \frac{e^{iqb_\perp}}{q^2 + m_n^2(j)} = \frac{K_0(m_n(j)b)}{2\pi}, \tag{F.29}$$

we obtain the scalar bulk-to-bulk propagator in impact parameter space

$$\tilde{G}_0(j,b,z,z') = \sum_n \psi_n(j,z)\psi_n(j,z') \frac{K_0(m_n(j)b)}{2\pi z z'}, \tag{F.30}$$

where $K_0(y)$ is the modified Bessel function of the second kind. The mass spectrum for the odd-spin glueballs in (F.24) is given by

$$m_n^2(j) = (4\kappa)^2 (n + \frac{1}{2}\Delta_g(j)) \equiv m_0^2 \left(n + 1 + \frac{1}{2}\sqrt{2\sqrt{\lambda}(j - j_{\mathbb{O}})} \right). \tag{F.31}$$

At large impact parameter b, the Bessel function K_0 in (F.28) may be approximated with

$$K_0(m_n(j)b) \approx e^{-m_n(j)b} \sqrt{\frac{\pi}{2m_n(j)b}}. \tag{F.32}$$

The steep potential introduced by the soft-wall leads to a localization of the wavefunctions $\psi_n(j,z)$ at small z. In this case, we may take the limit of the z-dependent piece in (F.24) to approximate

$$\begin{aligned} z^{\Delta} L_n^{\Delta-2}(z^2) &= \frac{z^{-2}e^{z^2}}{\Gamma(n+1)} \int \mathrm{d}x e^{-x} x^{n+\alpha/2} J_{\Delta-2}(2\sqrt{xz}) \\ &\approx \frac{z^{\Delta}}{\Gamma(n+1)\Gamma(\Delta-1)} \int dx e^{x} x^{n+\Delta-2} \\ &= z^{\Delta} \frac{\Gamma(n+\Delta-1)}{\Gamma(\Delta-1)\Gamma(n+1)} . \end{aligned} \tag{F.33}$$

As was the case for the conformal limit, the gamma functions are trivial when evaluated at the saddle point. To leading order, we thus have

$$\begin{aligned} G_1(s,t,z,z') \approx \int \mathrm{d}^2 b_\perp e^{-iqb_\perp} &\times \int_{\mathcal{C}_L} \frac{\mathrm{d}j}{4\pi i} \left(\frac{1-e^{-i\pi(j-1)}}{\sin(\pi(j-1))} \right) (\alpha' s z z')^{j-1} \\ &\times \sum_n \psi_n(j,z)\psi_n(j,z') \frac{e^{-m_n(j)b}}{2\pi z z'} \left(\frac{\pi}{2m_n(j)b} \right)^{\frac{1}{2}} \end{aligned} \tag{F.34}$$

The contour $\mathcal{C}_L$ in (F.28) is defined to the left of the branch point $j = j_{\mathbb{O}}$ as illustrated in Fig. 13.3. Considering the arguments presented above (13.36) in the main text and for $\tau/\sqrt{\lambda} \gg 1$, the j-integration along $\mathcal{C}_L$ is evaluated by a saddle point approximation, resulting in

$$\begin{aligned} G_1(s,t,z,z') \approx -f^-(\lambda) \int \mathrm{d}^2 b_\perp e^{-iqb_\perp} \frac{1}{8} \sqrt{\frac{m_0 b}{32\pi^2 (n+1)\mathcal{D}\tau^3}} \\ \times \sum_n \frac{\psi_n(j_{\mathbb{O}},z)\psi_n(j_{\mathbb{O}},z')}{zz'} e^{(j_{\mathbb{O}}-1)\tau - m_0 b\sqrt{n+1} - \frac{(m_0 b)^2}{64(n+1)\mathcal{D}\tau}} . \end{aligned} \tag{F.35}$$

We did not succeed in analytically evaluating this expression, though numerically, it agrees reasonably well with (F.16) when the first few modes are summed over.

TU Bibliothek WIEN Your knowledge hub
Die approbierte gedruckte Originalversion dieser Dissertation ist an der TU Wien Bibliothek verfügbar.
The approved original version of this doctoral thesis is available in print at TU Wien Bibliothek.

Bibliography

[1] G. P. S. Occhialini and C. F. Powell, *Nuclear disintegration produced by slow charged particles of small mass*, *Nature* **159** (1947) 186–190.

[2] H. Yukawa, *On the Interaction of Elementary Particles I*, *Proc. Phys. Math. Soc. Jap.* **17** (1935) 48–57.

[3] M. Gell-Mann, *A Schematic Model of Baryons and Mesons*, *Phys. Lett.* **8** (1964) 214–215.

[4] G. Zweig, *An SU_3 model for strong interaction symmetry and its breaking; Version 2*, *CERN-TH-412* (1964) .

[5] H. Fritzsch and M. Gell-Mann, *Current algebra: Quarks and what else?*, *eConf* **C720906V2** (1972) 135–165, [`hep-ph/0208010`].

[6] H. Fritzsch, M. Gell-Mann and H. Leutwyler, *Advantages of the Color Octet Gluon Picture*, *Phys. Lett. B* **47** (1973) 365–368.

[7] R. L. Jaffe and K. Johnson, *Unconventional States of Confined Quarks and Gluons*, *Phys. Lett. B* **60** (1976) 201–204.

[8] H. Fritzsch and P. Minkowski, *Ψ Resonances, Gluons and the Zweig Rule*, *Nuovo Cim. A* **30** (1975) 393.

[9] PARTICLE DATA GROUP collaboration, R. L. Workman, *Review of Particle Physics*, *PTEP* **2022** (2022) 083C01.

[10] UKQCD collaboration, G. S. Bali, K. Schilling, A. Hulsebos, A. C. Irving, C. Michael and P. W. Stephenson, *A Comprehensive lattice study of SU(3) glueballs*, *Phys. Lett. B* **309** (1993) 378–384, [`hep-lat/9304012`].

[11] C. J. Morningstar and M. J. Peardon, *The Glueball spectrum from an anisotropic lattice study*, *Phys. Rev.* **D60** (1999) 034509, [`hep-lat/9901004`].

[12] Y. Chen et al., *Glueball spectrum and matrix elements on anisotropic lattices*, *Phys. Rev. D* **73** (2006) 014516, [`hep-lat/0510074`].

[13] E. Gregory, A. Irving, B. Lucini, C. McNeile, A. Rago, C. Richards et al., *Towards the glueball spectrum from unquenched lattice QCD*, *JHEP* **10** (2012) 170, [`1208.1858`].

[14] W. Sun, L.-C. Gui, Y. Chen, M. Gong, C. Liu, Y.-B. Liu et al., *Glueball spectrum from $N_f = 2$ lattice QCD study on anisotropic lattices*, *Chin. Phys. C* **42** (2018) 093103, [`1702.08174`].

[15] A. Windisch, M. Q. Huber and R. Alkofer, *On the analytic structure of scalar glueball operators at the Born level*, *Phys. Rev. D* **87** (2013) 065005, [`1212.2175`].

[16] H. Sanchis-Alepuz, C. S. Fischer, C. Kellermann and L. von Smekal, *Glueballs from the Bethe-Salpeter equation*, *Phys. Rev. D* **92** (2015) 034001, [`1503.06051`].

[17] M. Q. Huber, C. S. Fischer and H. Sanchis-Alepuz, *Spectrum of scalar and pseudoscalar glueballs from functional methods*, *Eur. Phys. J. C* **80** (2020) 1077, [`2004.00415`].

[18] M. Q. Huber, C. S. Fischer and H. Sanchis-Alepuz, *Higher spin glueballs from functional methods*, *Eur. Phys. J. C* **81** (2021) 1083, [`2110.09180`].

[19] M. Q. Huber, *Nonperturbative properties of Yang–Mills theories*, *Phys. Rept.* **879** (2020) 1–92, [`1808.05227`].

[20] T. Regge, *Introduction to complex orbital momenta*, *Nuovo Cim.* **14** (1959) 951.

[21] G. F. Chew and S. C. Frautschi, *Principle of Equivalence for All Strongly Interacting Particles Within the S Matrix Framework*, *Phys. Rev. Lett.* **7** (1961) 394–397.

[22] G. F. Chew and S. C. Frautschi, *Regge Trajectories and the Principle of Maximum Strength for Strong Interactions*, *Phys. Rev. Lett.* **8** (1962) 41–44.

[23] J. M. Maldacena, *The Large N limit of superconformal field theories and supergravity*, *Adv. Theor. Math. Phys.* **2** (1998) 231–252, [`hep-th/9711200`].

[24] E. Klempt and A. Zaitsev, *Glueballs, Hybrids, Multiquarks. Experimental facts versus QCD inspired concepts*, *Phys. Rept.* **454** (2007) 1–202, [`0708.4016`].

[25] V. Crede and C. A. Meyer, *The Experimental Status of Glueballs*, *Prog. Part. Nucl. Phys.* **63** (2009) 74–116, [`0812.0600`].

[26] W. Ochs, *The Status of Glueballs*, *J. Phys.* **G40** (2013) 043001, [`1301.5183`].

[27] E. Klempt, *Scalar mesons and the fragmented glueball*, *Phys. Lett. B* **820** (2021) 136512, [`2104.09922`].

[28] H.-X. Chen, W. Chen, X. Liu, Y.-R. Liu and S.-L. Zhu, *An updated review of the new hadron states*, Rept. Prog. Phys. **86** (2023) 026201, [2204.02649].

[29] WA102 collaboration, D. Barberis et al., *A Partial wave analysis of the centrally produced $\pi^+\pi^-$ system in p p interactions at 450 GeV/c*, Phys. Lett. B **453** (1999) 316–324, [hep-ex/9903043].

[30] Crystal Barrel collaboration, A. Abele et al., *Evidence for a $\pi\eta$-P-wave in $\overline{p}p$ annihilations at rest into $\pi^0\pi^0\eta$*, Phys. Lett. B **446** (1999) 349–355.

[31] BESIII collaboration, M. Ablikim et al., *Partial wave analysis of $J/\psi \to \gamma\eta\eta$*, Phys. Rev. D **87** (2013) 092009, [1301.0053].

[32] CERN-College de France-Madrid-Stockholm collaboration, C. Dionisi et al., *Observation and Quantum Numbers Determination of the $E(1420)$ Meson in π^-p Interactions at 3.95 GeV/c*, Nucl. Phys. B **169** (1980) 1–19.

[33] F. E. Close and A. Kirk, *Implications of the glueball $q\overline{q}$ filter on the 1^{++} nonet*, Z. Phys. C **76** (1997) 469–474, [hep-ph/9706543].

[34] C. Amsler and N. A. Tornqvist, *Mesons beyond the naive quark model*, Phys. Rept. **389** (2004) 61–117.

[35] F. Chen, X. Jiang, Y. Chen, K.-F. Liu, W. Sun and Y.-B. Yang, *Glueballs at Physical Pion Mass*, 2111.11929.

[36] S. Donnachie, H. G. Dosch, O. Nachtmann and P. Landshoff, *Pomeron physics and QCD*, vol. 19. Cambridge University Press, 12, 2004.

[37] C. Rosenzweig, A. Salomone and J. Schechter, *A Pseudoscalar Glueball, the Axial Anomaly and the Mixing Problem for Pseudoscalar Mesons*, Phys. Rev. D **24** (1981) 2545–2548.

[38] C. Amsler and F. E. Close, *Is $f_0(1500)$ a scalar glueball?*, Phys. Rev. D **53** (1996) 295–311, [hep-ph/9507326].

[39] F. E. Close and A. Kirk, *Scalar glueball q anti-q mixing above 1 GeV and implications for lattice QCD*, Eur. Phys. J. C **21** (2001) 531–543, [hep-ph/0103173].

[40] F. E. Close and Q. Zhao, *Production of $f_0(1710)$, $f_0(1500)$, and $f_0(1370)$ in J/ψ hadronic decays*, Phys. Rev. D **71** (2005) 094022, [hep-ph/0504043].

[41] W.-J. Lee and D. Weingarten, *Scalar quarkonium masses and mixing with the lightest scalar glueball*, Phys. Rev. D **61** (2000) 014015, [hep-lat/9910008].

[42] S. Janowski, F. Giacosa and D. H. Rischke, *Is $f_0(1710)$ a glueball?*, *Phys. Rev. D* **90** (2014) 114005, [`1408.4921`].

[43] H.-Y. Cheng, C.-K. Chua and K.-F. Liu, *Revisiting Scalar Glueballs*, *Phys. Rev. D* **92** (2015) 094006, [`1503.06827`].

[44] CLQCD collaboration, L.-C. Gui, Y. Chen, G. Li, C. Liu, Y.-B. Liu, J.-P. Ma et al., *Scalar Glueball in Radiative J/ψ Decay on the Lattice*, *Phys. Rev. Lett.* **110** (2013) 021601, [`1206.0125`].

[45] A. V. Sarantsev, I. Denisenko, U. Thoma and E. Klempt, *Scalar isoscalar mesons and the scalar glueball from radiative J/ψ decays*, *Phys. Lett. B* **816** (2021) 136227, [`2103.09680`].

[46] E. Klempt and A. V. Sarantsev, *Singlet-octet-glueball mixing of scalar mesons*, *Phys. Lett. B* **826** (2022) 136906, [`2112.04348`].

[47] A. Masoni, C. Cicalo and G. L. Usai, *The case of the pseudoscalar glueball*, *J. Phys. G* **32** (2006) R293–R335.

[48] S. Scherer and M. R. Schindler, *A Primer for Chiral Perturbation Theory*, vol. 830. Springer Berlin, Heidelberg, 2012, 10.1007/978-3-642-19254-8.

[49] G. 't Hooft, *Symmetry Breaking Through Bell-Jackiw Anomalies*, *Phys. Rev. Lett.* **37** (1976) 8–11.

[50] G. 't Hooft, *Computation of the Quantum Effects Due to a Four-Dimensional Pseudoparticle*, *Phys. Rev. D* **14** (1976) 3432–3450.

[51] E. Witten, *Current Algebra Theorems for the U(1) "Goldstone Boson"*, *Nucl.Phys.* **B156** (1979) 269.

[52] G. Veneziano, *U(1) Without Instantons*, *Nucl.Phys.* **B159** (1979) 213–224.

[53] J. Wess and B. Zumino, *Consequences of anomalous Ward identities*, *Phys. Lett. B* **37** (1971) 95–97.

[54] E. Witten, *Global Aspects of Current Algebra*, *Nucl. Phys. B* **223** (1983) 422–432.

[55] M. Gell-Mann, R. J. Oakes and B. Renner, *Behavior of current divergences under SU(3) x SU(3)*, *Phys. Rev.* **175** (1968) 2195–2199.

[56] J. Dai, R. G. Leigh and J. Polchinski, *New Connections Between String Theories*, *Mod. Phys. Lett. A* **4** (1989) 2073–2083.

[57] P. Horava, *Background Duality of Open String Models*, *Phys. Lett. B* **231** (1989) 251–257.

[58] J. Polchinski, *Dirichlet Branes and Ramond-Ramond charges*, *Phys. Rev. Lett.* **75** (1995) 4724–4727, [`hep-th/9510017`].

[59] E. Witten, *String theory dynamics in various dimensions*, *Nucl. Phys. B* **443** (1995) 85–126, [`hep-th/9503124`].

[60] Y. Kim and D. Yi, *Holography at work for nuclear and hadron physics*, *Adv. High Energy Phys.* **2011** (2011) 259025, [`1107.0155`].

[61] S. S. Gubser, I. R. Klebanov and A. M. Polyakov, *Gauge theory correlators from noncritical string theory*, *Phys. Lett. B* **428** (1998) 105–114, [`hep-th/9802109`].

[62] E. Witten, *Anti-de Sitter space and holography*, *Adv. Theor. Math. Phys.* **2** (1998) 253–291, [`hep-th/9802150`].

[63] O. Aharony, S. S. Gubser, J. M. Maldacena, H. Ooguri and Y. Oz, *Large N field theories, string theory and gravity*, *Phys. Rept.* **323** (2000) 183–386, [`hep-th/9905111`].

[64] M. Ammon and J. Erdmenger, *Gauge/gravity duality: Foundations and applications*. Cambridge University Press, Cambridge, 4, 2015, 10.1017/CBO9780511846373.

[65] J. McGreevy, *Holographic duality with a view toward many-body physics*, *Adv. High Energy Phys.* **2010** (2010) 723105, [`0909.0518`].

[66] J. M. Maldacena, *Wilson loops in large N field theories*, *Phys. Rev. Lett.* **80** (1998) 4859–4862, [`hep-th/9803002`].

[67] G. Policastro, D. T. Son and A. O. Starinets, *The Shear viscosity of strongly coupled N=4 supersymmetric Yang-Mills plasma*, *Phys. Rev. Lett.* **87** (2001) 081601, [`hep-th/0104066`].

[68] E. Witten, *Anti-de Sitter space, thermal phase transition, and confinement in gauge theories*, *Adv. Theor. Math. Phys.* **2** (1998) 505–532, [`hep-th/9803131`].

[69] T. Sakai and S. Sugimoto, *Low energy hadron physics in holographic QCD*, *Prog. Theor. Phys.* **113** (2005) 843–882, [`hep-th/0412141`].

[70] K. Becker, M. Becker and J. H. Schwarz, *String theory and M-theory: A modern introduction*. Cambridge University Press, 12, 2006, 10.1017/CBO9780511816086.

[71] P. G. O. Freund and M. A. Rubin, *Dynamics of Dimensional Reduction*, *Phys. Lett. B* **97** (1980) 233–235.

[72] I. Kanitscheider, K. Skenderis and M. Taylor, *Precision holography for non-conformal branes*, *JHEP* **09** (2008) 094, [0807.3324].

[73] N. R. Constable and R. C. Myers, *Spin two glueballs, positive energy theorems and the AdS / CFT correspondence*, *JHEP* **10** (1999) 037, [hep-th/9908175].

[74] R. C. Brower, S. D. Mathur and C.-I. Tan, *Glueball spectrum for QCD from AdS supergravity duality*, *Nucl. Phys.* **B587** (2000) 249–276, [hep-th/0003115].

[75] T. Sakai and S. Sugimoto, *More on a holographic dual of QCD*, *Prog. Theor. Phys.* **114** (2005) 1083–1118, [hep-th/0507073].

[76] B. A. Burrington, V. S. Kaplunovsky and J. Sonnenschein, *Localized Backreacted Flavor Branes in Holographic QCD*, *JHEP* **02** (2008) 001, [0708.1234].

[77] F. Bigazzi and A. L. Cotrone, *Holographic QCD with Dynamical Flavors*, *JHEP* **01** (2015) 104, [1410.2443].

[78] A. Rebhan, *The Witten-Sakai-Sugimoto model: A brief review and some recent results*, *EPJ Web Conf.* **95** (2015) 02005, [1410.8858].

[79] J. Polchinski, *String Theory: Volume 2, Superstring Theory and Beyond.* Cambridge University Press, Cambridge, 1998.

[80] O. Bergman, S. Seki and J. Sonnenschein, *Quark mass and condensate in HQCD*, *JHEP* **12** (2007) 037, [0708.2839].

[81] M. B. Green, J. A. Harvey and G. W. Moore, *I-brane inflow and anomalous couplings on D-branes*, *Class. Quant. Grav.* **14** (1997) 47–52, [hep-th/9605033].

[82] T. H. R. Skyrme, *A Nonlinear field theory*, *Proc. Roy. Soc. Lond. A* **260** (1961) 127–138.

[83] G. S. Bali, F. Bursa, L. Castagnini, S. Collins, L. Del Debbio et al., *Mesons in large-N QCD*, *JHEP* **1306** (2013) 071, [1304.4437].

[84] T. Imoto, T. Sakai and S. Sugimoto, *Mesons as Open Strings in a Holographic Dual of QCD*, *Prog.Theor.Phys.* **124** (2010) 263–284, [1005.0655].

[85] J. H. Schwarz and E. Witten, *Anomaly analysis of brane - anti-brane systems*, *JHEP* **03** (2001) 032, [hep-th/0103099].

[86] A. Armoni, *Witten-Veneziano from Green-Schwarz*, *JHEP* **06** (2004) 019, [hep-th/0404248].

[87] J. L. F. Barbon, C. Hoyos-Badajoz, D. Mateos and R. C. Myers, *The Holographic life of the η'*, *JHEP* **10** (2004) 029, [hep-th/0404260].

[88] O. Aharony and D. Kutasov, *Holographic Duals of Long Open Strings*, *Phys.Rev.* **D78** (2008) 026005, [0803.3547].

[89] K. Hashimoto, T. Hirayama, F.-L. Lin and H.-U. Yee, *Quark Mass Deformation of Holographic Massless QCD*, *JHEP* **0807** (2008) 089, [0803.4192].

[90] A. Dhar and P. Nag, *Tachyon condensation and quark mass in modified Sakai-Sugimoto model*, *Phys.Rev.* **D78** (2008) 066021, [0804.4807].

[91] R. McNees, R. C. Myers and A. Sinha, *On quark masses in holographic QCD*, *JHEP* **0811** (2008) 056, [0807.5127].

[92] V. Niarchos, *Hairpin-Branes and Tachyon-Paperclips in Holographic Backgrounds*, *Nucl. Phys.* **B841** (2010) 268–302, [1005.1650].

[93] F. Brünner and A. Rebhan, *Constraints on the $\eta\eta'$ decay rate of a scalar glueball from gauge/gravity duality*, *Phys. Rev. D* **92** (2015) 121902, [1510.07605].

[94] M. Gell-Mann and F. Zachariasen, *Form-factors and vector mesons*, *Phys. Rev.* **124** (1961) 953–964.

[95] N. M. Kroll, T. D. Lee and B. Zumino, *Neutral Vector Mesons and the Hadronic Electromagnetic Current*, *Phys. Rev.* **157** (1967) 1376–1399.

[96] J. J. Sakurai, *Vector meson dominance and high-energy electron proton inelastic scattering*, *Phys. Rev. Lett.* **22** (1969) 981–984.

[97] J. J. Sakurai and D. Schildknecht, *Generalized vector dominance and inelastic electron-proton scattering*, *Phys. Lett. B* **40** (1972) 121–126.

[98] F. Hechenberger, J. Leutgeb and A. Rebhan, *Radiative meson and glueball decays in the Witten-Sakai-Sugimoto model*, *Phys. Rev. D* **107** (2023) 114020, [2302.13379].

[99] CLEO collaboration, D. M. Asner et al., *Hadronic Structure in the Decay $\tau^- \to \nu_\tau \pi^- \pi^0 \pi^0$ and the Sign of the Tau Neutrino Helicity*, *Phys. Rev. D* **61** (2000) 012002, [hep-ex/9902022].

[100] M. Suzuki, *Strange axial - vector mesons*, *Phys. Rev. D* **47** (1993) 1252–1255.

[101] F. Divotgey, L. Olbrich and F. Giacosa, *Phenomenology of axial-vector and pseudovector mesons: decays and mixing in the kaonic sector*, *Eur. Phys. J. A* **49** (2013) 135, [1306.1193].

[102] F. Ambrosino et al., *A Global fit to determine the pseudoscalar mixing angle and the gluonium content of the η' meson*, *JHEP* **07** (2009) 105, [0906.3819].

[103] R. R. Akhmetshin et al., *Study of* $\phi \to \pi^+\pi^-\pi^0$ *with CMD-2 detector*, *Phys. Lett. B* **642** (2006) 203–209.

[104] M. N. Achasov et al., *Study of the* $\pi\pi$ *mass spectra in the process* $e^+e^- \to \pi^+\pi^-\pi^0$ *at* $\sqrt{s}$ *= 1020 MeV*, *Phys. Rev. D* **65** (2002) 032002, [`hep-ex/0106048`].

[105] KLOE collaboration, A. Aloisio et al., *Study of the decay* $\phi \to \pi^+\pi^-\pi^0$ *with the KLOE detector*, *Phys. Lett. B* **561** (2003) 55–60, [`hep-ex/0303016`].

[106] PrimEx-II collaboration, I. Larin et al., *Precision measurement of the neutral pion lifetime*, *Science* **368** (2020) 506–509.

[107] D. T. Son and M. A. Stephanov, *QCD and dimensional deconstruction*, *Phys. Rev. D* **69** (2004) 065020, [`hep-ph/0304182`].

[108] L. Da Rold and A. Pomarol, *Chiral symmetry breaking from five dimensional spaces*, *Nucl. Phys. B* **721** (2005) 79–97, [`hep-ph/0501218`].

[109] J. Hirn and V. Sanz, *Interpolating between low and high energy QCD via a 5D Yang-Mills model*, *JHEP* **12** (2005) 030, [`hep-ph/0507049`].

[110] M. Bando, T. Kugo, S. Uehara, K. Yamawaki and T. Yanagida, *Is the* ρ *Meson a Dynamical Gauge Boson of Hidden Local Symmetry?*, *Phys. Rev. Lett.* **54** (1985) 1215.

[111] M. Zielinski et al., *Evidence for the Electromagnetic Production of the* A_1, *Phys. Rev. Lett.* **52** (1984) 1195.

[112] D. V. Amelin et al., *Study of the decay* $f_1(1285) \to \rho^0(770)\gamma$, *Z. Phys. C* **66** (1995) 71–76.

[113] M. Zanke, M. Hoferichter and B. Kubis, *On the transition form factors of the axial-vector resonance* f_1*(1285) and its decay into* e^+e^-, *JHEP* **07** (2021) 106, [`2103.09829`].

[114] L. D. Landau, *On the angular momentum of a system of two photons*, *Dokl. Akad. Nauk SSSR* **60** (1948) 207–209.

[115] C.-N. Yang, *Selection Rules for the Dematerialization of a Particle Into Two Photons*, *Phys. Rev.* **77** (1950) 242–245.

[116] L3 collaboration, P. Achard et al., $f_1(1285)$ *formation in two-photon collisions at LEP*, *Phys. Lett.* **B526** (2002) 269–277, [`hep-ex/0110073`].

[117] L3 collaboration, P. Achard et al., *Study of resonance formation in the mass region 1400 – 1500 MeV through the reaction* $\gamma\gamma \to K^0_S K^\pm \pi^\mp$, *JHEP* **03** (2007) 018.

[118] D. J. Gross and H. Ooguri, *Aspects of large N gauge theory dynamics as seen by string theory*, *Phys. Rev. D* **58** (1998) 106002, [`hep-th/9805129`].

[119] C. Csaki, H. Ooguri, Y. Oz and J. Terning, *Glueball mass spectrum from supergravity*, *JHEP* **01** (1999) 017, [`hep-th/9806021`].

[120] R. de Mello Koch, A. Jevicki, M. Mihailescu and J. P. Nunes, *Evaluation of glueball masses from supergravity*, *Phys. Rev. D* **58** (1998) 105009, [`hep-th/9806125`].

[121] A. Hashimoto and Y. Oz, *Aspects of QCD dynamics from string theory*, *Nucl. Phys. B* **548** (1999) 167–179, [`hep-th/9809106`].

[122] C. Csaki, J. Russo, K. Sfetsos and J. Terning, *Supergravity models for (3+1)-dimensional QCD*, *Phys. Rev. D* **60** (1999) 044001, [`hep-th/9902067`].

[123] F. Hechenberger, K. A. Mamo and I. Zahed, *Holographic Odderon at TOTEM?*, *Phys. Rev. D* **109** (2024) 036029, [`2311.05973`].

[124] F. Hechenberger, J. Leutgeb and A. Rebhan, *Spin-1 glueballs in the Witten-Sakai-Sugimoto model*, *Phys. Rev. D* **109** (2024) 074014, [`2401.17986`].

[125] H. Boschi-Filho and N. R. F. Braga, *QCD / string holographic mapping and glueball mass spectrum*, *Eur. Phys. J. C* **32** (2004) 529–533, [`hep-th/0209080`].

[126] P. Colangelo, F. De Fazio, F. Jugeau and S. Nicotri, *On the light glueball spectrum in a holographic description of QCD*, *Phys. Lett. B* **652** (2007) 73–78, [`hep-ph/0703316`].

[127] H. Forkel, *Holographic glueball structure*, *Phys. Rev. D* **78** (2008) 025001, [`0711.1179`].

[128] D. Li and M. Huang, *Dynamical holographic QCD model for glueball and light meson spectra*, *JHEP* **11** (2013) 088, [`1303.6929`].

[129] E. Folco Capossoli and H. Boschi-Filho, *Glueball spectra and Regge trajectories from a modified holographic softwall model*, *Phys. Lett. B* **753** (2016) 419–423, [`1510.03372`].

[130] A. Ballon-Bayona, H. Boschi-Filho, L. A. H. Mamani, A. S. Miranda and V. T. Zanchin, *Effective holographic models for QCD: glueball spectrum and trace anomaly*, *Phys. Rev. D* **97** (2018) 046001, [`1708.08968`].

[131] M. Rinaldi and V. Vento, *Meson and glueball spectroscopy within the graviton soft wall model*, *Phys. Rev. D* **104** (2021) 034016, [`2101.02616`].

[132] F. Brünner, J. Leutgeb and A. Rebhan, *A broad pseudovector glueball from holographic QCD*, *Phys. Lett. B* **788** (2019) 431–435, [`1807.10164`].

[133] F. Brünner, D. Parganlija and A. Rebhan, *Glueball Decay Rates in the Witten-Sakai-Sugimoto Model*, Phys. Rev. **D91** (2015) 106002, [1501.07906].

[134] Y.-Q. Chen and E. Braaten, *An Explanation for the ρ-π Puzzle of J/ψ and ψ' Decays*, Phys. Rev. Lett. **80** (1998) 5060–5063, [hep-ph/9801226].

[135] J. Leutgeb and A. Rebhan, *Witten-Veneziano mechanism and pseudoscalar glueball-meson mixing in holographic QCD*, Phys. Rev. D **101** (2020) 014006, [1909.12352].

[136] K. Hashimoto, C.-I. Tan and S. Terashima, *Glueball decay in holographic QCD*, Phys. Rev. **D77** (2008) 086001, [0709.2208].

[137] F. Brünner and A. Rebhan, *Nonchiral enhancement of scalar glueball decay in the Witten-Sakai-Sugimoto model*, Phys. Rev. Lett. **115** (2015) 131601, [1504.05815].

[138] C. Edwards et al., *Observation of a Pseudoscalar State at 1440 MeV in J/ψ Radiative Decays*, Phys. Rev. Lett. **49** (1982) 259.

[139] F. Brünner and A. Rebhan, *Holographic QCD predictions for production and decay of pseudoscalar glueballs*, Phys. Lett. B **770** (2017) 124–130, [1610.10034].

[140] V. Mathieu and V. Vento, *Pseudoscalar glueball and η-η' mixing*, Phys. Rev. D **81** (2010) 034004, [0910.0212].

[141] F. Giacosa, S. Jafarzade and R. D. Pisarski, *Anomalous interactions between mesons with nonzero spin and glueballs*, Phys. Rev. D **109** (2024) L071502, [2309.00086].

[142] (BESIII COLLABORATION)*, BESIII collaboration, M. Ablikim et al., *Observation of a State $X(2600)$ in the $\pi^+\pi^-\eta'$ System in the Process $J/\psi \to \gamma\pi^+\pi^-\eta'$*, Phys. Rev. Lett. **129** (2022) 042001, [2201.10796].

[143] L.-C. Gui, J.-M. Dong, Y. Chen and Y.-B. Yang, *Study of the pseudoscalar glueball in J/ψ radiative decays*, Phys. Rev. D **100** (2019) 054511, [1906.03666].

[144] BESIII collaboration, M. Ablikim et al., *Determination of Spin-Parity Quantum Numbers of $X(2370)$ as 0^{-+} from $J/\psi \to \gamma K^0_S K^0_S \eta'$*, Phys. Rev. Lett. **132** (2024) 181901, [2312.05324].

[145] A. Vereijken, S. Jafarzade, M. Piotrowska and F. Giacosa, *Is $f_2(1950)$ the tensor glueball?*, 2304.05225.

[146] L. Burakovsky and P. R. Page, *Scalar glueball mixing and decay*, Phys. Rev. D **59** (1999) 014022, [hep-ph/9807400].

TU Bibliothek Your knowledge hub WIEN
Die approbierte gedruckte Originalversion dieser Dissertation ist an der TU Wien Bibliothek verfügbar.
The approved original version of this doctoral thesis is available in print at TU Wien Bibliothek.

[147] WA102 collaboration, D. Barberis et al., *A Coupled channel analysis of the centrally produced K^+K^- and $\pi^+\pi^-$ final states in pp interactions at 450 GeV/c*, Phys. Lett. B **462** (1999) 462–470, [hep-ex/9907055].

[148] WA102 collaboration, D. Barberis et al., *A study of the $\eta\eta$ channel produced in central pp interactions at 450 GeV/c*, Phys. Lett. B **479** (2000) 59–66, [hep-ex/0003033].

[149] CRYSTAL BARREL collaboration, A. Abele et al., *4π decays of scalar and vector mesons*, Eur. Phys. J. C **21** (2001) 261–269.

[150] S. R. Cotanch and R. A. Williams, *Glueball enhancements in $p(\gamma, VV)p$ through vector meson dominance*, Phys. Rev. C **70** (2004) 055201, [nucl-th/0403051].

[151] BESIII collaboration, M. Ablikim et al., *Partial wave analysis of $J/\psi \to \gamma\eta\eta'$*, Phys. Rev. D **106** (2022) 072012, [2202.00623].

[152] R. S. Longacre et al., *A Measurement of $\pi^- p \to K^0_s K^0_s n$ at 22 GeV/c and a Systematic Study of the 2^{++} Meson Spectrum*, Phys. Lett. B **177** (1986) 223–227.

[153] M. Albaladejo and J. A. Oller, *Identification of a Scalar Glueball*, Phys. Rev. Lett. **101** (2008) 252002, [0801.4929].

[154] W. I. Eshraim, S. Janowski, F. Giacosa and D. H. Rischke, *Decay of the pseudoscalar glueball into scalar and pseudoscalar mesons*, Phys. Rev. D **87** (2013) 054036, [1208.6474].

[155] W. I. Eshraim and S. Schramm, *Decay modes of the excited pseudoscalar glueball*, Phys. Rev. D **95** (2017) 014028, [1606.02207].

[156] A. Tomasiello, *Geometry of String Theory Compactifications.* Cambridge University Press, 1, 2022, 10.1017/9781108635745.

[157] E. Bergshoeff, R. Kallosh, T. Ortin, D. Roest and A. Van Proeyen, *New formulations of D = 10 supersymmetry and D8 - O8 domain walls*, Class. Quant. Grav. **18** (2001) 3359–3382, [hep-th/0103233].

[158] J. Bartels, M. A. Braun, D. Colferai and G. P. Vacca, *Diffractive η_c photoproduction and electroproduction with the perturbative QCD odderon*, Eur. Phys. J. C **20** (2001) 323–331, [hep-ph/0102221].

[159] A. Dumitru and T. Stebel, *Multiquark matrix elements in the proton and three gluon exchange for exclusive η_c production in photon-proton diffractive scattering*, Phys. Rev. D **99** (2019) 094038, [1903.07660].

[160] Y. Jia, Z. Mo, J. Pan and J.-Y. Zhang, *Photoproduction of C-even quarkonia at the EIC and EicC*, Phys. Rev. D **108** (2023) 016015, [`2207.14171`].

[161] F. Giacosa, J. Sammet and S. Janowski, *Decays of the vector glueball*, Phys. Rev. D **95** (2017) 114004, [`1607.03640`].

[162] D. Parganlija, P. Kovacs, G. Wolf, F. Giacosa and D. H. Rischke, *Meson vacuum phenomenology in a three-flavor linear sigma model with (axial-)vector mesons*, Phys. Rev. D **87** (2013) 014011, [`1208.0585`].

[163] P. G. O. Freund and Y. Nambu, *Dynamics in the Zweig-Iizuka Rule and a New Vector Meson Below 2 GeV/c*^{2}, Phys. Rev. Lett. **34** (1975) 1645.

[164] W.-S. Hou and A. Soni, *Vector Gluonium as a Possible Explanation for Anomalous* ψ *Decays*, Phys. Rev. Lett. **50** (1983) 569.

[165] S. J. Brodsky, G. P. Lepage and S. F. Tuan, *Exclusive Charmonium Decays: The* $J/\psi(\psi') \to \rho\pi$*,* $K^*\bar{K}$ *Puzzle*, Phys. Rev. Lett. **59** (1987) 621.

[166] G. W. S. Hou, *(Vector) glueballs and charmonium decay revisited*, in *9th Annual Divisional Meeting (DPF 96) of the Division of Particles and Fields of the American Physical Society*, pp. 399–401, 1996, `hep-ph/9609363`.

[167] G. W.-S. Hou, *The Case for a vector glueball*, in *YITP International Workshop on Recent Developments in QCD and Hadron Physics*, 1997, `hep-ph/9707526`.

[168] C.-T. Chan and W.-S. Hou, *On the mixing amplitude of* J/ψ *and vector glueball* O, Nucl. Phys. A **675** (2000) 367C–370C, [`hep-ph/9911423`].

[169] X.-H. Mo, C.-Z. Yuan and P. Wang, *Study of the* $\rho - \pi$ *Puzzle in Charmonium Decays*, *Chin. Phys. C* **31** (2007) 686–701, [`hep-ph/0611214`].

[170] Belle collaboration, S. Uehara et al., *High-statistics study of* K^0_S *pair production in two-photon collisions*, PTEP **2013** (2013) 123C01, [`1307.7457`].

[171] E. H. Kada, P. Kessler and J. Parisi, *Two* γ *Decay Widths of Glueballs*, Phys. Rev. D **39** (1989) 2657.

[172] S. R. Cotanch and R. A. Williams, *Tensor glueball photoproduction and decay*, Phys. Lett. B **621** (2005) 269–275, [`nucl-th/0505074`].

[173] ARGUS collaboration, H. Albrecht et al., *Measurement of* K^+K^- *Production in* $\gamma\gamma$ *Collisions*, Z. Phys. C **48** (1990) 183–190.

[174] F. E. Close and A. Kirk, *The Mixing of the* $f_0(1370)$*,* $f_0(1500)$ *and* $f_0(1710)$ *and the search for the scalar glueball*, Phys. Lett. B **483** (2000) 345–352, [`hep-ph/0004241`].

[175] A. A. Godizov, *The ground state of the Pomeron and its decays to light mesons and photons*, *Eur. Phys. J. C* **76** (2016) 361, [1604.01689].

[176] I. I. Pomeranchuk, *The Conservation of Isotopic Spin and the Scattering of Antinucleons by Nucleons*, *Zh. Eksp. Teor. Fiz.* **34** (1958) 725.

[177] L. N. Lipatov, *Reggeization of the Vector Meson and the Vacuum Singularity in Nonabelian Gauge Theories*, *Sov. J. Nucl. Phys.* **23** (1976) 338–345.

[178] E. A. Kuraev, L. N. Lipatov and V. S. Fadin, *The Pomeranchuk Singularity in Nonabelian Gauge Theories*, *Sov. Phys. JETP* **45** (1977) 199–204.

[179] I. I. Balitsky and L. N. Lipatov, *The Pomeranchuk Singularity in Quantum Chromodynamics*, *Sov. J. Nucl. Phys.* **28** (1978) 822–829.

[180] L. N. Lipatov, *The Bare Pomeron in Quantum Chromodynamics*, *Sov. Phys. JETP* **63** (1986) 904–912.

[181] R. A. Janik and J. Wosiek, *Solution of the odderon problem*, *Phys. Rev. Lett.* **82** (1999) 1092–1095, [hep-th/9802100].

[182] J. Bartels, L. N. Lipatov and G. P. Vacca, *A New odderon solution in perturbative QCD*, *Phys. Lett. B* **477** (2000) 178–186, [hep-ph/9912423].

[183] J. Bartels, *High-Energy Behavior in a Nonabelian Gauge Theory (II): First Corrections to $T_{n\to m}$ Beyond the Leading $\ln s$ Approximation*, *Nucl. Phys. B* **175** (1980) 365–401.

[184] J. Kwiecinski and M. Praszalowicz, *Three Gluon Integral Equation and Odd c Singlet Regge Singularities in QCD*, *Phys. Lett. B* **94** (1980) 413–416.

[185] E. Iancu, A. Leonidov and L. D. McLerran, *Nonlinear gluon evolution in the color glass condensate. 1.*, *Nucl. Phys. A* **692** (2001) 583–645, [hep-ph/0011241].

[186] E. Ferreiro, E. Iancu, A. Leonidov and L. McLerran, *Nonlinear gluon evolution in the color glass condensate. 2.*, *Nucl. Phys. A* **703** (2002) 489–538, [hep-ph/0109115].

[187] Y. Hatta, E. Iancu, K. Itakura and L. McLerran, *Odderon in the color glass condensate*, *Nucl. Phys. A* **760** (2005) 172–207, [hep-ph/0501171].

[188] F. Gelis, E. Iancu, J. Jalilian-Marian and R. Venugopalan, *The Color Glass Condensate*, *Ann. Rev. Nucl. Part. Sci.* **60** (2010) 463–489, [1002.0333].

[189] TOTEM, D0 collaboration, V. M. Abazov et al., *Odderon Exchange from Elastic Scattering Differences between pp and $p\bar{p}$ Data at 1.96 TeV and from pp Forward Scattering Measurements*, *Phys. Rev. Lett.* **127** (2021) 062003, [2012.03981].

[190] A. Donnachie and P. V. Landshoff, *Lack of evidence for an odderon at small t*, *Phys. Lett. B* **831** (2022) 137199, [`2203.00290`].

[191] R. C. Brower, M. Djuric and C.-I. Tan, *Odderon in gauge/string duality*, *JHEP* **07** (2009) 063, [`0812.0354`].

[192] P. D. B. Collins, *An Introduction to Regge Theory and High Energy Physics*. Cambridge Monographs on Mathematical Physics. Cambridge University Press, 7, 2023, 10.1017/9781009403269.

[193] C. Ewerz, *The Odderon: Theoretical status and experimental tests*, in *11th International Conference on Elastic and Diffractive Scattering: Towards High Energy Frontiers: The 20th Anniversary of the Blois Workshops, 17th Rencontre de Blois*, 11, 2005, `hep-ph/0511196`.

[194] V. Petrov and N. Tkachenko, *Odderon: Lost or/and Found?*, `2201.06948`.

[195] F. Hechenberger, K. A. Mamo and I. Zahed, *Threshold photoproduction of η_c and η_b using holographic QCD*, *Phys. Rev. D* **109** (2024) 074013, [`2401.12162`].

[196] R. C. Brower, J. Polchinski, M. J. Strassler and C.-I. Tan, *The Pomeron and gauge/string duality*, *JHEP* **12** (2007) 005, [`hep-th/0603115`].

[197] R. C. Brower, M. J. Strassler and C.-I. Tan, *On The Pomeron at Large 't Hooft Coupling*, *JHEP* **03** (2009) 092, [`0710.4378`].

[198] R. C. Brower, M. S. Costa, M. Djurić, T. Raben and C.-I. Tan, *Strong Coupling Expansion for the Conformal Pomeron/Odderon Trajectories*, *JHEP* **02** (2015) 104, [`1409.2730`].

[199] M. A. Braun, *Odderon and QCD*, `hep-ph/9805394`.

[200] J. Polchinski and M. J. Strassler, *Hard scattering and gauge / string duality*, *Phys. Rev. Lett.* **88** (2002) 031601, [`hep-th/0109174`].

[201] J. Polchinski and M. J. Strassler, *Deep inelastic scattering and gauge / string duality*, *JHEP* **05** (2003) 012, [`hep-th/0209211`].

[202] R. C. Brower, M. Djuric, I. Sarcevic and C.-I. Tan, *String-Gauge Dual Description of Deep Inelastic Scattering at Small-x*, *JHEP* **11** (2010) 051, [`1007.2259`].

[203] ZEUS collaboration, J. Breitweg et al., *ZEUS results on the measurement and phenomenology of F_2 at low x and low Q^2*, *Eur. Phys. J. C* **7** (1999) 609–630, [`hep-ex/9809005`].

[204] R. A. Janik and R. B. Peschanski, *High-energy scattering and the AdS / CFT correspondence*, Nucl. Phys. B **565** (2000) 193–209, [`hep-th/9907177`].

[205] R. C. Brower, M. J. Strassler and C.-I. Tan, *On the eikonal approximation in AdS space*, JHEP **03** (2009) 050, [`0707.2408`].

[206] Y. Hatta, E. Iancu and A. H. Mueller, *Deep inelastic scattering at strong coupling from gauge/string duality: The Saturation line*, JHEP **01** (2008) 026, [`0710.2148`].

[207] L. Cornalba and M. S. Costa, *Saturation in Deep Inelastic Scattering from AdS/CFT*, Phys. Rev. D **78** (2008) 096010, [`0804.1562`].

[208] S. K. Domokos, J. A. Harvey and N. Mann, *The Pomeron contribution to* pp *and* $p\bar{p}$ *scattering in AdS/QCD*, Phys. Rev. D **80** (2009) 126015, [`0907.1084`].

[209] S. K. Domokos, J. A. Harvey and N. Mann, *Setting the scale of the* pp *and* $p\bar{p}$ *total cross sections using AdS/QCD*, Phys. Rev. D **82** (2010) 106007, [`1008.2963`].

[210] N. Anderson, S. K. Domokos, J. A. Harvey and N. Mann, *Central production of* η *and* η' *via double Pomeron exchange in the Sakai-Sugimoto model*, Phys. Rev. D **90** (2014) 086010, [`1406.7010`].

[211] N. Anderson, S. Domokos and N. Mann, *Central production of* η *via double Pomeron exchange and double Reggeon exchange in the Sakai-Sugimoto model*, Phys. Rev. D **96** (2017) 046002, [`1612.07457`].

[212] P. Lebiedowicz, J. Leutgeb, O. Nachtmann, A. Rebhan and A. Szczurek, *Central exclusive diffractive production of axial-vector* $f_1(1285)$ *and* $f_1(1420)$ *mesons in proton-proton collisions*, Phys. Rev. D **102** (2020) 114003, [`2008.07452`].

[213] Y. Hatta and D.-L. Yang, *Holographic* J/ψ *production near threshold and the proton mass problem*, Phys. Rev. D **98** (2018) 074003, [`1808.02163`].

[214] C. A. Ballon Bayona, H. Boschi-Filho and N. R. F. Braga, *Deep inelastic scattering from gauge string duality in the soft wall model*, JHEP **03** (2008) 064, [`0711.0221`].

[215] K. A. Mamo and I. Zahed, *Diffractive photoproduction of* J/ψ *and* Υ *using holographic QCD: gravitational form factors and GPD of gluons in the proton*, Phys. Rev. D **101** (2020) 086003, [`1910.04707`].

[216] A. Karch, E. Katz, D. T. Son and M. A. Stephanov, *Linear confinement and AdS/QCD*, Phys. Rev. D **74** (2006) 015005, [`hep-ph/0602229`].

[217] D0 collaboration, V. M. Abazov et al., *Measurement of the differential cross section $d\sigma/dt$ in elastic $p\bar{p}$ scattering at $\sqrt{s} = 1.96$ TeV*, Phys. Rev. D **86** (2012) 012009, [`1206.0687`].

[218] E. Avsar, Y. Hatta and T. Matsuo, *Odderon in baryon-baryon scattering from the AdS/CFT correspondence*, JHEP **03** (2010) 037, [`0912.3806`].

[219] D. Kharzeev, E. Shuryak and I. Zahed, *Higher order string effects and the properties of the Pomeron*, Phys. Rev. D **97** (2018) 016008, [`1709.04007`].

[220] E. D'Hoker and D. Z. Freedman, *Supersymmetric gauge theories and the AdS/CFT correspondence*, in *Theoretical Advanced Study Institute in Elementary Particle Physics (TASI 2001): Strings, Branes and EXTRA Dimensions*, pp. 3–158, 1, 2002, `hep-th/0201253`.

[221] E. D'Hoker and B. Pourhamzeh, *Emergent super-Virasoro on magnetic branes*, JHEP **06** (2016) 146, [`1602.01487`].

[222] H. Hata, T. Sakai, S. Sugimoto and S. Yamato, *Baryons from instantons in holographic QCD*, Prog. Theor. Phys. **117** (2007) 1157, [`hep-th/0701280`].

[223] N. Bence, L. Jenkovszky and I. Szanyi, *Recent LHC/TOTEM data challenging the standard Regge pole theory*, EPJ Web Conf. **191** (2018) 04009.

[224] M. Froissart, *Asymptotic behavior and subtractions in the Mandelstam representation*, Phys. Rev. **123** (1961) 1053–1057.

[225] A. Martin, *Unitarity and high-energy behavior of scattering amplitudes*, Phys. Rev. **129** (1963) 1432–1436.

[226] Y. Liu and I. Zahed, *Entanglement in Regge scattering using the AdS/CFT correspondence*, Phys. Rev. D **100** (2019) 046005, [`1803.09157`].

[227] A. Donnachie and P. V. Landshoff, *Elastic Scattering and Diffraction Dissociation*, Nucl. Phys. B **244** (1984) 322.

[228] TOTEM collaboration, G. Antchev et al., *Measurement of proton-proton elastic scattering and total cross-section at $\sqrt{s}$ = 7 TeV*, EPL **101** (2013) 21002.

[229] TOTEM collaboration, G. Antchev et al., *Measurement of elastic pp scattering at $\sqrt{s} = 8$ TeV in the Coulomb–nuclear interference region: determination of the ρ -parameter and the total cross-section*, Eur. Phys. J. C **76** (2016) 661, [`1610.00603`].

[230] TOTEM collaboration, G. Antchev et al., *First measurement of elastic, inelastic and total cross-section at $\sqrt{s} = 13$ TeV by TOTEM and overview of cross-section data at LHC energies*, *Eur. Phys. J. C* **79** (2019) 103, [`1712.06153`].

[231] TOTEM collaboration, G. Antchev et al., *First determination of the ρ parameter at $\sqrt{s} = 13$ TeV: probing the existence of a colourless C-odd three-gluon compound state*, *Eur. Phys. J. C* **79** (2019) 785, [`1812.04732`].

[232] ATLAS collaboration, G. Aad et al., *Measurement of the total cross section from elastic scattering in pp collisions at $\sqrt{s} = 7$ TeV with the ATLAS detector*, *Nucl. Phys. B* **889** (2014) 486–548, [`1408.5778`].

[233] ATLAS collaboration, M. Aaboud et al., *Measurement of the total cross section from elastic scattering in pp collisions at $\sqrt{s} = 8$ TeV with the ATLAS detector*, *Phys. Lett. B* **761** (2016) 158–178, [`1607.06605`].

[234] ATLAS collaboration, G. Aad et al., *Measurement of the total cross section and ρ-parameter from elastic scattering in pp collisions at $\sqrt{s} = 13$ TeV with the ATLAS detector*, *Eur. Phys. J. C* **83** (2023) 441, [`2207.12246`].

[235] PARTICLE DATA GROUP collaboration, R. L. Workman et al., *Review of Particle Physics*, *PTEP* **2022** (2022) 083C01.

[236] TOTEM collaboration, G. Antchev et al., *Proton-proton elastic scattering at the LHC energy of $\sqrt{s} = 7$ TeV*, *EPL* **95** (2011) 41001, [`1110.1385`].

[237] TOTEM collaboration, G. Antchev et al., *Evidence for non-exponential elastic proton–proton differential cross-section at low |t| and $\sqrt{s}$=8 TeV by TOTEM*, *Nucl. Phys. B* **899** (2015) 527–546, [`1503.08111`].

[238] TOTEM collaboration, G. Antchev et al., *Elastic differential cross-section $\mathrm{d}\sigma/\mathrm{d}t$ at $\sqrt{s} = 2.76$ TeV and implications on the existence of a colourless C-odd three-gluon compound state*, *Eur. Phys. J. C* **80** (2020) 91, [`1812.08610`].

[239] TOTEM collaboration, G. Antchev et al., *Elastic differential cross-section measurement at $\sqrt{s} = 13$ TeV by TOTEM*, *Eur. Phys. J. C* **79** (2019) 861, [`1812.08283`].

[240] TOTEM collaboration, G. Antchev et al., *Characterisation of the dip-bump structure observed in proton–proton elastic scattering at $\sqrt{s} = 8$ TeV*, *Eur. Phys. J. C* **82** (2022) 263, [`2111.11991`].

[241] Y. Liu, M. A. Nowak and I. Zahed, *The Nambu-Goto string in QCD: Dipole interactions, scattering and entanglement*, `2301.06154`.

[242] J. Czyzewski, J. Kwiecinski, L. Motyka and M. Sadzikowski, *Exclusive η_c photoproduction and electroproduction at HERA as a possible probe of the odderon singularity in QCD*, Phys. Lett. B **398** (1997) 400–406, [`hep-ph/9611225`].

[243] J. Czyżewski, J. Kwieciński, L. Motyka and M. Sadzikowski, *Exclusive η photo- and electroproduction at hera as a possible probe of the odderon singularity in qcd [phys. lett. b 398 (1997) 400]*, Physics Letters B **411** (Oct., 1997) 402.

[244] J. Bartels, M. Braun, D. Colferai and G. Vacca, *Diffractive η_c photo-and electroproduction with the perturbative qcd odderon*, The European Physical Journal C **20** (Apr., 2001) 323–331.

[245] J. P. Ma, *Diffractive photoproduction of η_c*, Nucl. Phys. A **727** (2003) 333–352, [`hep-ph/0301155`].

[246] H. R. Grigoryan and A. V. Radyushkin, *Structure of vector mesons in holographic model with linear confinement*, Phys. Rev. D **76** (2007) 095007, [`0706.1543`].

[247] K. A. Mamo and I. Zahed, *Electromagnetic radii of the nucleon in soft-wall holographic QCD*, `2106.00752`.

[248] European Muon collaboration, J. Ashman et al., *A Measurement of the Spin Asymmetry and Determination of the Structure Function g_1 in Deep Inelastic Muon-Proton Scattering*, Phys. Lett. B **206** (1988) 364.

[249] S. Aoki, M. Doui, T. Hatsuda and Y. Kuramashi, *Tensor charge of the nucleon in lattice QCD*, Phys. Rev. D **56** (1997) 433–436, [`hep-lat/9608115`].

[250] T. N. Pham, *Two-photon decay of heavy quarkonium from heavy-quark spin symmetry*, AIP Conf. Proc. **964** (2007) 124–131, [`0710.2846`].

[251] W.-Y. Liu and I. Zahed, *Photo-production of $\eta_{c,b}$ near Threshold*, `2404.03875`.

[252] E. Shuryak and I. Zahed, *Hadronic structure on the light front. I. Instanton effects and quark-antiquark effective potentials*, Phys. Rev. D **107** (2023) 034023, [`2110.15927`].

[253] A. Accardi et al., *Electron Ion Collider: The Next QCD Frontier: Understanding the glue that binds us all*, Eur. Phys. J. A **52** (2016) 268, [`1212.1701`].

[254] R. Abdul Khalek et al., *Science Requirements and Detector Concepts for the Electron-Ion Collider: EIC Yellow Report*, Nucl. Phys. A **1026** (2022) 122447, [`2103.05419`].

[255] U. Camerini, J. G. Learned, R. Prepost, C. M. Spencer, D. E. Wiser, W. Ash et al., *Photoproduction of the ψ Particles*, Phys. Rev. Lett. **35** (1975) 483.

[256] B. Gittelman, K. M. Hanson, D. Larson, E. Loh, A. Silverman and G. Theodosiou, *Photoproduction of the $\psi(3100)$ Meson at 11 GeV*, Phys. Rev. Lett. **35** (1975) 1616.

[257] GlueX collaboration, A. Ali et al., *First Measurement of Near-Threshold J/ψ Exclusive Photoproduction off the Proton*, Phys. Rev. Lett. **123** (2019) 072001, [1905.10811].

[258] TXL, T(X)L collaboration, G. S. Bali, B. Bolder, N. Eicker, T. Lippert, B. Orth, P. Ueberholz et al., *Static potentials and glueball masses from QCD simulations with Wilson sea quarks*, Phys. Rev. D **62** (2000) 054503, [hep-lat/0003012].

[259] S. K. Domokos and N. Mann, *Glueball-meson mixing in holographic QCD*, JHEP **06** (2022) 029, [2202.12963].

[260] L. J. Romans, *Massive N=2a Supergravity in Ten-Dimensions*, Phys. Lett. B **169** (1986) 374.

[261] E. Byckling and K. Kajantie, *Particle Kinematics: (Chapters I-VI, X).* University of Jyvaskyla, Jyvaskyla, Finland, 1971.

[262] S. J. Brodsky, E. Chudakov, P. Hoyer and J. M. Laget, *Photoproduction of charm near threshold*, Phys. Lett. B **498** (2001) 23–28, [hep-ph/0010343].

[263] Y. Guo, X. Ji and Y. Liu, *QCD Analysis of Near-Threshold Photon-Proton Production of Heavy Quarkonium*, Phys. Rev. D **103** (2021) 096010, [2103.11506].

[264] P. Sun, X.-B. Tong and F. Yuan, *Near threshold heavy quarkonium photoproduction at large momentum transfer*, Phys. Rev. D **105** (2022) 054032, [2111.07034].

[265] R. P. Feynman, *Very high-energy collisions of hadrons*, Phys. Rev. Lett. **23** (1969) 1415–1417.

[266] A. Deur, S. J. Brodsky and G. F. De Téramond, *The Spin Structure of the Nucleon*, 1807.05250.

[267] L. V. Gribov, E. M. Levin and M. G. Ryskin, *Semihard Processes in QCD*, Phys. Rept. **100** (1983) 1–150.

[268] A. H. Mueller, *Soft gluons in the infinite momentum wave function and the BFKL pomeron*, Nucl. Phys. B **415** (1994) 373–385.

[269] H1, ZEUS collaboration, H. Abramowicz et al., *Combination of measurements of inclusive deep inelastic $e^{\pm}p$ scattering cross sections and QCD analysis of HERA data*, Eur. Phys. J. C **75** (2015) 580, [1506.06042].

[270] D. K. Hong, T. Inami and H.-U. Yee, *Baryons in AdS/QCD*, *Phys. Lett. B* **646** (2007) 165–171, [hep-ph/0609270].

[271] D. K. Hong, M. Rho, H.-U. Yee and P. Yi, *Dynamics of baryons from string theory and vector dominance*, *JHEP* **09** (2007) 063, [0705.2632].

[272] D. K. Hong, M. Rho, H.-U. Yee and P. Yi, *Chiral Dynamics of Baryons from String Theory*, *Phys. Rev. D* **76** (2007) 061901, [hep-th/0701276].

[273] D. Britzger, C. Ewerz, S. Glazov, O. Nachtmann and S. Schmitt, *The Tensor Pomeron and Low-x Deep Inelastic Scattering*, *Phys. Rev. D* **100** (2019) 114007, [1901.08524].

[274] A. V. Manohar, *An Introduction to spin dependent deep inelastic scattering*, in *Lake Louise Winter Institute: Symmetry and Spin in the Standard Model*, 3, 1992, hep-ph/9204208.

[275] F. Halzen and A. D. Martin, *Quarks and Leptons: An Introductory Course in Modern Particle Physics.* Wiley & Sons Ltd, New York, USA, 1984.

[276] H1 collaboration, C. Adloff et al., *A Measurement of the proton structure function $F_2(x, Q^2)$ at low x and low Q^2 at HERA*, *Nucl. Phys. B* **497** (1997) 3–30, [hep-ex/9703012].

[277] ZEUS collaboration, J. Breitweg et al., *Measurement of the proton structure function F_2 and $\sigma_{tot}(\gamma^* p)$ at low Q^2 and very low x at HERA*, *Phys. Lett. B* **407** (1997) 432–448, [hep-ex/9707025].

[278] H1 collaboration, S. Aid et al., *Measurement of the total photon-proton cross-section and its decomposition at 200 GeV center-of-mass energy*, *Z. Phys. C* **69** (1995) 27–38, [hep-ex/9509001].

[279] ZEUS collaboration, S. Chekanov et al., *Measurement of the photon proton total cross-section at a center-of-mass energy of 209 GeV at HERA*, *Nucl. Phys. B* **627** (2002) 3–28, [hep-ex/0202034].

[280] G. M. Vereshkov, O. D. Lalakulich, Y. F. Novoseltsev and R. V. Novoseltseva, *Total cross section for photon nucleon interaction in the energy range $\sqrt{s}$ = 40 GeV - 250 GeV*, *Phys. Atom. Nucl.* **66** (2003) 565–574.

[281] C. Ewerz, M. Maniatis and O. Nachtmann, *A Model for Soft High-Energy Scattering: Tensor Pomeron and Vector Odderon*, *Annals Phys.* **342** (2014) 31–77, [1309.3478].

[282] K. A. Mamo and I. Zahed, *Quark and gluon GPDs at finite skewness from strings in holographic QCD: Evolved and compared with experiment*, *Phys. Rev. D* **108** (2023) 086026, [2206.03813].

List of Abbreviations

A

AdS Anti de-Sitter

ALICE A Large Ion Collider Experiment at the LHC

B

BELLE Experiment at KEK

BEPC Beijing Electron-Positron Collider

BES Beijing Spectrometer at the BEPC

BFKL Balitskii-Fadin-Kuraev-Lipatov

BKP Bartels-Kwiecinski-Praszalowicz

BLV Bartels-Lipatov-Vacca

BNL Brookhaven National Laboratory, New York (USA)

C

CDF Collider Detector at Fermilab

CEP Central Exclusive Production

CERN European Organization for Nuclear Research, Geneva (Switzerland)

CFT Conformal Field Theory

CGC Color Glass Condensate

Crystal Barrel Experiment at CERN searching for non-$q\bar{q}$ states in $p\bar{p}$ annihilation

CS Chern-Simons

D

DBI Dirac-Born-Infeld

DESY Deutsches Elektronen-Synchrotron, Hamburg (Germany)

DGI Dilute Gas of Instantons

DIS Deep Inelastic Scattering

DØ Experiment at the Tevatron Collider

DVCS Deeply Virtual Compton Scattering

E

EIC Electron-Ion Collider

eLSM Extended Linear Sigma Model

EMC European Muon Collaboration at CERN

F

FNAL Fermi National Accelerator Laboratory (Fermilab), Illinois (USA)

G

GAMS Experiment at CERN dedicated to resonant searches of non-$q\bar{q}$ states

GKPW Gubser-Klebanov-Polyakov-Witten

GPD Generalized PDF

GSO Gliozzi-Scherk-Olive

GTMD Generalized TMD

H

HERA Hadron Elektron Ring Anlage, DESY (Germany)

hQCD Holographic QCD

J

JLab Thomas Jefferson National Accelerator Facility, Virginia (USA)

JW Janik-Wosiek

K

KEK	High Energy Accelerator Research Organization, Tsukuba (Japan)

L

LHC	Large Hadron Collider
LIPS	Lorentz Invariant Phase Space
LSZ	Lehmann–Symanzik–Zimmermann

N

NS	Neveu-Schwarz

P

PDF	Parton Distribution Function
PDG	Particle Data Group
PGH	Pomeron Glueball Hypothesis
pQCD	perturbative QCD

Q

QCD	Quantum Chromodynamics

R

R	Ramond
RHIC	Relativistic Heavy-Ion Collider
RNS	Ramond–Neveu–Schwarz

S

SSA	Single Spin Asymmetry
SYM	Super Yang-Mills

T

TMD	Transverse Momentum Distribution
TOTEM	Total Elastic and Diffractive Cross Section Measurement at the LHC
TPM	Tensor Pomeron Model

U

UV	ultraviolet

V

VMD	Vector Meson Dominance

W

WA102	Experiment at CERN dedicated to search for centrally produced non-$q\bar{q}$ states
WSS	Witten-Sakai-Sugimoto
WZW	Wess-Zumino-Witten

Z

Zeus	Detector at HERA

Die approbierte gedruckte Originalversion dieser Dissertation ist an der TU Wien Bibliothek verfügbar.
The approved original version of this doctoral thesis is available in print at TU Wien Bibliothek.
TU Bibliothek WIEN Your knowledge hub

Index

Symbols
$\rho\pi$ puzzle, 86

A
A-roof genus, 25

E
Eikonalization in AdS, 136

F
Field-operator map
    Boundary asymptotics, 15
    Representations, 15
Forward Compton scattering, 202
Fragmented scalar glueball, 72
Froissart-Martin bound, 136

G
Gell-Mann matrices, 8
Gell-Mann-Oakes-Renner relation, 9
    in holographic QCD, 29
GKPW formula, 15
Gribov diffusion, 137
GSO projection, 24

H
Hadronic decays of the
    Dilaton scalar glueball, 67
    Exotic scalar glueball, 62
    Pseudoscalar glueball, 73
    Pseudovector glueball, 76
    Tensor glueball, 87
    Vector glueball, 79
Hadronic tensor, 201
    Unploarized, 203
Hard-wall model
    Mass spectrum
        Spin-1, 154
    Normalizable modes
        Spin-1, 154
Holographic dictionary, 14

L
Landau-Yang theorem, 37
Leptonic tensor, 201

M
Mass spectrum
    Dilaton scalar glueball, 49
    Exotic scalar glueball, 48
    Pseudoscalar glueball, 50
    Pseudovector glueball, 51
    Tensor glueball, 53
    Vector glueball, 52
Mixing
    $K_1(1270)K_1(1400)$, 33
    $\eta\eta'$, 29
    $f_1(1285)f_1(1420)$, 33
    Pseudoscalar glueball, 54
    Vector glueball, 56

O
Odderon
    in Gauge/Gravity duality, 111
    in pQCD, 109
Optical theorem, 202

P
Pomeron

- in Gauge/Gravity duality, 111
- in pQCD, 108

Pomeron glueball hypothesis, 108

Pontryagin classes, 25

R

Radiative decays of the
- Dilaton scalar glueball, 92
- Exotic scalar glueball, 90
- Pseudoscalar glueball, 96
- Pseudovector glueball, 97
- Tensor glueball, 103
- Vector glueball, 98

Reduced cross section, 204

Repulsive-wall model
- Bulk-to-bulk propagator
  - Odderon, 123
  - Pomeron, 122
- Eikonalized
  - Amplitude, 137
  - B parameter, 140
  - Differential cross section, 142
  - rho parameter, 139
  - Total cross section, 138
- Fermions, 127
- Fit
  - Differential cross section, 144
  - Forward quantities, 140
- Metric, 115
- Odderon-Nucleon vertex, 132
- Pomeron-Nucleon vertex, 131
- Signature factors, 134

S

Smeared branes, 179

Soft-wall model
- Bulk-to-boundary propagator, 153
- Bulk-to-bulk propagator, 153
- Charge radius
  - C-odd gluonic, 159
- Dilaton, 148
- Form factors
  - C-odd gluonic, 158
  - Electromagnetic, 157
- Mass spectrum
  - Fermion, 151
  - Pseudoscalar, 149
  - Spin-1, 152
- Metric, 147
- Normalizable modes
  - Fermion, 150
  - Pseudoscalar, 149
  - Spin-1, 152
- Parameter choice, 153
- Vertices
  - Odderon, 155
  - Photon, 156

Sommerfeld-Watson transform, 119

Structure functions
- $F_1,\ F_2$, 203
- $W_1,\ W_2$, 203

T

Transition form factor
- Tensor glueball, 205

W

Witten-Sakai-Sugimoto model
- Action
  - Chern-Simons, 25
  - Closed string, 24
  - Dirac-Born-Infeld, 25
- Background, 23
- Mass spectrum
  - Glueballs, 45
  - Mesons, 27
- Parameter choices
  - ’t Hooft coupling λ, 28
  - Kaluza-Klein mass M_{KK}, 28
- Parameter definitions

  - $\eta\eta'$ mixing angle θ_P, 30
  - ’t Hooft coupling λ, 26
  - AdS radius R_{D4}, 24
  - Kaluza-Klein mass M_{KK}, 23
  - Kaluza-Klein radius U_{KK}, 23
  - Pion decay constant f_π, 28
  - String tension σ_s, 28
  - Topological susceptibility χ_g, 29
  - Witten-Veneziano mass m_{η_0}, 29
- Witten-Veneziano mechanism, 28
- Wronskian, 120